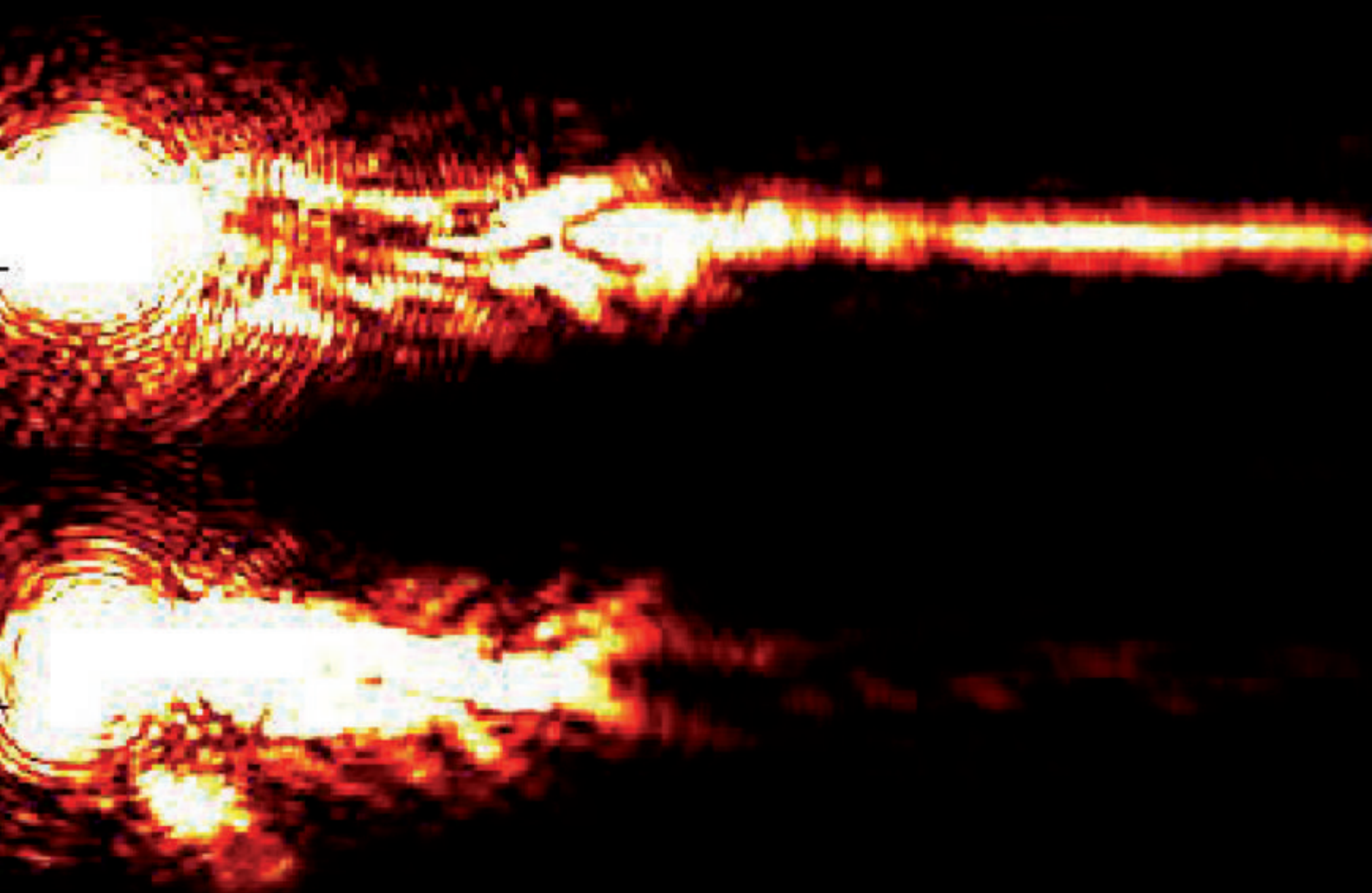


Andreas Seidel

**Plasmonic Components Fabricated
by Two-Photon Polymerization
and Nanoimprint Lithography**



Cuvillier Verlag Göttingen
Internationaler wissenschaftlicher Fachverlag

Plasmonic Components Fabricated by Two-Photon Polymerization and Nanoimprint Lithography

Von der Fakultät für Mathematik und Physik
der Gottfried Wilhelm Leibniz Universität Hannover
zur Erlangung des Grades eines

Doktors der Naturwissenschaften
- Dr. rer. nat. -

genehmigte Dissertation

von

Dipl.-Phys. Andreas Seidel
geboren am 27. Januar 1981, in Heidelberg

2010

Bibliografische Information der Deutschen Nationalbibliothek

Die Deutsche Nationalbibliothek verzeichnet diese Publikation in der Deutschen Nationalbibliografie; detaillierte bibliografische Daten sind im Internet über <http://dnb.d-nb.de> abrufbar.

1. Aufl. - Göttingen: Cuvillier, 2010

Zugl.: Hannover, Univ., Diss., 2010

978-3-86955-604-8

Referent: Prof. Dr. Boris Chichkov

Korreferent: Prof. Dr. Uwe Morgner

Tag der Promotion: 17. Dezember 2010

© CUVILLIER VERLAG, Göttingen 2010

Nonnenstieg 8, 37075 Göttingen

Telefon: 0551-54724-0

Telefax: 0551-54724-21

www.cuvillier.de

Alle Rechte vorbehalten. Ohne ausdrückliche Genehmigung des Verlages ist es nicht gestattet, das Buch oder Teile daraus auf fotomechanischem Weg (Fotokopie, Mikrokopie) zu vervielfältigen.

1. Auflage, 2010

Gedruckt auf säurefreiem Papier

978-3-86955-604-8

Kurzzusammenfassung

Die Plasmonik ist ein immer wichtiger werdender Bereich im größeren Forschungsgebiet der Photonik. Dabei ist ein Schwerpunkt die Entwicklung von photonischen Komponenten, die sich in den verschiedensten Konfigurationen von Metallen und Dielektrika die Eigenschaften von Oberflächenplasmonenmoden zunutze machen. Solche Komponenten können in einer Vielzahl von Anwendungen, sei es im meßtechnischen Bereich, oder in der Datenübertragung innerhalb elektronischer Bausteine, große Vorteile gegenüber herkömmlichen Bauteilen besitzen. Plasmonische Komponenten, die auf dielektrischen Plasmonenwellenleitern basieren, erzeugen in jüngster Vergangenheit ein ganz besonderes Interesse, da sie relativ leicht hergestellt werden können, und zur Miniaturisierung von optischen Schaltkreisen beitragen können.

Die Zwei-Photonen-Polymerisation ist bereits als leistungsfähiges Herstellungsverfahren bei der Produktion von plasmonischen Wellenleitern etabliert. Diese Dissertation baut auf den bisherigen Arbeiten zu diesem Thema auf, und erweitert die Herstellungsmethode um einen Nanolithographieprozess. Dieser Prozess behebt die größte intrinsische Schwäche der Zwei-Photonen-Polymerisation, indem er aus einem seriellen einen parallelen Prozess macht. Mit Hilfe dieses neuartigen Herstellungsverfahrens bleibt die Produktion von plasmonischen Wellenleitern optimal flexibel, wird aber deutlich schneller und billiger.

In dieser Arbeit werden plasmonische Wellenleiterstrukturen vorgestellt, wie zum Beispiel polarisierungsabhängige Strahlteiler, Mach-Zehnder Interferometer und eine neue Klasse von Strukturen - die Rennbahnresonatoren. Größtenteils mit Hilfe von Leckstrahlungsmikroskopie werden die Strukturen analysiert und charakterisiert, und mit auf anderen Wegen hergestellten Strukturen verglichen. Die Strukturen aus dieser Arbeit zeigen, insofern sie vergleichbar sind, verbesserte Charakteristika gegenüber den Ergebnissen aus früheren Arbeiten.

Es schließt sich an eine Diskussion von neuartigen optischen Phänomenen im Zusammenhang mit lokalisierten Oberflächenplasmonen, wie zum Beispiel die Interferenz zweier Plasmonenstrahlen und die Wechselwirkung eines Oberflächenplasmons mit metallischen Nanokorpuskeln. Einige der Effekte, die hier beschrieben werden, sind vorher noch nicht so beobachtet worden.

Im Laufe dieser Arbeit entstanden bereits neun wissenschaftliche Artikel, die in Fachzeitschriften veröffentlicht sind, sowie eine größere Anzahl an Konferenzbeiträgen und -verhandlungen.

Schlagworte: Nanoherstellung, Zwei-Photonen-Polymerisation, Plasmonik

Abstract

Plasmonics is an increasingly important field of research within the larger field of photonics. Photonic components utilizing surface plasmon polariton modes, supported by various metal-dielectric configurations, hold the promise of a variety of applications in sensing and on-chip data transmission. Plasmonic components based on dielectric-loaded plasmon polariton waveguides are in particular attracting attention recently, due to their comparative ease of manufacture and their potential to aid in miniaturizing optical circuits.

The two-photon polymerization direct laser writing technology has already been shown to be a powerful tool in the fabrication of plasmonic waveguides. This thesis builds on previous work that has already shown the viability of two-photon polymerization as a manufacturing technique, and expands upon it by adding a nanolithography process. The largest intrinsic disadvantage of direct laser writing is overcome in this fashion - instead of a purely serial process, a parallel fabrication process is developed. By aid of this process, the fabrication of plasmonic waveguides becomes not only optimally flexible, but also faster and cheaper.

The plasmonic waveguide structures presented in this thesis represent new designs not shown before, including polarization-dependent splitters, Mach-Zehnder interferometers, and a new class of structure called racetrack resonators. The designs are characterized largely by leakage radiation microscopy and compared to similar designs fabricated by different methods. Where comparison is possible, the structures presented here show much improved characteristics over results previously reported by other groups.

An investigation of localized surface plasmons is also made, which includes the interference of surface plasmons with each other and the interaction of surface plasmons with metal nanoparticles. This has led to new optical effects, which have not been observed in this way before.

This thesis resulted in nine scientific articles, that have been published in peer-reviewed journals, as well as a number of conference contributions and proceedings.

Key words: nanofabrication, two-photon polymerization, plasmonics

Contents

1	Introduction	1
1.1	A Brief Introduction to the History of Optics & Plasmonics	1
1.2	Introduction to Surface Plasmon-Polaritons	5
1.3	Motivation for DLSPPW	8
1.3.1	Silicon on Insulator	12
1.3.2	Photonic Crystals	13
1.3.3	Dielectric-Loaded Surface Plasmon-Polariton Waveguides	15
2	Fabrication Methods	16
2.1	Direct Laser Writing by 2-Photon Polymerization	16
2.1.1	2-Photon Polymerization	16
2.1.2	Description of 2PP setup	19
2.1.3	2PP Fabrication Software and Programmes	21
2.1.4	2PP Fabrication Procedures	21
2.1.5	2PP on Glass vs. Gold	22
2.2	Nanoimprint Lithography	23
2.3	Comparison with Other Fabrication Methods	25
2.3.1	UV Mask Lithography	25
2.3.2	Electron Beam Lithography	27
2.3.3	Less Common Methods & Tabular Comparison of Fabrication Methods	27
2.4	Overview of Equipment and Resist Materials	29
2.4.1	Lasers for 2PP	29
2.4.2	Photoresists Used in Fabrication	30
3	Simulation Tools	34
3.1	FDTD Simulations	34
3.2	Green's Tensor Calculations	39
4	Characterization Methods	44
4.1	Introduction to Leakage Radiation Microscopy	44
4.2	Principles of Leakage Radiation Microscopy	45
4.2.1	Description of Experimental Setup	46
4.2.2	Description of Result Analysis	49
4.3	Fibre-Coupled Measurements	52
4.4	Scanning Near-Field Optical Microscope	53
4.5	Comparison of Plasmonic Characterization Techniques	55
4.6	Other Characterization Tools	55
4.6.1	Optical Microscope	55
4.6.2	Scanning Electron Microscope	56
4.6.3	Confocal Imaging Profiler	57

5	Dielectric-Loaded Surface Plasmon-Polariton Waveguide Components Fabricated by Direct Laser Writing	58
5.1	Simple Structures - Lines and Bends	58
5.2	Mach-Zehnder Interferometers	70
5.3	Racetrack Resonators	75
5.4	Symmetric and Asymmetric Splitters	77
6	Nanoimprinted Dielectric-Loaded Surface Plasmon-Polariton Waveguides	85
6.1	Nanoimprinted DLSPPW for Leakage Radiation Microscopy	85
6.2	Fibre-coupled DLSPPW	89
7	Localized Surface Plasmon Experiments	106
7.1	Interference of SPPs	106
7.2	Interaction of SPPs with Gold Nanoparticles	109
7.3	Plasmonic Black Holes	119
8	Conclusion & Outlook	123
9	Bibliography	125
A	List of Scientific Publications by the Author	148
A.1	List of Journal Articles	148
A.2	List of Invited and Post Deadline Talks	149
A.3	List of Conference Contributions and Proceedings	149
B	Curriculum Vitae	152
C	Acknowledgements	153

List of Recurrent Acronyms

<i>1D</i>	one-dimensional
<i>2D</i>	two-dimensional
<i>2.5D</i>	two-and-a-half-dimensional: implies a technology using layer-by-layer fabrication, where new layers can only be placed over existing ones. No overhanging structures are possible. Also known as quasi-2D.
<i>2PA</i>	two-photon absorption
<i>2PP</i>	two-photon polymerization
<i>3D</i>	three-dimensional
<i>DLSPPW</i>	dielectric-loaded surface plasmon-polariton waveguide
<i>EIM</i>	effective index method
<i>FDTD</i>	finite-difference time-domain
<i>InGaAs</i>	Indium-Gallium-Arsenide
<i>LRM</i>	leakage radiation microscopy
<i>LZH</i>	Laser Zentrum Hannover
<i>M3D(L)</i>	LZH-built machine for 2PP fabrication
<i>MZI</i>	Mach-Zehnder interferometer
<i>NIR</i>	near infra-red, here taken to mean 0.8 - 1.6 μm in wavelength
<i>nm</i>	nanometer ($\equiv 10^{-9}$ meter)
<i>PDMS</i>	polydimethylsiloxane
<i>SEM</i>	scanning electron microscope
<i>SNOM</i>	scanning near-field optical microscope
<i>SPP</i>	surface plasmon-polariton
<i>TE</i>	transverse electric
<i>TM</i>	transverse magnetic

1 Introduction

The introductory section of this thesis aims to provide insight and introduction into the field of research of surface plasmonics in general and dielectric-loaded surface-plasmon polariton waveguides in particular. The motivation for this research is given by illuminating the background and the history of the field.

1.1 A Brief Introduction to the History of Optics & Plasmonics

Optics is, beyond any doubt, one of the main drivers behind a revolution in the world of science and technology today, and has been for the past decades [1, 2, 3, 4]. But the story of optics is an incredibly old one, older than man, older even than the Solar System. In order to shed some light on this issue, we will divide the story of optics into two parts - the part where humans actively shape and control light, and the part where optical phenomena and devices appeared and developed without the influence of man. We will deal with the latter part first.

Beyond any doubt, the oldest and by far the largest lenses in existence are the astrophysical gravitational lenses, composed of stellar bodies (from individual stars up to galaxy clusters) whose gravitational field warps space so that light travelling through them becomes distorted as if it were passing through an optical lens. These lenses were first considered by Albert Einstein in 1936 [5], and have been put to very good use since, despite Einstein's skepticism concerning their utility. We will leave these lenses aside. We will also leave aside the plethora of primeval astrophysical masers (coherent microwave beam sources), of which an ever-increasing number has been discovered since 1965 [6, 7], and even the much rarer astrophysical lasers, which are a comparatively recent discovery [8]. While these subjects are fascinating, the content of this thesis will remain closer to Earth, and closer to optics applications which all humans may one day use.

Biological development of optical devices, however, still precedes human involvement by some five hundred million years, with the "invention" of the first image-forming eye around 543 million years ago in trilobites, a group of extinct marine arthropods [9]. It has been suggested that nature's developing of this first image-forming device sparked the Cambrian Explosion in evolution, as the size, shape, colour, and behaviour of animals were revealed, and tremendous evolutionary pressure was created to evolve hard external parts as defences, as well as limbs for swimming and clasping, either to catch prey or to escape [10]. Over the course of millions of years since the "invention of the eye", nature continued to evolve ever more specialized optical components. Diffraction gratings, narrow- and broadband reflectors, liquid crystals, anti-reflection coatings, and photonic crystals including photonic crystal fibres have all been found both in prehistoric and extant animal and plant species, sometimes in surprisingly distinct forms [10]. Human research, it seems, is only slowly catching up to what nature developed long ago.

It is not known how or when man gained consciousness or started to think abstractly about his surroundings. But it is very likely that his eyesight had a major part in the origin of his consciousness. When man first gazed at the heavens and pondered on their origins, when he first conceived simple forms of astronomical observation and religious worship of heavenly bodies, he was, in fact, already laying the foundations for optics. One could make a case that the first optical instruments were the vast neolithic monuments at Stonehenge and elsewhere [11, 12]. The real history of optics, that is the manipulation of light to serve humanity's needs, begins with the first lens-making activity by the ancient Egyptians [13] and Assyrians [14]. While the precise use of the lenses fabricated in antiquity is not always entirely clear, and their everyday occurrence has been questioned [15], it is hardly conceivable that their remarkable optical properties escaped notice.

But man was never a pure experimentalist. He soon discovered that all things in nature, including all things optical, can be described in laws and mathematics. The law of refraction, first discovered in its correct form by Ibn Sahl in 984 and rediscovered by Snellius in 1621 [16, 17, 18] was one of the earliest optical laws to be discovered. When the telescope was invented, credited today to the German lensmaker Hans Lippershey, and improved by Galileo Galilei a short time later, this was the beginning of a revolution both in science and our view of the world as a whole [19].

Since that moment, optical science has progressed in leaps and bounds as a multitude of linear and nonlinear optical processes were discovered, characterized, and formulated as scientific laws, to be harnessed in applications or used to enable further discoveries. In 1861 and 1865, James Clerk Maxwell published two papers, in which he concluded that light was an electromagnetic wave and also laid down four fundamental equations, known today as "Maxwell's Equations" that form the basis of all modern attempts at electromagnetic and optical engineering [20, 21].

The latest revolution in optics could be said to have started when Theodore H. Maiman built the first working laser in 1960 [22]. This "solution without a problem" soon became the most vital instrument in modern research and has also become a ubiquitous tool in our everyday lives, be it in our computer, DVD player, or simply the provider of communications signal when we make a long-distance telephone call.

As the field of optics continues to evolve, with feature sizes steadily decreasing in efforts to miniaturize and economize, new factors come into play. Materials change their properties at short length scales, and on the nano-scale, significantly so [23]. The next big challenge, which may lead to the next revolution in optics and science as a whole, is to harness the electromagnetic characteristics of materials at the nanoscale, and the key to this is plasmonics.

The history of plasmonics probably begins with the Lycurgus Cup, which today is in the British Museum in London, shown in figure 1.1. The cup is highly unusual in many respects, but from a physical (and plasmonic) point of view, most interesting of all are its optical properties. The cup is made of glass which contains gold and silver nanoparticles [24]. The nanoparticles have a strong influence on the scattering of the

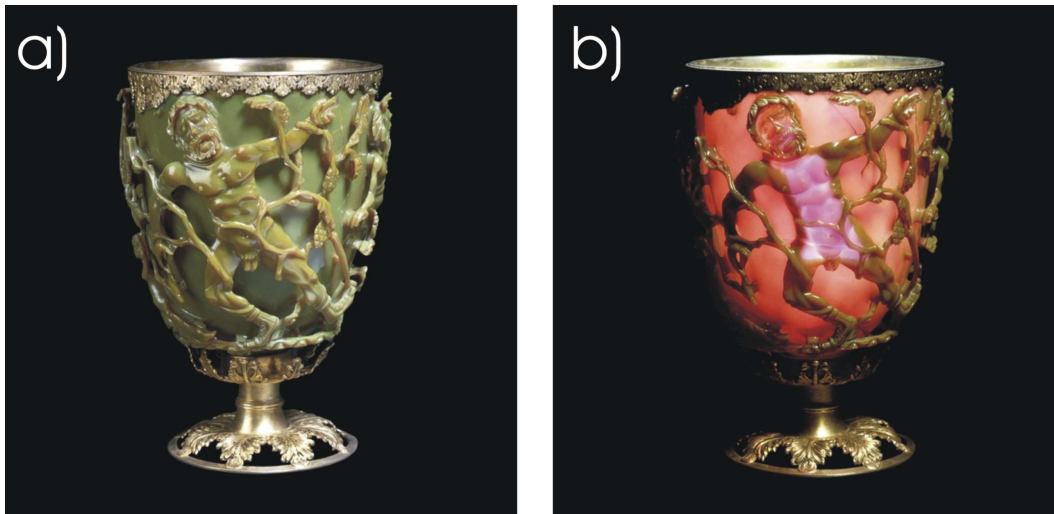


Figure 1.1: The Lycurgus Cup. Late Roman, 4th century AD. Probably made in Rome. A dichroic glass cup with a mythological scene. Source of images and caption: British Museum

light so that the cup looks opaque green when viewed in reflection and translucent red to pink when viewed in transmission. The Romans presumably knew about this effect, because the cup is thought to be designed not for drinking but as a lamp, and in this role the glass cup would display its properties at their best. Several other fragments of similar glass from Roman times have been found, but no whole vessels. It seems likely that the art of making this kind of colloid-coloured glass was lost, since no evidence of continued production has been found. It seems possible that the knowledge was constrained to one single glass workshop, and perhaps even only one single master glass-maker, an explanation that has also been proffered for a rare group of Islamic lustre ceramics with similarly spectacular metal-based optical effects [25]. An alternative explanation is that there was only one lucky block of raw glass, which was created with these properties accidentally.

In Europe, research or work of any kind involving colloidal gold began again only at the end of the 16th century [26]. At the same time, it should be emphasized that the use of silver and copper in glass colouring and glazing was commonplace since antiquity and remained so [25]. Medieval stained-glass church windows, insofar as they have been investigated, are not coloured with colloidal gold. All examples of red stained-glass from this period that have been analyzed were found to be either clear glass coloured with a thin overlay of copper or painted red [24, 27].

The resurgence of colloidal gold was possibly inspired by Islamic use of gold-ruby glass [28], but certainly Georgius Agricola mentioned a ruby-red colour to be obtained by dissolving gold in a liquid in his works [26]. The great German alchemist and father of modern chemistry Andreas Libau (a.k.a. Libavius) mentions the same thing in his most well-known work *Alchemia*, published in 1597 [29]. Johann Rudolf Glauber takes up the idea and proposes rebuilding the German economy (devastated

by the Thirty Years' War) by, amongst other things, large-scale production of high-quality glassware using gold-based red as the colourant, and gives a recipe for it as well [30]. Following early experiments with gold colloid solutions by Andreas Cassius [31] and Johann Christian Orschall [32], the breakthrough discovery of a repeatable and controllable process for using gold nanoparticles to colour glass are made by Johann Kunckel in the early 18th century [33], who at the time was the chief glass-maker of Friedrich Wilhelm of Brandenburg. The process quickly became widely popular, with the largest centres of ruby glass production later to be found in Bohemia and Victorian Britain.

Gold colloid solutions were also rapidly adopted as an enamel paint for porcelain, used in Meissen no later than 1719 and in China a mere four years later [26], possibly introduced through German Jesuits [28]. However, due to the lack of high-resolution microscopes at the time, none of the aforementioned early scientists really knew the exact physical nature of the gold solution they were using. It was not until the very late 19th century that the full explanation was finally given by Richard Adolf Zsigmondy, who was able to show that the colour was due to the absorption spectrum of gold nanoparticles, and who became the first person to measure what we know today as the “plasmon resonance” [34].

The connection between the absorption behaviour of colloidal gold and electromagnetic waves was established only slowly. The German physicist Paul Drude developed a model to explain the electric conductivity of metals [35, 36]. This model was later refined by Arnold Sommerfeld, who applied quantum mechanics and replaced the Maxwell-Boltzmann statistics of the model with Fermi-Dirac statistics [37, 38]. This model has established itself as the “free electron model” today and can be used to describe a situation involving non-bound electrons that are freely movable in metals or plasmas. Doubtless, this model was of some use to the American Irving Langmuir, who discovered and analyzed oscillations of electrons in plasma a short time later in 1929 [39]. Such oscillations of electrons can not only take place in plasmas, or nanoparticles, but also on conducting surfaces.

Initial interest in electromagnetic surface waves came from wireless telegraphy at the beginning of the 20th century, as scientists such as Jonathan Zebeck and Arnold Sommerfeld considered the effect of the ground (be it water, earth or a good conductor such as metal) on radio signals [40, 41]. Consequently, Zebeck was originally called onto this field of research in the year 1900 to replace a seasick post-doctoral researcher on the steamer *Silvana* and was introduced to electromagnetic waves by steaming about the North Sea taking measurements [42]. This certainly seems more entertaining than most research in electromagnetic surface waves today, which is conducted in blacked-out laboratories in order to contain laser radiation.

The first deliberate excitation of electromagnetic surface waves was performed rather more directly, by using fast electrons and shooting them at a target. Electric excitation of plasma oscillations was proposed by Bohm and Pines in the early 1950s [43, 44] and confirmed experimentally in 1955 by analyzing the losses of an electron beam passing through a thin metal film [45]. While some people believed these losses

to be due to interband transitions of conduction band electrons in the metal, instead of the generation of plasmons, these doubts were laid to rest after the early results were expanded upon and generalized briefly afterwards [46]. In the year 1968, a study on the excitation of plasmons in metal particles, the exact phenomenon that had fascinated glass-workers from the Romans until the Victorian era, was presented by Fujimoto and Komaki, which also included a section on the optical effects we now associate with plasmons [47].

In the 1950s, people began considering electromagnetic surface waves as useful for the characterization of the surface quality of metal parts. This motivated the early research by Otto and Kretschmann, who were the first to deliberately excite plasmon waves on metal surfaces at optical frequencies using prisms [48, 49].

With the coming of improved microscopy techniques, such as electron beam microscopes and confocal microscopy, this field too receded and faded away. What launched the current wave of research in plasmonics was really the ground-breaking discovery by Ebbesen, which he made in 1989 and published nine years later in 1998 when he could finally explain it [50]. He had made a thin gold film perforated with holes a couple of hundred nanometers wide, which according to scientific opinion at the time should not have transmitted measurable quantities of light. Not only did the film transmit light - more light was transmitted than actually struck the holes. Surface plasmons were the answer [51]. This amazing discovery sparked a wide range of investigations into plasmonic phenomena, which is still continuing [52].

1.2 Introduction to Surface Plasmon-Polaritons

In physical terms, a plasmon is the quantum of plasma oscillations [43, 46], analogous to the photon as the quantum of electromagnetic wave oscillations, or the phonon as the quantum of mechanical oscillations in a crystal lattice. The easiest way to understand what a plasmon is, is to consider a metal nanoparticle that is struck by an electromagnetic wave. The free electrons in the metal particle form something like a free electron gas and this, of course, reacts to the electric field of the electromagnetic wave. What ensues is a driven harmonic oscillator, with the electromagnetic field driving the oscillation of the electron gas. Like any other harmonic oscillator, the electron gas oscillation has a resonance frequency (which is mostly dependent on the geometry of the particle). If broadband (white) light is used to excite the oscillations, a peak will appear in the absorption spectrum where the energy of the photons is transformed into electron oscillations. This is known as the plasmon resonance. Plasmons may also occur on surfaces. In this case they are called surface plasmon-polaritons (SPPs) and may be understood as longitudinal electron density waves, which can propagate along a metal surface. The phenomenon of plasmon resonances and SPPs has attracted a large amount of interest in recent years [53, 54].

The difficulty of exciting a propagating SPP wave on a metal surface is best illustrated by looking at the dispersion relations of light and SPPs, shown in figure 1.2. The dispersion curve of light is a straight line, while the dispersion curve of an SPP is curved. For low values of wavelength and k-vector the two curves appear

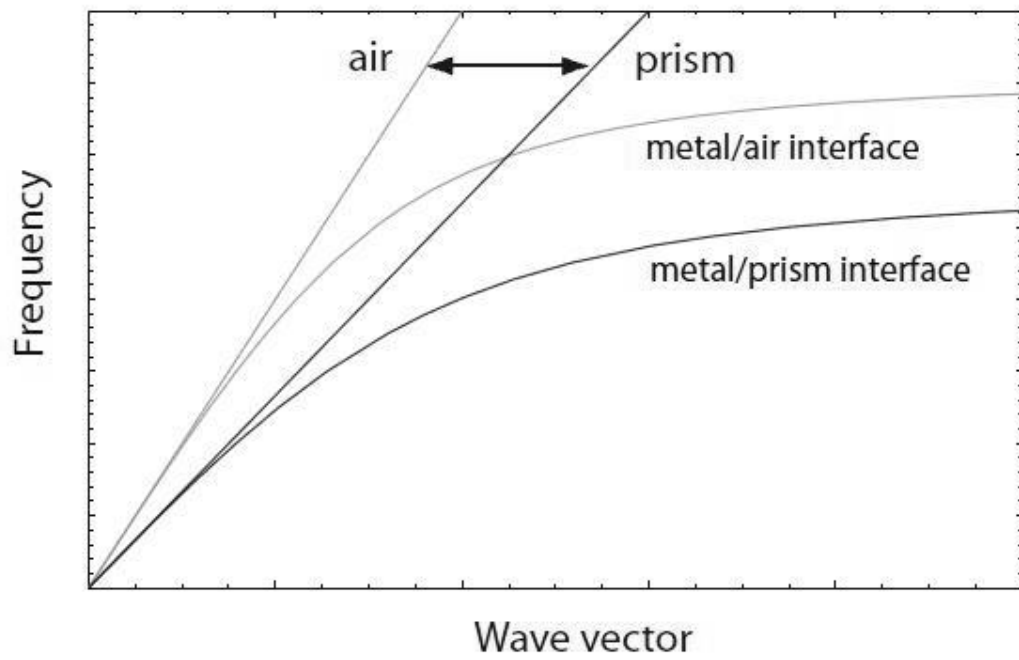


Figure 1.2: Prism coupling and SPP dispersion. Only propagation constants between the light lines of air and the prism (usually glass) are accessible, resulting in additional SPP damping due to leakage radiation into the latter: the excited SPPs have propagation constants inside the prism light cone. Source: [53]

to be colinear. However, this is not true. There is no point where the two curves intersect or are tangential, except the origin, which is of course of no practical use.

To excite an SPP wave, some trick must be used to compensate for the k-vector mismatch. The graph in figure 1.2 illustrates how this may be done using a glass prism, the method proposed by both Otto and Kretschmann [48, 49]. The prism configurations exploit the fact that the dispersion curve for light in an optically dense medium is shallower than in vacuum. Consequently, there is an intersection between the light line in the prism and the SPP dispersion curve at the metal/air interface, which allows direct excitation of a plasmon. This is precisely what happens in the Otto and Kretschmann configurations, with the configurations differing only in details.

Another method is the one used most frequently in this thesis - the coupling by grating or a surface defect [55]. That a grating can impart an additional k-vector component to an incoming light wave is well known [56, 57]. When contemplating the k-vector mismatch between the dispersion curves for light and SPPs, the idea that a grating could be used to couple light into SPPs, analogous to the way it is done with, for example, slab waveguides and photonic crystal slabs [58, 59, 60, 61, 62, 63], is not too far-fetched.

On the other hand, scattering by a surface defect is a similar mechanism, but much simpler to realize experimentally, because it is much less wavelength-specific than a grating. The efficiency of scattering by a surface defect is of course lower, and it was first explored in the context of light scattering problems involving rough metal surfaces where roughness-induced excitation of SPP's naturally occurs [64, 65]. The subject quickly matured into a field of research in its own right, with special attention paid to surface defects that scattered SPPs themselves [66, 67].

The connection between plasmonics and optical gratings did not first arise out of the intention to couple light into an SPP wave via a grating, but the opposite way round, when surface plasmon resonance effects were discovered in grating diffraction [68]. It was some years before it was recognized that an SPP propagating across a grating experienced losses, although an early theoretical study failed to draw the conclusion between the radiation losses and a potential coupling method [69]. The first study to propose and demonstrate grating coupling of light into SPPs as an alternative to the Otto configuration aimed to improve the measurement of the optical properties of metals [70], and presumably the authors did not realize - as is very common in physics in general - that their new discovery could be put to use in the telecommunications field many years later.

Once grating coupling of SPPs was discovered, it rose continuously in popularity. Not long after the initial discovery, grating-coupled surface plasmons at microwave frequencies were reported [71], followed by terahertz frequencies [72] and the near infrared (NIR), where they were even used for direct imaging of the SPP [73]. Coupling into SPPs using an elastomeric grating has been shown [74] as well as the integration of a grating SPP coupler into a metallic photonic crystal [75]. Today, the relationship between gratings and plasmons continues to evolve. Recent results

include efforts to excite SPPs on gold coated single mode optical fibres [76] and a proposal for broadside input and output coupling of long-range plasmons [77].

That gratings are useful in connection with dielectric-loaded surface plasmon-polariton waveguides was already well-known before this thesis was even begun, but the manner of SPP excitation inside the waveguides was not published formally until 2008 [55], and it was also published that the grating can in practice be simplified to just one single ridge or even just the edge of one ridge.

A technology for the excitation of plasmons that has been called highly influential in the field of SPP research [78] is excitation by the use of a surface near-field optical microscope (SNOM). In this method the optical probe of a SNOM is used as a point source of SPPs on gold and silver films [79, 80]. A detailed description of this excitation and characterization method is given in section 4.4 of this thesis.

Somewhat more exotic is the proposal to excite SPPs by means of X-rays [81]. This was not used in this thesis, but it is mentioned here for the sake of completeness.

1.3 Motivation for DLSPW

In the year 1965, in his article in *Electronics* [82], the now globally famous co-founder of Intel Gordon E. Moore made a claim that surpassed his own expectations in veracity. He wrote: “*The complexity for minimum component costs has increased at a rate of roughly a factor of two per year*”. Ten years later, he altered this claim [83] to a doubling every two years, instead of each year.

While the original 1965 article (now also available in reprint [84]) is visionary in several other ways as well, as it forecasts consumer retailing of computers and the still-revolutionary phased-array radar [82], it is the forecast of computing power doubling every two years that has stuck and become widely-known as “Moore’s Law”. In both articles, however, the horizon he gives his own forecast is limited. The 1965 article focuses on the trend only until the year 1970, and in his second version ten years later, presumably when Moore realized he had been a bit optimistic, he reduced the speed of the increase but again made his forecast only until 1980. This time, however, the forecast was spot-on, and has taken on a life of its own, becoming one of the guidelines of the semiconductor industry [85]. So, somewhat ironically, what was once a description of the rate of technological development in the semiconductor industry has now become the target that is set by the industry itself. The graph in figure 1.3 illustrates this trend and the future plans of the semiconductor industry until the year 2022.

By limiting his forecast to the next five to ten years only, Moore was able to ignore physical limits insofar as they interfere with his hypothesis. He writes himself in the 1975 paper: “With respect to dimensions, in these complex devices we are still far from the minimum device sizes limited by such fundamental considerations as the charge on the electron or the atomic structure of matter. Discrete devices with submicrometer dimensions show that no basic problems should be expected at least until the average linewidth and spaces are a micrometer or less.” [83]

Today we are no longer in the position to ignore the fundamental changes that

occur at short length-scales, even though we have remained unaffected by them for far longer than Moore suspected. It turned out that by improving fabrication techniques, the semiconductor industry was able to avoid the problems at the one-micrometer-linewidth, and has in fact progressed considerably beyond that stage. Today, state-of-the-art devices are fabricated with feature sizes on the order of 45 nm, and devices using this technology have played a considerable part in this thesis (by performing valuable service either in support of experiments or word-processing).

Today, the charge of the electron and the atomic structure of matter have become major problems for the semiconductor and electronics industry. For more than thirty years now, there has been talk of photonics and optics as a possible supplement or replacement for electronics [86, 87, 88, 89, 90, 91], frequently hailed first as “integrated optics” [92] and later in its more elaborate form as “integrated photonics” [93, 94]. While there has been considerable progress in the field [3, 95], considering its thirty-year history progress has been relatively slow, at least when compared to the rapid development of the electronics sector. This may seem surprising, and to explain this we must examine the reasoning behind the switch from electronics to photonics.

The reasoning is, in fact, closely linked to Moore’s Law [96]. Thanks to the overwhelming success of Moore’s Law, and its adoption by the semiconductor industry as a development roadmap, computers are now expected to become twice as capable every two years, and if possible also cheaper. Until now this could be achieved by making components smaller and increasing their quality to allow them to operate faster. But in recent times, the electron and the structure of matter itself have increasingly become the main stumbling blocks, and it has become clear that the physical limits Moore was talking about will soon be reached. Thus one of the main points of attack for research efforts has become an attack on the electron itself, and a quest to find a replacement.

The advantages of photonics over electronics are so great that optical computers have always been expected to exceed the performance of even the most powerful electronic ones [86]. Optical data transmission has already replaced electric wires in all long-haul and many short-haul communications applications due to its enormous bandwidth and the low noise of data transmission. The large bandwidth is due entirely to the much higher frequency of electromagnetic waves in the optical range when compared to the radio frequency signals of electronic data transmission. Since frequency modulation requires a fixed portion of frequency-space to operate correctly, it transpires that much more information can be sent optically. Noise is the limiting factor, since a high noise level requires a stronger signal, a more strongly-modulated signal or the multiple sending of a signal, which can then be checked for errors. All this subtracts from the bandwidth available, so it is little wonder that noise reduction was the main focus of optical communications research for a long time and that Charles K. Kao was awarded the Nobel prize in physics in 2009 for groundbreaking achievements concerning the transmission of light in fibres for optical communication.

Heat generation and dissipation, which has always been one of the primary concerns in electronics, is still a concern in integrated photonics and optical computing. A simple way to illustrate this is to imagine a NAND gate, with two “ones” as input and a “zero” as output. The input should be absorbed, somehow, since there is no direct output. While field-effect transistors can accomplish this without allowing very much of an electric current, an optical transistor-based NAND gate would continuously absorb photons, each of which could be expected to have at least 1 eV of energy. In general, heat accumulation inside a photonic chip and how to minimize it is still a very big challenge [97].

A photonic chip could be expected to process a lot more data a lot faster than an electronic one. Apart from the speed advantages already mentioned, some operations which are somewhat arduous for an electronic computer could be extremely simple for an optical one. A good example is the Fourier transformation, which an optical computer can accomplish simply by transmission of the signal through a lens [98].

In addition, currents of light at different wavelengths can intersect each other without interference, which electric currents can not [97]. There is hope that, inside a photonic computer, a single waveguide could carry many different light signals at the same time, replacing the 3D-wiring now in use. Photonic computers, so it is hoped, might consequently be not only faster but also smaller [88].

Considering the hoped for decrease in size, it is ironic that the largest disadvantage of photonics is currently the size of its components. The optical fibres that carry most of the world’s data traffic have an 8 μm core waveguide, surrounded by 125 μm of cladding (plus protective coatings, which may range from a few hundred μm in thickness up to about one meter for intercontinental submarine cables). But even 8 μm core diameter is far too large. The semiconductor industry has set its sights on 8 nm feature sizes by the year 2022 [85]. It is hardly conceivable that the semiconductor industry will relish the idea of scaling their new devices up by three orders of magnitude in order to accommodate photonic components.

The reason why optical waveguides are so large is the same reason - in a way - why they can carry so much data. The reason is closely related to the wavelength of light. The telecommunications wavelength bands lie from 1260 to 1675 nm, with the most common wavelengths being those in close proximity to 1550 nm, since this wavelength has very low losses in the optical fibre. A propagating electromagnetic wave cannot be confined inside an arbitrarily small waveguide, because each waveguide has a cutoff wavelength. Wavelengths larger than the cutoff wavelength will attenuate inside the waveguide instead of propagating [56].

It is clear that fibre optics is not a suitable technology to be used in an on-chip or even an inter-chip regime, since the dimensions are so different. A different technology is needed. A figure that shows the respective strengths and weaknesses of electronics and photonics, which was originally published in reference [52], is shown in figure 1.4. This representation already gives a clue what the answer to the technology question may be - plasmonics is by nature of its combined optical and

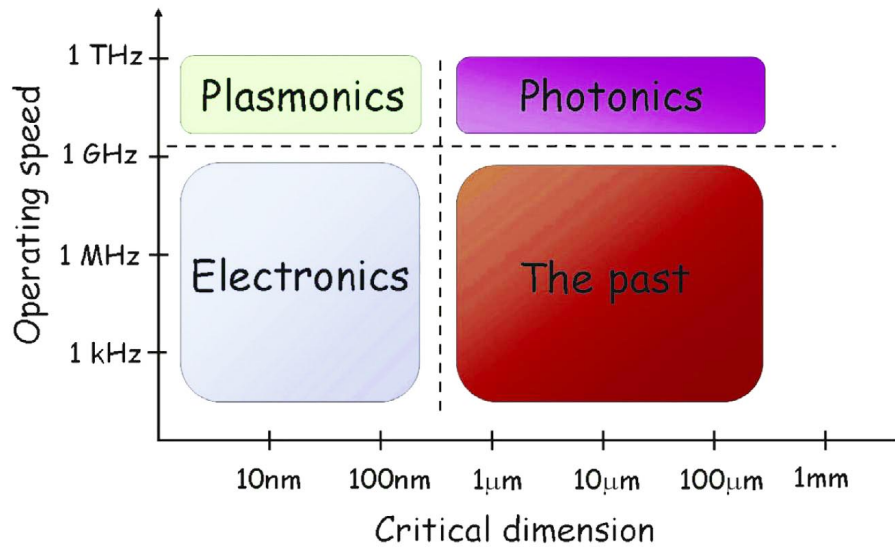


Figure 1.4: A by now somewhat famous and frequently cited image that illustrates vividly the respective advantages and disadvantages of electronics, photonics, and plasmonics by grouping them according to their operating speeds and critical feature sizes. Source: [52]

electrical properties a prime candidate for the future on-chip technology. However, there are other technologies that are also viable and these will be briefly discussed.

1.3.1 Silicon on Insulator

Silicon-on-insulator (SOI) is a technology where a layered silicon-insulator-silicon substrate is used instead of a pure silicon wafer in the semiconductor industry. This technology is widely used in microelectronic applications, but has also started to gain momentum in silicon photonics and integrated optics.

Use of SOI had become established in the fabrication facilities of the electronics industry by 1992 [99], so it is remarkable that it was not much earlier, only in the year 1988, when an optical waveguide based on SOI technology was first proposed [100]. The realisation of the first SOI single-mode waveguide at 1.3 and 1.55 μm was reported in 1991 [101].

SOI as a material has several advantages. Of great practical importance to the industry is the fact that SOI is fully compatible with complementary metal-oxide-semiconductor (CMOS) fabrication processes, which means only a minimum of re-tooling if SOI technology is chosen as the primary material for commercial photonics. Both silicon and its oxide are transparent at the typical telecommunications wavelengths of 1.3 and 1.55 μm . Furthermore, waveguides with a silicon core ($n = 3.45$) and oxide cladding ($n = 1.45$) have a high refractive index contrast. This allows the size of the waveguide to be reduced, and waveguides ca. 1 μm wide are common [102], but waveguides with a linewidth as small as 550 nm have been reported [103]. Waveguides can be designed with very tight corners, with a radius of curvature of 1.5 μm [104] and even 1 μm [105] reported recently.

There is currently great scientific interest in SOI, with recent results including a proposal for ultra-fast logic gates [106] and a wideband Y-splitter, which is remarkable for its linewidth of only 120 nm thanks to plasmonic enhancement [107].

A drawback of SOI structures is their sensitivity to scattering at rough features on the core-cladding interface, which may be caused by inaccurate manufacturing [108], but this is a problem for all optical waveguide technologies and not specifically a problem of SOI.

Probably the largest challenge for SOI technology is the issue of light sources. It is well known that silicon is not easily induced to emit light, due to the fact that it has an indirect band gap, requiring a change of wavevector for an electronic transition between the extrema of the conduction and valence band [109]. Because of the great potential of a reliable silicon light source, enormous research efforts have been devoted to finding one. Among the avenues explored are surface-structured bulk silicon [110], silicon nanocrystals [111, 112], erbium-doped silicon-rich oxides [113] or nitrides [114], Si/SiO₂ superlattices [115], Si/SiGe quantum cascade structures [116], and Raman lasing [117]. None of these solutions are absolutely ideal. Raman lasing, for example, requires very powerful external pump lasing to work [117].

Further challenges in the development of active silicon photonic components are a variety of higher-order nonlinear effects that result from sudden changes in the physical environment, such as high field strength, which have both slow and fast relaxation times, and the centrosymmetry of the silicon crystal, which hinders the development of electro-optic silicon modulators because it prevents electrooptic effects [118].

However, in conclusion, one must note that, today, SOI remains a viable candidate for bringing photonics and electronics together, although not all challenges have been fully overcome. The feature sizes of SOI are entirely comparable to those of technology that is discussed in this thesis.

1.3.2 Photonic Crystals

The term “photonic crystal” today describes a periodic optical nanostructure which is specifically designed to guide photons in a certain way. They are often compared to semiconductors since they are engineered to do with photons what semiconductors do with electrons [119, 120]. As such, they have often been proposed as a possible technological route for optical computing, which would seem like a natural evolution due to the similarity in physics [121, 122].

As long ago as the year 1888, Lord Rayleigh showed that a certain category of stacked materials exhibits a very high reflectivity within a certain spectral range, known as a one-dimensional band-gap [123]. Many years later, it was proposed to use such materials to suppress spontaneous emission from atoms and molecules [124]. The extension of this idea to more dimensions than one was performed in two breakthrough publications in the year 1987 by Yablonovitch [125] and John [126]. It is not known when exactly the term “photonic crystal” was coined, but it was published in 1991 [127] and firmly established from then onwards.

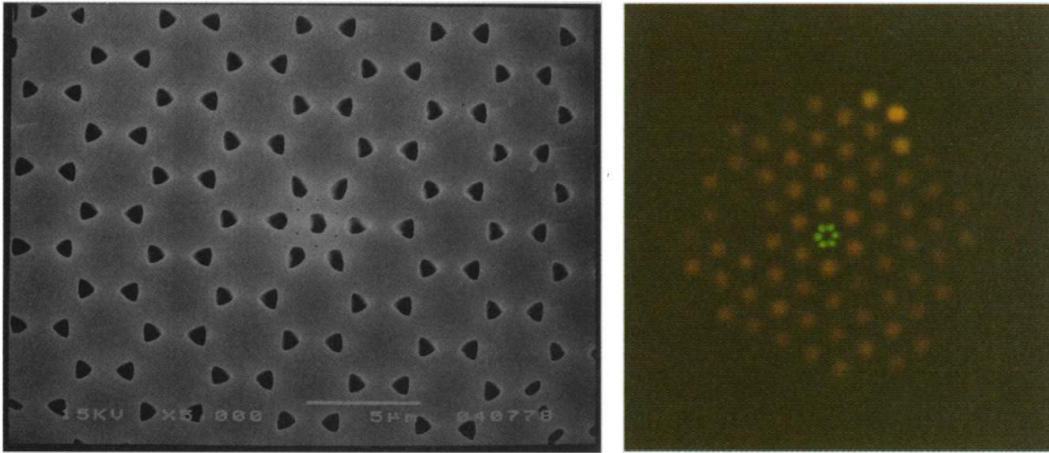


Figure 1.5: An SEM image of a cleaved end of the first photonic crystal fibre. Note the dimensions of the fibre (more than $25\ \mu\text{m}$ across) and compare with the current semiconductor industry's goal of $8\ \text{nm}$ feature size. Source: [128]

Hopes quickly ran high that photonic crystals would rapidly revolutionize computing and telecommunications, with the first photonic crystal fibre reported in 1998 [128] and control of light on a chip reported some years later [121, 122]. However, photonic crystals have always had several major drawbacks. On the one hand, development of photonic crystal technology did not proceed quite as fast as initially thought, and in particular rapid and reliable fabrication remains a considerable challenge. On the other hand, and far more serious, photonic crystals are very large compared to the integrated circuits in use today due to their intrinsic feature size of $\lambda/2$. This is illustrated in figure 1.5, where the cross-section of the first photonic crystal fibre is shown. Photonic crystals are even larger in many cases than the optical fibres, which are themselves, as mentioned above, several orders of magnitude larger than features on a state-of-the-art computer chip.

Research in the field is still ongoing nevertheless. It has been recently shown that it is now possible to create quantum-dot doped photonic crystals with nonlinear optical properties [129], which show some potential for optical switching and demultiplexing. However, the main focus of photonic crystal research has moved away from integrated photonics towards photonic crystal fibres [130, 131] and enhancement of light-emitting diodes (LEDs) [132] or vertical-cavity surface-emitting lasers (VCSELs) [133], where there has been remarkable development and considerable potential for applications.

In conclusion, one could say that photonic crystals, while still academically of very great interest, are no longer conceivable as the perfect solution to the on-chip photonics problem as which they were once hailed. They may one day be a part of integrated optics, but will most likely play no more than a niche role.

1.3.3 Dielectric-Loaded Surface Plasmon-Polariton Waveguides

The origins of dielectric plasmonic waveguides lie with early metal-dielectric waveguide structures, which were studied as part of the research effort into integrated optics [92]. A lot of attention was initially focused on metal-polymer-metal slab waveguides, which were analyzed in detail theoretically as early as 1972 [134, 135]. To quantify losses of optical waveguides in close proximity to metal, IBM examined a quasi-slab waveguide consisting of an optically transparent liquid sealed between a metal layer and a quartz cover [136]. Enough interest was generated to initiate a general study of three-layered slab waveguides, which considered, among others, the cases air-polymer-metal and metal-polymer-metal [137]. Waveguide directionality was drastically enhanced by moving from slab waveguides to line waveguides, which can also be made much smaller and are a necessary step towards integrated optics and photonics. An early prototype for a dielectric plasmonic line waveguide, based directly on the metal-clad polymer slab waveguides, was to make a slit in one of the metal layers. This slit then defined the path that the electromagnetic wave would take [138].

A dielectric-loaded surface plasmon-polariton waveguide (DLSPPW), as it will be discussed in this thesis, consists of a dielectric waveguide sited on a metal surface, which can guide SPP modes. The idea for dielectric plasmonic waveguides stems from the desire to make the waveguide dimensions as small as possible, which is not easy with other SPP waveguide technologies. While many other such technologies exist, such as line defects in surface polaritonic crystals [139], metallic stripes and wires [140, 141], grooves or gaps in a metal film [138, 142, 143], chains of metallic nanoparticles [144, 145], and metal heterostructures [146], all of these technologies have the disadvantage that they cannot be easily scaled down without large increases in scattering losses and a decline of efficiency. For example, scaling down of wide metal stripes leads to a significant increase of scattering on the stripe edges.

The use of a dielectric material to overcome the difficulties with mode confinement and edge-scattering losses was proposed by several research groups immediately prior to this thesis [147, 148]. The term “dielectric-loaded surface plasmon-polariton waveguide” (DLSPPW) was coined by two papers from close collaboration partners, which form much of the base of this thesis, and first conducted thorough theoretical investigations of DLSPPWs by full three-dimensional numerical modelling [149] and the effective index and finite element methods [150].

The success of the DLSPPW field is perhaps best illustrated by the fact that since the term was coined a little more than three years ago, there have been more than fifty publications on this topic and a significant number are currently in press or in preparation.

2 Fabrication Methods

In the course of this work, two principal fabrication technologies have been used - direct laser writing by two-photon polymerization (2PP) and nanoimprint lithography using masters made by 2PP. These two fabrication methods are described in detail. Other fabrication methods that can and have been used or proposed to make plasmonic waveguide structures are briefly outlined. A tabular comparison of the advantages and disadvantages of the fabrication methods is provided in table 1.

2.1 Direct Laser Writing by 2-Photon Polymerization

2.1.1 2-Photon Polymerization

The two-photon polymerization rapid prototyping technology is based on the process of two-photon absorption (2PA). The 2PA process was first predicted by Nobel laureate Maria Göppert Mayer in her 1931 dissertation [151] and first demonstrated in 1961, when fluorescent light at $\lambda = 425$ nm was detected in a $\text{CaF}_2:\text{Eu}^{2+}$ crystal after irradiation with focused 694.3 nm wavelength light from a ruby laser [152].

One of the most well-known applications of the 2PA process is two-photon excitation microscopy, where the 2PA process is harnessed to provide intrinsic three-dimensional resolution [153]. This field, started in 1990 and expanded to include multi-photon microscopy in 1996 [154], is still one of the most rapidly growing fields in the area of microscopy today, testament to the importance of Maria Göpper Mayer's discovery in 1931.

A more recent application of the 2PA process is research into optical quantum memories with gigahertz bandwidths [155]. The 2PA process has also been studied in other contexts such as optical power limiting [156], sub-diffraction-limited local chemistry [157], photodynamic therapy [158] and other special photochemistry applications [159, 160].

It is a different area of 2PA application that plays a fundamental role in this thesis, however, namely two-photon polymerization.

Two-photon polymerization (2PP) is based on the use of a 2PA process to induce polymerization of a polymer with a photoinitiator. Instead of using a single UV photon, two photons from the visible or IR spectrum can be combined to give the same energy. First observations of this effect date from the mid-1990s [161, 162, 163, 164], but the first application of 2PP to 3D-microfabrication came with the breakthrough of the Kawata group in 1997 [165].

This sparked a flurry of research into 2PP and potential applications, and it was not long before the focus turned towards optical and photonic devices and components. One of the main motivations the Kawata group gave for their research into 2PP was the enhanced resolution attainable over conventional UV lithographic methods [165], which makes it easier to control structure dimensions. Such control is crucial for the fabrication of high-quality optical components, so it is no surprise that suggestions involving 2PP and optical applications in fact predate the reliable

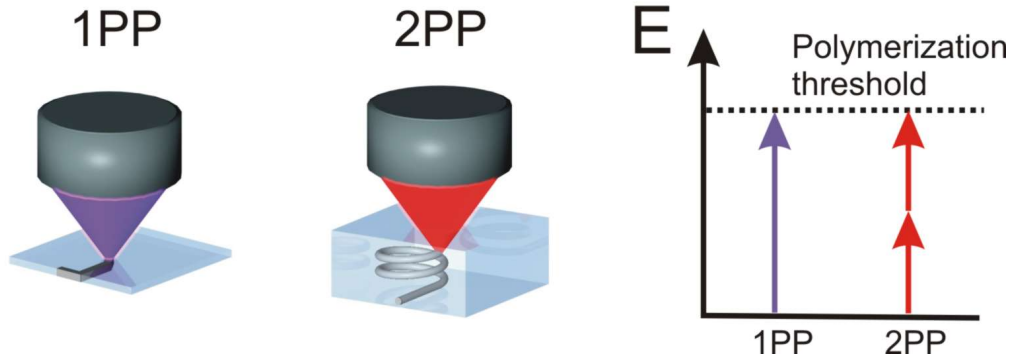


Figure 2.6: Illustration of the 1PP and 2PP processes. While the 1PP process, shown with a UV laser, can only produce a 2D-structure, arbitrary 3D shapes are possible with 2PP, with IR light. This is because, as the energy diagram shows, a single UV photon is enough to reach the polymerization threshold of the photoresist, while the energy of two IR photons is required. Consequently, polymerization with IR photons requires a very high incidence of photons in a small volume - it can only occur in the focus while the rest of the photoresist is unaffected.

demonstration of 2PP as a 3D microfabrication technology [166]. A wide range of optical applications followed in the next few years, including photonic crystals [167], optical data storage [168] and holographic recording [169].

Today, 2PP is a well-established technology for rapid prototyping and fabrication of such diverse applications as micro-valves [170], templates for the production of mesoporous silicas [171], microneedles for transdermal drug delivery [172] and scaffolds for tissue engineering [173].

The ever-increasing speed of computers and the inherent miniaturization of components has long foreshadowed a shift from electronic to optical computing, which has still not begun to take root even though the introduction of first optical components into PCs has been announced to take place this year [174]. This anticipated shift has been a major driver of research into miniaturized optical components, integrated optics and the associated fabrication technologies.

An optical single-mode waveguide fabricated by 2PP was demonstrated in 2002 [175], and the first plasmonic (DLSPPW) waveguide in 2006 [147].

The principle of 2PP is simple, illustrated in figure 2.6. A standard UV-sensitive photoresist is used for polymerization. However, instead of a single UV photon, two photons from the IR or visible spectrum initiate the photopolymerization process. This has several advantages. The first and most crucial advantage is that the threshold for 2PP to occur is very high, so a very large concentration of photons is required. This is achieved by employing a fs-pulse laser and using very high focusing. The 2PP process will then only take place in the focal spot and not at any other point of the beam. This is a vast difference to 1PP, where polymerization takes place along the entire beam. If the focus can be moved around inside a volume of photoresist, the 2PP process acts a bit like a three-dimensional pencil, with "drawing"

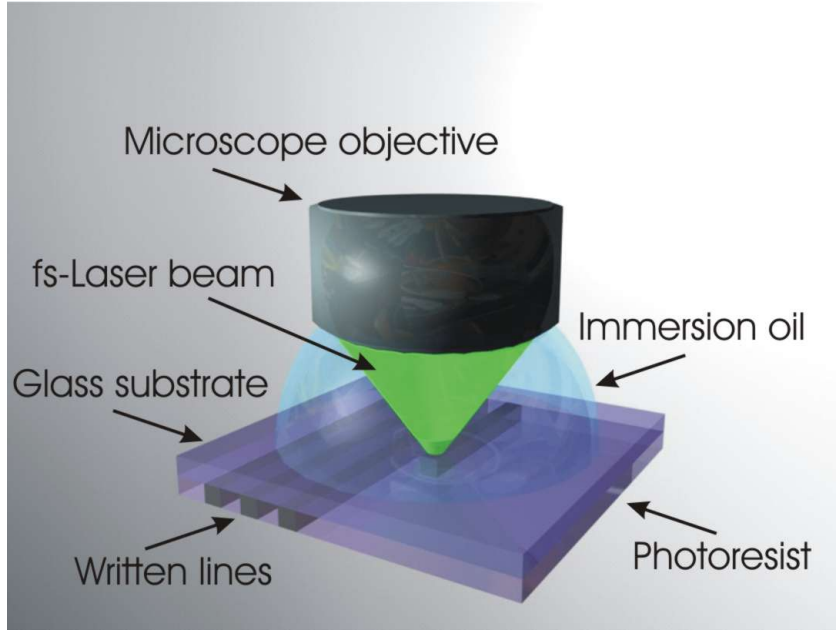


Figure 2.7: Schematic illustration of the typical configuration for high-resolution 2PP structure fabrication as used in this work.

taking place wherever the focus is moved. In this way, arbitrary 3D structures can be fabricated, whereas 1PP only yields 2D structures, with the possibility of $2\frac{1}{2}$ D structures using a sophisticated and time-consuming layer-by-layer approach. The second main advantage of 2PP is that because it is a nonlinear approach requiring such a high photon density, the resolution becomes much higher and the process is not strictly bound to the diffraction limit like 1PP. Thus, for a 2PP process using an 800 nm wavelength laser, it is possible to fabricate 100 nm feature sizes [176, 177].

An illustration of the typical configuration for writing high-resolution structures with 2PP as it was done for this work is shown in figure 2.7 (less elaborate configurations may be used for low-resolution structures). In this example, a UV-sensitive photopolymer is spin-coated onto a glass substrate (usually a 150 micron thick microscopy cover slip) and placed upside-down below the objective. Optical index-matching immersion oil is then placed between the objective and the glass to ensure a minimum of disturbance from refraction and the smallest possible focus spot. The objective is naturally an immersion-oil objective, a frequently used objective was a 100x magnification objective from Zeiss with a numerical aperture (NA) of 1.4. A fs-pulse laser is focused by the objective to produce the lines.

However, this configuration for high-resolution structures is not the only one thinkable. A wide variety of possibilities for structuring exist. Apart from the one outlined above, the method most frequently used in this thesis involves either a 100x magnification objective or a 40x magnification objective without oil immersion, in which case the sample is of course structured with the polymer on the top side. Less frequently, the 100x immersion oil objective was used without oil, due to its longer working distance than the immersion oil version. This method is a little

unorthodox, but still provides higher resolution than a 40x objective. It is necessary to use this when structures with high resolution and heights of more than 20 μm on opaque substrates are necessary. In addition to this, objectives with 63x and 20x magnification were also used, but rarely. While the 63x magnification (with oil immersion) has adequate resolution, it is still inferior to the 100x and its main advantage - large field of view - is quite useless in the context of 2PP as long as no scanner is employed, as was the case in this work. The 20x objective was only used occasionally for very large-area structures with low resolution features.

2.1.2 Description of 2PP setup

The setups used for 2PP fabrication have evolved in recent years from piezo-driven stage systems to air-bearing axis systems that may or may not be coupled to a laser scanner. The system used for the majority of this work is the currently final evolution of 2PP setup designs built in the Laser Zentrum Hannover, known as an M3DL (microfabrication in 3D, laboratory version). These systems were commercialized at the beginning of this work, and building and refining these systems was part of the routine day-to-day business that accompanied this thesis.

The M3DL system consists of the following units:

- a hard stone bridge structure, holding the axes (X,Y, and Z), camera and optical components;
- a number of optical and opto-mechanical components that are attached to an optical table or the hard stone bridge;
- a switch cabinet containing the entire control electronics;
- a control computer;

Two views of the M3DL is shown in figure 2.8. The hard stone bridge structure, which forms the basis of the entire device, is made from South African diabase by the company Johann Fischer Aschaffenburg (JFA) based in Aschaffenburg, Germany. Diabase is an igneous rock similar to basalt, which is chosen for its rigidity, stiffness, and its machining properties [178]. To ensure optimal accuracy during the 2PP fabrication process, and that the axes run smoothly, the stone must be machined to a very high degree of accuracy. Indeed, in the final step, the axes-bearing surfaces are lapped by hand.

The axis system consists of three air-bearing axes made by the company Aerotech Inc. based in Pittsburgh, USA. Two axes move in the horizontal plane (X, Y) and one is vertical (Z). The air bearing stages are chosen because of their combination of several unique qualities. They have a large travel range, offering a structurable area of 100 x 150 mm^2 , which is far superior to the 80 x 80 μm^2 that were obtainable with piezo systems. Each air bearing stage has an accuracy better than 10 nm, which is very important when the fabrication of waveguide structures is considered. The maximum practical travel speed of the axis lies at 30 mm/s, which is about three

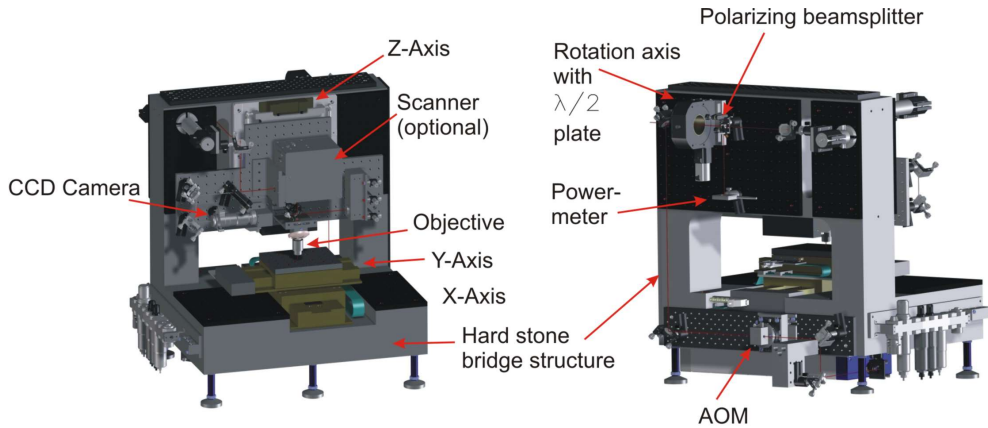


Figure 2.8: Computer-generated image of the latest version of the M3DL, viewed from the front and the rear. The most important components are pointed out with arrows.

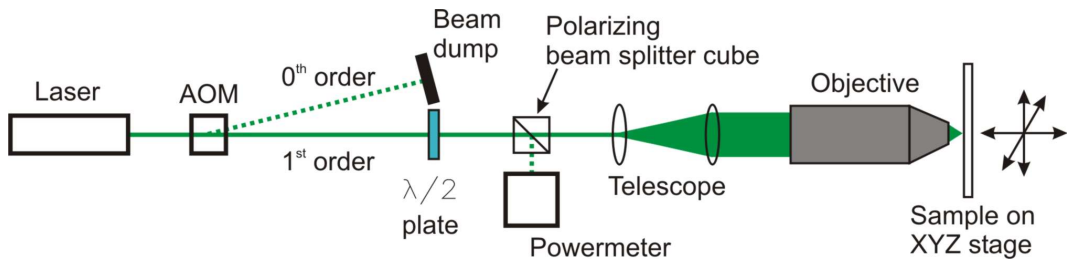


Figure 2.9: Schematic illustration of the beam path in the 2PP setup, excluding all mirrors and the process observation camera. The laser beam is shown in green, representative of the 515 nm wavelength used in much of this work, although other wavelengths are equally possible.

orders of magnitude higher than for piezo systems and makes large-scale structures possible ([165] uses a piezo which cannot have been faster than $100 \mu\text{m/s}$; [179] mentions a scanning speed of only $1 \mu\text{m/s}$ and a size of $40 \times 40 \mu\text{m}^2$).

The camera attached to the setup serves as a process observation tool. It is a standard black and white CCD camera made by Watec.

The beam path in the 2PP fabrication setup is shown schematically in figure 2.9. A wide variety of lasers can be used for 2PP fabrication, the laser is coloured green to represent the 515 nm wavelength with which the majority of the structures of this thesis were made. The first active component in the beam path is an acousto-optic modulator (AOM), a device which uses a standing acoustic wave in a crystal to create a grating. This grating diffracts the laser beam, in the 2PP setup typically the first three orders are visible. The AOM is aligned so that there is a maximum of intensity in the 1st diffraction order. The 0th order is the undiffracted beam and is discarded in a beam dump, while the 1st order beam is passed on. This means that that AOM is now a very fast switch for the laser, capable of sending light into the 2PP setup at radio frequency.

A rotatable $\lambda/2$ plate, together with a polarizing beam splitter cube, serves as a means of adjusting the laser intensity for 2PP fabrication. The $\lambda/2$ plate is mounted on a high-speed and very precise Aerotech rotation stage, giving very good control over the laser power inside the setup. Real time information about the laser power is provided by a powermeter which collects light discarded by a polarizing beam splitter cube. As the $\lambda/2$ plate rotates, the splitting ratio between powermeter and 2PP setup changes.

A telescope increases the beam width just before entering the microscope objective in order to ensure that the aperture of the objective is fully illuminated. The objective finally just focuses the beam onto the sample, where structuring takes place.

While the above description addresses all the important elements of the 2PP fabrication beam line, the real setup in the laboratory is slightly more complex. Missing from the above description are all the mirrors, as well as the process observation camera. These mirrors are necessary to guide the beam through all the optical components, up onto the hard stone bridge and onto the translation stages. A scanner was not used for the experiments in this thesis, although it could be added just before the objective.

2.1.3 2PP Fabrication Software and Programmes

The M3DL is controlled by its own separate software package, which was used to fabricate all of the 2PP-made structures presented in this thesis. The software was also expanded and modified greatly in the course of this work. Two primary methods were used in structure fabrication.

The first method is the creation of a custom subroutine for the M3DL software to fabricate a specific structure. This involves the creation of a graphical user interface (GUI), the translation of user input into machine code, and the integration of the subroutine with the main programme. Such subroutines were created specifically for this work, amongst others, for the creation of Mach-Zehnder interferometers, racetrack resonators, and fibre-coupled waveguides.

The second method involves a subroutine that can read and process object files in .STL format. STL stands for stereolithography, and is now widespread in both this field and other rapid prototyping or engineering applications [180, 181, 182]. Most computer-assisted design programmes can export STL files, so this format is the method of choice when a more complicated 3D structure is needed. STL was used in this work for the fabrication of large voluminous structures like fibre-coupled waveguides, plasmonic black holes, and demonstration objects.

2.1.4 2PP Fabrication Procedures

This section aims to give an overview of the various possibilities of fabricating DL-SPPW structures using 2PP. There are various ways to do this, which is why this section is necessary.

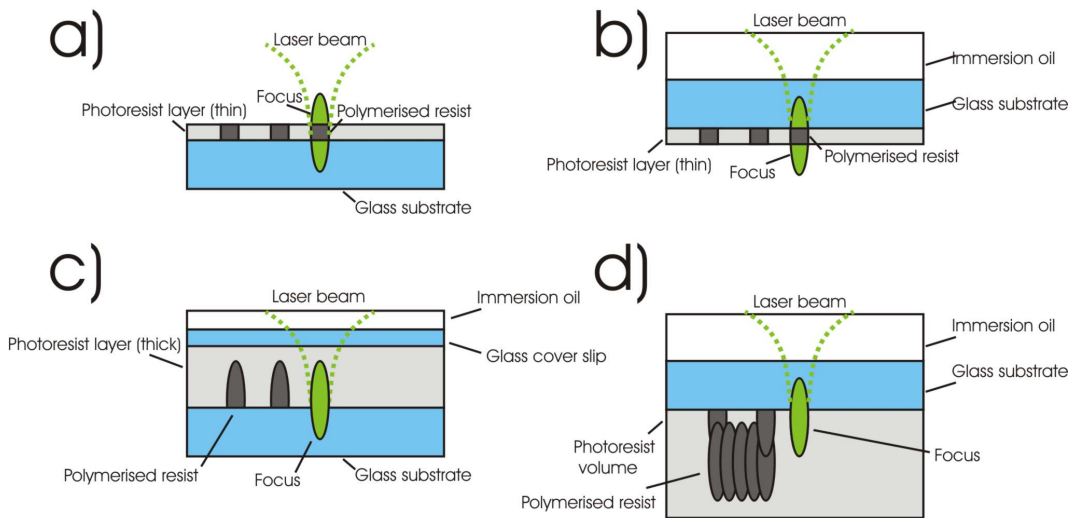


Figure 2.10: Schematic illustration of the 2PP fabrication process in the four main fabrication modes. a) and b) show 2D and c) and d) show 3D structure fabrication. a) Shows 2PP fabrication on a thin spin-coated photoresist layer without immersion oil at low resolution. b) Shows the same process using a higher-resolution oil-immersion objective. The sample is simply turned upside-down. c) Shows a possibility to make low 3D structures using oil immersion. d) Shows a method to fabricate 3D structures in a large photoresist volume, also using immersion oil. The proportions of the focus point are approximate, depending on the objective in use the focus may be much longer or shorter.

In general, there are several options to make structures using 2PP. Structures can be made either with or without oil immersion and either using a large volume of photoresist for 3D structures or with a thin layer for 2D structures. These options are illustrated in figure 2.10. Note that the oil may be omitted in figure 2.10 b)-d) if the objective used is not an oil immersion objective and high resolution is not required.

2.1.5 2PP on Glass vs. Gold

At a relatively early stage in this thesis, it was discovered that the choice of substrate during the 2PP fabrication of a structure plays a very great role. The primary substrates used for this work are several types of glass, most notably BK-7 glass and fused silica or quartz glass, and glass of any sort coated with 50 nm gold. Minor roles have been played by silicon and various types of polymer.

The main difference between the substrates mentioned above lies in the higher reflectivity of silicon or gold-covered glass compared to plain glass. This means that power which would be unavailable for structuring close to the surface when

using transparent glass, because the focus is half-submerged inside the material, is suddenly thrown back into the photoresist. This can result in great differences between suitable parameters for structuring near the surface and inside the resist volume.

The situation is much exaggerated when metals are involved, in particular gold. The strong focusing of the laser at the gold surface leads to plasmonic effects and consequently field enhancement. This field enhancement can make the power density near the surface so high that the resist explodes. In the worst case, depending on the laser system and the photoresist, it may not be possible to find a suitable set of parameters for structuring on a gold surface.

This is particularly the case for 2.5D and 3D structures on gold, which require radically different power settings for 2PP fabrication near the surface and inside the polymer volume. Two solutions for this problem present themselves.

The first solution is to increase control of the 2PP process. By installing additional equipment and sensors in the 2PP fabrication setup it would be possible to monitor the fabrication results in real-time and to adjust the parameters until the desired result is achieved. This is clearly a complex engineering problem, whose focus lies outside of this thesis, but will be the topic of two large research projects that have recently been granted and will tackle this exact aspect.

The second solution is to use a multi-step sample fabrication process to avoid direct 2PP writing on gold, using nanoimprint lithography. This is the focus of the next section.

2.2 Nanoimprint Lithography

Nanoimprint lithography (NIL) is a method that has been gaining steady popularity in the fabrication of DLSPPW structures [183], but which has been practically applied to this area only very recently [184].

The nanoimprint lithography process used in this work is based on master structures fabricated by 2PP on glass. These master structures are then used to fabricate a stamp from the flexible and transparent polymer polydimethylsiloxane (PDMS).

This technique is schematically shown in figure 2.11. The first step of this is master fabrication (in figure 2.11 a), the finished master sample is shown), followed by creation of a mold for replication. This is done by filling a small cylindrical form with liquid PDMS which is placed over the structures on its open end, as shown in figure 2.11 b). The viscosity of PDMS prevents any outflowing. The mold is then placed on a hotplate where it is baked for approximately 120 minutes at 110 degrees Celcius, during which the stamp hardens (step c).

Following the hardening, first the cylindrical form and then the mold itself is removed from the master sample (step d). This process is damage-free for the master structures, so several molds can be fabricated from the same master. What then follows is the nanoimprinting.

A drop of liquid photoresist, we use mr-NIL 6000.5 (micro resist technology GmbH, Berlin, Germany) for the structures presented in this thesis, is deposited

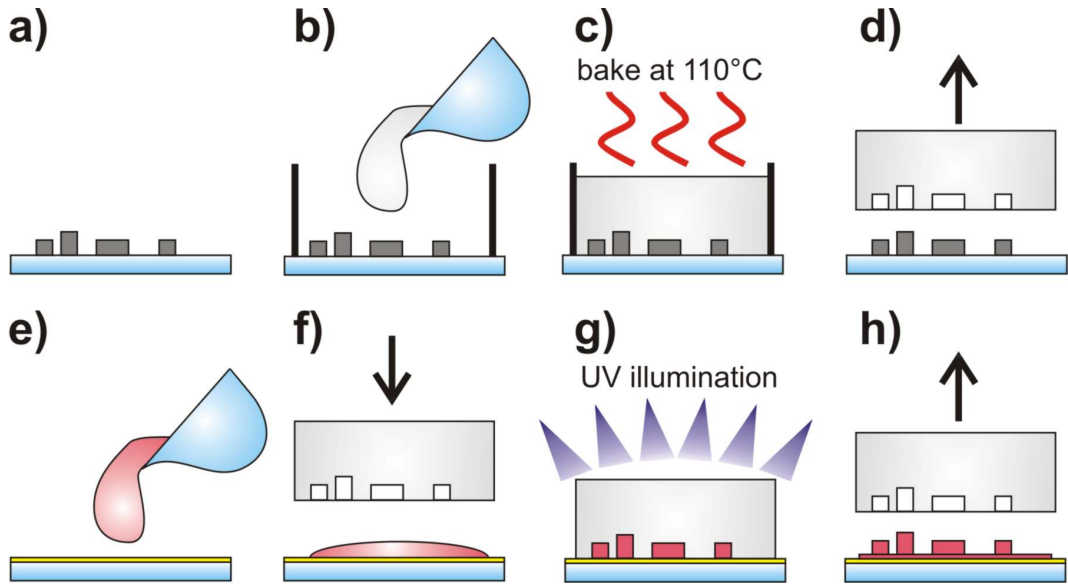


Figure 2.11: A schematic showing the nanoimprint lithography technique used to fabricate nanoimprinted structures. Steps: a) master sample; b) creation of PDMS stamp; c) baking of PDMS stamp; d) stamp removal; e) preparation of new substrate with a different photoresist; f) stamp pressed into new photoresist; g) UV exposure of photoresist; h) stamp removal.

on a fresh glass substrate covered with a 50 nm gold layer (step e). The PDMS mold is then placed on the drop and light pressure applied to ensure a good spread of the photoresist and a thin residual layer (step f). The samples are then pre-baked for three minutes at 110 degrees Celsius and after that exposed under a UV lamp for 120 minutes (step g). They are then post-baked at 110 degrees Celsius for five minutes. The mold can then be removed, leaving the imprinted structures standing on the substrate surface (step h). This method has proved extraordinarily reliable over the course of the experiments, with nearly no failures.

The NIL process leaves a very thin layer of polymerised photoresist on the substrate surface called the "residual layer", which is shown in 2.11 h) as an additional layer above the gold in the same shade as the structures. The residual layer is, similar to the gold layer, considerably exaggerated in thickness for the purpose of making it visible in this schematic. The residual layer must be considerably thinner than the DLSPPW structures to ensure photonic confinement in the DLSPPW. Since our structures are functional the upper limit of residual layer thickness is at least 500 nm. The exact thickness of the layer has proven difficult to measure and this is still part of ongoing research.

A special setup was designed and built for nanoimprinting, a schematic of which is shown in figure 2.12. The setup consists of a X-Y-translation stage and a rotation stage on which the stamp rests, and a further translation stage mounted in Z-direction which holds the new substrate onto which the structures are to be imprinted. The whole process can be viewed through a camera and a microscope objective for precise alignment of the sample.

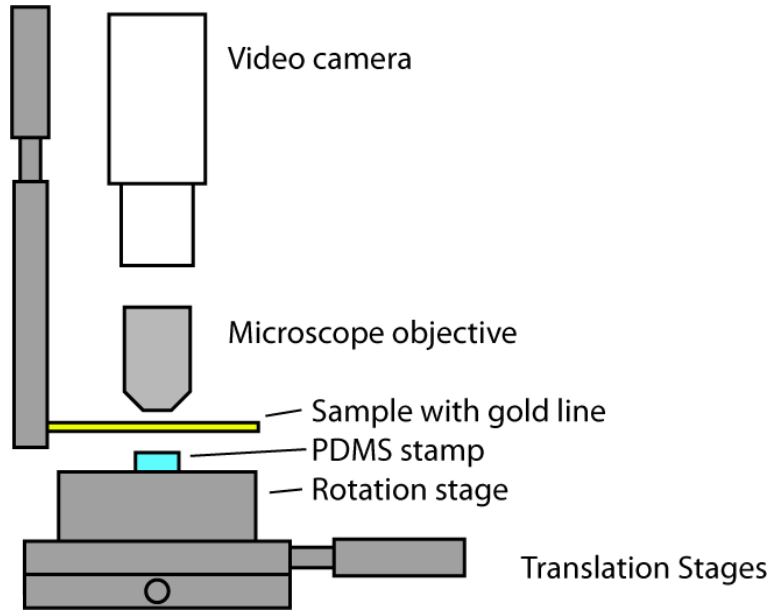


Figure 2.12: A schematic drawing of the setup used for nanoimprinting.

The process is very simple and requires nearly no specialised equipment. It represents a considerable simplification and improvement over comparable processes that require vacuum or hard stamps [185].

2.3 Comparison with Other Fabrication Methods

2PP and nanoimprint lithography are not the only methods used in the fabrication of DLSPPW structures and components. A number of other technologies exist, which are outlined in this section. They are compared to nanoimprint lithography and especially 2PP wherever applicable. A tabular overview is given in table 1.

2.3.1 UV Mask Lithography

Out of the fabrication technologies presented here, UV lithography is the only one in widespread industrial use. It has been one of the main driving forces in electronic miniaturization since it was introduced by Fairchild and Texas Instruments in the early 1960s [186].

The basic principle of UV mask lithography is to use UV light directly to polymerize a layer of photopolymer, and to select which areas are to be illuminated by employing a non-transparent mask (examples include metal masks for high resolution applications and black areas printed on plastic foil for budget solutions). Among the earliest types of UV lithography is contact printing, where the mask is in direct contact with the polymer. This method has the disadvantage of high mask wear, and has been replaced in industrial applications, first by proximity printing and later by projection. Projection technology has continued to evolve and remains the basis of most modern industrial UV lithography systems, which are of the step

and scan reduction type [186]. However, for scientific applications, contact printing remains popular because masks are typically used much less frequently than in industrial applications, and mask wear is not an issue.

The details of a UV lithography procedure are typically as follows. A substrate is covered with a layer of photopolymer which is UV-sensitive. Since the entire volume of the polymer is UV-sensitive and will polymerize upon illumination, thin films make the most sense with UV mask lithography, such as can be obtained by spin-coating or dip-coating. The substrate can in principle be any material, since transmission through the substrate and reflection are not issues.

The substrate is illuminated by a UV source, which can be a UV lamp or a UV laser (such as a He-Cd laser), through the mask. If contact printing is employed, the mask lies directly on the photoresist layer on the polymer. In the case of proximity printing, the mask is held just above the photoresist, not contacting it. In the case of projection, optical components are used to guide the UV light through the mask and onto the sample. These may involve a reduction of the image size, however such complex setups have so far not been reported in the area of DLSPW fabrication. The mask is typically made of very thin metal and is itself often laser-processed. However, other materials can also be used, the main criterion is that the mask is non-transparent. UV lithography has been used in the fabrication of DLSPW structures by [187, 188, 189] and others.

The largest disadvantage of UV mask lithography compared to 2PP (in experimental physics) is the fact that every conceivable structure must be present on the mask once it is made, since the mask cannot be altered later. High resolution masks with resolutions of less than $1\ \mu\text{m}$, which are needed for DLSPW fabrication, are very expensive and time-consuming to make, requiring special equipment which does not equip even lavishly furnished laboratories. Consequently, should experiments show that the structures on a mask are not adequate for experiments, a new mask has to be procured, which is expensive and lengthy. In addition, structures can only be 2D. To make structures with additional features in height, multiple illuminations using several masks are necessary. These further illuminations would require high-precision alignment of the masks with the substrate and even with the utmost care would only provide 2.5D structures without true 3D capability. The creation of 2.5D structures with even medium resolution in Z-direction, however, requires an enormous amount of masks and effort disproportional to the result achievable.

The clear advantages of UV mask lithography are that, once the mask is available, sample fabrication is quite simple and it is capable of high-throughput fabrication of 2D structures. Only one illumination, which may take less than a minute, is necessary to fabricate all the structures in the mask. This is the primary reason why the technology is so well-established in the semiconductor industry (where the design does not change rapidly, and throughput is extremely important) and has reached such a high state of industrial development [186]. Consequently, UV lithography techniques are still being considered as the likely method of industrial fabrication of future nanophotonics components [190].

2.3.2 Electron Beam Lithography

Electron beam lithography (EBL) is a nanofabrication technique going back to the (at the time) unconventional use of an electron microscope by Möllenstedt and Speidel, where an electron beam is used to polymerize a photoresist [191]. Since the electron beam can be focused to a diameter of only a few nanometers, extremely high resolutions are possible. The first "application" produced by EBL was an acoustic surface wave transducer, presented by Broers et al. in 1969 [192]. Today, the electron microscopes used by the pioneers in their work have been superseded by specialized EBL fabrication machines, which were already well developed by the mid-1990s [193]. It is possible to fabricate both 2D [194] and 3D [195] structures using EBL, although 3D fabrication is considerably more time-consuming.

EBL shares most of its advantages and disadvantages with 2PP, although some parameters of the technologies differ considerably.

EBL is, like 2PP, a serial technology and a direct writing technology. The freedom of design and structure shape is akin to the freedom of a pencil on paper. Structures manufactured by electron beam are as close to identical as the machine will allow, with low rates of loss and good overall homogeneity. The resolution can be close to one nanometer, nearly two orders of magnitude better than 2PP can achieve. Due to this high resolution, EBL enjoys considerably popularity in the metamaterials community, with many interesting results such as the proof of Babinet's principle for optical frequency metamaterials and nanoantennas [196], or the simultaneous negative phase and group velocity of light in a metamaterial [197] were achieved with EBL-fabricated samples.

The technique also has its disadvantages, which do not necessarily pose a challenge for research institutes but certainly stand in the way of widespread commercial application. The process is slow and only a comparatively small area of a sample can be structured. In a typical process, a single $100 \times 100 \mu\text{m}^2$ area takes about three minutes. This is still acceptable for the fabrication of certain plasmonic waveguide structures, and in fact EBL has been used with success in the fabrication of metal stripe waveguides [140] and hybrid plasmonic slab waveguides [198]. Nevertheless, EBL is clearly unsuitable for the fabrication of waveguides larger than a few hundred micrometers, such as those required to couple directly to optical fibres (as presented in this thesis).

2.3.3 Less Common Methods & Tabular Comparison of Fabrication Methods

In addition to the methods mentioned so far, there are further ways to fabricate DLSPPW structures which have not been mentioned and which are rarely mentioned in the literature, but which are standard methods in the field of micro- and nanostructuring and which will therefore be briefly mentioned with an explanation why they are not commonly used for DLSPPWs.

Focused ion beam (FIB) lithography is one such technology. This is a technology where a focused ion beam is used to polymerize a photoresist, ablate material directly or effect other material changes, such as refractive index changes. Known for its incredible accuracy and precision, with an achievable resolution commonly in the range of 100 nm or less [199], FIB nevertheless has some severe draw-backs for fabrication of DLSPPWs. While the implantation of unwanted ions into the substrate or waveguide material [200] is a negligible issue in DLSPPW structures, the writing speed of any FIB system is slow compared to 2PP, and the cost is significantly higher, even if it is lower than for advanced EBL systems [201]. FIB is also severely limited in the size of structures it is able to fabricate, the limit typically being on the order of hundreds of microns.

Consequently, its use in plasmonic and photonic applications has been limited, with only few applications where its special advantages can be put to good use, such as in fabrication of waveguides inside lithium niobate [202] or nanodot plasmonic waveguide structures [203]. It should be noted additionally, especially in comparison with 2PP, that FIB is seldomly used alone. It has been used in direct conjunction with UV mask lithography [201] and EBL [202]. These multi-step processes using multiple high-end technologies make fabrication of structures both time- and capital-intensive.

FIB was used only once during the course of this work. FIB was employed to cut the ends of nanoimprinted waveguides to produce a straight and evenly cut waveguide end. This was not entirely successful, in particular it was impossible to produce cuts that had sufficient quality for low-loss coupling. However, it was established that FIB was fully capable of cutting the polymer waveguide material as well as the glass substrate. A brief description of this can be found in section 6.2.

Another technology worth mentioning here is stereolithography. Stereolithography is a rapid prototyping technology that is based on a light-induced layer-stacking manufacturing process [204]. Already commercially available by 1986, stereolithography is known for its ability to create structures ranging in size from the sub-micron to the decimeter range and is increasingly popular in, for example, the biomedical sector [205]. The resolution of stereolithography is, however, not good enough for DLSPPW applications.

Nanoimprint lithography has already been broadly discussed in section 2.2. As noted there, it is an increasingly popular method of structure fabrication due to its parallel nature. If a master for printing can be provided, nanoimprinting is very fast and cheap. The necessity of one master sample for every kind of structure does not make the technology - when considered by itself - particularly flexible, however.

A tabular overview of the different fabrication methods for DLSPPW components including their technical parameters and relative speed and flexibility ratings is given below in table 1.

Table 1: Comparison of the fabrication methods used for DLSPPW components. 2PP - two photon polymerization; EBL - electron beam lithography; FIB - focused ion beam; STL - stereolithography; UV-L - ultra-violet lithography; NIL - nanoimprint lithography

fabrication method	dim.	resolution [nm]	speed	serial / parallel	flexibility	reference
2PP	3D	<100	very fast	serial	very high	[147]
EBL	2D	<5	slow	serial	high	[192]
FIB	2D	<100	medium	serial	high	[199]
STL	2.5D	<1000	fast	serial	medium	[205]
UV-L	2D	<300	very fast	parallel	very low	[189]
NIL	2.5D	<10	very fast	parallel	medium	[184]

2.4 Overview of Equipment and Resist Materials

This section aims to give an overview of the main pieces of equipment used in this thesis, as this may be of interest to following generations of students and researchers working in this field.

2.4.1 Lasers for 2PP

A variety of lasers is suitable for 2PP, and many are not. This section will detail those lasers that have been used in the course of this work and analyze their suitability for 2PP, culminating in a tabular comparison in table 2. In principle the main requirements of any laser contemplated for 2PP usage are that the wavelength of the laser does not trigger any reaction in the photopolymer as long as it is not focused (since otherwise we would be talking about 1PP and not 2PP!) and that two-photon polymerization can be induced in the photoresist. In addition, of course, the laser should be pulsed to guarantee a high photon density in the pulses. Since many photoinitiators are UV-sensitive and transparent in the visible to NIR range, this - generally speaking - means that all pulsed lasers with a wavelength somewhere between 500 and 1000 nm may be considered suitable for 2PP.

In practice, the suitability depends on a wide range of variables, including the exact application. The choice of photoresist, substrate and structure geometry may play a very large role. The wavelength sensitivity of any photoresist is quite obvious. It can be tuned - if the photoresists are self-made - by selecting a photoinitiator particularly suited to the laser in use. The influence of the substrate is less obvious. The challenge lies in resonances in the electronic structure of, for example, metals, which can lead to heat accumulation near the surface, which, when combined with the high reflection from a metal surface compared to glass, can lead to extreme laser intensities near the surface which literally boil (and, by a steam-explosion, detonate!) a photoresist even at low laser power settings. Structure geometry also plays a part when viewed in light of the repetition rate of a given laser. Large structures, if

they are to be completed within a reasonable time, require high fabrication speeds if there is a simultaneous need for high resolution. A laser with a low repetition rate means a low number of pulses per second, which strongly limits the fabrication speed, since the translation stage can only move so far that the next pulse still overlaps with the last one. In practice, this means that a recommendation for any structure larger than a hundred micrometers in any direction, with a resolution of at least one micrometer, is to use a laser with a repetition rate of at least 1 MHz.

The first laser used (in the early stages of this work) for 2PP fabrication was a Spectra Physics Tsunami laser, a Ti:Sapphire femtosecond (fs) laser operating in the wavelength range from 780 to 800 nm and a repetition rate of 80 MHz and a pulse duration of 120 fs. The repetition rate is high enough to allow fast structuring and the wavelength was also suitable for the fabrication of structures on gold surfaces.

The laser with which the majority of the structures in this thesis were fabricated is an Yb:glass fs-laser operating at 1030 nm wavelength and frequency-doubled to 515 nm. The repetition rate of this laser is 10 MHz and the pulse duration ca. 150 fs. The laser is a unique model sold by Polar Lasers, and was in fact designed, built and for a long time operated by the Institute of Quantum Optics at the Leibniz Universität Hannover. The laser has a high repetition rate that allows very fast structuring, but is not particularly well-suited for fabrication on gold surfaces.

Several models of Femtotrain lasers from HighQ Lasers have been tested for 2PP, and in fact are also commonly sold in the commercially available version of the M3D 2PP fabrication system. There are two primary types of laser available, a Yb:glass laser operating at 1040 nm wavelength (which is frequency-doubled to 520 nm) and a Ti:sapphire laser tunable from 790 to 870 nm. Both types have repetition rates high enough to allow very high-speed structuring with good results on any type of substrate material.

For a brief period, a very compact and very cheap nanosecond-pulse laser (μ Flare GR made by InnoLight GmbH in Hannover, Germany) operating at 532 nm was tested for 2PP structuring. The main drawback of the laser was the extremely low repetition rate of 50 kHz. For high-resolution fabrication, this meant that even at the slowest of structuring speeds, with the axis moving only $100 \mu\text{m}/\text{s}$, each individual pulse could be distinguished in a line structure. At higher speeds the pulses separated into chains of dots. At very high speeds, a $100 \mu\text{m}$ long line was represented by only a single pulse, that is instead of a line $100 \mu\text{m}$ long, the fabrication result consisted of a single $500 \times 500 \text{ nm}$ dot at a random position somewhere along a $100 \mu\text{m}$ line. For very low-resolution structures, this laser would still be a useful and cheap fabrication tool, but not in the fabrication of DLSPW structures.

The technical parameters of all laser systems is summarized in table 2.

2.4.2 Photoresists Used in Fabrication

A large number of different photoresist materials were used in this work. Each and every photoresist has specific advantages and disadvantages, which are briefly

Table 2: Laser data

laser name	manufacturer	wavelength [nm]	pulse duration	repetition rate	average power
Tsunami	Spectra Physics	780	120 fs	80 MHz	300 mW
Yb:glass	Polar Lasers	1030	200 fs	10 MHz	200 mW
		515	150 fs	10 MHz	50 mW
Femtotrain Yb:glass	HighQ Laser	520	250 fs	76 MHz	200 mW
Femtotrain Ti:sapphire	HighQ Laser	790	100 fs	73 MHz	200 mW
μ Flare GR	InnoLight	532	5 ns	50 kHz	50 mW

outlined here. The photoresists used in this work can be separated into two main groups - those that are voluminous and those that are spin-coated as a thin layer.

Initially, the primary voluminous photoresist material was Ormocer (made by the company micro resist technology GmbH in Berlin, Germany). Ormocers are a group of organic-inorganic hybrid polymers developed by the Fraunhofer Gesellschaft. The Ormocers have the advantage that they are transparent at all interesting wavelengths and that they are specially developed for lithographic purposes.

After great success with Ormocer in the first phase of this work, it was discovered that the material ages rapidly and is also prone to shrinkage. Since part of this thesis deals with very large (by microfabrication standards) structures of 4-5 mm length, an alternative had to be found.

The best material was discovered to be a new hybrid polymer based on an "Ormosil" hybrid sol-gel, which was developed by a partner institute in Greece and is a very good material in 2PP fabrication [206]. The material is a 20:80 zirconium-silicon sol-gel containing 4,4-bis(diethylaminobenzophenone) as a photoinitiator [207].

Ormosil has many advantages compared to Ormocer for 2PP applications. The photoresist does not age noticeably and is still suitable for structure fabrication after years of shelf storage. It is also transparent, does not shrink significantly [208] and has a large processing window [207]. Unlike Ormocers, which require specialized developers, development of Ormosil takes place with isopropanol. It is now the primary voluminous photoresist, with samples prepared by drop-casting. A pre-exposure bake has been tested. A generally successful method was found to be a slow heating of the samples by baking for thirty minutes at 40°C, 60°C and 80°C successively.

There are also a number of spin-coated resists that were used. Typically the spin-coated layers are 500 nm thick, since this is the thickness required for the DLSPW waveguides to be single-mode.

Initially the spin-coated resists included ma-N 1405 and mr-UVL 6000. The resist ma-N 1405 is one of the standard negative tone photoresists for UV-lithography, conventional pattern transfer and single-layer lift-off, offered by the company micro

resist technology GmbH in Berlin, Germany. The resist mr-UVL 6000 is a photoresist offered by the same company specifically developed for UV lithography. Both resists have their core sensitivity in the 300-400 nm wavelength range. When we compare this to the 2PP laser wavelengths in use (see above), we find that the 780 nm wavelength used initially lies exactly in this window (370 nm), but the 515 nm wavelength that was substituted for it does not (267.5 nm). Experiments with these photoresists were consequently reduced after the change of laser system.

Fortunately, it was found that the curing polymer used in all nanoimprint lithography experiments in this work, mr-NIL 6000 (also made by the company micro resist technology GmbH), also performed well as a spin-coatable photoresist for two-photon polymerization. This resist was consequently used in two different roles.

As a 2PP-photoresist, mr-NIL 6000 is spin-coated onto a substrate, for 30 seconds at 3000 rpm and for five seconds at 4500 rpm, to produce a 500 nm thick layer of resist. It is then pre-baked at 110°C for three minutes, after which it is processed - in this thesis that means structured using 2PP. After structuring, it is post-baked at 110°C for five minutes and then developed using mr-dev 600, a solvent-based developer also produced by the company micro resist technology GmbH.

As a nanoimprint lithography material, mr-NIL 6000 is prepared by drop casting it onto a substrate and stamping with a combination of UV light and thermal exposure. The exact procedure is already given above in the section on nanoimprint lithography.

A lesser-used material from the Ormocer family was "Ormostamp" (again distributed by the company micro resist technology GmbH), which was chosen for a very special purpose, namely the fabrication of ultra-high aspect ratio structures by 2PP. The fabricated structures, intended to be attached to gold nanoparticles and used for wind-tunnel testing of microstructures, are up to 300 μm high and have aspect ratios of up to 40:1 (see figure 2.13). Ormostamp was chosen for this task because of its high elasticity modulus of 0.650 GPa (figure supplied by manufacturer), which would allow easy bending under wind pressure.

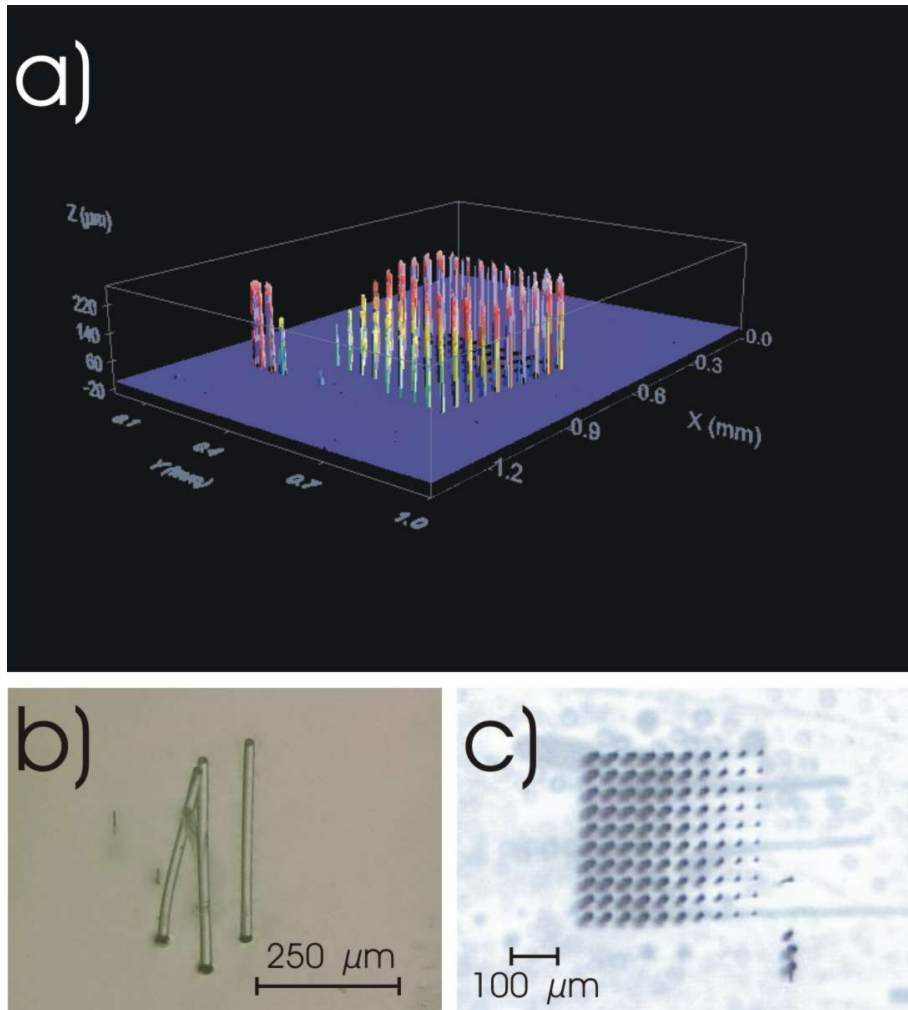


Figure 2.13: Images of ultra-high aspect ratio structures fabricated by 2PP with the photoresist Ormostamp. a) Shows a 3D view of a field of pillars made using an optical profiler. b) Shows an optical microscope image showing the tallest pillars, $350\ \mu\text{m}$ high and $15\ \mu\text{m}$ wide. c) Shows an optical microscope image of a field of pillars just after fabrication by 2PP.

3 Simulation Tools

Two families of simulation tools were used in the course of this thesis, one for the experiments with DLSPPW components and one for the experiments with localized surface plasmons without waveguides. All simulation methods used in the course of this thesis are numerical.

For the waveguide experiments, the Photonic Component Design Suite developed by RSoft was used. This is a software package that allows design and simulation of both passive and active photonic devices, and was consequently ideally suited for the simulation of plasmonic waveguide devices. The most-heavily used part of the suite was the FDTD programme "FullWAVE", which will be introduced in more detail in this section.

In the case of the experiments with localized surface plasmons without waveguides, a series of Matlab programmes developed primarily by Andrey B. Evlyukhin was used [209, 210]. This method is based on the Green's function formalism and the point-dipole approximation.

3.1 FDTD Simulations

FullWAVE is a highly sophisticated simulation tool for studying the propagation of light in a wide variety of photonic structures including integrated and fibre-optic waveguide devices as well as circuits and nanophotonic devices such as photonic crystals. The software employs the Finite-Difference Time-Domain (FDTD) [211] method for the full-vector simulation of photonic structures. It is used in this thesis primarily to investigate SPP and light propagation in photonic and plasmonic components and devices.

The largest advantage of FDTD simulations is the fact that they are direct solutions of Maxwell's equations. As such they offer more exact solutions than alternative methods that require approximations. The FDTD method is a rigorous solution to Maxwell's equations and does not have any approximations or theoretical restrictions [212].

In a region of space which contains no flowing currents or isolated charges, Maxwell's curl equations in can be written in Cartesian coordinates as six simple scalar equations:

$$\frac{\partial H_x}{\partial t} = -\frac{1}{\mu} \left(\frac{\partial E_y}{\partial z} - \frac{\partial E_z}{\partial y} \right) \quad (3.1)$$

$$\frac{\partial H_y}{\partial t} = -\frac{1}{\mu} \left(\frac{\partial E_z}{\partial x} - \frac{\partial E_x}{\partial z} \right) \quad (3.2)$$

$$\frac{\partial H_z}{\partial t} = -\frac{1}{\mu} \left(\frac{\partial E_x}{\partial y} - \frac{\partial E_y}{\partial x} \right) \quad (3.3)$$

$$\frac{\partial E_x}{\partial t} = -\frac{1}{\varepsilon} \left(\frac{\partial H_z}{\partial y} - \frac{\partial H_y}{\partial z} \right) \quad (3.4)$$

$$\frac{\partial E_y}{\partial t} = -\frac{1}{\varepsilon} \left(\frac{\partial H_x}{\partial z} - \frac{\partial H_z}{\partial x} \right) \quad (3.5)$$

$$\frac{\partial E_z}{\partial t} = -\frac{1}{\varepsilon} \left(\frac{\partial H_y}{\partial x} - \frac{\partial H_x}{\partial y} \right) \quad (3.6)$$

It can be noted that for each set of equations for E_i or H_i , it is sufficient to know a single equation. The others can be easily obtained by cyclically exchanging the values x , y , and z .

Maxwell's equations describe a situation in which the temporal change in the \vec{E} field is dependent upon the spatial variation of the \vec{H} field, and vice versa. A FDTD software programme, like the one used here, works by numerically solving discretized versions of Maxwell's equations. For the discretization, central differences in time and space are required.

In our case, Yee's mesh [213] is used as the method to solve the equations and to compute the \vec{E} and \vec{H} field. The mesh consists of points on a 3D grid with the grid points spaced at intervals of Δx , Δy , and Δz . The \vec{E} and the \vec{H} field components are then interlaced in all three spatial dimensions as shown in Fig. 3.14. Time is also broken up into discrete steps of Δt . The \vec{E} field components are computed at the point in time $t = n\Delta t$ and the \vec{H} fields at the slightly later point in time $t = (n + 1/2)\Delta t$, where n is an integer representing the compute step. For example, the \vec{E} field at a time $t = n\Delta t$ is equal to the \vec{E} field at $t = (n - 1)\Delta t$ plus an additional term computed from the spatial variation, or curl, of the \vec{H} field at time t .

This method results in six equations that can be used to compute the field at a given mesh point, denoted by integers i , j , k . Since, as above, the other equations may be obtained by cyclically exchanging values x , y , and z , we will restrict ourselves to showing only two of them:

$$H_{x(i,j,k)}^{n+1/2} = H_{x(i,j,k)}^{n-1/2} + \frac{\Delta t}{\mu\Delta z} (E_{y(i,j,k)}^n - E_{y(i,j,k-1)}^n) - \frac{\Delta t}{\mu\Delta y} (E_{z(i,j,k)}^n - E_{z(i,j-1,k)}^n) \quad (3.7)$$

$$E_{x(i,j,k)}^{n+1} = E_{x(i,j,k)}^n + \frac{\Delta t}{\varepsilon\Delta y} (H_{z(i,j+1,k)}^{n+1/2} - H_{z(i,j,k)}^{n+1/2}) - \frac{\Delta t}{\varepsilon\Delta z} (H_{y(i,j,k+1)}^{n+1/2} - H_{y(i,j,k)}^{n+1/2}) \quad (3.8)$$

These equations are iteratively solved in a leapfrog manner, alternating between computing the \vec{E} and \vec{H} fields at subsequent $\Delta t/2$ intervals.

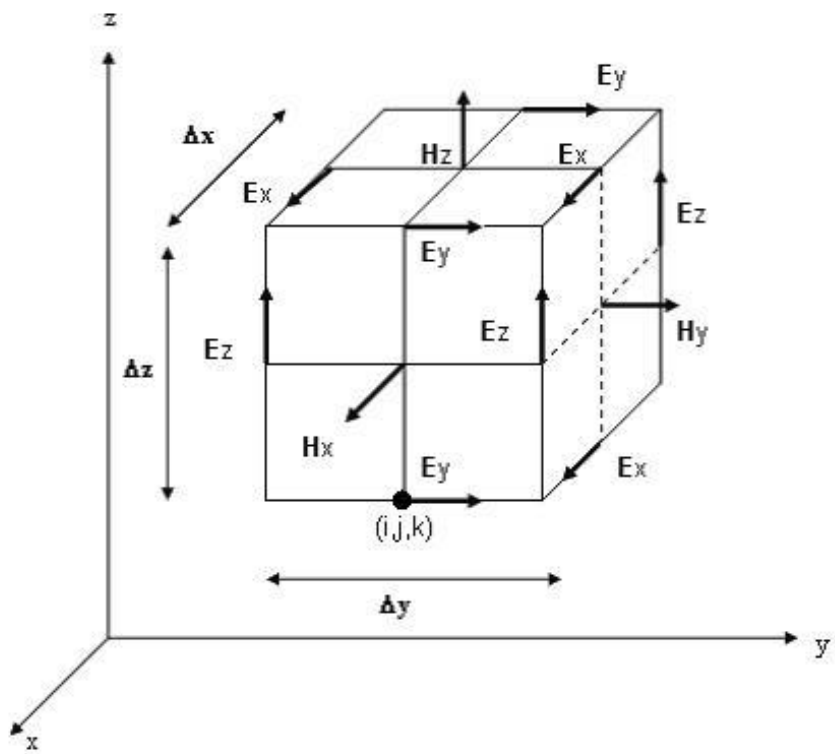


Figure 3.14: In a Yee cell of dimension Δx , Δy , Δz , note how the H field is computed at points shifted one-half grid spacing from the E field grid points [213].

For the calculations using this software package, physical and numerical parameters are required. The two sets of physical parameters that are necessary to perform a simulation are the material parameters, including the relative permittivity $\varepsilon(\vec{r}, \omega)$ and relative permeability $\mu(\vec{r}, \omega)$ as a function of space and/or frequency, and the electromagnetic field excitation. Once these parameters are given, physics dictates the electromagnetic field as a function of (\vec{r}, t) , or space and time.

The material parameters simply define the electromagnetic properties of the material of the waveguide, substrate, and surrounding medium (air, in our case). The programme FullWAVE utilizes the following formulas to specify the material properties of a waveguide:

$$\vec{D} = \varepsilon_0 \vec{E} + \vec{P} \quad (3.9)$$

$$\vec{B} = \mu_0 \vec{H} + \vec{M} \quad (3.10)$$

where

$$\vec{P} = \varepsilon_0 \left(\chi(\omega) \vec{E} + \chi^2 \vec{E}^2 + \chi^3(\omega) \frac{I}{1 + c_{sat} I} |\vec{E}^2| \vec{E} \right) \quad (3.11)$$

$$\vec{M} = \mu_0 \left(\chi_m(\omega) \vec{H} + \chi_m^2 \vec{H}^2 + \chi_m^3(\omega) \frac{I}{1 + d_{sat} I} |\vec{H}^2| \vec{H} \right) \quad (3.12)$$

Which can be re-written as:

$$\vec{D} = \varepsilon_0 \left(\vec{E} + \chi(\omega) \vec{E} + \chi^2 \vec{E}^2 + \chi^3(\omega) \frac{I}{1 + c_{sat} I} |\vec{E}^2| \vec{E} \right) \quad (3.13)$$

$$\vec{B} = \mu_0 \left(\vec{H} + \chi_m(\omega) \vec{H} + \chi_m^2 \vec{H}^2 + \chi_m^3(\omega) \frac{I}{1 + d_{sat} I} |\vec{H}^2| \vec{H} \right) \quad (3.14)$$

These equations (3.13 and 3.14) have four terms, each of which corresponds to a different effect. The first term takes into account the linear index of the system. The second term takes into account material dispersion, or the change of index as a function of wavelength. The third and fourth terms in these equations are non-linear terms, and correspond to a second order nonlinearity and a frequency-dependent third-order non-linearity. It is also possible to define anisotropic effects in the programme.

In order to perform a simulation, an initial launch condition ϕ_L at time $t = 0$ is needed, as well as a driving function in time. This consists of both a spatial and temporal excitation, such as

$$\phi_L(\vec{r}, t) = f(\vec{r}_0)g(t), \quad (3.15)$$

where $f(\vec{r}_0)$ is the spatial excitation at the launch plane and $g(t)$ is the temporal excitation.

In addition, the software's solution algorithm requires additional input in the form of the numerical simulation parameters. These parameters are used to define the region of interest for the programme, and tell it exactly in which area of space and time to perform its calculations. For example, the software must have a finite computational domain, defined by $\{x \in (x_{min}, x_{max})\}$, $\{y \in (y_{min}, y_{max})\}$, and $\{z \in (z_{min}, z_{max})\}$. More simply put, the software must know where the world it is interested in ends. The computational domain was always chosen to include the entire structure under investigation and a certain volume of substrate below and air above, as well as a little distance to the sides.

If we arbitrarily define z as the direction of propagation here for demonstration purposes, the following equations define the typical setup of the computational domain in the studies performed here:

$$x_{max} - x_{min} \approx 3x_{comp} , \quad (3.16)$$

$$y_{max} - y_{min} \approx 3y_{comp} , \quad (3.17)$$

$$|z_{max} - z_{min}| \approx z_{comp} , \quad (3.18)$$

where i_{comp} denotes the overall length of a component in dimension i .

The boundary conditions at the borders of the computational domain are equally important. Inside the simulation software, it is possible to choose an absorbing boundary layer that eliminates any outward-propagating energy. A particularly effective version of this is the perfectly matched layer [214], in which both electric and magnetic conductivities are introduced in such a way that the wave impedance remains constant, absorbing the energy without inducing reflections. It is also possible to define periodic boundary conditions in order to simulate photonic band gaps in periodic structures, but this was not used in this thesis. The basic idea behind this is that the boundary condition is chosen such that the simulation is equivalent to an infinite structure composed of the basic computational domain repeated endlessly in all dimensions.

Of fundamental importance is the size of the spatial grid, defined by the values for Δx , Δy , and Δz , and the temporal grid, defined by the time step Δt . The grid size is very important for the accuracy of the simulation. A close-mesh grid results in a very high resolution and high-quality results, but at the same time this requires a lot of computing power and/or time, so it is necessary to find a compromise.

The software FullWAVE supports both a uniform and non-uniform spatial grid. In order to produce an accurate simulation, the spatial grid must be small enough to resolve the smallest feature of the field to be simulated. Usually this is dictated by the wavelength in the material(s) to be simulated, but, in some cases, can be dictated by the geometry of the photonic device. Typically, the grid spacing must be able to resolve the wavelength in time, and therefore usually be less than $\lambda/10$ where λ is not the free space wavelength, but rather the wavelength in the material(s).

Since the FDTD algorithm is based in the time domain, FullWAVE has several parameters which relate to the temporal grid. To obtain a stable simulation, one

must adhere to the Courant condition [215] which relates the spatial and temporal step size:

$$c\Delta t < \frac{1}{\sqrt{\frac{1}{\Delta x^2} + \frac{1}{\Delta y^2} + \frac{1}{\Delta z^2}}}, \quad (3.19)$$

where c is the velocity of light and, for the case of a non-uniform grid, the grid sizes represent the smallest grid size in the simulation. FullWAVE will automatically enforce this condition.

It is also necessary to define the total length of time for the simulation t_{tot} . For the structures investigated in this thesis, it was sufficient to have

$$t_{tot} > 2t_0, \quad (3.20)$$

where t_0 is the time required for the electromagnetic wave to reach the end of the structure. Since the FDTD simulations in this thesis were used to investigate the behaviour of components where for the excitation intensity

$$\frac{\partial I}{\partial t} = 0 \quad (3.21)$$

was true, it was never necessary to have the total length of the simulation much longer than the time necessary for the \vec{E} and \vec{H} fields inside the structure to reach their equilibrium states, which happens some time after the wave reaches the end of the structures.

The computational steps in FDTD are relatively simple, using only addition, subtraction, and multiplication which improves the simulation speed. The technique is extremely versatile because it is inherently full-vectorial without limitations on optical effects such as direction of propagation, index contrast, or backward reflections. The FDTD method is time-tested and stable, and can efficiently handle material dispersion and nonlinearities. Also, because it is based in the time-domain, it can cover a wide frequency range with a single simulation run. Furthermore, FDTD lends itself to cluster computing. This allows the computational demand for a single problem to be shared among several computers on a network, and permits researchers to simulate problems otherwise impossible on a single computer. The calculations performed in the course of this thesis were invariably performed on a cluster of five quad-core PCs, with a total of 20 CPUs and 20 GB of RAM to run the simulation.

3.2 Green's Tensor Calculations

The experiments using localized surface plasmons could be simulated with the same approach from the dielectric waveguide structures, however there is a different modeling method available which is significantly faster. The programme used here in this thesis is a numerical modeling tool based on the Green's tensor approach and the electric dipole approximation [216].

The system under consideration is a spherical gold nanoparticle surrounded on one side by air (in the region $z > 0$) with the dielectric constant $\varepsilon_d = 1$ and on the other side by gold (in the region $z < 0$) with the dielectric constant ε_m . The nanoparticle is placed on a gold surface in the air half-space and is irradiated by a SPP Gaussian beam, so that the particle is in the beam centre, as shown in figure 3.15 (a).

In the electric dipole approximation, the absorption cross-section exceeds the scattering one, for small spherical particles with a radius $R \ll \lambda$, when the particle volume V satisfies the condition

$$V < 3\lambda^3\varepsilon_d\text{Im}(\varepsilon_p)/4\pi^2([\text{Re}(\varepsilon_p) + \varepsilon_d]^2 + [\text{Im}(\varepsilon_p)]^2), \quad (3.22)$$

where, λ is the wavelength of the incident wave in the dielectric medium, $\varepsilon_p = \text{Re}(\varepsilon_p) + i\text{Im}(\varepsilon_p)$ and ε_d are the particle and the surrounding dielectric permittivities, respectively [217, 218]. This condition strongly depends on the wavelength and on the real and imaginary parts of the electric permittivity in the particle. In [217] it is also shown that the magnetic dipole contribution for small particles with a large dielectric constant can be of the same order of magnitude as the electric dipole contribution when the following condition is fulfilled

$$|2\pi\sqrt{\varepsilon_p}R/\lambda| \gg 1, \quad (3.23)$$

Thus, the possibility is given to choose precisely the particle's material, shape, and size, which is of principal importance for an accurate simulation of the interaction of a localized surface plasmon with a metallic nanoparticle [216].

In general, one can say that the total electric field is given by the sum of the external electric field $\vec{E}_0(\vec{r})$ and the field of the particle $\vec{E}_p(\vec{r})$, giving the equation

$$\vec{E}(\vec{r}) = \vec{E}_0(\vec{r}) + \vec{E}_p(\vec{r}). \quad (3.24)$$

In the framework of the Green's function approach, the total electric field in the system can be determined from the Lippmann-Schwinger integral equation (the fields are assumed to be monochromatic, oscillating at a frequency ω) [219]

$$\vec{E}(\vec{r}) = \vec{E}_0(\vec{r}) + k^2 \int_V \hat{G}(\vec{r}, \vec{r}') [\varepsilon_p(\vec{r}') - \varepsilon_d] \vec{E}(\vec{r}') d\vec{r}', \quad (3.25)$$

where $\vec{E}_0(\vec{r})$ is in our case the electric field of the incident SPP Gaussian beam [220], k is the free-space wave number, V is the volume occupied by the particle, ε_p is the dielectric constant of the nanoparticle, and ε_d is the dielectric constant of the surrounding area. The propagation of the electric field in the system without the nanoparticle is described by the Green's tensor $\hat{G}(\vec{r}, \vec{r}')$. This tensor can be represented as a sum of several contributions [221] that govern the excitation of SPPs, s - and p -polarized waves propagating away from the interface, and a quasistatic (near) field [216].

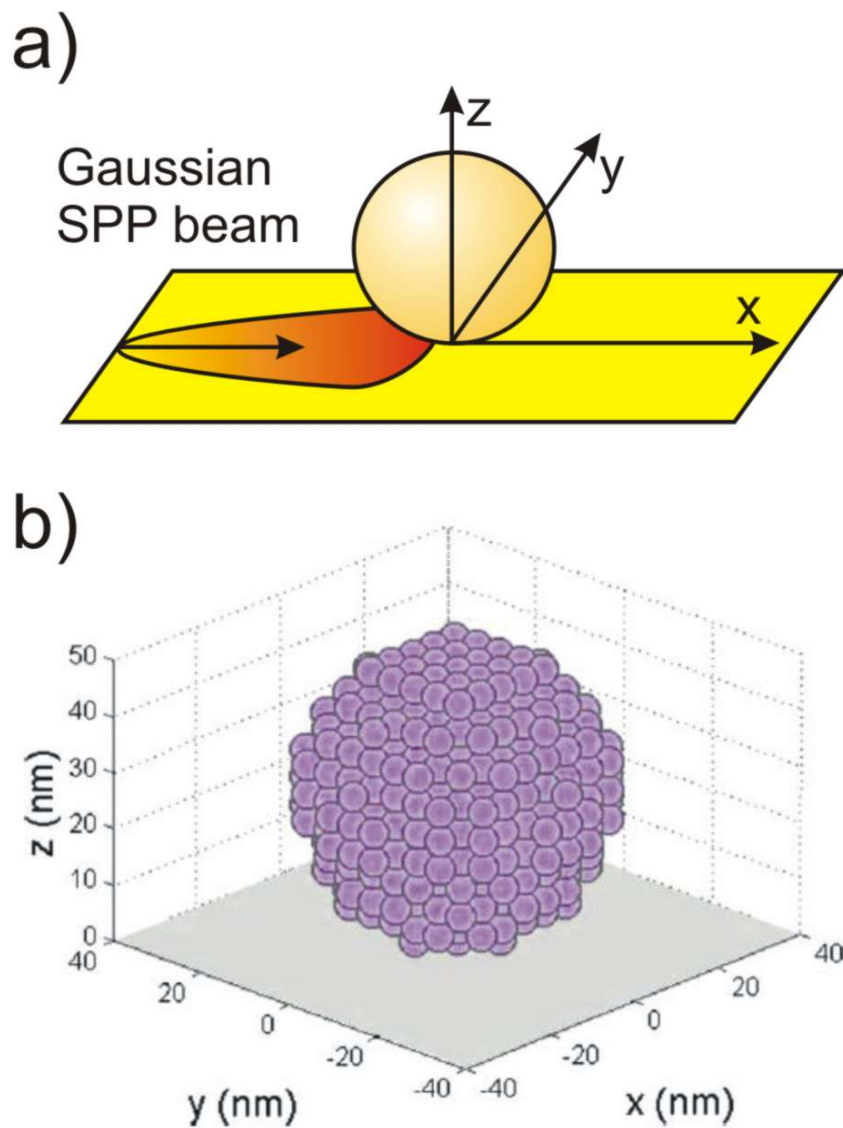


Figure 3.15: Schematic representation of the particles: a) a spherical particle on the metal surface, b) a spherical particle consisting of multiple dipole elements after the discretization procedure.

This representation can be used for the investigation of different SPP scattering channels [222]. The solution of equation (3.25) in the domain occupied by the scattering nanoparticle is obtained numerically by the coupled dipole method also known as the discrete dipole approximation [223, 224]. In this approach, the scatterer is discretized into a number of sampling volumes, as illustrated in figure 3.15 (b). In each sampling volume the electric field amplitude is considered constant [225, 226]. Introducing polarizabilities for these sampling volumes, one can obtain a set of linear simultaneous equations for the electric fields or dipole moments of all volume elements [223, 224].

The accuracy of the calculations depends on the discretization step and on the proper choice of polarizabilities. For small discretization steps, the polarizability is taken in the quasistatic approach and coincides with that for a spherical particle with its diameter equal to the discretization step. This polarizability also takes into account the interaction of every sampling cell with the flat metal surface (the dressing effect [227]).

The knowledge of the total electric field distribution inside the scattering particle and the tensor $\hat{G}(\vec{r}, \vec{r}')$ allows the calculation of the field distribution in different places outside the scatterer (equation 3.25) and to obtain the scattered powers into different channels (SPP - SPP and SPP - light) [222, 228]. Moreover, using the Poynting theorem it is possible to estimate the extinction power and, by subtracting the total scattering power, to determine the absorption by the particle. Note that in the calculations of the scattered power, the imaginary part in the permittivity of the reference system (without the scattering particle) is neglected [216].

For small spherical nonmagnetic particles (with the radius much smaller than the wavelength of the incident wave), the electric dipole approach is usually used for estimations of the absorption and scattering cross sections [217]. In this case, the scatterer, in the first approximation, can be considered as an electric dipole located in the particle centre and having a dipole moment

$$\vec{p} = \varepsilon_0 \int_V [\varepsilon_p(\vec{r}) - \varepsilon_d] \vec{E}(\vec{r}) d\vec{r}, \quad (3.26)$$

where ε_0 is the vacuum permittivity and $\vec{E}_0(\vec{r})$ is the total electric field inside the scatterer.

It is then possible to calculate the total electric field outside the particle, which can be written as

$$\vec{E}(\vec{r}) = \vec{E}_0(\vec{r}) + \frac{k^2}{\varepsilon_0} \int_V \hat{G}(\vec{r}, \vec{r}') \vec{p} d\vec{r}'. \quad (3.27)$$

With increasing particle size the magnetic moment of the particle calculated from the equation

$$\vec{m} = \frac{-i\omega\varepsilon_0}{2} \int_V \vec{r} \times [\varepsilon_p(\vec{r}) - \varepsilon_d] \vec{E}(\vec{r}) d\vec{r} \quad (3.28)$$

should be taken into account [216]. The magnetic field can then also be calculated.

In order to estimate the contribution from higher multipole terms, including the magnetic dipole, the calculated results in the dipole approximation are compared with those obtained numerically in the general case and experimental results. This allows an estimation of the particle sizes when the higher-order terms start to play an important role for SPP scattering [216].

4 Characterization Methods

In this section the methods will be outlined that were used to characterize the components produced during the course of this thesis. This includes both the experimental characterization techniques used to demonstrate the functionality of fabricated structures, such as leakage radiation microscopy and plasmon excitation by end-fire coupling using optical fibres, as well as all methods used to verify structure geometry, such as electron beam microscopy and confocal optical profiling.

4.1 Introduction to Leakage Radiation Microscopy

Several methods exist to visualize and measure surface plasmon-polaritons. The difficulty with making SPPs visible is that they are in principle no more than an electron density wave. SPPs can exist only under certain conditions, as mentioned in the introduction, which must be taken into account when designing an experimental setup for the reliable and efficient observation of SPP waves.

Several approaches to the problem exist, including the well-known and pioneering Otto [48] and Kretschmann [49] configurations, however both methods have the disadvantage of requiring a prism, and are a little unwieldy to handle.

The scanning near-field optical microscope (SNOM) is another much-favoured approach. SNOM was already used in the 1990's to examine surface plasmon resonances [229], and has been used by partners closely associated with this work on a number of occasions recently [187, 230, 231]. SNOM has some major disadvantages, including the need for a large amount of specialized equipment and the long scanning time it takes to characterize a single SPP.

To provide a quick, rapid and flexible approach with excellent capabilities, leakage radiation microscopy (LRM) was chosen. LRM has also been used by several groups recently in conjunctions with DLSPWs [232, 233, 189, 234, 235, 236], often in direct collaboration with this work. The principle of LRM was refined over earlier improvements [237] for this thesis.

LRM has several main advantages over all other methods. It is essentially still an optical microscope, so it is possible to easily view the DLSPW structures at the same time while characterizing their SPP-guiding properties. Because of its purely optical nature, it is also easy to increase or decrease the field of view and magnification by simply choosing different optical components. The magnification and field of view was, in fact, changed several times during the course of this work. Generally, the SPP can be seen in its entire length from excitation spot to the point where propagation losses have decreased its intensity below the observation threshold in one measurement image. That means that for a typical measurement, only one single snapshot with a CCD camera is necessary, unlike SNOM where a scan may take up to an hour.

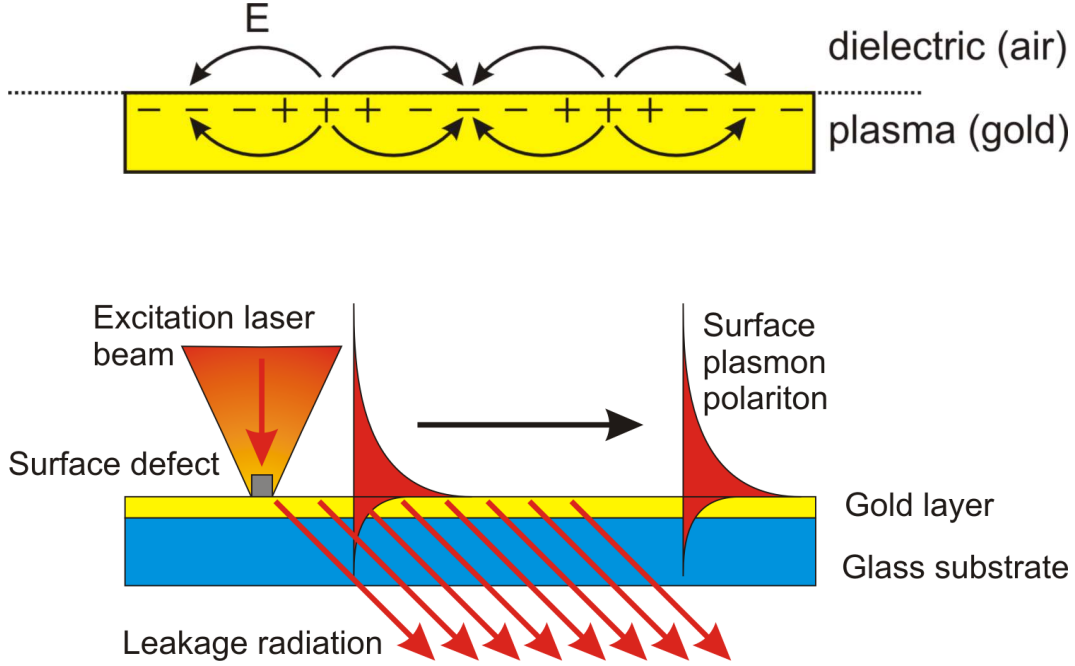


Figure 4.16: This figure illustrates the fundamental properties of a propagating surface plasmon polariton (SPP). Top: The charges and electric field of a an SPP propagating on a metal surface are shown schematically. Bottom: The excitation of a propagating SPP using a surface defect is shown. The exponential dependence of the electric field is indicated by the shape of the SPP.

4.2 Principles of Leakage Radiation Microscopy

As shown in figure 4.16 (top), an SPP is in principle nothing more than a propagating wave of electron density oscillations on the surface of a plasma [54]. The frequency of this oscillation ω is connected to its wave vector k_x (if we assume propagation in x-direction) by the dispersion relation $\omega(k_x)$, which was already shown in figure 1.2 and discussed in section 1.2.

The electric field of the SPP is described by

$$E = E_0^\pm e^{i(k_x x \pm k_z z - \omega t)}, \quad (4.29)$$

where the $+$ is for $z \geq 0$ and $-$ for $z \leq 0$. The factor k_z is imaginary, so the exponential decay of the field in z-direction can be characterized briefly by writing

$$E_z \sim e^{-|k_z|z}. \quad (4.30)$$

The SPP can be excited by focusing the excitation laser beam onto a surface defect such as a ridge. This is shown schematically in figure 4.16 (bottom). If a dielectric material with $\epsilon > 1$, such as glass, is in contact with the metal film on the other side of the metal-air interface, then the evanescent SPP wave transforms into a plane wave and can be observed [54]. This leads to the emission of the so-called "leakage radiation", which is emitted under a fixed steep angle. This angle

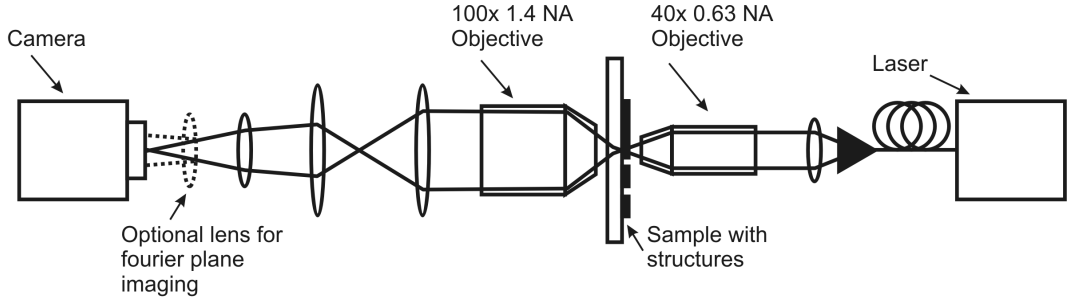


Figure 4.17: A schematic drawing of the fundamental components of any LRM setup.

necessitates the choice of high-NA, liquid immersion objectives for leakage radiation microscopy.

The thickness of the gold layer influences the propagation length L_{prop} of the SPP, since leakage radiation can only occur when the gold is thin enough and this is a loss mechanism for the SPP [54]. The propagation length L_{prop} is defined as the distance an SPP can propagate before its intensity has decayed to $1/e$:

$$I = I_0 e^{-\frac{L}{L_{prop}}}, L_{prop} = -\frac{L}{\ln\left(\frac{I}{I_0}\right)}, \quad (4.31)$$

where I is the intensity of the SPP after it has propagated the distance L and I_0 is the intensity at $L = 0$.

A gold layer between 50 nm and 100 nm thick has become the standard in SPP research [235, 150] due to its balance between long propagation length and ease of SPP observation using leakage radiation microscopy. Unless otherwise noted, the gold film thickness of samples used in this thesis is always 50 nm.

4.2.1 Description of Experimental Setup

A schematic drawing of a typical LRM setup is shown in figure 4.17. These components are to be found in any LRM setup. From the light source (shown here as a fibre-coupled laser, although any laser can be used in practice), the light is collimated and focused onto the sample through a 40x objective with an NA of 0.63. The focus is also the excitation spot of the SPP, if the sample has been correctly positioned. The light is collected by a 100x or 63x objective with an NA of 1.4. The NA must be as large enough to collect the leakage radiation from the SPPs, which is emitted under a steep angle as discussed above. This necessitates the use of oil immersion objectives. A series of lenses follows to collect and re-focus the light from the objective and onto the camera. The camera can be of different kinds of types. In this thesis, CMOS, CCD and InGaAs-based cameras were used.

In reality, the setup is a little more complex, and has evolved through several iterations in the course of this thesis. A schematic drawing of the setup is shown

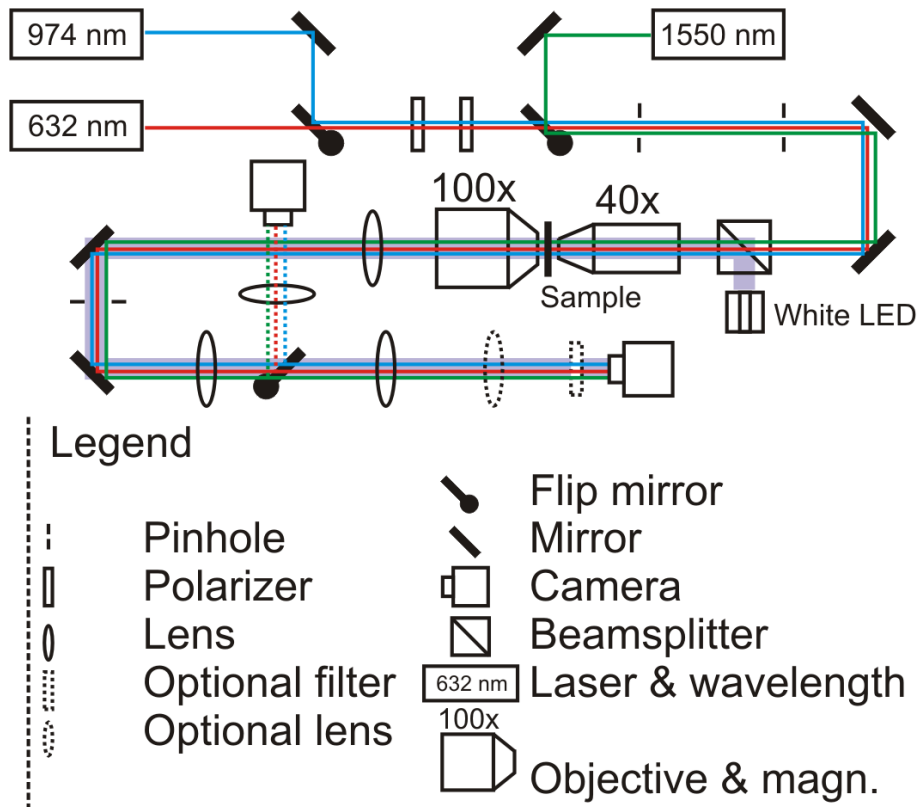


Figure 4.18: A schematic drawing of the LRM setup which was used for most of the experimental LRM measurements in this work. Note the three different light sources available - 632, 970 and 1550 nm. Two different methods are available for the imaging of the Fourier plane - either by adding an additional lens in the solid beamline just in front of the camera, or by using the flip mirror to activate the dashed beamline, where another lens is permanently installed.

in figure 4.18. Three different lasers can be used as the light source in this setup. This includes a 632 nm helium-neon laser, a 974 nm fibre-coupled diode laser and a 1550 nm fibre laser. The first part of the setup contains two flip mirrors to merge all light sources into the same beamline. Only one laser can be used at one time, however. The beam then passes through two optical elements, which serve to regulate both beam intensity and polarization. The first is an absorptive polarizer and serves to regulate intensity. The second is a $\lambda/2$ plate which rotates the polarization of the beam to the desired setting. Since each $\lambda/2$ plate is designed for one specific wavelength, these were changed according to the wavelength used. After the polarization management module, the beam passes through two pinholes, which serve to aid re-alignment and remove stray ambient light from the beamline.

Background illumination is provided by a very powerful (3 Watts) white-light LED. A beamsplitter cube serves to combine the background illumination with the laser radiation. The use of a beamsplitter cube at this point is slightly inefficient and deserves an explanation. When only one specific wavelength is used, such as the

632 nm line of a He-Ne laser, a dielectric mirror with high reflectivity for this specific wavelength and high transmission for all others, basically an optical bandpass filter, would be more efficient and would conserve laser power. This was in fact also used in early versions of the setup which only included one operational wavelength. As more wavelengths were added, however, this would have meant replacement of the mirror whenever the wavelength was switched or the procurement of a custom mirror with a multiple bandpass design. The first option was ruled out due to its involving the frequent replacement of an alignment-critical component and the second option turned out to be prohibitively expensive. The only solution left was to sacrifice laser intensity in return for broadband illumination capability.

After the unification of all light sources into one beam, the beam is focused onto the sample by a 40x objective with an NA of 0.63. The leakage radiation, transmitted excitation beam, and background illumination are collected by the 100x objective with 1.4 NA. The lenses that follow serve to collimate the beam and then as a simple telescope to increase the field of view or magnification. The image is focused onto the camera by a final lens. The position of this lens is very important, since by choosing one out of two precise locations, it is possible to image the structures and SPPs directly, or to image the Fourier plane. The Fourier plane is a plane which shows the angular distribution of light radiation. Consequently, the leakage radiation, which is emitted under a specific angle, shows up in this plane as an arc or a line a fixed distance from the excitation beam.

In this setup, imaging of the Fourier plane is possible via two different approaches. It is either possible to introduce an additional lens into the normal beamline, just in front of the camera, or to use a flip mirror to change to a different beamline where the lens is permanently installed. The former approach has the advantage of needing only one single camera, while the latter approach has the advantage that both images can be viewed near-simultaneously.

The various ways to obtain an image with the LRM setup are shown in detail in figure 4.19. One method for imaging the sample plane (a) and two methods for imaging the Fourier or back-focal plane are shown (b) & (c). The sample S is shown with a gold surface, a grey DLSPW structure, and a transparent (glass) substrate. Immersion oil fills the space between the sample and the second objective O_2 . The substrate is followed by In (a) the sample plane is imaged, i.e. the structures are visible and the SPPs are shown as jets. In (b) and (c) the Fourier plane or back-focal plane is imaged, and the structures are not visible at all while the propagating SPPs are shown as a crescent and the DLSPW modes are shown as straight lines. The difference between (b) and (c) lies in the exact configuration. While in (b) the position of a lens (L_3) is changed, in (c) an additional lens L_4 is added to (a). Compared to figure 4.18, (a) corresponds to the solid lower beamline without any additional lenses, (b) corresponds to the dashed beamline with the flip-mirror activated, and (c) corresponds to the solid beamline with the additional (dashed) lens. As mentioned above, all these approaches were used, depending on necessity and convenience.

In figure 4.19, the background illumination is not shown at all. The solid blue beam near the optical axis shows the excitation laser beam, which is eventually blocked by an (optional) beam block shown as a black box in the centre of lens L_2 . The beam block is a thin metal foil circle, cut by laser, attached to a glass microscope slide. In the real setup it is situated somewhat forward of lens L_2 , not exactly on it. The beam block serves only to eliminate the excitation laser beam, and several different sizes of beam block are available. When the beam block is not in place, the excitation laser beam of course continues to propagate, this is shown in white-blue checkered filling. The locations of the lenses in the drawing are not exactly corresponding to the positions in the actual setup, since the focal lengths in the real setup are longer and not standardised.

Several types of camera were used in the setup. Initially, the setup was equipped with a pair of heavily-modified webcams. While being easy to use and very cheap, webcams have several major drawbacks. The first one is that they use CMOS sensors, which are not linearly sensitive to light. This means that it is not possible to draw any quantitative conclusions from any single image, since the representation of brightness in the image is not directly proportional to light intensity on the chip. Another disadvantage is that the webcams invariably come with proprietary software not intended for scientific usage. Typical webcam software does not allow any control over illumination length or gain factors, since it is designed to automatically adjust everything for typical webcam applications like video chatting. Automatic gain adjust unfortunately also means that there is no way to compare two different images to each other quantitatively, either.

For some measurements, a beam profiler was used. The device used here is a WinCamD-U Series CCD beam imager from the company DataRay, USA (distributed in Germany by the company Laser2000, Germany). The advantage of this tool is that it provides full quantitative information, but it does not allow simple imaging of the structures using background illumination very well, which poses some difficulties when trying to navigate around the sample.

Most measurements in the optical regime were performed with a CCD camera produced by the company ehd Imaging GmbH, Germany. The specific model used was the UKP-1156C, a colour CCD camera. In some cases, a colour CMOS camera, model UKP-1155C, from the same company was used.

For the infrared measurements, an InGaAs-based NIR camera from the company Hamamatsu is used, model C10633-23. A separate camera for the NIR regime was inevitable, since silicon-based cameras such as CMOS and CCD are not sensitive to any radiation with a longer wavelength than 1000 nm. Likewise, the NIR camera was also not useful in the optical regime because it is not sensitive there. So, many different camera types were necessary to fill all roles.

4.2.2 Description of Result Analysis

Leakage radiation microscopy (LRM) is primarily an imaging method. It allows the imaging of surface plasmon-polaritons (SPPs), which are generally neither easy to excite nor to observe.

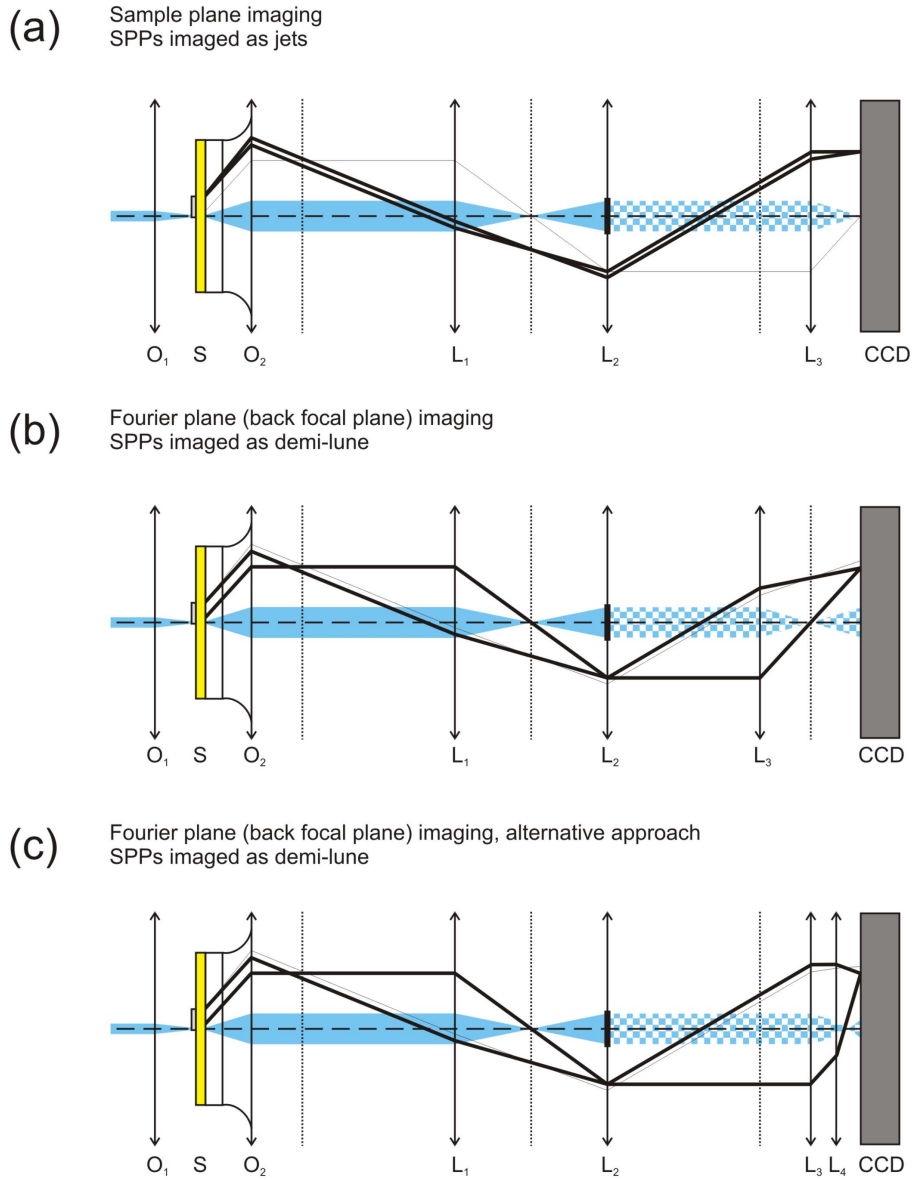


Figure 4.19: All beampaths used in this work in the LRM setup are shown here. The letters O and L denote an objective or a lens respectively. The sample S is shown with a gold surface, a grey DLSPW structure, and a transparent (glass) substrate. Immersion oil fills the space between the sample and the second objective O_2 . The substrate is followed by In (a) the sample plane is imaged, i.e. the structures are visible and the SPPs are shown as jets. In (b) and (c) the Fourier plane or back-focal plane is imaged, and the structures are not visible at all while the propagating SPPs are shown as a crescent and the DLSPW modes are shown as straight lines. The difference between (b) and (c) lies in the exact configuration. While in (b) the position of a lens (L_3 is changed, in (c) an additional lens L_4 is added to (a).

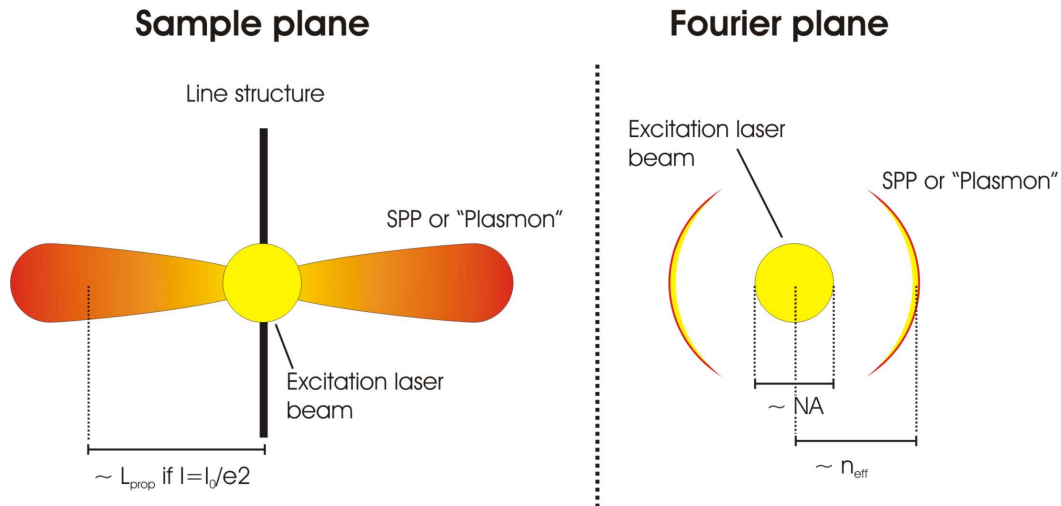


Figure 4.20: Schematic illustrations of the typical leakage radiation microscope images which are generated by exciting two plasmons on a simple line structure on a gold surface (gold surface not shown). The sample plane (left) and the Fourier plane or back-focal plane (right) are both shown. In the sample plane, the image shows the bright spot of the excitation laser beam on the line structure and two SPPs which propagate directly away from it. In the Fourier plane, the dimension of the excitation laser spot corresponds to the numerical aperture of the incoupling objective (in this work, the NA was always 0.63), while the SPPs are imaged as semi-circular wedges. The distance of the SPPs from the centre of the beam corresponds to the effective refractive index seen by the SPP.

A typical method for the excitation of an SPP is to focus a laser on a surface defect or a structure, such as a long line. An example of this and the images that are produced in LRM is shown in figure 4.20. This figure displays schematically the LRM images which are generated by exciting two plasmons on a simple line structure on a gold surface (gold surface not shown). The sample plane (left) and the Fourier plane or back-focal plane (right) are both shown. In the sample plane, the image shows the bright spot of the excitation laser beam and two SPPs which propagate directly away from it. In the Fourier plane, the dimension of the excitation laser spot corresponds to the numerical aperture of the incoupling objective (in this work, the NA was always 0.63), while the SPPs are imaged as semi-circular wedges. The distance of the SPPs from the centre of the beam corresponds to the effective refractive index seen by the SPP.

Figure 4.21 shows what LRM produces when dielectric waveguide structures such as those which constitute a large part of this thesis are involved. In this case, the situation is slightly different. The excitation of the plasmon takes place at the end of the waveguide or at the base of a specially-designed funnel, as shown in the image. The funnel serves to channel the plasmon into the waveguide. Once the plasmon is

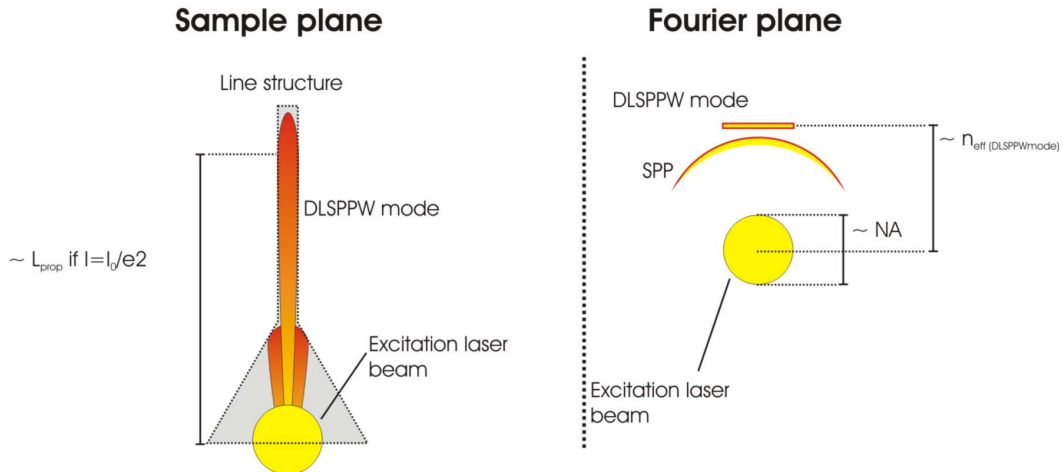


Figure 4.21: Image showing schematically the leakage radiation microscope images which are generated by exciting a plasmonic mode inside a dielectric waveguide structure with funnel (shown in grey in the sample plane). Both the sample plane (left) and the Fourier plane (right) are imaged.

inside the waveguide it is very well confined inside. This changes the Fourier plane image as well. Instead of just an arc as in the freely-propagating case, the DLSPPW mode shows up as a straight line even further away from the centre of the excitation beam.

4.3 Fibre-Coupled Measurements

Those samples with suitable in- and out-coupling waveguides, are characterized by exciting plasmons in an end-fire configuration with the help of optical fibres, a method which has already been reported previously in a slightly different context [238]. Two different setups were used.

A schematic of the first experimental setup is shown in figure 4.22. We use a fibre-coupled 1550 nm laser. It is connected to a polarization controller by a standard 8 μm core fibre. Following this there is a small-core fibre to match the mode size to the optical waveguides on the sample. Using a 4.5 μm mode-field diameter fibre provides much better mode matching than standard fibres when we take into account that the on-sample optical waveguides are only 2 μm wide. The end of the fibre is brought within several microns of the waveguide entrance. Coupling can be observed from above by a microscope, which is not shown in the schematic.

The second experimental setup is shown in figure 4.23. It is slightly simpler than the first setup, consisting of components which are, in total, about ten percent as expensive as the first setup. The light source is here only a laser diode (both 630 nm and 1550 nm are possible to use), which are fibre-coupled and can be connected to the same 4.5 μm mode-field diameter fibre mentioned above. A polarization rotator is fitted to the fibre to allow for polarization control. The light can be collected by

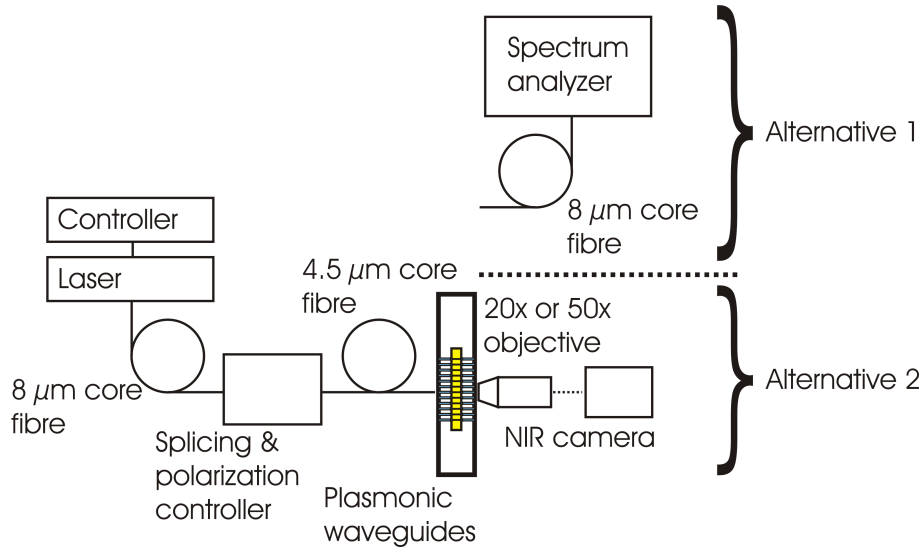


Figure 4.22: A schematic showing the layout of the first experimental setup for the characterization of fibre-coupled plasmonic waveguides.

two different possibilities. The most simple is to use a fibre with a $60\ \mu\text{m}$ core, which is linked directly to a NIR-sensitive photo diode. The light intensity information is then given by a digital multimeter. The collection fibre is mounted on a 3-axis-stage and can be scanned across an area to provide a low-resolution image.

The second way to collect and analyze the light is by using an objective and a NIR or visible-range camera (depending on the laser diode used), analogous to the first setup. Observation of the sample from the top was also possible through a small microscope with 10x and 20x magnification available, which was quite sufficient. In contrast to the first setup, the observation microscope could not be fitted with a camera and could not be used to take images of the waveguides.

4.4 Scanning Near-Field Optical Microscope

A scanning near-field optical microscope (SNOM, sometimes also called near-field scanning optical microscope - NSOM) is a very common and popular method to analyze surface plasmon-polaritons. It was not used directly in this work, but a short description will be given in order to compare it to leakage radiation microscopy and make the advantages of LRM vs. SNOM clear.

SNOM was developed by two groups independently of each other in 1984 as a high-resolution optical microscopy technique with a resolution limit of $\lambda/20$, a drastic improvement over conventional optical microscopes [239, 240]. A great variety of SNOM devices has been developed since then, but all share the detection mechanism - a sensitive tip is brought close enough to an illuminated structure to detect the evanescent waves of the optical near field. By scanning the tip across the sample surface, an image of the surface can be generated. Detection mechanisms that have been reported to achieve lateral resolutions of 50 nm or less include optical

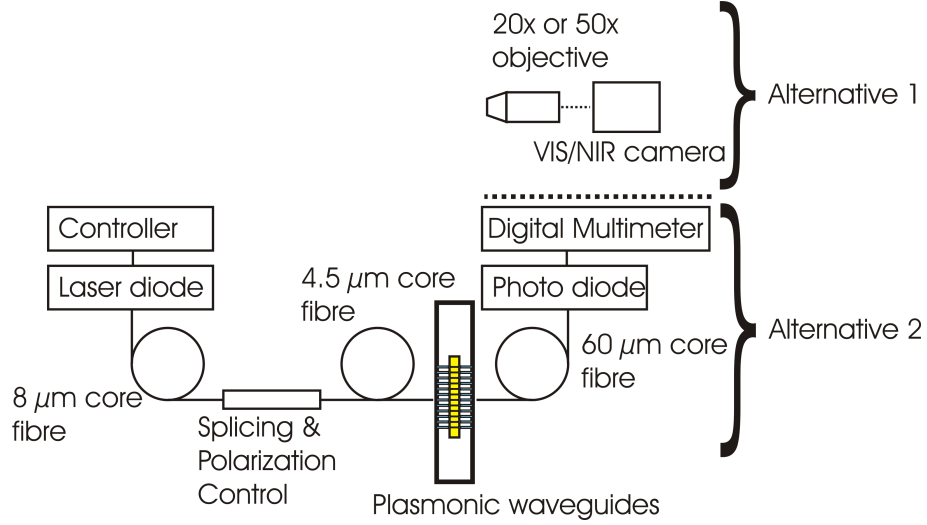


Figure 4.23: A schematic showing the layout of the second experimental setup for the characterization of fibre-coupled plasmonic waveguides. The laser could be either a 630 nm or 1550 nm laser diode, and the camera could be either NIR or visible-range.

fibre tips with a small aperture, apertureless silicon tips with 2 nm radius, small polystyrene spheres, and gold-coated tetrahedral glass tips that are illuminated by surface plasmons [241].

Since surface plasmon polaritons (SPPs) have a very strong evanescent field [54], which makes SNOM a very suitable investigation and characterization method [78]. Given this fact, it is hardly surprising that some of the early and highly-influential works of the late 1990s concerning SPPs utilized SNOM to a very high degree [79, 80], and that the connection between plasmonics and SNOM remains strong.

As already mentioned above, SNOM was not used directly in this thesis as a characterization tool. However, samples fabricated within the larger context of this thesis, using geometries and characteristics that are highly similar to those presented here, were analyzed by our collaborators and partners using SNOM, for example in references [187] and [231]. These results in turn naturally influenced this thesis to some degree.

In comparison with leakage radiation microscopy (LRM), SNOM has much higher resolution, but is much slower. Since LRM is - in principle - a conventional optical microscope, it is still restricted by the diffraction limit and has a maximum resolution of approximately $\lambda/2$. SNOM, as noted above, can achieve a resolution which is a factor of ten higher. On the other hand, while LRM generates the complete image at the same instant, SNOM generates an image pixel-by-pixel. The high resolution becomes a disadvantage here because it necessarily increases the number of pixels and the time required to generate the image.

In this work, the propagation lengths involved are on the order of tens of micrometers, and the smallest feature sizes of the investigated structures never lie below $\lambda/2$.

For this reason, LRM is a more suitable characterization technology. In addition, if we view this matter in terms of rapid prototyping technology, a fast characterization process is more desirable in combination with a fast fabrication technology than a slow one (see also the tabular comparison in table 3).

4.5 Comparison of Plasmonic Characterization Techniques

In addition to leakage radiation microscopy, end-fire excitation and SNOM, there are a few other techniques for the excitation and characterization of SPPs. This section will provide a short comparison of the main advantages and drawbacks of each method. A tabular comparison is shown in table 3.

A less than well-known method to image surface plasmon fields is the use of fluorescence imaging. In this method, a metal surface on which a plasmon can propagate is coated with a fluorescent molecular film. The surface plasmons cause excitation of the film, which provides real-time images of the plasmons. The plasmons can be excited using defect excitation [242]. This method, while able to image plasmons in real time, has the disadvantage of requiring special preparation and being less versatile than an additive-free technique like LRM.

Considerably more prominent and common is the excitation of surface plasmons using cathodoluminescence [243, 244]. In this regime, plasmons are excited by a beam of electrons, generated by an electron gun, which collides with the metal and leads directly to the electron density waves we know as surface plasmons. The plasmons generated thus can be imaged directly using the same setup that excites them [245].

Table 3: Surface plasmon characterization techniques

method	speed	resolution	reference(s)
leakage radiation	real time	$\lambda/2$	[232, 246]
end-fire coupling	real time	not applicable	[238, 247]
SNOM	scanning	$\lambda/20$	[239, 187]
fluorescence	real time	$\lambda/2$	[242]
cathodoluminescence	real time / scanning	$< \lambda / \lambda/40$	[245] / [248]

4.6 Other Characterization Tools

In addition to the methods outlined above, which were the primary methods for optical and functional characterization, several other standard methods were used to investigate structure topography and composition.

4.6.1 Optical Microscope

All fabricated structures were first studied using an optical microscope. With few exceptions, a Zeiss Axiotech Vario was used, equipped with both normal and darkfield

operating modes. It was possible to view structures using transmitted or reflected light. Magnifications from 5x to 100x were available (see table 4). In addition, the microscope was fitted with a Mituyo digimatic indicator for the position of the objective in z-direction, and with a sensor control display from Märzhäuser Sensotech for display of the x-y-axis position. All three axes positions could be displayed with 1 μm precision, allowing very accurate measurement of large structures, and adequate estimation of line widths.

Table 4: Available objectives for optical microscope

magnification	NA	type
5x	0.13	Zeiss epiplan
10x	0.20	Zeiss epiplan
20x	0.40	Zeiss epiplan
50x	0.70	Zeiss epiplan
100x	0.75	Zeiss epiplan

Initially, the microscope was equipped with a SONY Hyper HAD CCD-IRIS RGB colour video camera. During a general upgrade of the microscope performed during this work, the camera was replaced with a black and white CMOS camera from EHD, model UK-1155. The control computer and camera software was also replaced.

4.6.2 Scanning Electron Microscope

Two different models of scanning electron microscope (SEM) were used in the course of this work. These microscopes operate by scanning a sample surface using a high-energy beam of electrons in a raster scan pattern (hence their German name "*Rasterelektronenmikroskop* - REM"). Their utility, due in part to their ability to capture the three-dimensionality of scanned structures, is so universal that they have become ubiquitous in the scientific world. A vivid demonstration of the imaging capabilities of an SEM is shown in the right image of figure 4.24.

The first system that is used in this work is a CamScan S2. This system was used for most of the early SEM investigations of this work, after which a new SEM was introduced.

The second system is a FEI Quanta 400 F. It comes with the option of using high or low vacuum, advanced user interface features such as computer centric rotation and has generally much better resolution than the former device. Furthermore, due to an enhanced user interface and increasing automation, it is considerably easier and more convenient to use.

The SEM is used in this work to characterize and measure the geometry of structures fabricated by 2PP or NIL. One of the most important geometric characteristics of a waveguide is its linewidth, and the SEM is used almost exclusively to measure this parameter. A full account on how to measure linewidths very accurately and precisely with an SEM is given in [249].

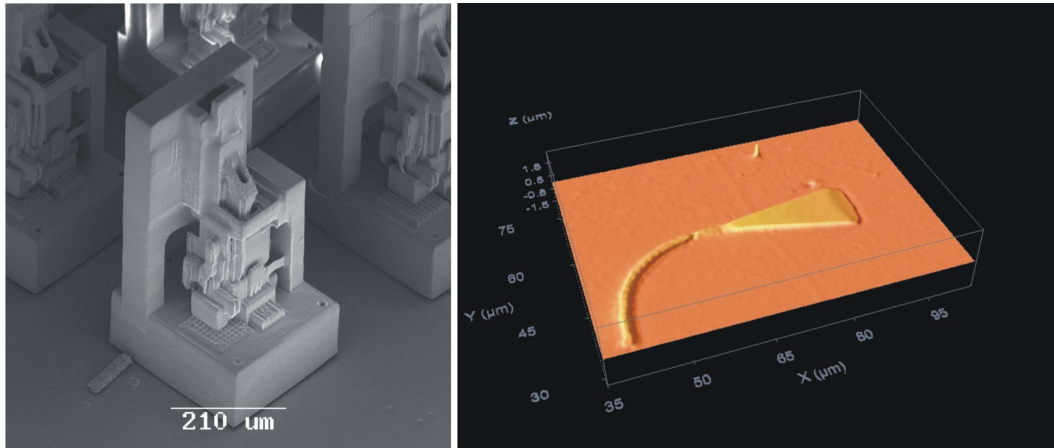


Figure 4.24: Left: An SEM image of a miniature model of a 2PP fabrication setup. Both images show the 3D imaging capabilities of these technologies. Right: An image made with the confocal imaging profiler of a plasmonic waveguide with a 90 degree bend.

In principle, measurement of linewidths of waveguides can also be done using atomic force microscopy (AFM). This method was used on occasion to characterize structures which were produced in the context of this thesis, most notably by our European partners in Belfast. However, AFM measurements can become inaccurate when high aspect ratios are involved, as is the case with rectangular waveguides, so SEM measurements are chosen due to their higher reliability in this thesis.

4.6.3 Confocal Imaging Profiler

A confocal imaging profiler, the ATOS PL μ was also used in this work. In essence, this is little more than a confocal microscope with an attached camera, which takes confocal images of an object and scans it layer by layer. After this, an algorithm calculates the surface of the sample and this is displayed to the user.

While it is less accurate than an SEM or AFM, the confocal imaging profiler is also valuable to this thesis, since it provided a quick look at the result of a 3D structure when access to an SEM was not available. An example of an image obtained with the profiler is shown on the right side of figure 4.24.

5 Dielectric-Loaded Surface Plasmon-Polariton Waveguide Components Fabricated by Direct Laser Writing

This section will discuss the experimental results obtained in this work from experiments on dielectric-loaded surface plasmon-polariton waveguide (DLSPPW) components. A wide range of structures, from simple straight lines and bends to more complex structures such as Mach-Zehnder interferometers and racetrack resonators will be discussed. The functionality of the structures and their utility is shown.

Directly written DLSPPW structures presented in this section are fabricated on the intended substrate (in nearly all cases, this is glass covered with a 50 nm gold layer) by 2PP. This is the most direct method to fabricate DLSPPW structures that is shown in this thesis. All other methods are, however, connected to this one, since 2PP is used for the fabrication of master structures in all cases.

5.1 Simple Structures - Lines and Bends

The most simple DLSPPW structure is a straight line. The second-most simple structure is the line with a bend in it. The structures exist in two variations - with and without an incoupling funnel. A schematic drawing of line and bend structures with funnels is shown in figure 5.25.

Measurements were performed using leakage radiation microscopy at three different wavelengths: the Helium-Neon laser wavelength 632 nm, 974 nm and the telecommunications wavelength 1550 nm.

First we will examine the basic structure composed of a funnel and a line at the 632 nm wavelength. The funnel serves only one purpose - to funnel the plasmon efficiently into the line waveguide. The funnel dimensions have changed slightly over the course of the work, in particular the angle of the taper has changed. The base is nearly always 10 μm wide and the length lies between 10 and 30 μm .

Figure 5.26 shows leakage radiation microscope (LRM) images of a 10 \times 10 μm funnel with an attached line waveguide. The excitation laser beam is focused onto the base of the funnel, at different positions. The effect of the funnel can be clearly seen. In image a) the plasmon which is excited at the funnel base, even though it is not perfectly aligned with the waveguide, is channeled into the line waveguide by the funnel with minimal scattering. In the second image b) the excitation spot is far-removed from the waveguide and the plasmon is reflected from the funnel wall so that it strikes the other funnel wall nearly vertically and is strongly scattered. A small amount of SPP radiation continues beyond the dielectric structure on the gold surface, but no significant radiation is visible inside the waveguide.

The funnel is not strictly necessary for experiments, although it is very useful for applications and to demonstrate the robustness of a plasmonic component against small inaccuracies in alignment. Figure 5.27 shows the LRM images of a single line waveguide without a funnel which are generated by using differently-polarized light,

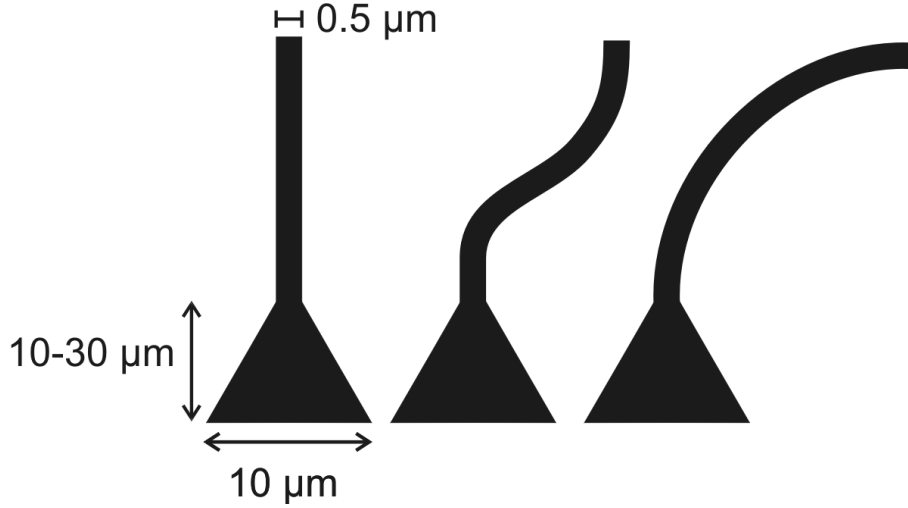


Figure 5.25: A schematic drawing of the most simple DLSPW structures discussed in this thesis. A straight line, a line with a bend that reverses on itself, and a 90 degree bend. All of these structures are shown with the triangular incoupling funnel, which can be omitted in some cases. The waveguides are 500 nm high, the line structures are of varying length but usually longer than 10 μm the other dimensions are shown in the image.

transverse electric (TE) and transverse magnetic (TM). The waveguide is 20 μm long with a 500 nm \times 500 nm cross-section, made from the material mr-NIL. In the TM case, the electric field is parallel to the waveguide and the desired direction of propagation for the plasmon. When the TM_{00} mode is excited, as in image b), an SPP propagating on the gold surface beyond the waveguide is visible after transmission through the waveguide. This is not visible in the (optical) TE case, shown in image a). It is not possible to excite plasmons in TE configuration. These results have been published in reference [250].

In the images shown in figure 5.27, only a single mode is excited. It is possible to selectively excite different modes and even a superposition of modes inside a waveguide [250]. Figures 5.28 and 5.29 show some results in both sample plane and Fourier plane. Figure 5.28 shows the LRM images of a waveguide in which three different modes are excited (a-c) with the excitation laser spot shown for comparison. In image a), the TM_{00} mode is excited, characterized by a straight and smooth line confined within the waveguide. In image b), the TM_{01} mode is excited, which is characterized by two parallel straight and smooth lines which appear to lie on the edge of the waveguide. In image c) we see the simultaneous excitation of both modes, i.e. a $\text{TM}_{00}+\text{TM}_{01}$ situation, which is characterized by a distinct beating signal. Simulations performed using a self-developed tool in Matlab, which are shown in the images d)-f) confirm that this is the case and correspond with remarkable accuracy to the experimental results.

The images in figure 5.29 show the corresponding Fourier plane images. Image a) corresponds to the TM_{00} mode, which is now shown as a straight central line.

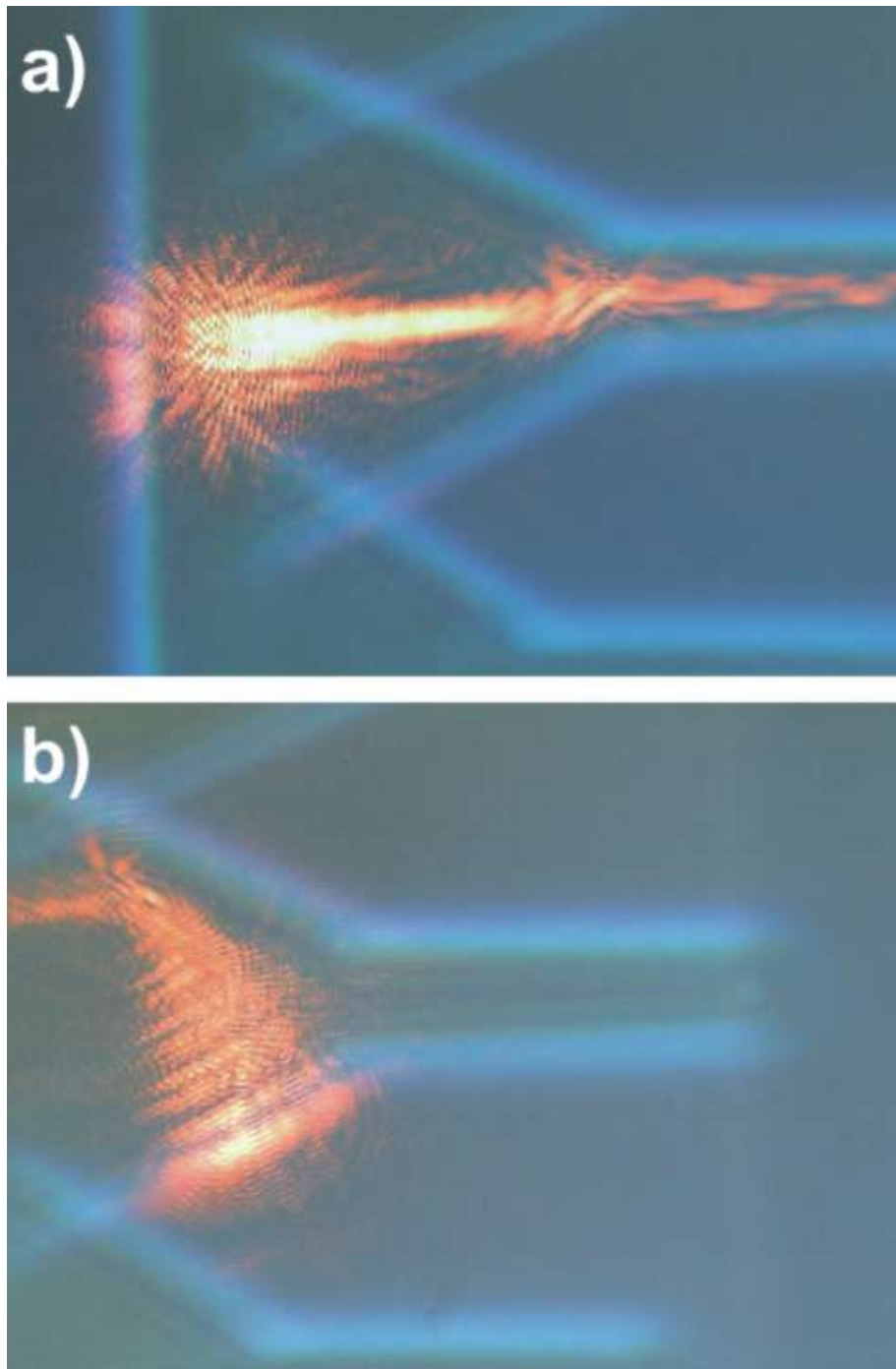


Figure 5.26: Two leakage radiation microscope images showing a funnel and a line with the excitation laser beam at 632.8 nm wavelength focused on the base of the funnel. The dimensions of the structure are: funnel base width $10\ \mu\text{m}$, funnel length $10\ \mu\text{m}$, waveguide length $10\ \mu\text{m}$, structure height and waveguide width $500\ \text{nm}$. a) Shows the plasmon propagating inside the line waveguide after being guided inside by the funnel. b) shows the plasmon reflecting off the funnel wall without coupling to the line waveguide.

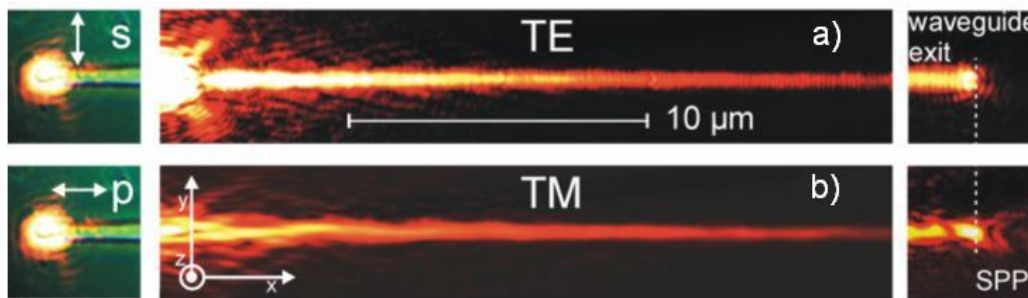


Figure 5.27: These images illustrate the excitation of a dielectric waveguide structure in the leakage radiation microscope setup. The excitation spot (left), the waveguide (centre) and the waveguide exit (right, with the waveguide end indicated by a superimposed dashed line) are shown. The excitation laser wavelength is 632.8 nm. a) shows the TE_{00} optical mode excited while b) shows the TM_{00} plasmonic DLSPW mode.

Image b) corresponds to the TM_{01} mode and the mode shows up as two separate straight lines spaced symmetrically around the optical axis. Image c) shows the superposition of the two modes, with each mode distinctly visible, unlike in the sample plane where the interference leads to the beating effect. From the Fourier plane images it is possible to derive the effective indices of the modes $n_{e,0} = 1.15$ for the TM_{00} modes and $n_{e,1} = 1.07$ for the TM_{01} mode.

It is possible to utilize this effect, as detailed in [250], to tune the output intensity of a DLSPW Y-splitter structure, that is to change the splitting ratio between the two output arms. In this way it becomes a useful optical switching mechanism for optical switches, which are of the utmost importance in future optical communication networks.

Figure 5.30 shows ten leakage radiation microscope images of line waveguides in which the superposition of the TM_{00} and TM_{01} mode is excited. In this set of images, a 974 nm laser is used as the excitation laser source. The geometry of the waveguides was chosen to be single-mode for the 1550 nm telecommunications wavelength, which automatically means that they are multi-mode for this considerably shorter wavelength. The waveguides are 600 nm wide and 500 nm high and have lengths varied between 5 μm and 50 μm . As for the 632 nm case shown above, the characteristic beating pattern caused by the superposition of both modes can be clearly seen.

In the Fourier plane images shown in figure 5.31 both modes are clearly visible as straight lines. As in the 632 nm case, the central and outward-lying line corresponds to the TM_{00} mode and the two closer ones correspond to the TM_{01} mode. From the Fourier plane images, it is possible to obtain the effective indices for the modes. We obtain an effective index of $n_{e,0} = 1.217$ for the TM_{00} mode and $n_{e,1} = 1.001$ for the TM_{01} mode.

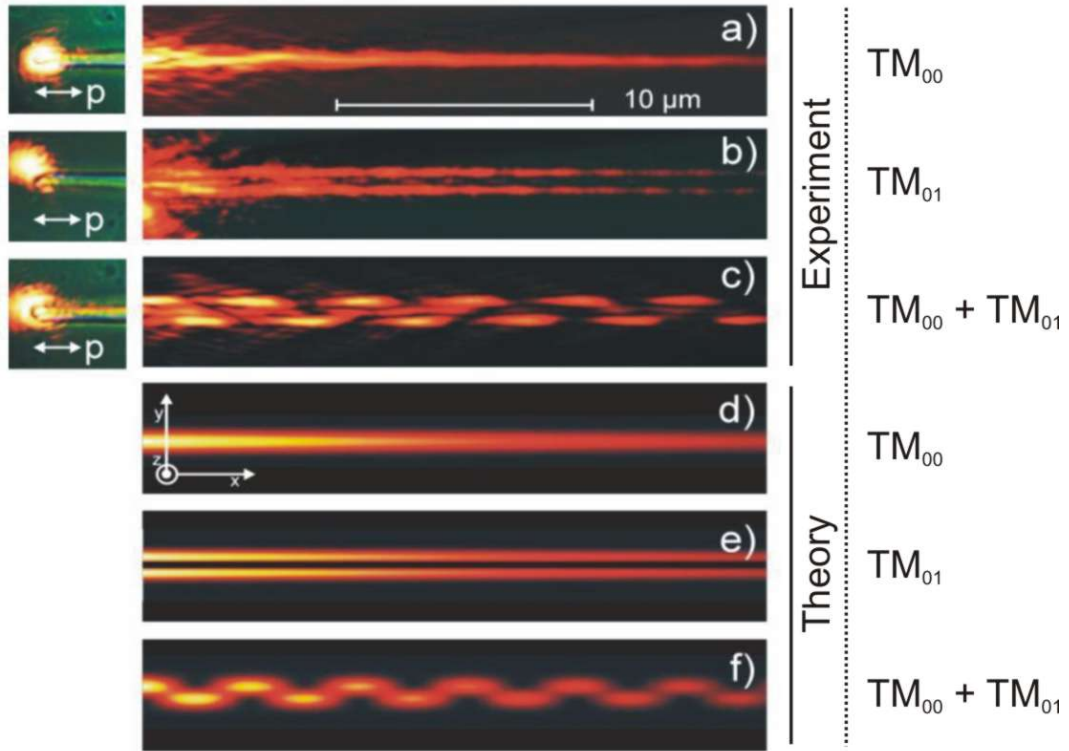


Figure 5.28: Images (a) - (c) show leakage radiation microscope images of a straight DLSPW structure $25 \mu\text{m}$ long. (a) shows the excitation of the TM_{00} mode, (b) shows the TM_{01} mode, and (c) shows the $\text{TM}_{00} + \text{TM}_{01}$ mode. Corresponding images of the Fourier plane are shown in figure 5.29. The excitation laser beam at 632.8 nm wavelength is focused on the left side of the images and the polarization is shown. TM modes are excited using p-polarization. The TM_{00} mode is excited by focusing directly onto the centre of the waveguide end. The TM_{01} mode is excited when the excitation beam is focused onto the edge of the waveguide. The $\text{TM}_{00} + \text{TM}_{01}$ mode is excited by choosing a position between these two excitation locations. Images (d) - (f) show numerical simulations describing the modes in terms of Hermite polynomials using the experimentally determined effective indices $n_{e,0} = 1.15$ and $n_{e,1} = 1.07$. (d) shows the TM_{00} mode, (e) the TM_{01} mode, and (f) the $\text{TM}_{00} + \text{TM}_{01}$ mode. The simulations are in agreement with the experimental results.

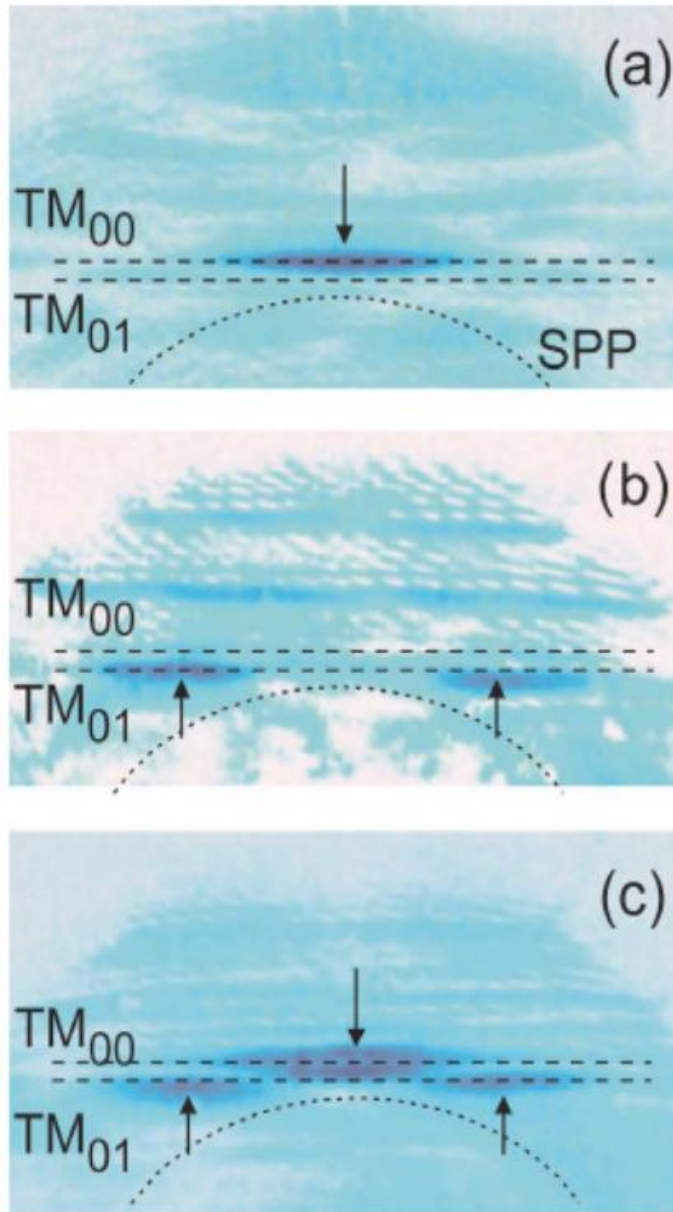


Figure 5.29: False colour leakage radiation microscope images showing the Fourier plane during excitation of different SPP modes with p-polarized light from a He-Ne laser at 632.8 nm wavelength. Image (a) shows the TM_{00} mode, (b) the TM_{01} mode, and (c) the superposition of both, the $TM_{00} + TM_{01}$ mode. A freely-propagating SPP on a metal surface shows up as a characteristic circular arc in the Fourier plane, which has been indicated by a dashed line. The waveguide modes show up as straight lines (also indicated as dashed lines). By taking into account the NA of the focusing objective ($NA = 0.63$), it is possible to determine the effective indices from the positions of the TM modes: $n_{e,0} = 1.15$ and $n_{e,1} = 1.07$.

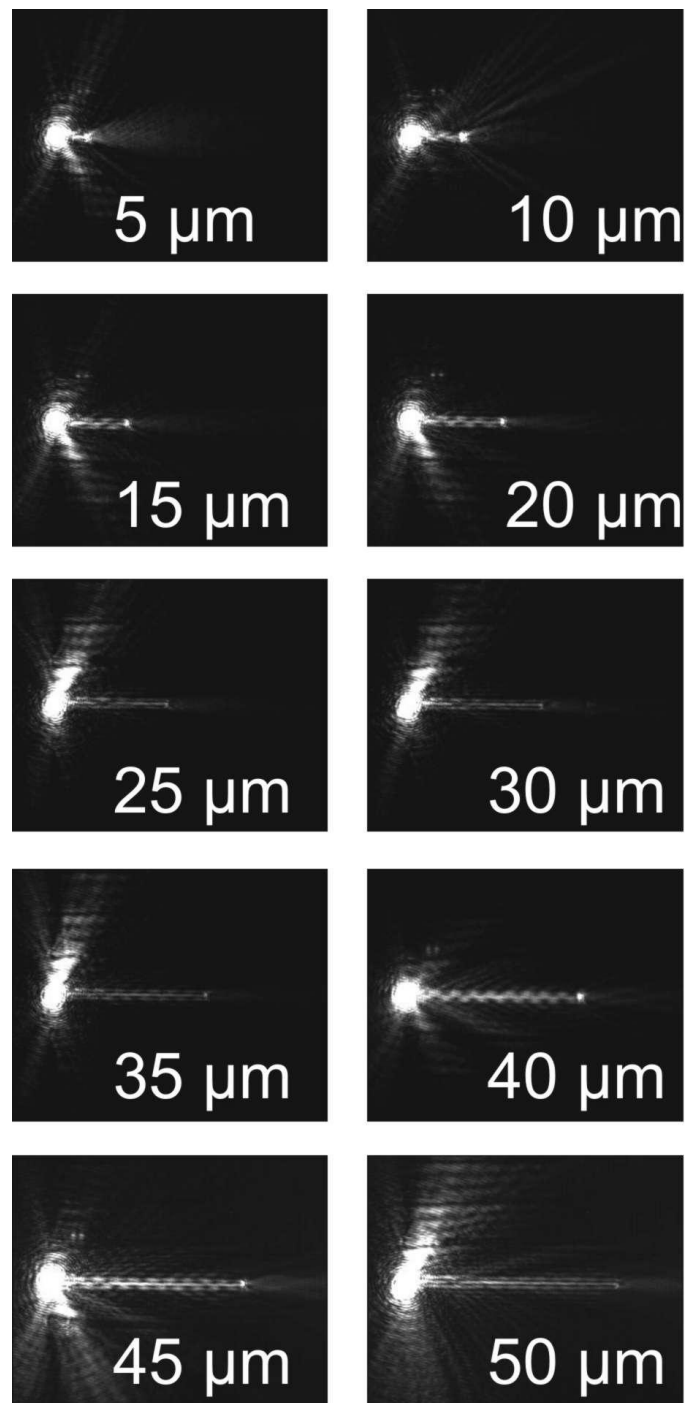


Figure 5.30: These are LRM images showing line waveguides from $5 \mu\text{m}$ to $50 \mu\text{m}$ length with a TM_{00} and TM_{01} mode excited by a 974 nm laser at one end of the waveguide.

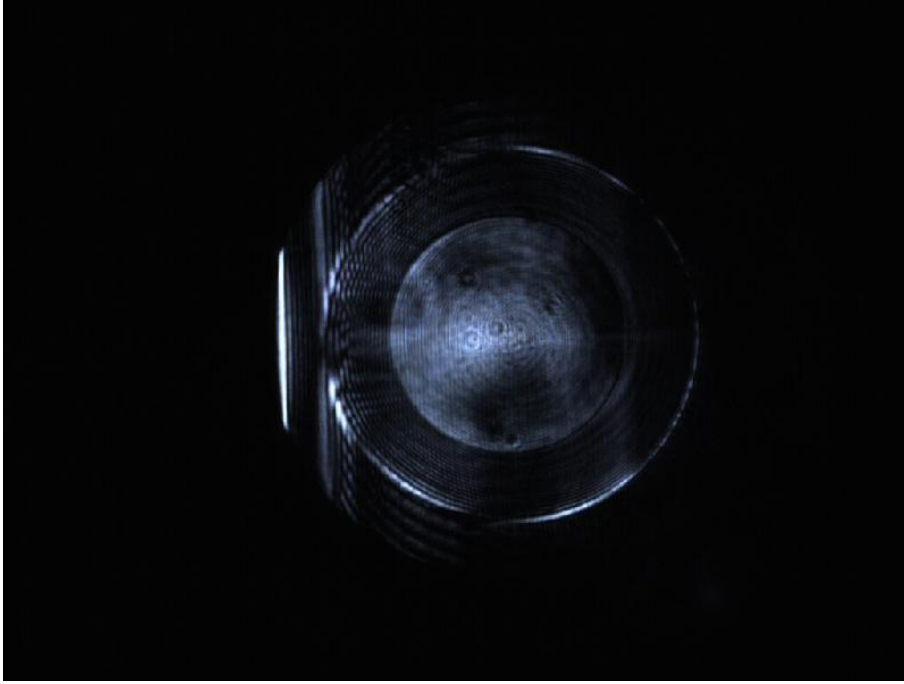


Figure 5.31: The Fourier plane image corresponding to the $40\ \mu\text{m}$ long line waveguide from figure 5.30. From the position of the characteristic features of the modes it is possible to obtain the effective indices $n_{e,0} = 1.001$ and $n_{e,1} = 1.217$.

Line structures with and without incoupling funnels were also investigated at the telecom wavelength of $1550\ \text{nm}$. This wavelength is particularly interesting from the applications side and was the design wavelength for many of the DLSPPW structures. The line waveguides are single-mode at this wavelength, and can no longer support an optical TE mode. This can be seen in the images in figure 5.32, where a line waveguide with a funnel is shown. The excitation laser spot is focused on the base of the funnel. In the TM case, we can see that the plasmon is channeled into the waveguide by the funnel and that it propagates inside the waveguide as a TM_{00} mode. In the TE case, we can see that while the funnel area is brightly illuminated by scattered light, the waveguide itself remains completely dark. The Fourier plane is also shown with the DLSPPW TM_{00} mode clearly visible. From the image it is possible to obtain the effective index $n_{eff} = 1.206$ for the TM_{00} mode.

The intensity distribution of the DLSPPW mode along the waveguide is measured using the leakage radiation, which is fitted to an exponential curve to extract the propagation length L_{prop} . That this is a reasonable method and provides a good match can be seen in figure 5.33, where such a fit curve is superimposed on the experimental results. The waveguides are clearly single-mode, an improvement over the multi-mode waveguides published previously [250]. An analysis of the decay rate of the DLSPPW mode in several straight waveguides (line waveguides) with funnels, combined with the effective index $n_{\text{eff}} = 1.206$, gives us an average propagation length of $L_{\text{prop}} = 20 \pm 1\ \mu\text{m}$. This shows some improvement compared to figures previously published using similar structures fabricated by UV mask lithography

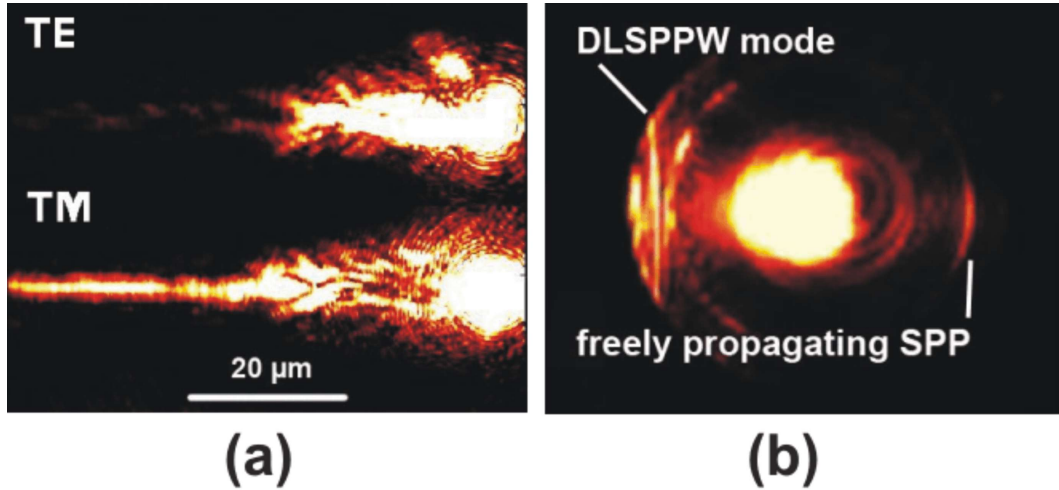


Figure 5.32: False colour leakage radiation microscope images of a single-mode line waveguide with funnel, being excited at the funnel end by TE and TM polarised light at 1550 nm wavelength respectively. As can be seen in (a), the waveguide cannot support an optical TE mode but only a plasmonic TM_{00} mode. The Fourier plane image of the TM_{00} mode is shown in (b).

[188], and demonstrates that 2PP is capable of producing superior-quality DLSPPW waveguides.

To realize fully the potentials of DLSPPW structures for proposed miniature photonic-plasmonic hybrid circuits [251], curved waveguides are necessary. In fact, the minimal bend radius with tolerable signal losses defines the level of miniaturization that is obtainable, so the investigation of bended DLSPPWs is a prerequisite for more complicated components.

First we investigate bended waveguide structures at 632.8 nm wavelength. The structures that are investigated are shown in the images in figure 5.34. The structures consist of the incoupling funnel, a straight waveguide, an S-shaped bend and another straight waveguide. The funnel dimensions are 10 μm width and 15 μm length, the waveguides are 60 μm long in direction of propagation and have a 500 nm x 500 nm cross-section. The material used for the fabrication is mr-NIL 6000. The goal of these investigations at visible wavelength is to show that bend waveguiding works in principle before moving to the telecom wavelength of 1550 nm.

Results from the LRM investigations are shown in the images in figure 5.35. It can be seen that the waveguides work in principle, although they are not optimized for this wavelength, and are consequently multi-mode.

A series of 90° bends fabricated directly on gold by 2PP was investigated at 1550 nm excitation wavelength. We find that for bend radii of 2, 3 and 4 μm , the DLSPPW mode is guided through the bend, albeit with some scattering out of the waveguide. An image of the bends is shown in figure 5.36. An SEM image showing the design of the entire structure is also shown. The bend structure is designed

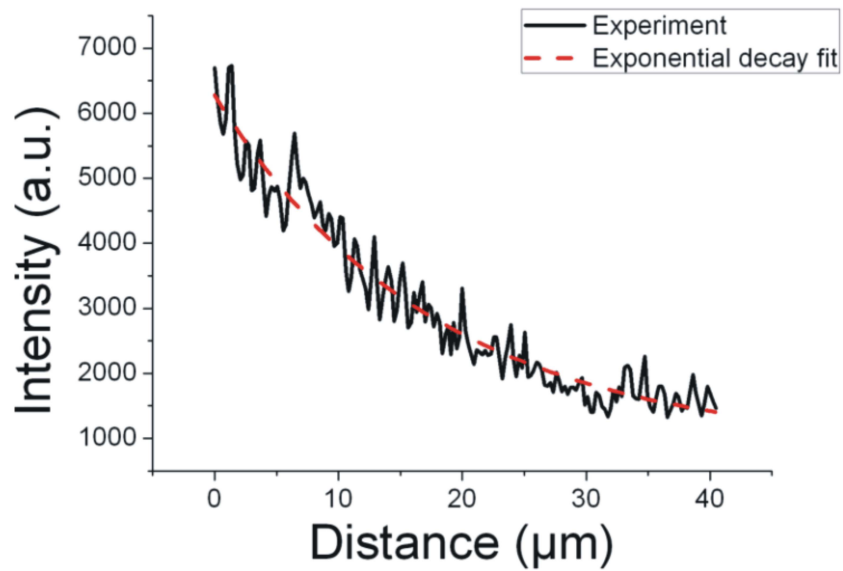


Figure 5.33: Plot of the leakage radiation measured inside a line waveguide which is a direct indication of radiation intensity. An exponential fit is also shown.

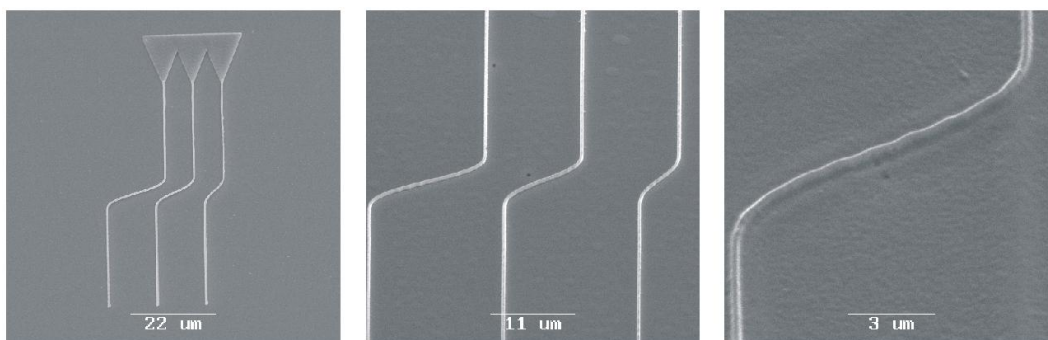


Figure 5.34: SEM images of bend structures used for the 632.8 nm investigations.

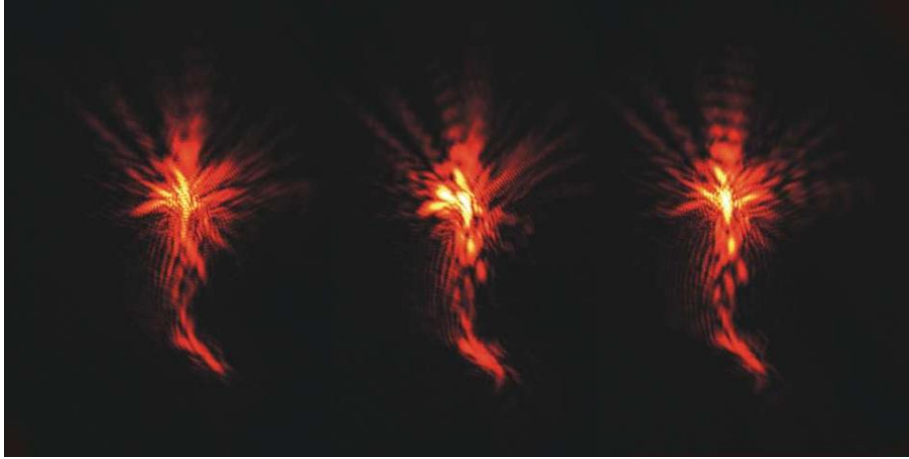


Figure 5.35: LRM images of DLSPPW modes in bended waveguide structures at 632.8 nm wavelength. The funnel dimensions are 10 μm width and 15 μm length, the waveguides are 60 μm long in direction of propagation and have a 500 nm x 500 nm cross-section. The material used for the fabrication is mr-NIL 6000.

to ease fabrication and characterization by providing a compact structure with a common baseline.

Transmission measurements were performed using the leakage radiation, where the transmission is simply give by

$$T = \frac{I}{I_0}, \quad (5.32)$$

where I_0 is the input intensity and I is the output intensity.

The starting and ending points of the waveguide bend itself were taken as reference points for each waveguide, without regard to the incoupling waveguides. The results, which are listed in table 5), show that waveguides with larger bend radii are more efficient at guiding the DLSPPW mode around a corner due to the reduction in bend scattering losses.

The transmission values provide a good measure of the usefulness of the waveguide bends in application, since they include all losses. If we are interested in separating bend losses from the propagation losses, it is possible to calculate the transmission corrected for propagation losses:

$$T_c = T e^{\frac{\pi r}{2L_{prop}}}, \quad (5.33)$$

where T is the measured transmission, r is the bend radius, and L_{prop} is the propagation length.

The values calculated for T_c are also shown in table 5. The values show that propagation losses play a considerable role in bended waveguides and should be taken into account when designing a DLSPPW component or circuit.

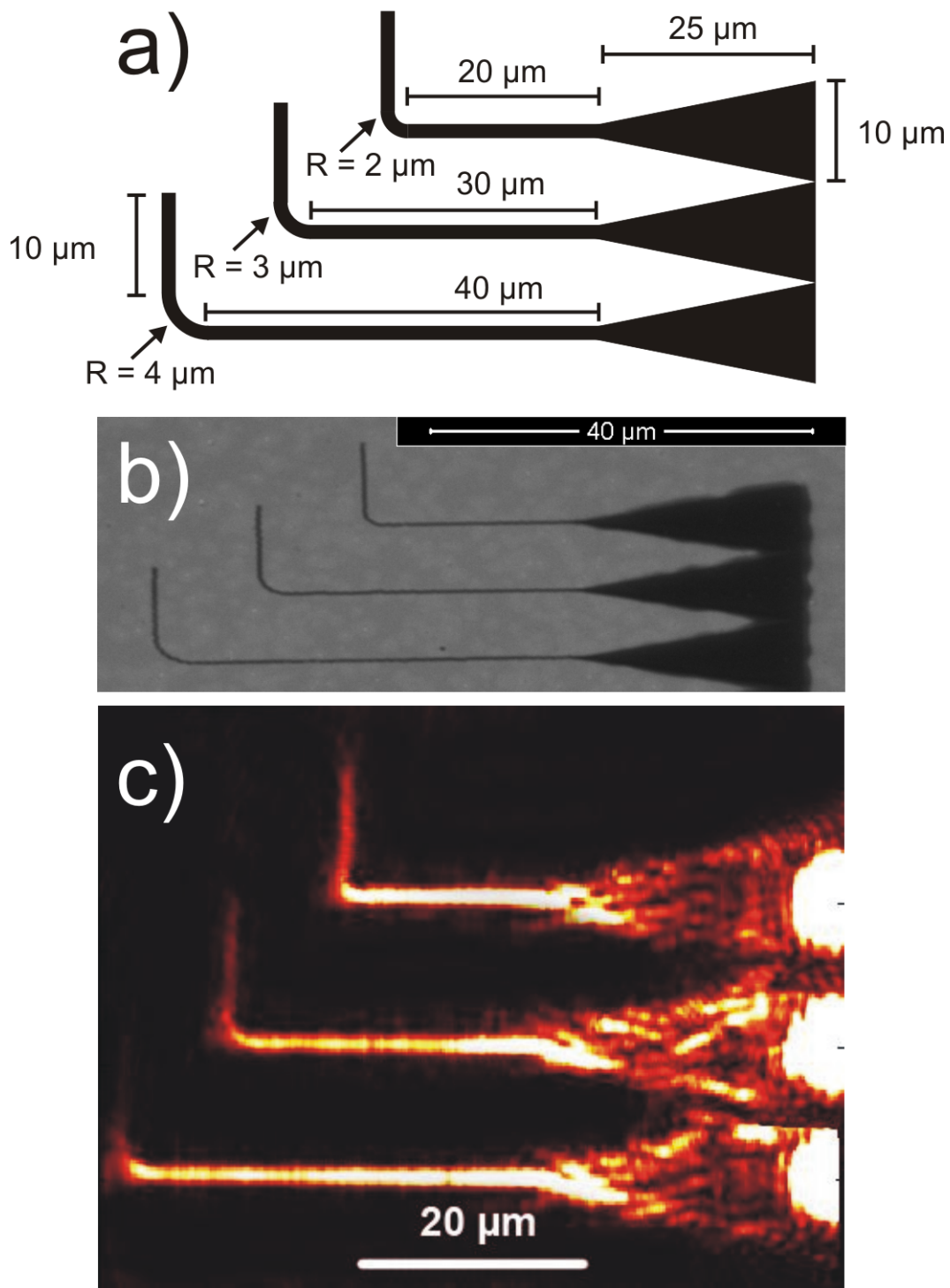


Figure 5.36: a) A schematic drawing of the structures. The structures are 500 nm high and the waveguides are 500-600 nm wide. b) SEM image of the structures. c) False colour leakage radiation microscope images of three bends with different curve radius. Descending from top to bottom the curve radius is 2, 3 and 4 μm . The three images were taken separately and then merged.

Table 5: Transmission results for bend DLSPW structures.

bend radius (μm)	transmission	transmission without propagation losses
2	0.17	0.22
3	0.26	0.33
4	0.31	0.43

5.2 Mach-Zehnder Interferometers

In this section, we focus on DLSPW Mach-Zehnder interferometers (MZI) fabricated by direct laser writing through two-photon polymerization (2PP) technology. 2PP technology is a technology particularly suited to the fabrication of such more complex DLSPW structures due to its great flexibility, as has been repeatedly shown [252, 253, 254]. The DLSPW structures are characterized by leakage radiation microscopy at the 1550 nm telecom wavelength.

A Mach-Zehnder interferometer, as a brief reminder, is an optical device used to determine the relative phase shift between two collimated beams from a coherent light source, developed by Ludwig Mach and Ludwig Zehnder [255, 256]. The principal setup is shown in figure 5.37 a). The initial collimated beam is split in a beam splitter, each part is sent through a beam path which is called the "arm" of the interferometer, and they are brought back into overlap with each other in a second beam splitter, where the beams interfere. If there is no other modification of the setup, the interference will always be constructive, and the MZI will serve no purpose. However, if one of the MZI arms is changed by inserting a delay or a phase-shifting device, everything changes and the MZI becomes a very accurate measurement tool, since the phase of the beam in the modified arm has an immediate and very measurable effect on the interference of the two beams and hence the output intensity.

While the MZI has been put to many different uses today, including complex micro-optical devices in the telecommunications sector [257] and optofluidic sensors [258], it should be noted here as an historical curiosity that the original MZI, as developed by Ludwig Mach together with his father Ernst Mach, was used to increase the accuracy of the measurement of the compression of air in front of artillery shells in flight and was used frequently on a testing range belonging to the company Krupp as well as in cooperation with the k.u.k. Marine-Akademie in Fiume of the Imperial Austrian Navy [259, 260].

The design of the MZI was adapted to DLSPW technology. Instead of beam splitters, Y-splitter geometries were used. The Y-splitter geometry has been thoroughly tested and examined and shown to be a very reliable method to achieve 50/50 splitting of intensity in a DLSPW structure [254]. Mirrors are not necessary in the DLSPW regime, it is much simpler just to curve the waveguide to shape the arm, using a sine shape for the curve and an adiabatic change of curvature to minimize scattering losses. This design is shown in figure 5.37 b). The delay from the traditional setup is created by making an asymmetric MZI, where one arm is

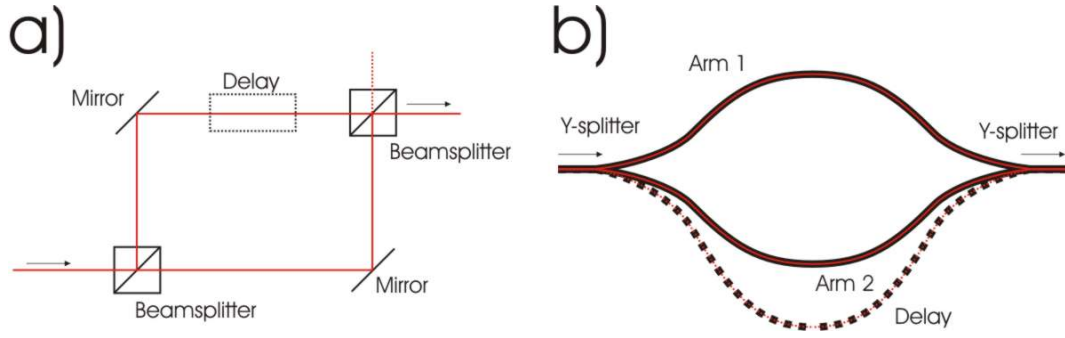


Figure 5.37: a) shows a schematic drawing of a typical Mach-Zehnder interferometer. b) Shows a schematic drawing of the DLSPPW geometry used to achieve the same effects.

longer than the other (shown dashed in the image). It is also possible to dope one arm with a material with nonlinear effects and consequently to use the MZI to design an electro-optical, thermo-optical or all-optical switch, which has been realized with structures based directly on those presented in this thesis [261, 262].

Challenges encountered during operation of the DLSPPW MZI are the strong ohmic losses experienced by the DLSPPW mode as well as scattering due to surface roughness and fabrication imperfections.

A very similar MZI design for SPPs has been proposed as a refractive index sensor, validating our design [263].

A total of 28 different geometries of Mach-Zehnder interferometers are examined, divided into four sub-sets. Three instances of each geometry are characterized, so the total of examined interferometers comes to 84. Averages of each geometry are taken.

The MZI geometry has a total length that was varied between 40 and 50 μm , with a 5 μm straight waveguide section on both sides for in- and outcoupling, and a 15 or 20 μm section for each bend of the MZI. The waveguides are 500 μm high and 900 nm wide. This means they are multimode waveguide for 1.55 μm excitation wavelength.

The excitation of the DLSPPW mode occurs with a 1.55 μm wavelength laser at the waveguide end in all cases. Leakage radiation images of one sub-set of MZI geometries are shown in figure 5.38, along with scanning electron microscope (SEM) images of the structures. In the images, the excitation takes place on the right side of the MZI and the output is on the left. The leakage radiation images show TM_{01} and $\text{TM}_{00} + \text{TM}_{01}$ modes propagating inside the MZIs. To preserve their functionality, the MZIs were not sputtered with additional gold prior to the SEM measurements. This causes the lines to look darker in the images than the substrate as well as other effects, such as a dark shadow around the dielectric structures as well as a perceived half-transparency.

To obtain values for the output intensity, the leakage radiation visible at the waveguide output area is integrated and normalized by using the MZIs with equal

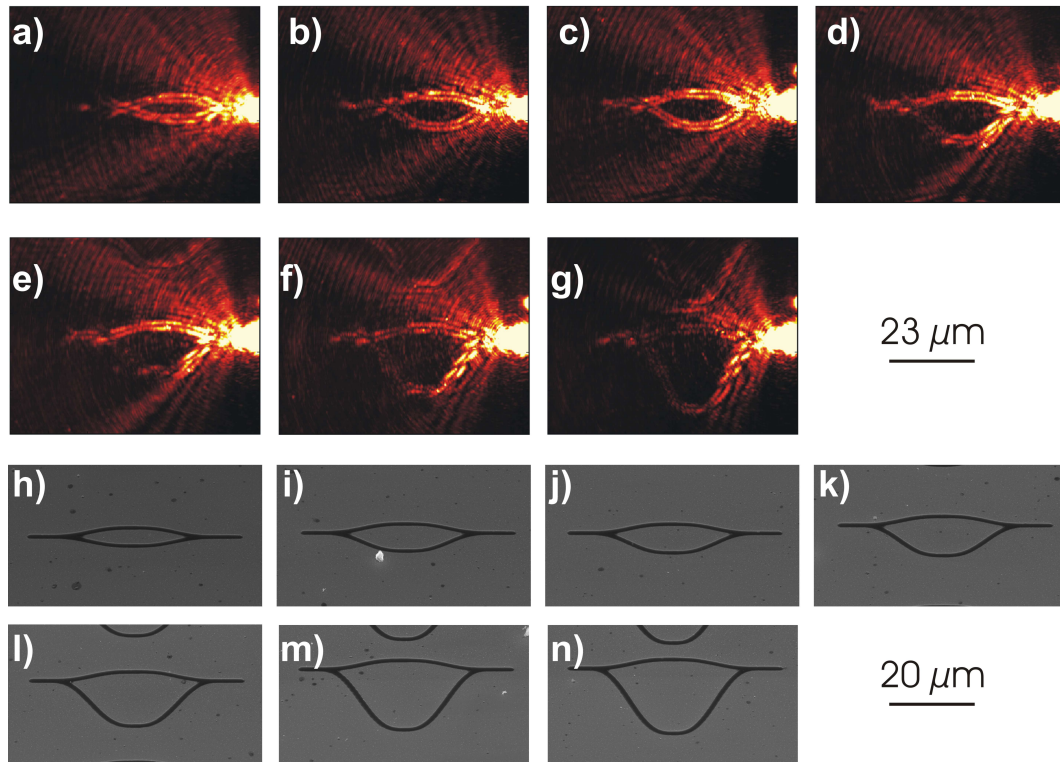


Figure 5.38: a)-g) False colour leakage radiation microscope images of DLSPPW Mach-Zehnder interferometers with different arm lengths. Excitation with a $1.55 \mu\text{m}$ wavelength laser takes place at the right side of the structures, the output is on the left side. The top arm has the same length in each image, $40.55 \mu\text{m}$. The length of the lower arm is a) $40.55 \mu\text{m}$, b) $42.13 \mu\text{m}$, c) $42.86 \mu\text{m}$, d) $45.58 \mu\text{m}$, e) $51.47 \mu\text{m}$, f) $58.52 \mu\text{m}$, and g) $63.12 \mu\text{m}$. h)-n) Scanning electron microscope images of the same structures with the same arm lengths as above.

arm lengths as a reference. This is a suitable reference waveguide because when both arms are equal in length there is maximum constructive interference between the two arms and maximum intensity. By using such a waveguide as a reference, it becomes possible to compare all structures to one another in a quantitative way. The expectation is that for different arm lengths, the output intensity will vary as phase shift results in different levels of constructive or destructive interference at the output.

The theoretical values are based on the known propagation length of the DL-SPPW mode within the waveguide and the effective index of the waveguide to determine the intensity and the phase shift of the mode, from which the total output intensity can be calculated. For the theoretical values we obtain

$$I_{theory}(L_i) = \frac{1}{2} \left(1 + \cos \left[\frac{L_i - L_0}{2\pi\lambda_{eff}} * \exp \left(-\frac{L_i - L_0}{L_{prop}} \right) \right] \right) \quad (5.34)$$

where L_i is the length of the variable MZI arm and L_0 is the length of the reference MZI arm in μm respectively and $\lambda_{eff} = 1.37 \mu m$ is the effective wavelength of the SPP inside the waveguide and $L_{prop} = 20.43 \mu m$ is the propagation length of the SPP inside the waveguide.

For the set of MZIs shown in figure 5.38, the resulting experimental and theoretical intensities dependent on arm length are shown in figure 5.39 . While the difference in arm length is the defining feature of the MZI structures, the resulting plot is not easy to read, since there is no recognizable pattern discernible from the seemingly scattered data points without the aid of the tapered sine curve with a period of about $2 \mu m$, on which the theoretical points all lie.

A clearer representation of the results is to display the intensity dependent on phase shift of the mode in the second MZI arm, which is shown in figure 5.40. Here the results from all MZI structures are shown, normalized with respect to each other and combined into one plot. Displaying the data in this form entails some mathematical processing, which will be outlined shortly.

The length difference between two MZI arms in units of wavelength D_λ can be obtained by calculating for each MZI arm:

$$D_\lambda = \frac{L_i - L_0}{\lambda_{eff}} : \quad (5.35)$$

where L_i is the length of the variable MZI arm and L_0 is the length of the reference MZI arm in μm respectively and $\lambda_{eff} = 1.37 \mu m$ is the effective wavelength of the light inside the waveguide.

It is then simple to convert this length difference in wavelengths into a phase difference simply by subtracting all whole wavelengths and multiplying the remainder by 360° .

However, the intensity values for these waveguides would still be incomparable due to differences in propagation length, which must be accounted for. Longer

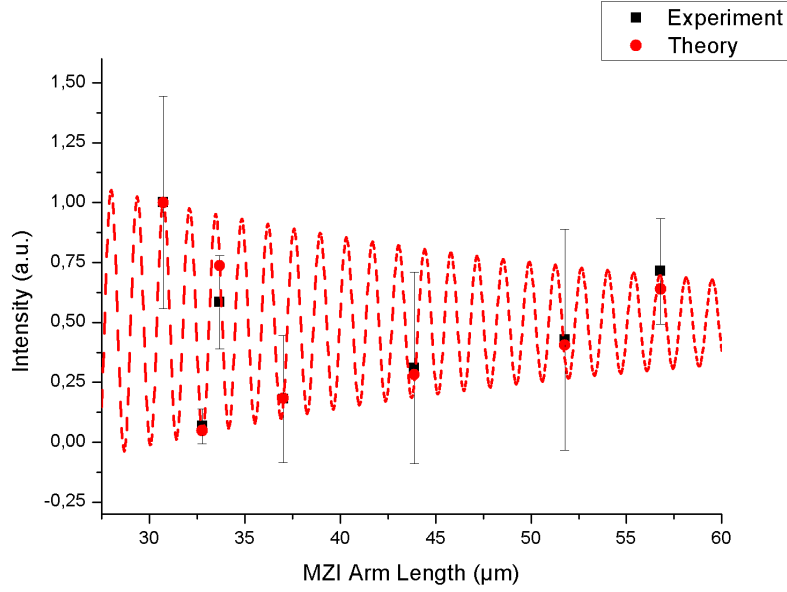


Figure 5.39: Plot showing experimental and theoretical results for MZI output intensity dependent on MZI arm length for one series of MZIs. The values are averages from several separate structures. The red dashed line shows the theoretical output intensity, with the red round dots only serving as visual markers for direct comparison with the experimental results.

arms will always lead to a lower signal intensity owing to the comparatively short propagation length of the SPP in these structures of $L_{prop} = 20.43 \mu m$. The intensity must be modified to account for this, adjusting for losses by

$$I_{phase} = (I_n - 0.5) * \exp\left(\frac{D_\lambda}{L_{prop}}\right) + 0.5 \quad (5.36)$$

where I_n is the normalized intensity used before, D_λ is the length difference in units of wavelength calculated above and L_{prop} is the propagation length. Bending losses are not accounted for in this calculation since they are present in both waveguides and the bend radii are very large in all structures, large enough not to cause significant losses beyond the regular absorption losses.

As one can see from the resulting plot shown in figure 5.40, DLSPPW MZIs function as expected within certain margins of error. The greatest sources of errors in these experiments are the inability to excite the DLSPPW mode in each structure in exactly the same way due to the inaccuracy of sample positioning, which is an issue due to the multimode character of these structures, and the possibility of fabrication errors in individual structures that may not be apparent even under an optical microscope. These sources of errors are evened out by characterizing three sample structures of each geometry and averaging the results.

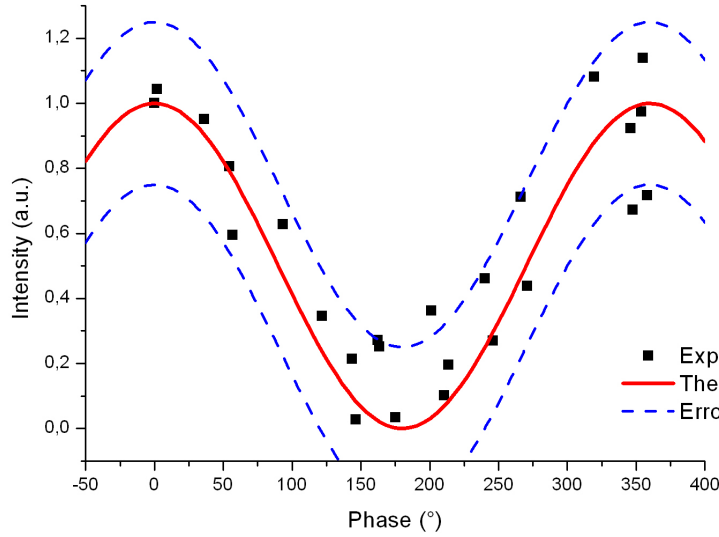


Figure 5.40: Plot showing experimental and theoretical results for MZI output intensity dependent on phase shift of the signal in the variable interferometer arm. The error bands are shown as two dotted lines and contain nearly all the experimental data points, showing an excellent match between experiment and theory.

5.3 Racetrack Resonators

A more complex DLSPW component is a racetrack resonator. These resonators consist of a racetrack-shaped waveguide loop in close proximity to a straight line waveguide. In our investigations, the gap between racetrack and line was 500 nm. The DLSPW mode can couple from the line waveguide in which it is launched to the racetrack resonator. Depending on wavelength or resonator length, the radiation inside the racetrack will be either in phase or out of phase with the mode in the line waveguide, which will lead to constructive or destructive interference. As such, these racetrack resonators can act as resonant filters for a variable-frequency signal. Ring-shaped DLSPW resonators fabricated by UV-lithography have already been shown to work in very similar fashion with variable laser frequency [264].

Racetrack resonators differ from ring resonators [265, 266] in that they have a straight interaction section which runs parallel with the waveguide, thus elongating the interaction region. This implies that one can increase the waveguide-resonator separation for a desired coupling ratio to the resonator, thus relaxing the requirements on the resolution in the fabrication. This feature is demonstrated by calculations performed by research collaboration partners in Denmark, most notably Tobias Holmgaard, using effective index method (EIM) calculations and the supermode approach, which has previously proven accurate for describing the coupling between two adjacent DLSPWs [267]. The results of the calculation of the accumulated phase difference throughout the whole racetrack resonator are shown in

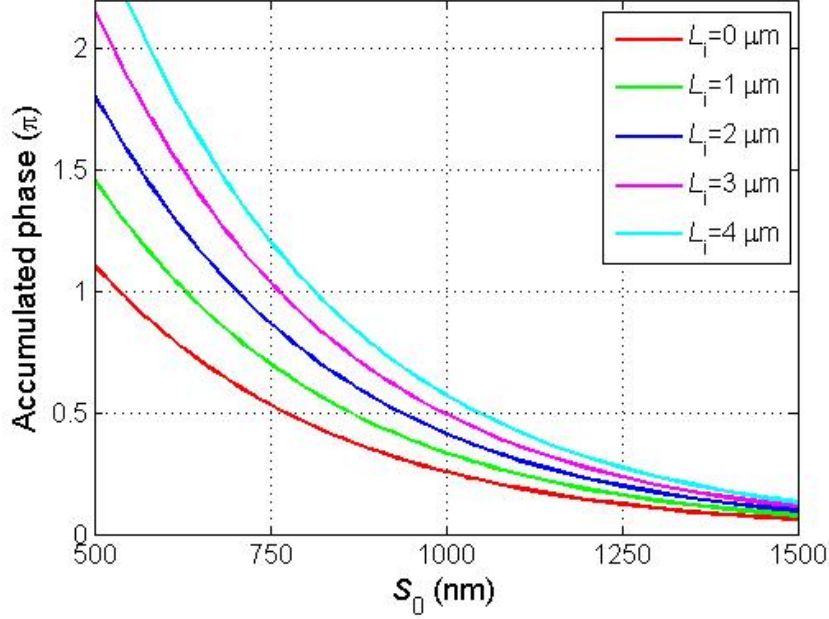


Figure 5.41: Graphs plotting the effective index method calculation performed by research collaboration partners of the accumulated phase difference ($\lambda=1550$ nm) throughout the racetrack resonator as a function of the centre-to-centre separation of the (500 nm wide and 600 nm high) waveguide ridges in the parallel section ($S_0 = 500$ nm corresponds to the absence of gap). The accumulated phase is plotted in units of π for different lengths of the parallel section ranging from $L_i = 0$ μm (ring resonator) to $L_i = 4$ μm . The waveguide parameters are adapted from ref. [267].

figure 5.41. The accumulated phase difference determines the interference of the DLSPPW mode in the straight waveguide and in the racetrack, and consequently also the extinction efficacy of the whole structure. The suitability of the racetrack resonator for modulator and filter applications is further validated in addition to the work presented here by a recent analytical and numerical study, which notes that an extinction ratio of -34.5 dB is attainable [268].

In plasmonic resonators one usually requires ca. 50% coupling to the resonator [264] in order to obtain critical coupling, which translates into an accumulated phase difference of $\pi/2$. For a ring resonator this can be achieved with a centre-to-centre separation of $S_0=770$ nm, implying a gap of only 270 nm, whereas a racetrack resonator with a parallel section of 3 μm , increases this gap to 500 nm, as shown in figure 5.41. Such an increase is in many fabrication techniques crucial in order to realize well resolved structures, thus making the racetrack resonator a promising structure in plasmonics.

An example of racetrack resonators, fabricated directly on gold by 2PP, in operation is shown in figure 5.42 where two slightly different racetrack resonators are

shown. The wavelength used for the excitation of the DLSPPW modes is $1.55 \mu\text{m}$. The single-mode waveguides are ridges 500 nm high and 600 nm wide. The differences between the racetrack resonators are the interaction length, which is $2 \mu\text{m}$ in one case and $3 \mu\text{m}$ in the other.

The long waveguide (at the top in the image) shows constructive interference in the output waveguide. The difference in length of the racetrack resonators in the two pictures is $2 \mu\text{m}$. To translate this into effective wavelengths, we must first calculate the value of the effective wavelength in the waveguide using the effective index $n_{\text{eff}} = 1.13$ which gives us $\lambda_{\text{eff}} = 1.3717 \mu\text{m}$. If we then divide the length difference by this value, we get a difference of 1.46 wavelengths. Consequently, the phase change is nearly 180° , leading to an expectation of a high suppression of output in the case of the shorter resonator, which is precisely what we see in the experimental results. However, the racetrack resonator and subsequent interference is not the main cause of this result. The measured propagation length for the $5 \mu\text{m}$ semi-circular bend is $L_{\text{prop}} = 4.92 \pm 0.72 \mu\text{m}$, indicating some scattering out of the waveguide, which is also visible in the image. A plot of the intensity inside the bend and a superimposed exponential fit is shown in figure 5.43.

When we now consider the total length of the racetrack resonator, it becomes clear that the signal inside the racetrack becomes too weak to interfere significantly with the signal inside the line waveguide. The results stem from the fact that in the case of a $3 \mu\text{m}$ interaction length, the phase difference along this stretch is close to 2π , which means that the mode couples to the racetrack and back again. In the case of the shorter interaction length, the mode couples only to the racetrack and is diverted away. The large coupling is due to the low mode effective index of 1.13 and the corresponding low mode confinement.

5.4 Symmetric and Asymmetric Splitters

It can be necessary for many different kinds of reasons to split up an SPP propagating in a waveguide into two (or more) parts. The easiest way to achieve this is using a waveguide splitter. The splitters we will discuss in this part are either all-plasmonic or all-optical with a direct connection to DLSPPW waveguides. Only splitters with two branches are discussed, although more are theoretically possible.

A splitter consists of one input waveguide and two output waveguides, shaped as the letter Y, which also leads to their designation as "Y-splitters". The first splitter design we will consider here consists of a straight incoupling section, two sinusoidal bends in opposite direction at the splitting point, and two straight outcoupling sections on the ends of these.

In such a design, it is possible to exploit the mode-beating effect discussed in section 5.1 to control the intensity of SPP propagation in each of the outcoupling arms of a Y-splitter. This is shown in figure 5.44. The overall length of the splitter is $15 \mu\text{m}$. The distance between the two arms is $5 \mu\text{m}$. The waveguide is ridge-shaped, 500 nm high and approximately $1 \mu\text{m}$ wide. It is therefore a multimode waveguide at the characterization wavelength of 632.8 nm .

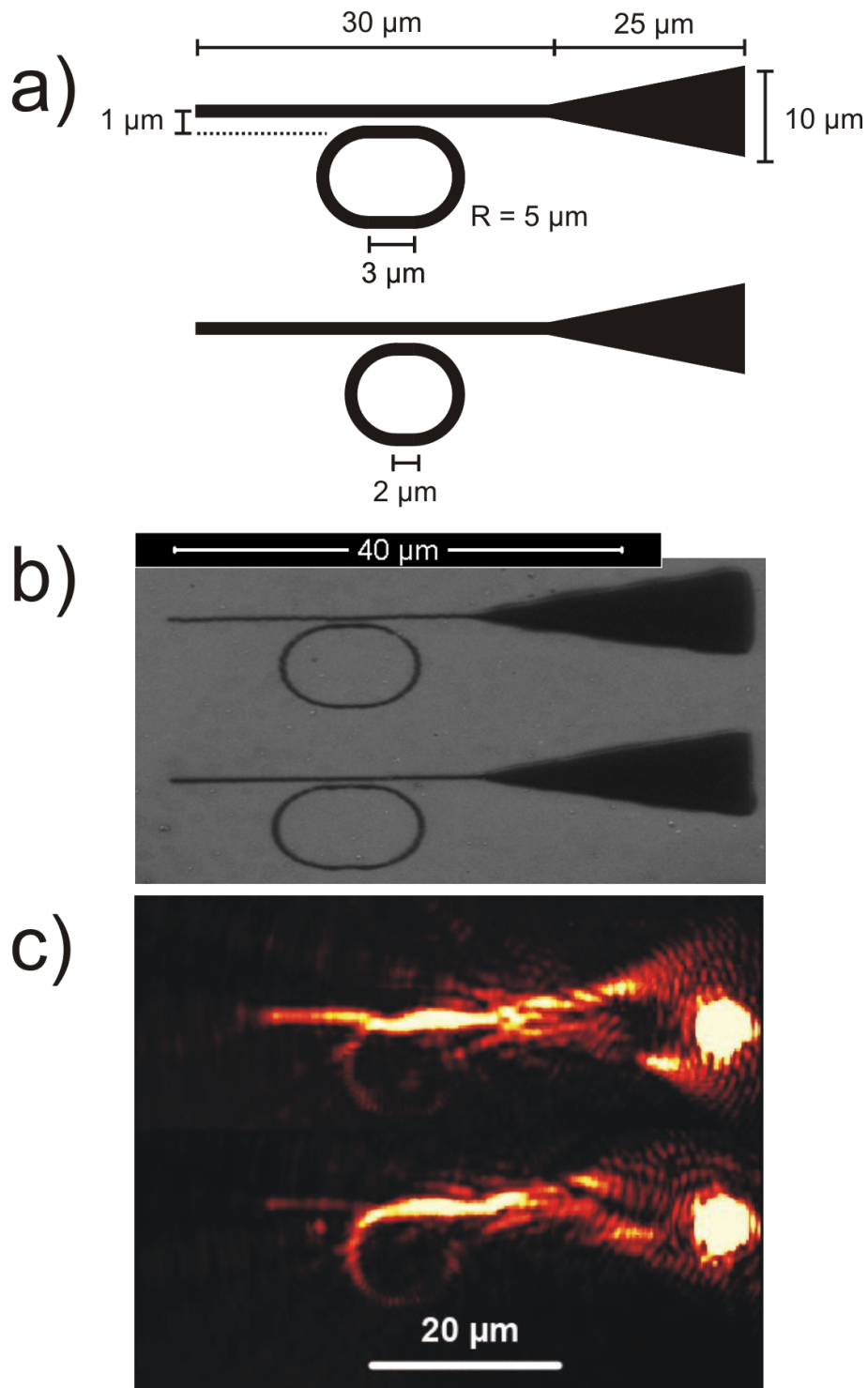


Figure 5.42: a) A schematic drawing of the structures. b) SEM image of the structures. The structures are 500 nm high and the waveguides are 600 nm wide. c) False colour leakage radiation microscope images of two racetrack resonator structures taken at 1.55 μm excitation wavelength. The length difference between the two racetracks is 2 μm , which amounts to a nearly 180° phase difference, resulting in destructive interference at the waveguide output in the case of the shorter racetrack resonator. The damping is in excess of 16 dB.

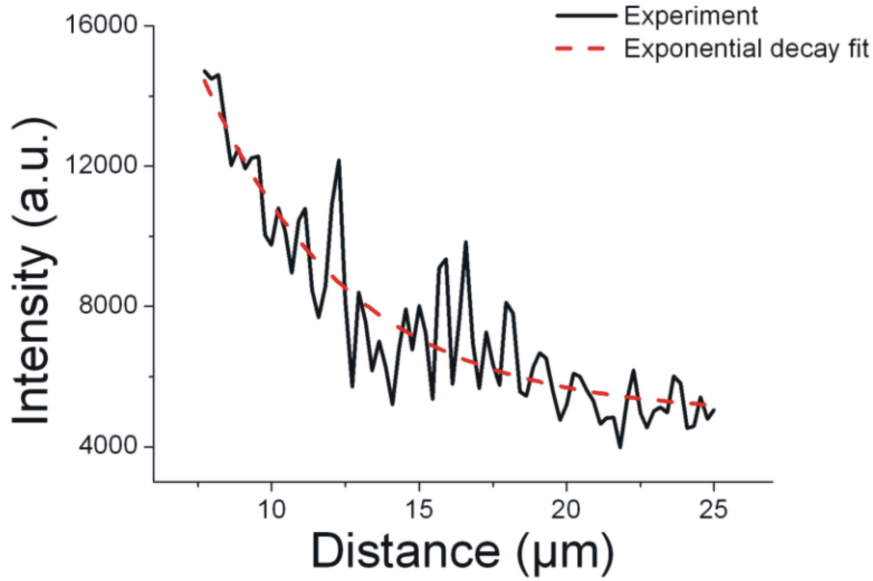


Figure 5.43: Plot of the leakage radiation intensity inside the semi-circular bend of a racetrack waveguide. An exponential fit is also shown.

As discussed in section 5.1, it is possible to excite different propagating DLSPW modes inside the waveguide, if the waveguide is multimode, by focusing the excitation laser beam on different parts of the waveguide end. If the focus lies exactly on the optical axis, the TM_{00} mode is excited. If the excitation beam is shifted from the optical axis, it becomes possible to excite a superposition mode, the $TM_{00}+TM_{01}$ mode, where the SPP intensity oscillates between the two waveguide edges.

It is possible to use this superposition mode to guide intensity selectively into one or both of the Y-splitter arms, as shown in figure 5.44. The shift of the focus position necessary for this effect is smaller than 400 nm [250].

The splitter shown above is a purely plasmonic splitter, that can only work with TM DLSPW modes, and not with optical modes. However, when the integration of DLSPW components with fibre optics is considered, it becomes clear that there is a need for an optical splitter that can produce two different output states depending on the polarization of the input light.

A splitter with two output waveguides, of which one allows only TE modes and the other only TM modes, can be used as an optical switch. The input polarization can be used to choose into which output waveguide of the splitter the mode should propagate. The splitter could also be used as a simple polarization detector. A further use for this splitter is that it can provide two outputs with clearly defined and orthogonal polarization from a randomly polarized input medium, such as an optical fibre. In principle this allows the use of unpolarized light from an optical fibre in plasmonics experiments.

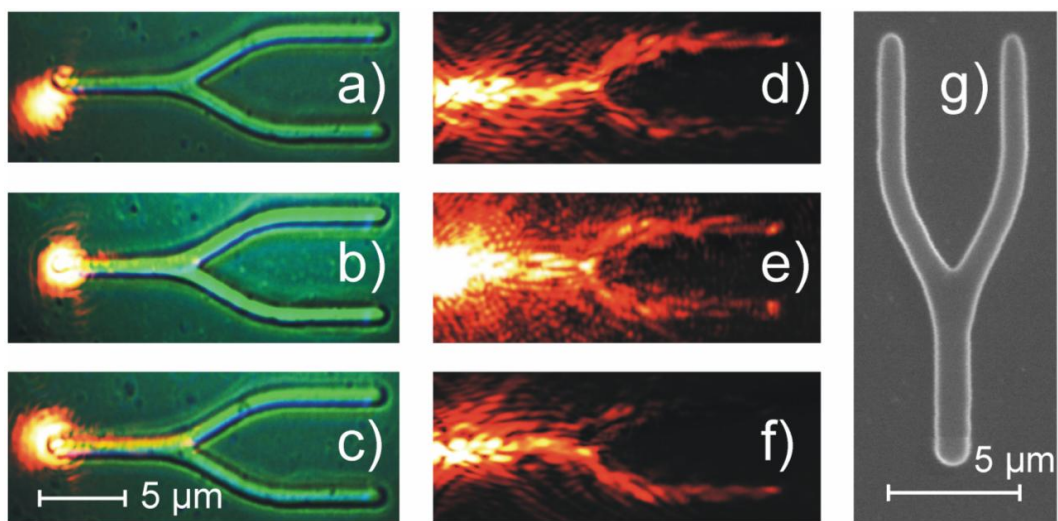


Figure 5.44: Images of a DLSPPW Y-splitter structure. Images a)–c) show leakage radiation microscope images with background illumination, which makes it easy to see the precise location of the excitation beam focus, a He-Ne laser at 632.8 nm wavelength. Images d)–f) are leakage radiation microscope images without background illumination, to illustrate the SPP intensity distribution in the waveguides. Image g) is an SEM images of the Y-splitter written in mr-UVL 6000.5. In images a) and d) the intensity is strongest in the upper arm, in images b) and e) it is equally distributed, and in images c) and f) it is strongest in the lower arm.

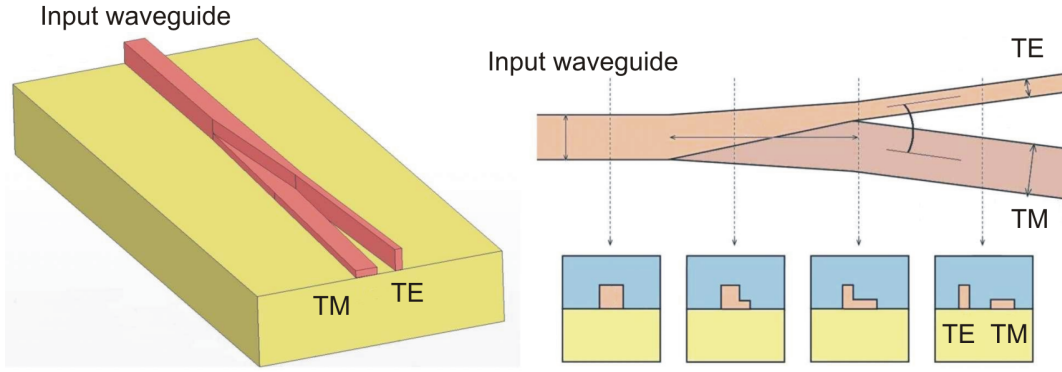


Figure 5.45: Schematic images showing the design of the asymmetric polarization-dependent splitter. A 3D view, a top view and cross-sections of the waveguide at four points are shown. This figure is adapted from images made by the company SILIOS.

In order to fully support TE and TM modes without large intrinsic losses, the splitter is designed to be all-optical, i.e. without a plasmonic part. In a plasmonic circuit, the splitter would be the incoupling component, and attached to DLSPPW structures.

While symmetrical polarization-dependent splitter designs have been proposed [269], the splitter presented here is asymmetrical. The origins of this structure lie within the accomplishments of a joint project with European partners, and the French company SILIOS and in particular its employees Stephane Tisserand, Fabien Reservat and Thierry Berthou had a very large role in its design, and credit should be given to them. The functional principle is that each output waveguide is designed to strongly prefer one kind of mode over the other. Therefore, as can be seen in figure 5.45, the TE waveguide is thin and high while the TM waveguide is broad and flat. The mode emitted by the TM branch can immediately be converted to a DLSPPW mode, while the mode emitted from the TE branch can be rotated using a polarization rotator [270, 271], and then also converted into a DLSPPW mode.

The main advantages of this asymmetric Y-splitter design are that it can be shorter than the symmetric designs proposed so far, and is more tolerant to fabrication errors. In addition, it can operate over a broad wavelength range [272, 273].

The basic structure of the asymmetric Y-splitter, as can be seen in figure 5.45 is an input section, followed by a slightly tapered junction region, and finally the two separate output waveguides. The design is made for $1.55 \mu\text{m}$ wavelength input light. The input section is nearly square in cross-section and can support any mode. The tapered junction region slowly separates the two output waveguides by tapering the input cross-section into the cross-sections of the output waveguides. The output waveguides each have a strong preference for one mode, either TE or TM.

Propagation simulations and optimization of the structure were made with the software C2V Prometheus and the beam propagation method (BPM) by the French project partners. These simulations took into account that mode evolution or mode sorting theory predicts [272, 273] that light propagating in the tapered junction

section will prefer the waveguide branch where its confinement is higher. The output waveguides are designed to have strong confinement for the TE and TM mode respectively while having low confinement for the opposite polarization. This is achieved simply by tapering the waveguide core into a rectangular cross-section, which is vertical for the TE mode and horizontal for the TM mode. This change of the cross-section along the length of the splitter is illustrated in figure 5.45. During simulations, the parameters of the waveguide were optimized to provide low transmission losses and high polarization separation, all at the wavelength of $1.55 \mu\text{m}$.

In order to accommodate the respective mode cutoffs of the two output waveguides with the tapering mechanism, it is necessary to increase the dimensions of the input waveguide. The input waveguide is consequently multi-mode, but this is not critical in this case because the excitation of higher modes can be suppressed by appropriate alignment of the splitter and the fibre.

Initially, simulations were performed to find the optimal geometrical aspect ratios for each output waveguide to obtain polarization splitting. An aspect ratio of approximately 3:1 was found (for height:breadth in the case of the TE waveguide and vice versa for TM). Calculations to see which modes the waveguide can support (in 2D, cross-section only) resulted in the exact dimensions of the waveguide, which are $3 \mu\text{m} \times 1 \mu\text{m}$ for the TE waveguide. Further optimization in the case of the TM output waveguide resulted in a cross-section of $1.12 \mu\text{m} \times 3 \mu\text{m}$. The extinction level in the waveguide for the unwanted mode is 27-35dB. The input section consequently has a cross-section of $3 \mu\text{m} \times 3 \mu\text{m}$.

The next step was to optimize the length of the tapered junction region. A longer region increases the efficiency of the splitting, but entails transmission losses. The same is true for the splitting angle - a higher angle has better splitting properties but increases losses. It was found that a tapered junction region of $200 \mu\text{m}$ length with a splitting angle of 2 degrees has 97% transmission for either polarization state.

The coupling efficiency of the TM mode output waveguide to a DLSPPW structure was calculated. Assuming the DLSPPW structure is perfectly connected to the TM output waveguide (achievable by fabricating the whole combination of structures in one 2PP process, for example), a transmission of 75% is achieved.

Finally, the coupling efficiency from a standard SMF-28 fibre to the input waveguide section of the splitter was also calculated. This resulted in a calculated transmission of 22% for either polarization due to the large size mismatch. This is due to the choice of the fibre. In principle, a small-core fibre as used in the fibre-coupled experiments above, or a tapered fibre could be used to mitigate this and increase transmission to above 80%.

Originally, the structure was intended to be characterized using fibers for the input. However, due to availability issues, leakage radiation was chosen as the initial characterization mechanism, and the design parameters had to be modified. Since the field of view of the objectives in the leakage radiation setup is on the order of $50 \mu\text{m}$, the structure was shrunk to this length to allow the whole structure

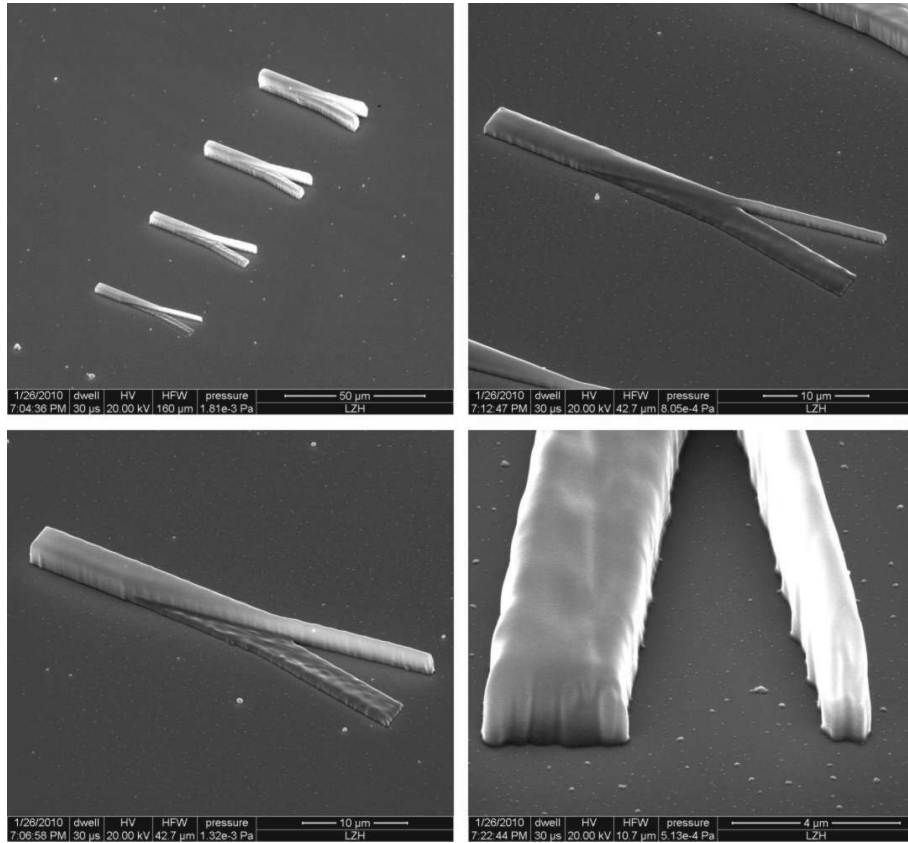


Figure 5.46: SEM images of the polarization dependent splitters fabricated by 2PP.

to be viewed and for light to be coupled in at the input end. This resulted in a considerable enlargement of the splitting angle in the tapered junction region as well, and consequently the losses of this structure are now significantly higher than they would be under ideal circumstances.

The structure is fabricated directly on a gold surface using the "Ormosil" photoresist by 2PP. 2PP is an optimal method to efficiently fabricate a structure such as this with different height features, which would require multiple exposures using UV lithography. In order to reproduce the structure design faithfully, a 3D model of the splitter is created using CAD software. During this process, the size of the focus point and the nature of the software running on the 2PP setup is taken into account, and the features in the model are made smaller than they should be to accommodate the full radius of the focus spot. The resulting structures are shown in figure 5.46. As can be seen, the 2PP fabrication technique is fully capable of reproducing the complex structure features exactly as required.

In order to be able to characterize and evaluate the properties of the polarization-dependent Y-splitter in the leakage radiation microscopy (LRM) setup, the design had to be modified slightly. It was necessary to achieve a shorter overall length of about $50 \mu\text{m}$ in order to accommodate the field of view afforded by the 100x objective in the LRM setup. At the same time, it was necessary to increase the splitting angle

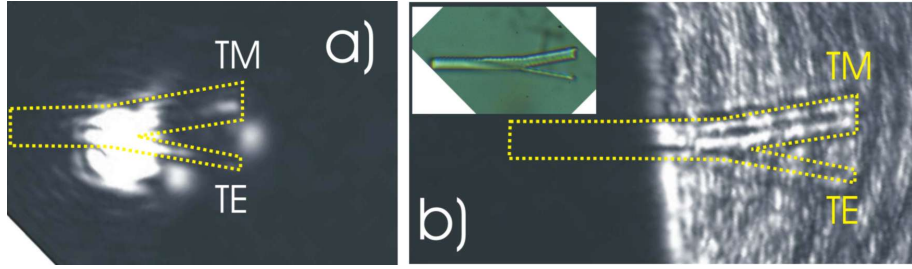


Figure 5.47: LRM images of the polarization dependent splitters fabricated by 2PP in Ormosil. The incoupling wavelength is $1.55 \mu\text{m}$. The inset in image b) shows the structure without any excitation beam present. The DLSPPW mode excitation takes place at the end of the incoupling waveguide. Due to the very strong scattering, the excitation area is blocked from view by a beam blocker. The outline of the asymmetric Y-splitter is shown as a dashed yellow line. In image a) the polarization is TM and only the TM-polarized waveguide contains strong intensity. In image b) the input polarization is TE and the TE-polarized waveguide contains light, while the TM-polarized waveguide is much darker.

of 2° in order to have two clearly separate output waveguides.

The waveguides are characterized by leakage radiation microscopy. By tuning the laser beam from TE to TM, it is possible to observe the splitting of the intensity in by the asymmetric polarization-dependent Y-splitter. The results are shown in the images in figure 5.47.

6 Nanoimprinted Dielectric-Loaded Surface Plasmon-Polariton Waveguides

In this section, experimental results will be discussed that were obtained from experiments with nanoimprinted dielectric-loaded surface plasmon-polariton waveguide (DLSPPW) components. It will be shown that components fabricated by nanoimprinting, such as straight line and bend waveguides are fully functional.

A special application which requires nanoimprinted waveguides due to the required waveguide geometry and their alignment with a substrate will be shown in the form of fibre-coupled plasmonic waveguides.

6.1 Nanoimprinted DLSPPW for Leakage Radiation Microscopy

As mentioned above and in a recent review [274], one method of nanoscale patterning that is attracting increasing amounts of interest is two-photon-polymerization (2PP). The advantages of this method compared with electron beam lithography (EBL) are considerably higher writing speed and a structurable area several orders of magnitude larger than achievable with EBL, while retaining full freedom concerning the structure's spatial configuration. In addition, fabrication of three-dimensional structures is possible with 2PP, which is not attainable with EBL, a purely two-dimensional technique. However, both methods are serial in the sense that structures are written point by point [252, 253]. Until now, it has been very challenging to modify such patterning methods to allow parallel processing. In this thesis a method of combining the advantages of highly-versatile patterning by two-photon polymerisation with those of nanoimprint lithography using flexible molds from polydimethylsiloxane (PDMS) is presented by demonstrating the fabrication of dielectric loaded surface plasmon polariton waveguides (DLSPPW), a class of photonic components that is attracting increasing attention (see section 1.3.3 above and [150, 149]).

Until now, there have been two common methods used in the manufacture of DLSPPWs. One method has been standard mask lithography [187], another more flexible method has been the two-photon-polymerization-based laser direct writing technique [275, 147]. 2PP technology, as detailed above, is a technology where a UV-sensitive photopolymer is exposed by a two-photon-absorption process, that allows complete freedom of structure design in all three dimensions. This is particularly useful in the case of DLSPPW structures that require features of different heights, which are duly replicated by the nanoimprinting method described in this thesis.

We manufacture by 2PP photonics components for surface plasmon polaritons (SPPs) that have already been simulated and characterized, namely line and bend waveguide structures with a funnel structure to enable efficient coupling into the waveguides [187]. A schematic of the 2PP structuring process used for the master samples is shown above in the section on fabrication. In a simplification of earlier

methods [275] we now use the glass substrate in a dual role as cover glass as well and write structures on its back side upside-down.

The structures are written on the plain glass substrate without any additional coatings using Ormosil as a photoresist mixed with 2% of the photostarter Irgacure 369. The laser employed is a frequency-doubled Yb:glass laser producing 150 fs pulses at 515 nm with a repetition rate of 10 MHz and an average power of 1 mW at the 2PP setup. A 100x oil-immersion microscope objective is used.

Our structures are simple lines and bends with coupling funnel structures. The lines are 22 μm long, the bends also have a total length of 22 μm with a curvature radius of ca. 7 μm . The structures are approximately 600nm high and 300nm wide, measured by SEM. Attached to the waveguides are funnel structures to ensure that SPPs are coupled into the DLSPPWs. These funnel structures have a base width of 10 μm , a length of 12 μm and are fully connected to the waveguides.

To produce these structures, we apply a nanoimprint technique. This technique is schematically shown in figure 2.11. The first step of this is master fabrication (step a in figure 2.11), followed by creation of a mold for replication (step b). This is done by filling a small cylindrical form with liquid PDMS which is placed over the structures on its open end. The viscosity of PDMS prevents any outflowing. The mold is then placed on a hotplate where it is baked for approximately 120 minutes at 110 degrees Celcius, during which the stamp hardens.

Following the hardening, first the cylindrical form and then the mold itself is removed from the sample (step c). This process is damage-free for the master structures, so several molds can be fabricated from the same master. What then follows is the nanoimprinting.

A drop of liquid photoresist, we use mr-NIL 6000.5 (micro resist technology GmbH, Berlin, Germany) for the structures presented in this thesis, is deposited on a fresh glass substrate covered with a 50nm gold layer (step d). The PDMS mold is then placed on the drop and light pressure applied to ensure a good spread of the photoresist and a thin residual layer. The residual layer must be considerably thinner than the DLSPPW structures to ensure photonic confinement in the DLSPPW, since our structures are functional the upper limit of residual layer thickness is at least 500nm. The exact thickness of the layer has proven difficult to measure and this is still part of ongoing research. The samples are then pre-baked for three minutes at 110 degrees Celcius and after that exposed under a UV lamp for 120 minutes (step e). They are then post-baked at 110 degrees Celcius for five minutes. The mold can then be removed, leaving the imprinted structures standing on the substrate surface (step f). This method has proved extraordinarily reliable over the course of the experiments, with nearly no failures.

A series of measurements was undertaken on these nanoimprinted structures using leakage radiation microscopy (LRM), a method that has previously proved very useful in the investigation of SPPs (above and [79, 276]). The primary mode of plasmon excitation in our experiments is defect excitation. In our LRM measurements, a He-Ne laser beam is focussed on the edge of the incoupling funnels to generate

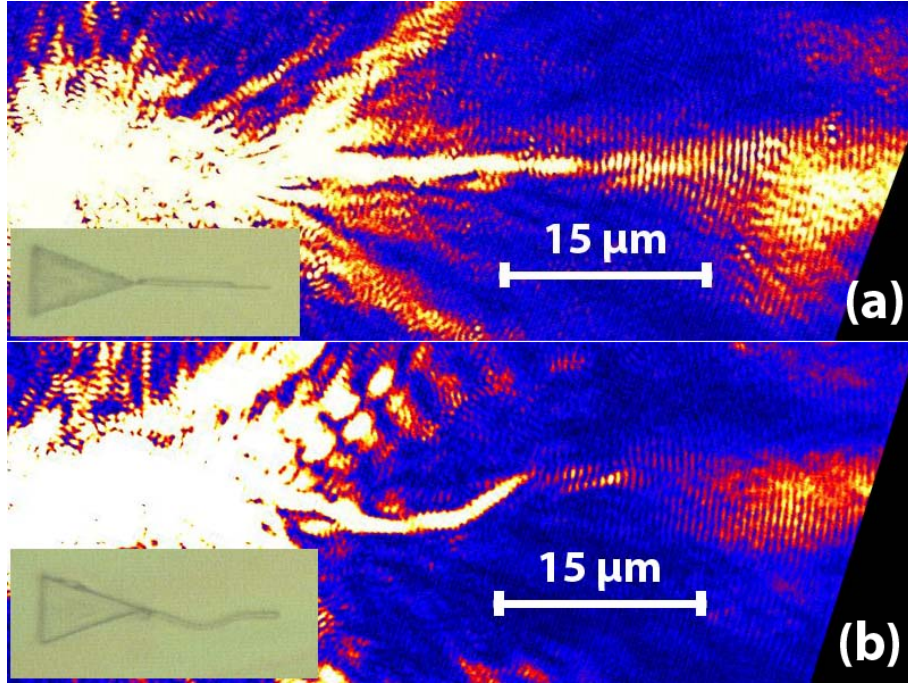


Figure 6.48: Two false colour LRM images showing guided DLSPW modes in nanoimprinted DLSPW structures. Image (a) shows a line with incoupling funnel, image (b) shows a bend with incoupling funnel. The excitation laser wavelength for these experiments is 632.8 nm. The SPP is clearly confined within the superimposed structure outlines, which were retrieved from optical micrographs. Visible to the right of the DLSPW structures is divergent light at the end of the waveguide, a clear sign of guided DLSPW modes within the DLSPW structure. Inset are optical microscope images showing structure geometry.

modes that are coupled into the waveguides, or it is focussed on the line waveguide itself to generate SPPs propagating perpendicularly to the waveguide. We eliminate the transmitted laser beam by fourier filtering to enhance contrast. We also investigate the fourier image plane of our LRM setup in order to determine the nature of the observed leakage radiation, where non-guided propagating surface plasmons are recognizable by their distinct crescent shape due to their angle of emission, while guided DLSPW modes are characterised by a straight line.

Figure 6.48 shows the propagating guided DLSPW modes as imaged in the LRM setup while figure 6.49 shows the corresponding images taken in the fourier plane. The excitation laser wavelength for these experiments is 632.8 nm. The guided DLSPW modes are clearly visible within the bounds of the superimposed DLSPW structures. In the fourier-plane pictures these modes show up as straight lines, contrasting with the crescent-shaped signature of non-guided SPPs [235].

The intensity of SPP distribution along the waveguide is extracted from the leakage radiation images and plotted to determine the propagation losses. This is done by fitting an exponential decay to the curves. This is considered a valid

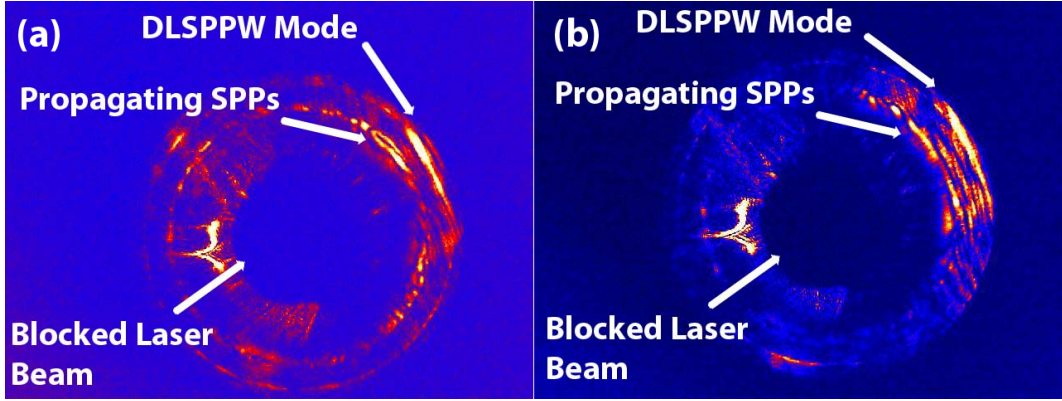


Figure 6.49: Two false colour LRM images showing DLSPPW modes in the fourier plane. The excitation laser wavelength for these experiments is 632.8 nm. The optical characteristic of the guided DLSPPW modes are the straight lines. (a) line structure. (b) bend structure.

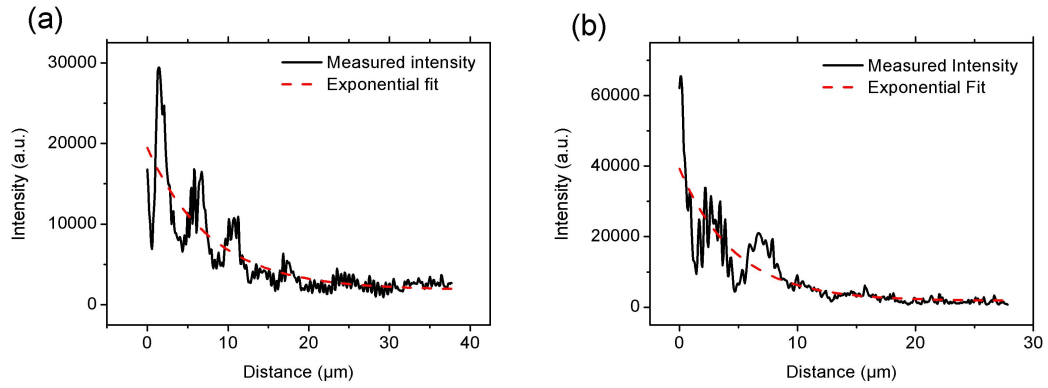


Figure 6.50: Measured and fitted SPP intensity graph for the line structure (a) and bend structure (b).

method because the fit curve averages out the amplitude modulations visible in the intensity graphs. From this the propagation length of the mode can be derived. For the line structure, the intensity graph is shown in figure 6.50 (a). The exponential fit leads to a DLSPPW mode propagation length of $7.89 \pm 0.53 \mu\text{m}$. In the case of the bend structure, the graph is shown in figure 6.50 (b) and the propagation length is $4.69 \pm 0.31 \mu\text{m}$. The DLSPPW mode propagation length is considerably lower in the bended structure, which can be explained by bend losses [230]. Other losses that determine the propagation length are given by ohmic losses, leakage radiation and scattering.

Nanoimprinted waveguides are also studied at the 1550 nm telecommunications wavelength. Figure 6.51 shows a DLSPPW mode propagating inside a nanoimprinted line waveguide. Analysis of the mode decay rate in these nanoimprinted waveguides reveals an effective index $n_{\text{eff}} = 1.11$ and a propagation length of $L_{\text{prop}} =$

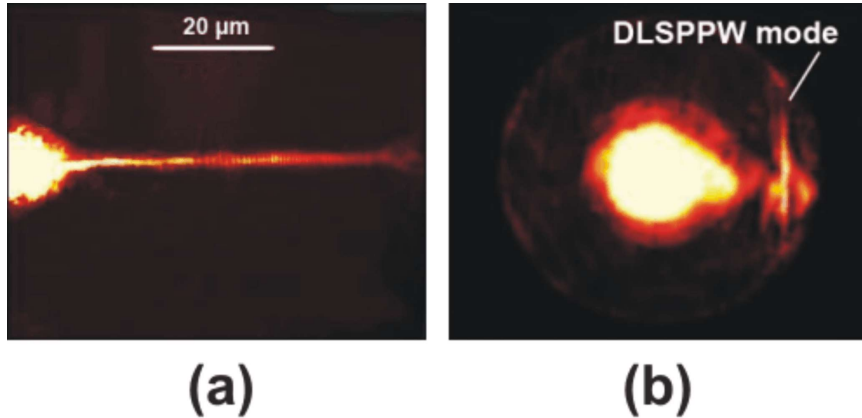


Figure 6.51: (a) Leakage radiation microscopy image showing a nano-imprinted line waveguide with incoupling funnel. (b) The Fourier plane image of the same line. The excitation laser wavelength for these experiments is $1.55 \mu\text{m}$, the images are in false colour.

$7.6 \pm 0.3 \mu\text{m}$. These results are in the same range as previous results from nanoimprinted waveguides examined at 632 nm wavelength ([184] and above), but in contrast to the previous waveguides these are single-mode.

There is a significant difference in the value of the propagation length when we compare the nanoimprinted and the directly written case. The explanation for this is the presence of a thin residual layer of polymer covering the sample surface in the nanoimprinted case, which leads to increased scattering, and the inclusion of dust particles in the nanoimprinting process, which leads to increased roughness and minor distortions of the structures. Both of these aspects could be improved by using more advanced equipment in a cleanroom environment.

These results show guided DLSPPW modes for the first time in structures produced using nanoimprint lithography from masters fabricated by the 2PP technique. This demonstrates that nanoimprint lithography is a viable technology for use in the fabrication of operational DLSPPW waveguides and that the intrinsic parallelisation of the nanoimprinting process is one step on the way to industrial application of DLSPPW technology. The results presented above are published in reference [184].

Another advantage of nanoimprint lithography is that it is a technology which can be used to fabricate structures from materials which are not processable by 2PP. Two examples which were used in this work are the optically nonlinear polymer 3BCMU and the resist mr-NIL 6000 doped with an amount of the optically nonlinear disperse dye Disperse Red 1.

6.2 Fibre-coupled DLSPPW

An important aspect for DLSPPW components is their compatibility with various optical configurations. Most optical systems and optical data transmission networks are fibre-based, so it is particularly important to provide the ability to interconnect

plasmonic waveguides and optical fibres for integration purposes. There has been a connection between fibre optics and surface plasmons since more than twenty years, although early research efforts concentrated on using surface plasmons to manipulate or control light inside the fibre rather than use it to launch SPPs inside a plasmonic waveguide circuit [277]. However, recently a couple of groups have begun work on launching SPPs on silver metallic waveguides directly with light from a fibre [278, 279], which shows that the need for an efficient coupling mechanism is gaining recognition.

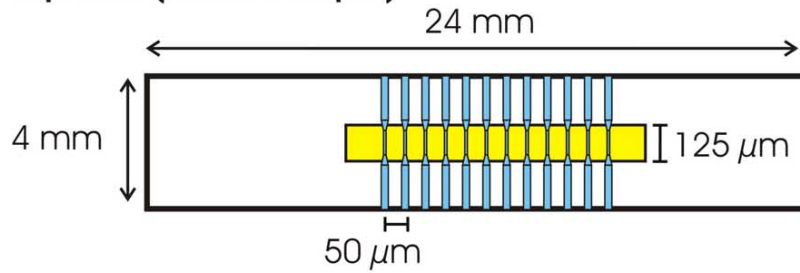
In this thesis we present plasmonic-optical hybrid waveguides fabricated by nanoimprint lithography from master structures made by the two-photon polymerization technique. The plasmonic waveguides are interconnected with tapered dielectric waveguides suitable for end-fire coupling with optical fibres. The layout of the structures is derived from the design that has been studied in some detail using LRM above, but was not suited to a fibre-based environment due to the impossibility of approaching the structures with a fibre close enough for coupling. This has been remedied by the inclusion of optical waveguides in the design that can be coupled to optical fibres [figure 6.52 (a)].

The substrate used is a quartz glass slab measuring 24 x 4 mm. The refractive index of the glass is 1.44 at a wavelength of 1.55 μm . In the centre of the glass slab there is a longitudinal gold stripe measuring 125 μm across and several millimeters long, which is patterned using electron beam lithography and a lift-off process. The gold layer deposited by evaporation is 50 nm thick. For the waveguide material we use the nanoimprint lithography resist mr-NIL 6000 made by the company micro resist technology GmbH in Berlin. The refractive index of the polymer waveguide is 1.523 according to the manufacturer. The waveguides run across the sample at a right angle to the gold stripe and are thus also 4 mm long. The waveguides consist of optical waveguide parts for in- and outcoupling and a dielectric loaded surface plasmon-polariton waveguides (DLSPPW) [150, 147, 149, 148] section 100 μm long in the centre, where the gold layer is located. It is necessary to have single mode waveguiding from fibre to fibre, and this places restraints on the possible dimensions of our waveguides. The DLSPPW section has a rectangular 0.6×0.6 μm cross-section, which is single-mode for 1.55 μm light [150, 187]. The optical section of the waveguide has a rectangular 2×2 μm cross-section, which also makes it single-mode, as was obtained by numerical simulations [280, 281, 282]. To have a single-mode optical waveguide is important, since a multi-mode waveguide would incur very large losses when coupling to the single-mode plasmonic waveguide. SEM images of the different waveguide sections showing their respective widths are shown in figure 6.52 (b) and (c). The taper between the two sections is 50 μm long.

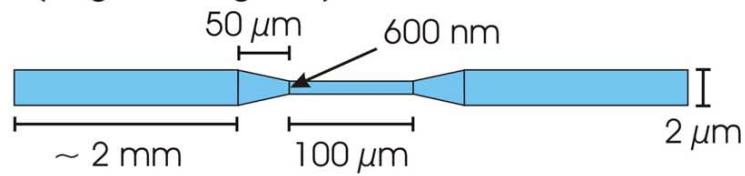
The funnel length was chosen to provide an optimum of transmission. A longer funnel requires more space but has lower transmission losses. Several funnel designs, shown in figure 6.53, with lengths from 5 to 50 μm were tested in finite-difference time-domain (FDTD) simulations using the FullWAVE simulation software made by RSoft. The most illustrative results are displayed in figure 6.54. The result of

(a)

Top view (whole sample)



Top view (single waveguide)



Side view (single waveguide)

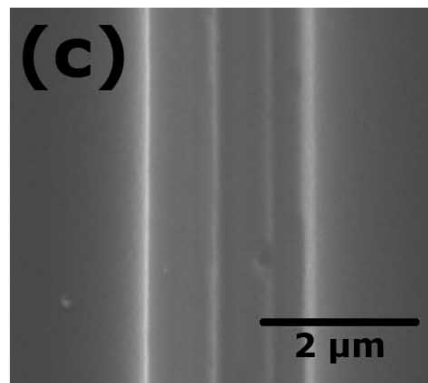
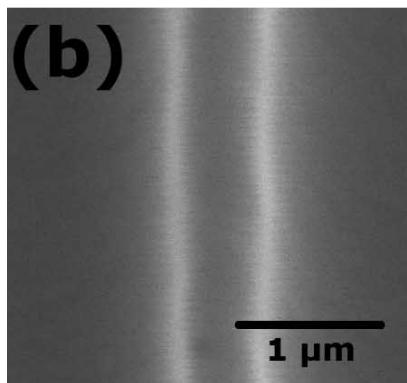
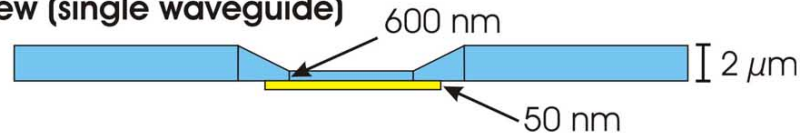


Figure 6.52: (a) A schematic showing the layout of a sample with plasmonic waveguides. The waveguides consist of optical waveguides at either end which taper down to a 100 micro-meter long plasmonic waveguide only 600 nm wide. (b) SEM image of the DLSPPW section. (c) SEM image of the optical waveguide section.

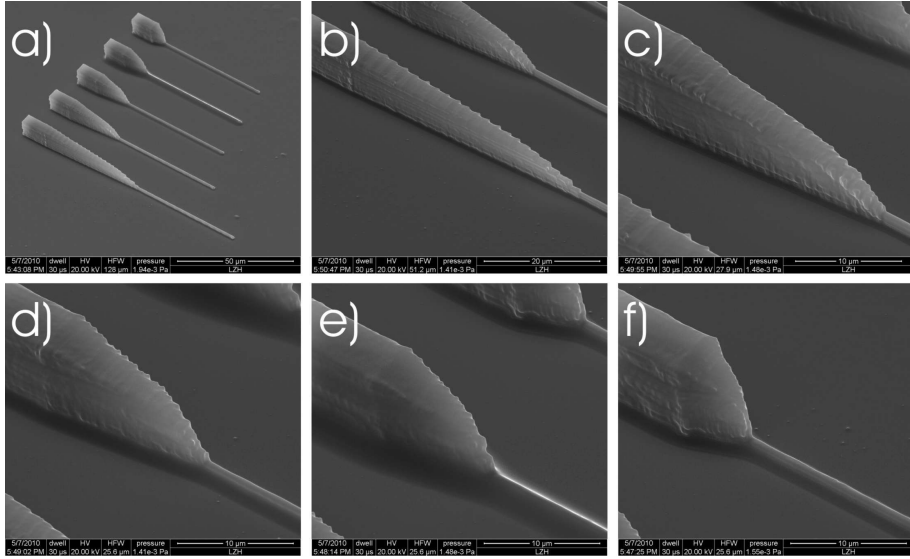


Figure 6.53: SEM images of the 3D coupling funnels from the optical to the DLSP waveguide. a) Overview of all funnel lengths. b) 50 μ m funnel. c) 25 μ m funnel. d) 15 μ m funnel. e) 10 μ m funnel. f) 5 μ m funnel.

these simulations is that the 50 μ m long waveguide taper shows low scattering losses to the substrate and into air while in all other cases most of the radiation goes into the substrate with very little transmission into the waveguide.

It is therefore clear that the 50 μ m long taper is the best choice for the waveguide.

Sample fabrication is a multi-step process. In the first step, the waveguide structures are fabricated by two-photon-polymerization (2PP) on a highly-polished glass mirror substrate using custom-made ormosil [283] as a photo resist. 2PP is a very versatile micro- and nano-patterning technique [252, 253] and is the only suitable technique for the fabrication of these structures due to their geometry and dimension. Traditional UV mask lithography, which would provide the necessary resolution of 600 nm, cannot handle the three-dimensional aspect of the required structures and stereo lithography, while being able to make 3d structures, lacks resolution.

After 2PP fabrication of the masters, a stamp is made for nanoimprint lithography. The stamp material used is polydimethylsiloxane (PDMS). The stamp is used in combination with an imprint resist to create a copy of the master structures on the substrates using mr-NIL 6000 as resist material. This procedure for making functional plasmonic components by this method has already been shown to work well [184]. After stamping, overhanging edges of imprint resist are removed using a micro-mechanical cleavage technique.

The fabrication method may seem a bit roundabout and complicated, but it is the most efficient way to fabricate these waveguides. To directly write them using 2PP on the correct substrate may seem a faster and more straightforward fabrication method. There are two major challenges which make this unpractical, however.

The first challenge is the fact that the structuring process takes place on two

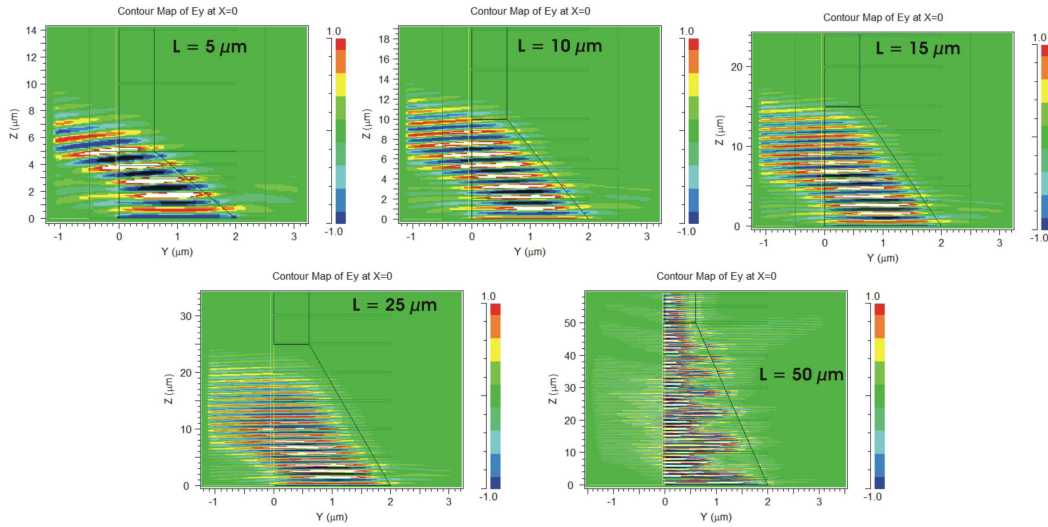


Figure 6.54: Results of FDTD simulations of the 3D taper from the optical $2 \mu\text{m} \times 2 \mu\text{m}$ to the DLSPW $500 \text{ nm} \times 500 \text{ nm}$ waveguide. The $50 \mu\text{m}$ long taper clearly works best, with most of the radiation being lost to the substrate in the other cases.

different substrate materials, with substantially different reflectivities. By far the largest part of the waveguide (the optical part) is situated on glass, while the short but critical DLSPPW section is located on gold. As noted above, fabrication on glass and gold requires very different parameters and it proved difficult to produce a single structure in one go with different parameters. The challenge was partly overcome by creating a special software programme which tuned the laser power to a different value when the laser was above the gold stripe, which worked satisfactorily even at very high speed.

The second challenge is posed by the surface tension of the photoresist and the substrate format. In order to ensure acceptable coupling between the optical fibre and the waveguide, it is absolutely necessary to obtain flat waveguide faces at the ends of the waveguide, and to ensure that the waveguides extend all the way to the end of the substrate. This is not possible by using the final substrate and coating it with photoresist, since the photoresist layer will always be thinner at the edge of the sample due to surface tension. In the experiments made using this configuration, the waveguides persistently either did not reach the edge of the substrate or were reduced in height to a maximum of two hundred nanometers when they did so, becoming unusable. Consequently, the only method to fabricate the waveguides was to use the nanoimprint lithography method outlined above and first published in [184].

The fibre-coupled DLSPPW structures are unique in their geometry amongst those presented in this thesis for several reasons. Due to the fact that the waveguides must out of necessity extend in their full dimensions to the edge of the substrate, the two-step fabrication process of 2PP and nanoimprint lithography is used. Due to the combination of optical and DLSPW waveguide in a single structure, which

involves a change of dimensions from $2\ \mu\text{m} \times 2\ \mu\text{m}$ to $500\ \text{nm} \times 500\ \text{nm}$ cross-section, 2PP is also the only technology which can fabricate such a structure efficiently.

The most difficult and demanding process in the fabrication of these structures is the nanoimprint lithography step including the exact alignment of the structures with the pre-fabricated gold stripe. To ensure that the optical waveguides really extend to the end of the sample, it is necessary to fabricate the master structures a little longer than necessary. After imprinting, the waveguides extend beyond the edge of the sample into free space. Figure 6.55 shows some images which demonstrate this effect. To the author's knowledge, this is the first demonstration of substrateless nanoimprint lithography.

As one can see from image a) of figure 6.55, the waveguides are not a purely accidental result. The waveguides extend into free space for more than $100\ \mu\text{m}$, even though, admittedly, the quality decreases in the last quarter. The explanation for this result is, of course, the capillary force between the photoresist and the waveguide mold, which is sufficient to draw the photoresist out so far from the glass substrate.

Several methods to cut the waveguides at the sample edge were investigated. The primary concern in this area is to leave the waveguide face as flat as possible and as close as possible to the edge of the glass substrate. Everything else is only of secondary importance.

Initially, it was suggested that a simple cut of the glass substrate with diamond tools or cut-induced breakage would be sufficient to achieve the desired result. However, practical trials invariably showed that this process was too destructive to be considered. If the cut took place on the side with the waveguides, the waveguides would be utterly destroyed in sections up to twenty microns long, with no recognizable waveguide faces left. If the cut took place on the other side, the side of the glass, the glass would break smoothly, but the photoresist would tear in a random location up to twenty microns away from the break. In some cases, the residual layer of photoresist proved strong enough to simply peel off along with the waveguides and the entire sample would prove ruined.

This left three methods for cutting the waveguides. These are: ion beam milling, excimer laser cutting and micromechanical cleavage. The results of all three options are depicted in figure 6.56. The first option, ion beam milling, could only be tried with the help of a partner. Trials quickly showed that the polymer was melted and burnt during ion beam milling, causing the photoresist to retreat from the sample edge and the waveguide faces to become merged in a molten wall of resist that formed inwards of the edge.

Excimer laser cutting could be done in-house, but was also not successful. Due to the difference in dimensional scale between the DLSPPW structures and the tasks to which the excimer laser was usually accustomed, alignment of beam and sample proved a major difficulty. Even when the beam was aligned correctly, results were not satisfactory. Excimer laser cutting of the resist proved too destructive with sections as large as $10\ \mu\text{m} \times 10\ \mu\text{m}$ of the resist shattering and the waveguide

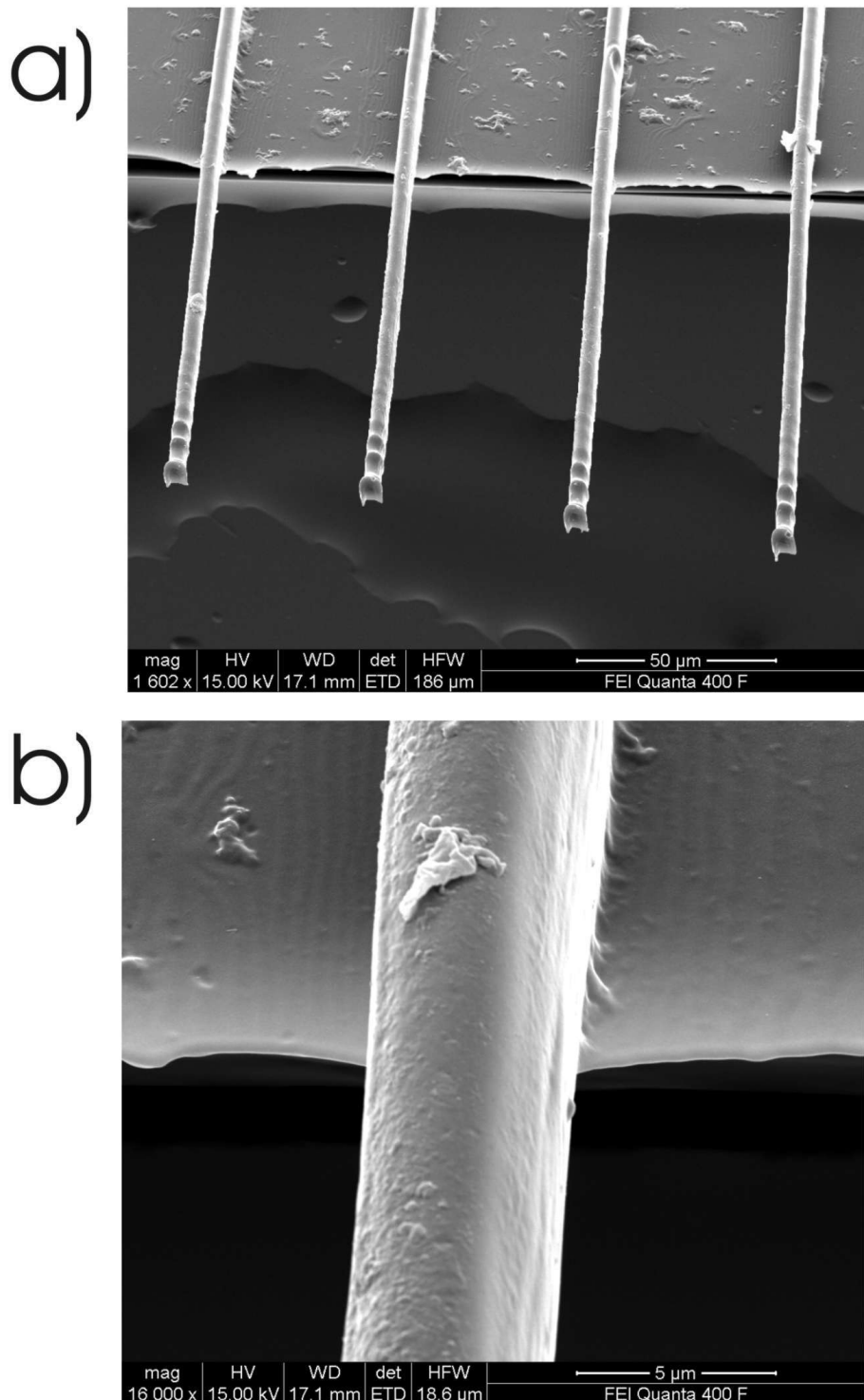


Figure 6.55: Images of nanoimprinted waveguides made from mr-NIL 6000 for fibre-coupled measurements at the edge of the sample before cleavage. Due to the great distance from the DLSPPW section of the structure, only the optical parts of the waveguides are visible. a) An overview of several waveguides. b) The transition area between glass sample and air for a single waveguide.

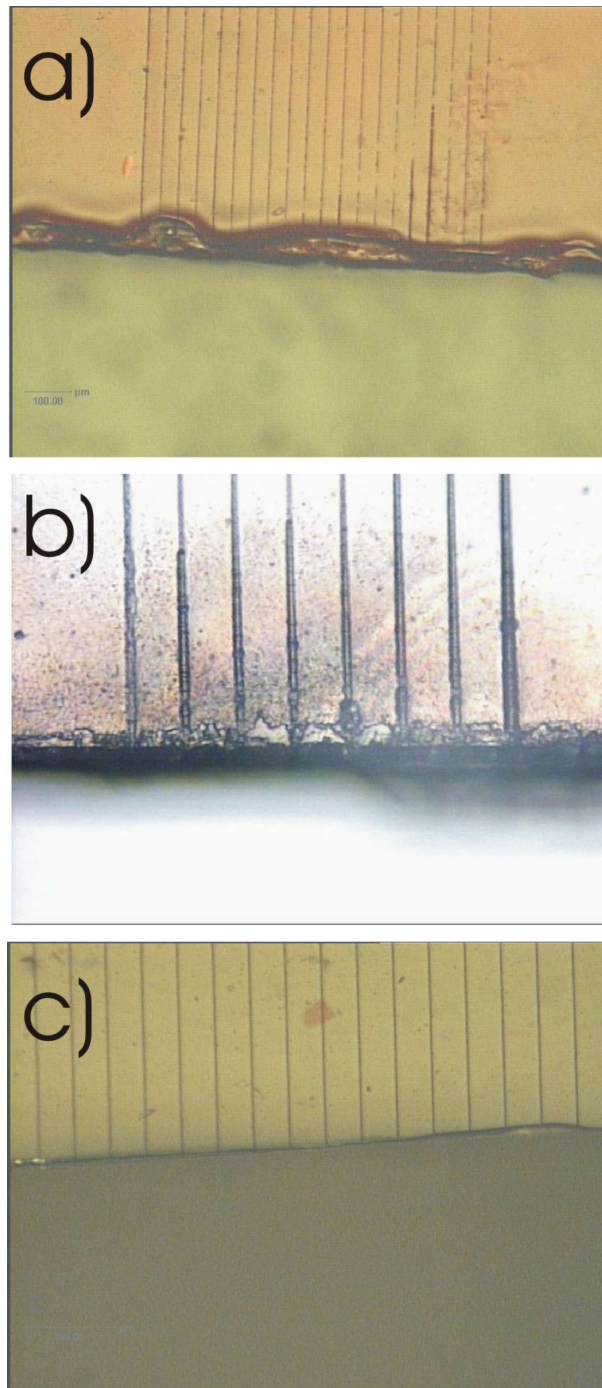


Figure 6.56: Results of cutting the nanoimprinted waveguides made of mr-NIL 6000 at the sample edge. a) Ion beam milling. b) Excimer laser cutting. c) Micromechanical cleavage.

faces also becoming destroyed. In addition, ablated material was scattered onto the sample edge including the waveguides, further degrading the waveguide faces. This material could not be removed by cleaning.

The micromechanical cleavage method used in all samples that were characterized can be understood as an extension of the simple diamond-tool cutting method mentioned above. A very sharp syringe is used to induce a crack in the photoresist that accumulates naturally at the sample edge. By twisting the needle so that the sharp edge faces slightly away from the edge and downwards, and then moving the needle briskly along the sample edge, the crack is propagated along the edge and becomes a clean and straight cut. Minor, very minor, deviations from this cut occur at the point of the waveguides, where the crack must propagate upwards into the waveguide and is not controllable in this period. The deviations, however, are on the order of nanometers instead of micrometers as with the other techniques. An image of a typical cleaved waveguide face is provided in figure 6.57.

The face of the waveguide ends should be as plane as possible, and cut as close as possible to a 90° angle. Unfortunately with current technology, as can be seen in figure 6.57 results are often produced that do not perfectly match the ideal conditions. Typical problems are that the cleavage is not perfectly perpendicular to the waveguide and that minor scratches remain in the waveguide face. These problems could be solved by polishing the waveguide ends, however this is difficult considering that the relatively soft polymer waveguide is located on top of a relatively hard substrate and polishing methods that are currently available would be over-abrasive on the polymer, leading to an unsatisfactory result.

Polishing waveguides was attempted but quickly abandoned. The greatest difficulties in the polishing of the waveguides are the different hardness values for the glass substrate and the polymer waveguides. Since the polymer is softer, it would inevitably be removed faster than the glass, giving no usable result. Consequently, in order to be polished with any chance of success, the waveguides should be sandwiched between two hard substances. No suitable configuration for this can be found, however. In any case, it was discovered that the micromechanical cleavage process produces waveguide faces that are suitably flat for experiments.

A critical section of the fibre-coupled waveguide structure is the transition between the optical waveguide and the DLSPPW section. Here the waveguide narrows from $2\ \mu\text{m} \times 2\ \mu\text{m}$ to $500\ \text{nm} \times 500\ \text{nm}$, and in the case of some test structures the optical waveguides were even larger at $5\ \mu\text{m} \times 5\ \mu\text{m}$. The design calls for a 3D taper structure. The taper structure must be of especially high quality because here the light is confined into smaller dimensions and irregularities in the surface will cause strong scattering.

Unfortunately, the only viable fabricating process involved splitting the tapers into layers and structuring them layer by layer, so a step structure in the funnels is inevitable. Nevertheless, as the SEM images in figure 6.53 show, a very high quality of 3D funnel is achievable.

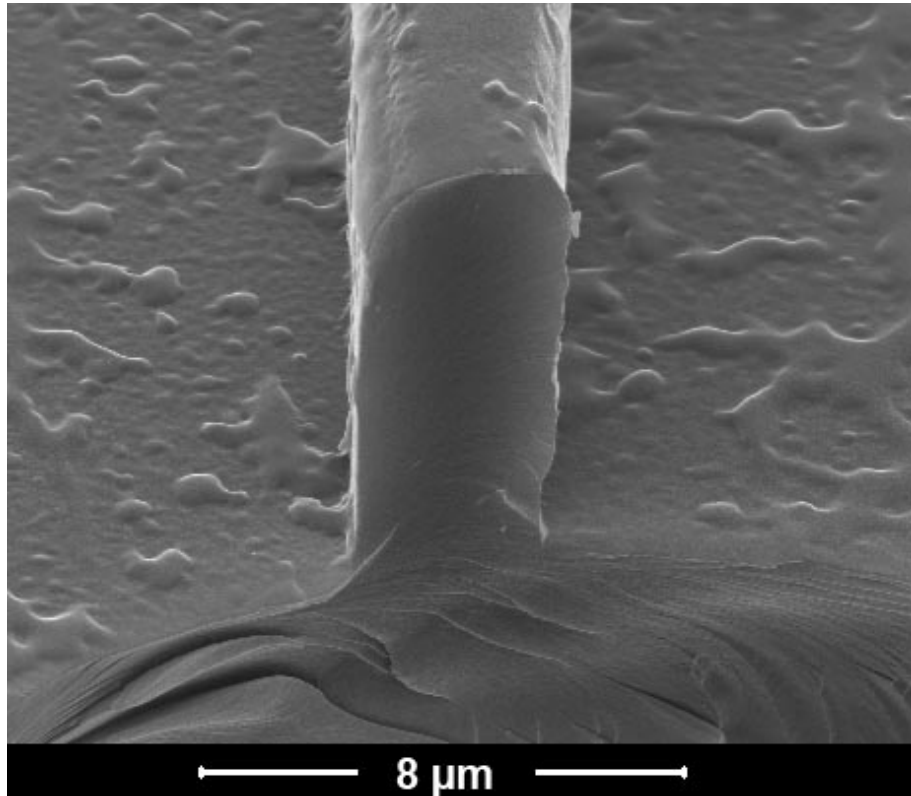


Figure 6.57: SEM image showing the cleaved end of a nanoimprinted optical waveguide made from mr-NIL 6000. As can be seen, the cut is quite clean, however it is not perfectly perpendicular to the waveguide nor is it perfectly flat, and in addition there are some minor scratches in the waveguide. All of these features have an impact on the outcoupling of light from the waveguide and all of them can differ from waveguide to waveguide.

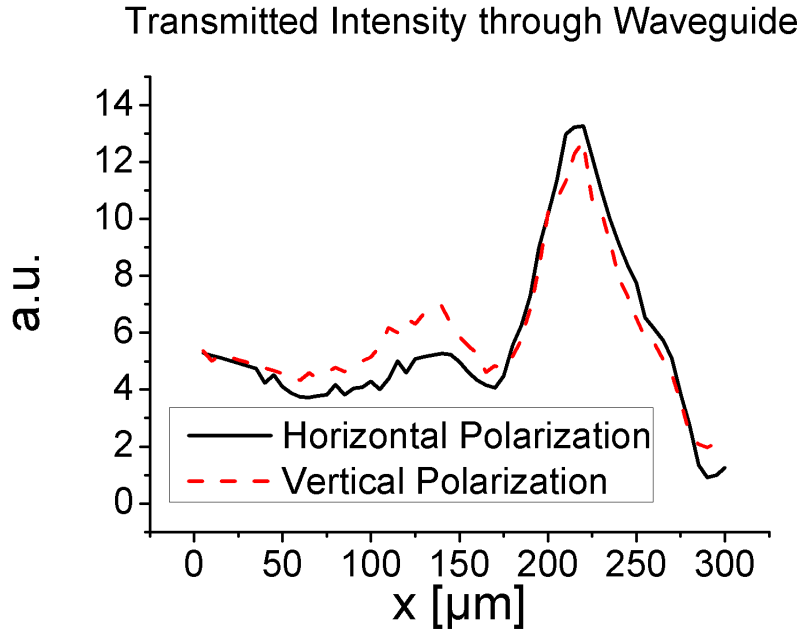


Figure 6.58: Graph showing the measured output intensity dependent on the x-axis position of an imprinted waveguide relative to the in- and outcoupling optical fibres. The strong transmission of 630 nm wavelength light through the 4 mm long $2 \mu\text{m} \times 2 \mu\text{m}$ waveguide is clearly visible.

In addition to the investigations at $1.55 \mu\text{m}$ wavelength, waveguides in this fibre-coupled configuration were also characterized using 630 nm wavelength light from a pigtailed laser diode.

Initially, it was necessary to show transmission through the waveguide in principle. For these measurements, a simple setup with a laser diode and a photodiode was used. The waveguide is aligned to the in- and outcoupling waveguides and then it is shifted perpendicularly to this axis. The measurement data then shows the transmission peak when the fibres and the waveguide are aligned. A graph showing a representative result of such an experiment at 630 nm wavelength with an all-optical waveguide 4 mm long with a $2 \mu\text{m} \times 2 \mu\text{m}$ cross-section is shown in figure 6.58.

Subsequently, following the proof of principle measurements noted above, the photodiode was replaced with a microscope objective and a CCD camera for measurements in the visible spectral range. Results of these measurements are shown in figure 6.59. As can be seen in the images, all of the twelve waveguides on the sample are functional.

The top image of figure 6.59 shows the camera image obtained when the waveguides are not aligned with the incoupling fibre. The red semicircle is an image of the scattered 630 nm light from the incoupling fibre, which is emitted by the fibre without collimation. The interference pattern is due to reflections off the substrate surface and diffraction at the substrate edge. In the lower half of the image, the glass substrate is visible. The camera is focused on the outcoupling end of the substrate, where the waveguides, when they transmit light, show up as bright white spots.

All twelve waveguides of the sample show strong transmission, which shows that the fabrication of these waveguide structures is reliable. Interestingly, there is also no radiation visible from the substrate, which indicates that very little radiation is lost to the substrate and that the index contrast between waveguide and substrate is high enough for low-loss waveguiding. The inhomogeneities visible in the substrate are illuminated by ambient light in the laboratory and represent the inaccuracies of the cut glass samples, which do not interfere with the waveguides above.

The samples with a DLSPPW section in the middle are characterized by exciting plasmons in an end-fire configuration using a laser diode at $1.55\ \mu\text{m}$ wavelength. A schematic of the experimental setup is shown in the previous chapter. Here we show a computer rendering of the experiment in figure 6.60. The in- and outcoupling fibres can be clearly seen as they couple to the waveguides. The waveguide taper and the DLSPPW section above the gold layer are also visible.

We present results of both qualitative and quantitative measurements. Two alternatives exist for analyzing and viewing the outcoupled light in our setup. The first possibility is to use a microscope objective and near infra-red camera to image the far end of the sample. This is convenient for adjusting the incoupling efficiency and monitoring the experiment and is used for qualitative measurements. The second possibility is to couple the light back into a fibre to a spectrum analyzer. This is used for quantitative measurements.

Figure 6.61 shows camera images gained from the first method with a laser operating at $1.55\ \mu\text{m}$ wavelength. The camera uses an automatic gain adjustment so the images are not comparable in a quantitative way. Transmitted light through the waveguide is shown. Since the DLSPPW section of the waveguide is too small to allow an optical mode, light must be converted into a plasmon and then converted back to an optical mode for detection. A strong polarization dependency is expected. At this point we will set the reference point for the polarization of the input light with 0° coincidental with TM polarization, i.e. the electrical field is perpendicular to the sample surface and is suitable for exciting SPP modes. The results show this - figure 6.61 (a) shows the transmission at 0° polarization. Here, maximum intensity is expected and observed. Figure 6.61 (b) shows the waveguide at 45° polarization and (c) finally at 90° . As can clearly be seen, the intensity of transmitted light drops drastically as polarization is turned and the plasmonic mode cannot be excited. The light visible in the images not originating from the waveguide facet is due to light scattered at the coupling point of plasmonic to optical waveguide, which is scattered by irregularities on the sample edge.

Further observations confirm this. Figure 6.62 shows the samples from a top-down view using the near infra-red camera, focused on the DLSPPW section of the waveguide, i.e. the plasmonic part. The gold stripe is visible in the images as a bright band. Light is incoupled from the left in the images. The two bright spots originate from scattering at the tapers where the waveguide changes from purely optical to plasmonic and back. The input light polarization is changed from 0° (a)

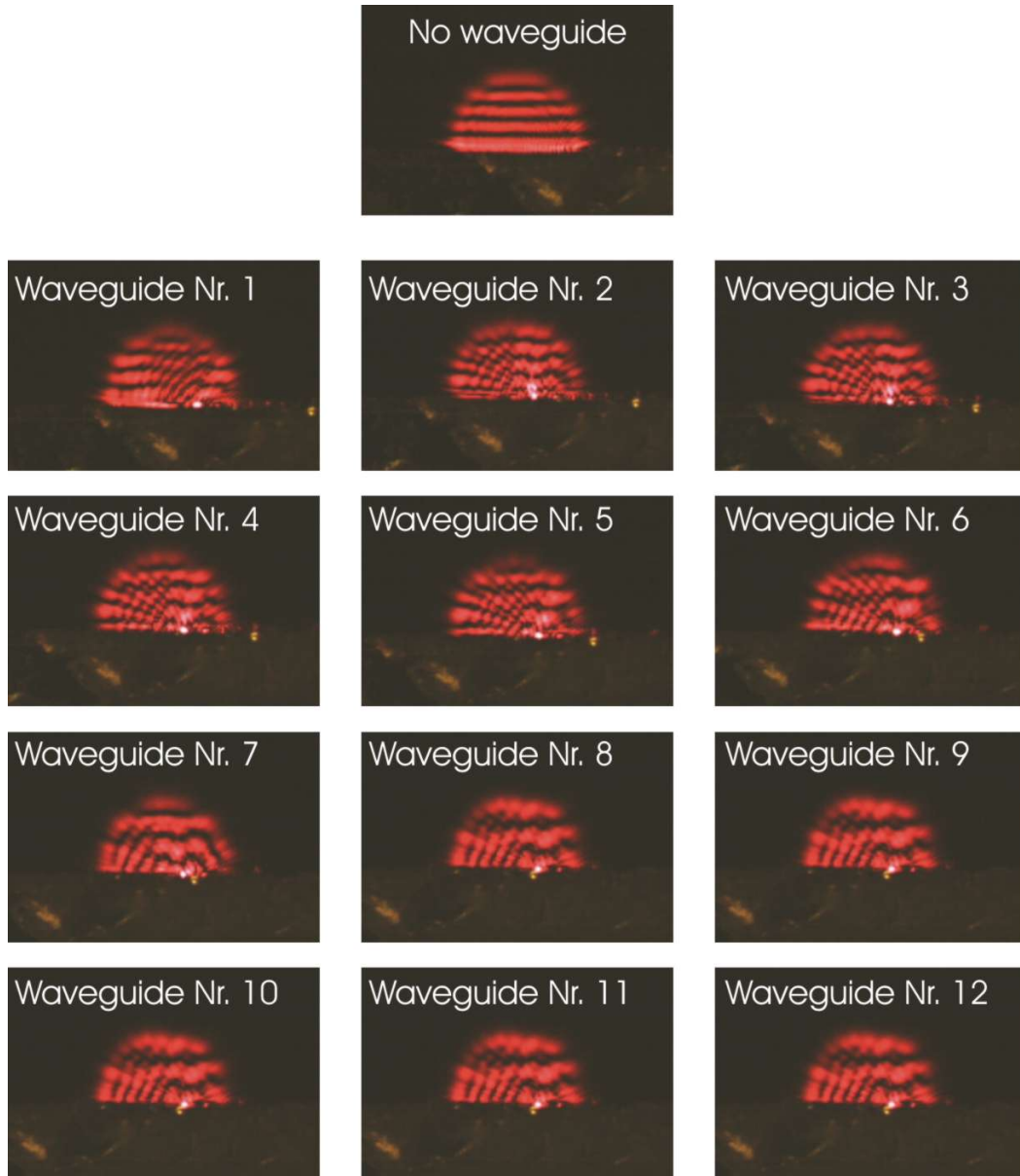


Figure 6.59: Images of transmission of 630 nm diode laser through DLSPW waveguides. The top image shows a reference image with no waveguide. The white spot visible in each of the other images is the transmission spot through the waveguide itself, which saturates the camera locally and appears white.

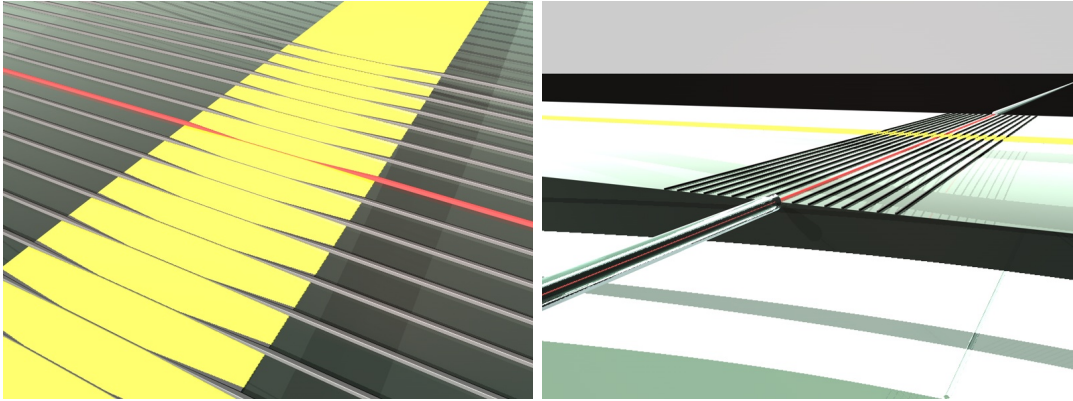


Figure 6.60: An artistic impression of the fibres attached to the waveguide and the gold stripe with the plasmonic waveguides.



Figure 6.61: Images from the near infra-red camera show the output of the DLSPW waveguides at different polarizations of input light (at $1.55 \mu\text{m}$ wavelength). (a) 0° Polarization (b) 45° Polarization (c) 90° Polarization. As can be seen, output intensity decreases drastically with polarization.

through 45° (b) to 90° (c). Figure 6.62 (d) shows an optical microscope image of the structure for comparison and (e) shows the transition region from optical to plasmonic waveguide in detail. We observe that the incoupling spot remains bright at all polarizations, while the outcoupling spot rapidly decreases in intensity. This is due to the plasmonic mode not being excited at 90° polarization, and transmission thus suppressed. As before, the camera uses automatic gain adjust, which accounts for inconsistencies in overall brightness.

The spectrum of the transmitted mode was measured and is shown in figure 6.63 (a). This provides an easy means to quantify the intensity of the output mode. Quantitative measurements of the transmission changes with the polarization of the input light were performed. Results are shown in figure 6.63 (b). As can be seen, the graph follows a cosine pattern, which is in line with expectations.

Measurements show average transmission losses of 49 ± 2 dB. Propagation losses in the DLSPPW section, which is 100 micrometers long, can be calculated and amount to 8 dB, a figure which is backed up by early experiments (above and [184]). The remainder of the losses can be attributed to several causes. One cause is the loss at the insertion point between the optical fibre and the optical waveguide due to scattering from the waveguide end face. The waveguide end faces are not perfectly flat or perfectly perpendicular to the waveguide and this causes a large amount of scattering. A further source of loss lies in the optical waveguides themselves due to scattering and waveguide imperfections. And finally there are losses at the coupling between optical and DLSPPW mode.

To quantify the coupling efficiency from optical to plasmonic mode and back, reference measurements were undertaken with all-optical waveguides under the same conditions. The optical waveguides use the same substrate as before but without gold. The waveguides are 4 mm long and have a $2 \times 2 \mu\text{m}$ rectangular cross-section, identical to the optical in- and out-coupling waveguides on the plasmonic samples. Measurements showed that the insertion and optical guiding losses amount to $37.5 \text{ dB} \pm 0.7 \text{ dB}$ on average. This is a relatively high loss for an optical waveguide, which can be explained by several things. One source of losses is the surface roughness along the length of the waveguide. The surface of the waveguide is not perfectly smooth due to fabrication irregularities, as can be seen in the images in figures 6.52 (c) and 6.62 (d). Another source of losses is the low reproducibility in quality of the cleaved ends of the waveguides, already mentioned briefly above. An additional source of loss is the coupling from optical fibre to waveguide and back again. Currently this is achieved only by careful alignment through a very narrow air gap, and clearly an amount of light is lost in this way. Experiments could be made in the future with index-matching oil to provide a link between optical fibre and waveguide.

If we take this data together, the calculated 8 dB loss for the DLSPPW mode, and the 37.5 ± 0.7 dB loss for the transmission through the optical waveguides and the coupling to the fibre, and combine this with the experimental results for the DLSPPW waveguides, we can estimate the coupling losses between optical waveguide and DLSPPW waveguide and back again to lie at 3.5 ± 2 dB.

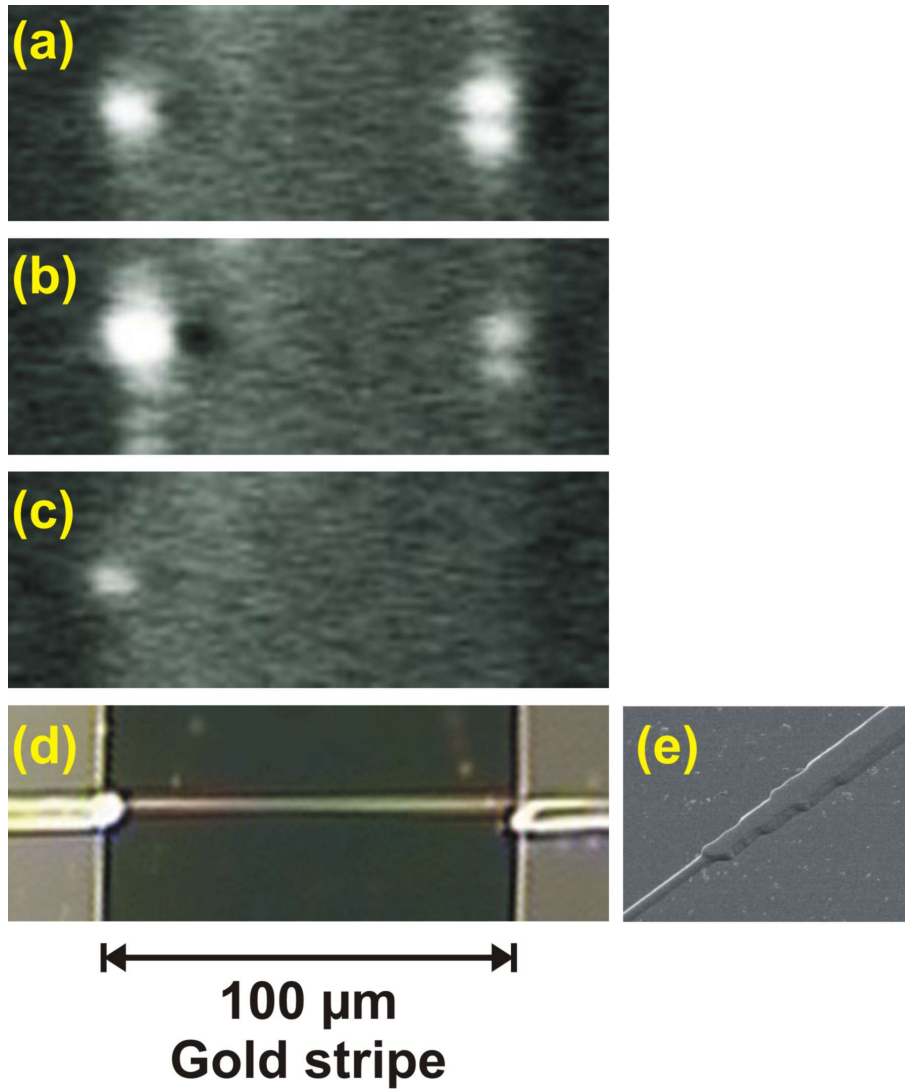


Figure 6.62: Images from the near infra-red camera showing a top-down view of the sample centred on the DLSPPW part of the waveguide. Left side is the incoupling, right side is the outcoupling. Input light at $1.55 \mu\text{m}$ wavelength has (a) 0° polarization, (b) 45° polarization, (c) 90° polarization. While the incoupling spot stays bright, the outcoupling spot rapidly decreases in intensity, showing that the plasmonic mode is suppressed with changing polarization. (d) Optical microscope image of waveguide showing gold stripe and DLSPPW section shown for comparison. (e) SEM image (same scale as optical images) showing the transition from plasmonic to optical waveguide at an angle of 45° .

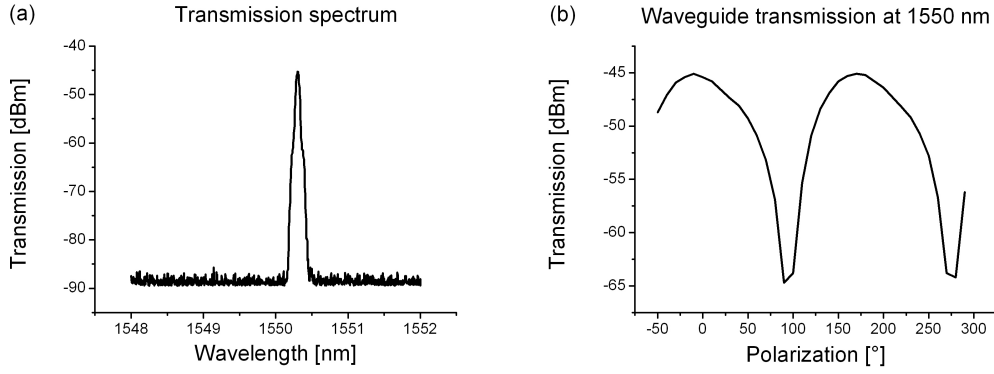


Figure 6.63: (a) The spectrum of the transmitted mode.(b) Graph showing the dependency of transmission through the waveguide on the polarization of the input light - a characteristic of the DLSPPW mode.

We have shown excitation of DLSPPW modes in end-fire coupling configuration in fibre-coupled waveguides. The transmitted intensity was compared to reference measurements on all-optical waveguides and this resulted in a range for the coupling loss from optical to plasmonic mode in our structures. There are several points which could be improved to increase the overall quality of these waveguides. One part is certainly the coupling between optical fibre and optical waveguide. Here future research will focus on finding ways to guarantee a flat waveguide end, possibly by polishing, and on ways to reduce scattering by using index-matching oil or similar materials to connect fibre and waveguide. Another area of focus for future research on this topic is the design of the optical waveguide to DLSPPW section tapers. Currently the shape and form of the tapers still leaves room for optimization and research in this area has already begun.

7 Localized Surface Plasmon Experiments

This section concerns experiments made with surface plasmon polaritons (SPPs) outside of a waveguide, that is freely propagating on a metal surface, or inside a waveguide but interacting with other structures. The interference of SPPs on a metal surface is discussed, as well as the interaction of an SPP with a gold nanoparticle. The effect of gold nanoparticles in close proximity to a DLSPPW structure is discussed and its potential as a coupling tool. Finally, the possibility of using surface plasmons to model astrophysical phenomena is examined in the context of "plasmonic black holes".

7.1 Interference of SPPs

Self-interference of an SPP has already been shown in conjunction with a Bragg reflector [233], and complex plasmonic interferometry has been proposed for a plasmonic demultiplexer [284]. The study of SPP-SPP interference that will be shown here, however, is something entirely new. The results shown here still represent only a preliminary result, the preparatory stage of future experiments on nonlinear SPP-SPP interactions.

The interference of two SPPs, in which the electron-electron interactions in the interference zone play a certain part, has great potential as a field for the study of nonlinear plasmonic phenomena. For example, it has been proposed to create a plasmonic switch based on ultrafast nonlinear plasmonics using precisely this mechanism [285].

The plasmon-plasmon interference is observed in this work by using the standard leakage radiation microscope (LRM) setup as outlined in the chapter above. However, the setup is modified by the addition of a Michelson interferometer immediately in front of the excitation microscope objectives. The interferometer is deliberately misaligned to produce two separate excitation beams that can be individually aligned to separate focal positions on the plasmonic sample. By this method, two separate excitation spots can be generated, and consequently, two separate SPP beams. The setup is shown schematically in figure 7.64.

The ideal structure for SPP interference with two beams is a structure that is "L"- or "V"-shaped. A set of appropriate structures was designed and then fabricated by 2PP. SEM images of the structures are shown in figure 7.65. The angle between the two arms of the structure is varied from 90 degrees to 30 degrees. When two SPP beams are generated on the arms, they will propagate from them at 90 degrees incidence. This means that, using these structures, interference angles between 90 degrees and 150 degrees are possible.

The interference of two SPP beams was simulated using the Green's Function Method (GFM). Some results of these simulations are shown in figure 7.66. In these simulations, which were performed for the wavelength $\lambda = 850$, the beam waist of one Gaussian SPP beam was varied, while the other was kept constant, for an angle of 90 degrees. The effect on the interference pattern is an increase in the

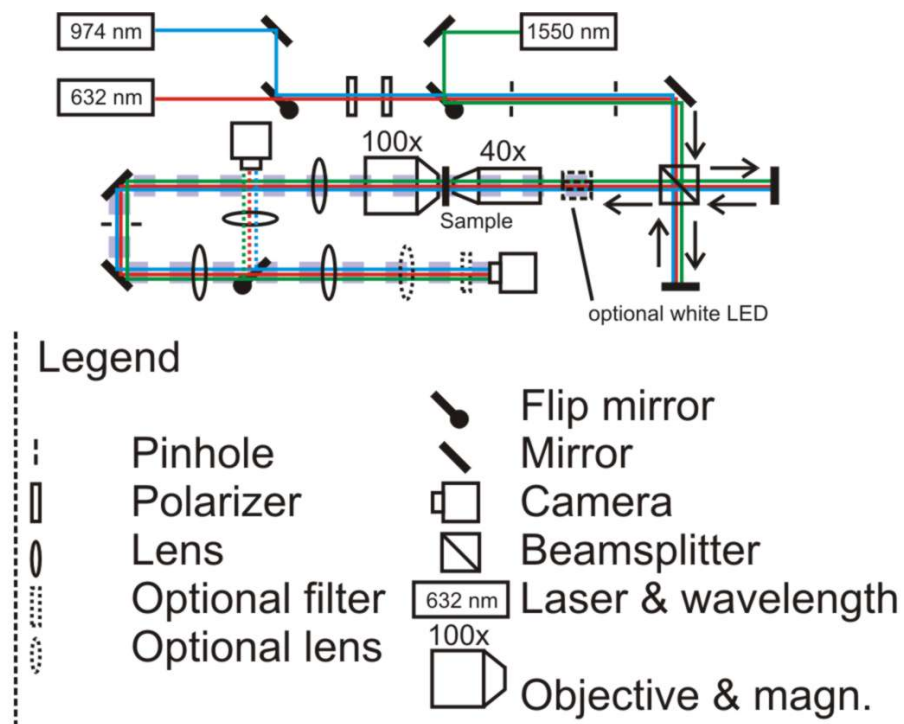


Figure 7.64: Schematic drawing of the leakage radiation microscope setup used for the experiments with two separate SPP beams. The major addition/modification compared to the setup shown previously is the Mach-Zehnder interferometer just before the first microscope objective.

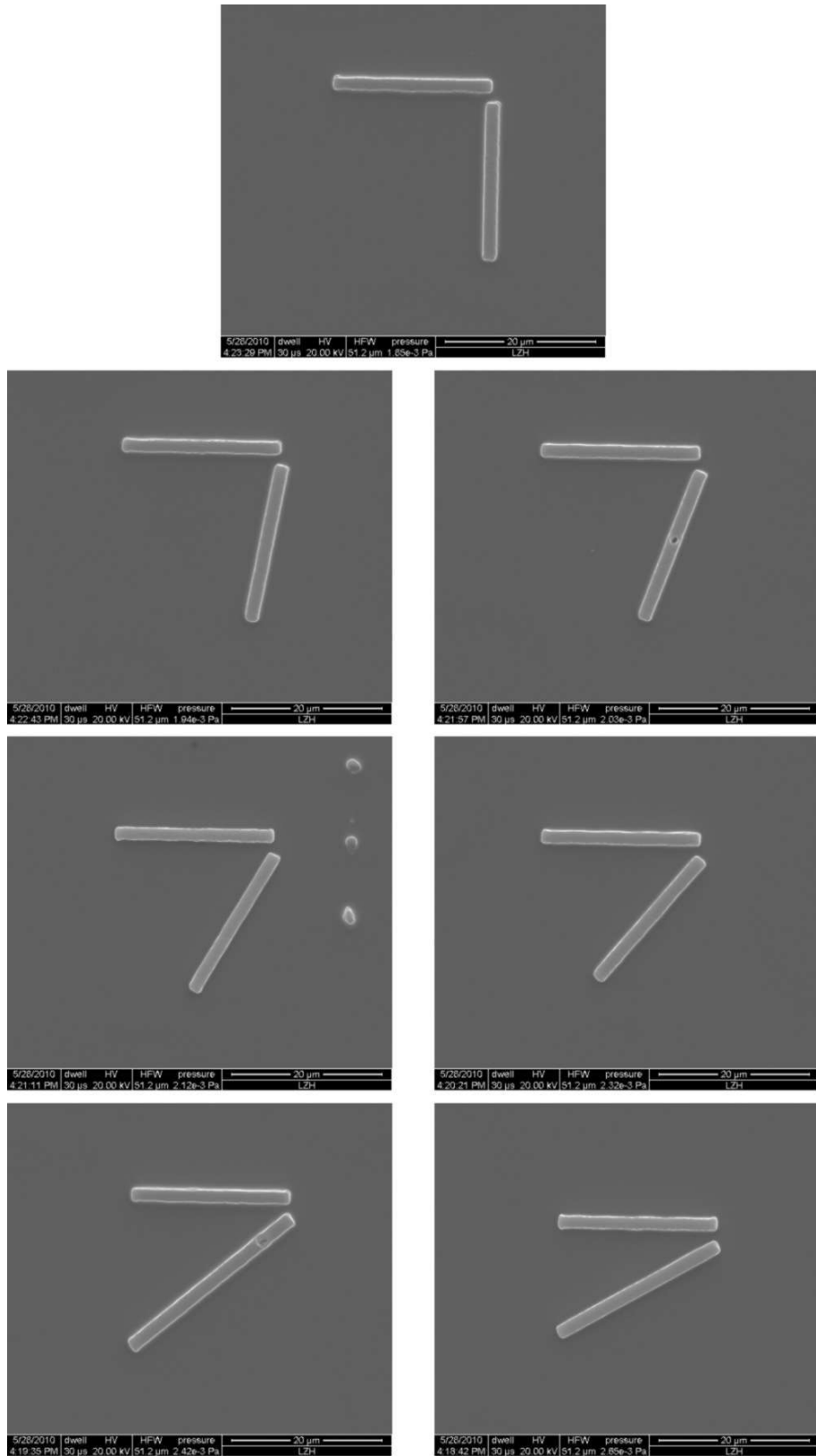


Figure 7.65: Seven SEM images showing the angled line structures used in the plasmonic interference experiments. The angle between the lines changes from 90 degrees in the top image in steps of 10 degrees to 30 degrees.

contrast between the minima and maxima of the interference zone with increasing beam waist. The interference of two equal SPP beams at 45 degrees angle was also simulated.

Experimental results are shown for the characterization of SPP-SPP interference at different crossing angles in figure 7.67. The angle of interference changes from 90 degrees to 150 degrees, while the beam waist of the SPP beam remains constant. The characterization wavelength is the He-Ne laser wavelength of 632.8 nm. For an angle larger than 120 degrees, the interference pattern becomes weakly imaged, which is to be expected when the comparatively low resolution of the LRM setup is taken into account. However, the results nevertheless are in strong accordance with the numerical simulations obtained by the GFM.

The effects of varying the SPP beam waist are also studied, and are shown in the LRM images in figure 7.68. The characterization wavelength is again the He-Ne laser wavelength of 632.8 nm. Only the 90 degrees angle is used in these measurements, due to the higher resolution obtainable at this angle. The beam waist was adjusted by altering the position of the focus of the excitation beams with respect to the sample surface. The interference pattern becomes more clearly pronounced with increasing beam waist size, which is due largely to the resolution of the CCD camera in the LRM setup. The experimentally measured images of SPP-SPP interference strongly match the numerical simulations.

In the future, SPPs will be generated on these - or advanced evolutions of these - structures by ultrashort laser pulses, in order to study nonlinear optical effects caused by the electron-electron interaction. Careful tuning of laser intensity will be necessary to maximize intensity and at the same time avoid ablation of the sample material. The advantage of LRM with its inherent capability to perform optical Fourier transformation will enable angle-resolved observation of additional optical signals generated by nonlinear processes in the interference zone.

These experiments may ultimately culminate in an ultrafast plasmonic switching element, producing a signal through nonlinear processes inside the interference zone and controllable by either one of the two SPP beams. The potential speed of such a switching element should not be underestimated. If we consider a pulse with a duration of 200 fs, this leads to a switching frequency of 5 THz.

Another approach is to equip the Michelson interferometer in the LRM setup with a delay line, which would allow the imaging of ultrafast nonlinear plasmonic processes in real time by adjusting the delay between the two pulses.

7.2 Interaction of SPPs with Gold Nanoparticles

The interaction of surface plasmon-polaritons (SPPs) with gold nanoparticles is a relatively new field of research, even inside the context of plasmonics in general. It is well-established that the characteristics of nanoparticles that govern their interaction with SPPs are their size, shape and material composition as well as their physical environment [223, 286]. A large amount of interest initially focused on the guiding of plasmons using chains of metal nanoparticles [287, 288], and this is still

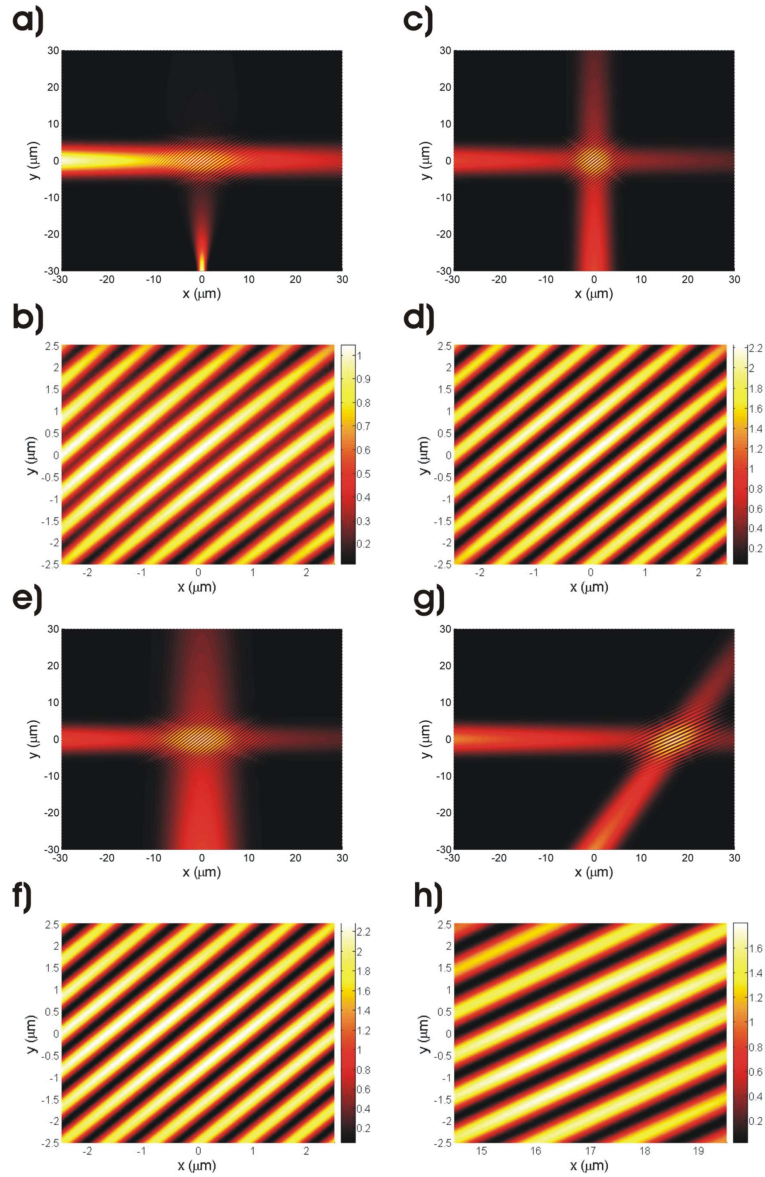


Figure 7.66: Simulations using the Green's Function Method and performed by A. B. Evlyukhin. The plasmon excitation wavelength is $\lambda = 850$ nm and the beam waist of the horizontal beam is $w_{SPP1} = 5 \mu\text{m}$ for all cases. a) SPP interference at 90 degrees angle, the second SPP beam has a beam waist of $w_{SPP2} = 1 \mu\text{m}$. b) The central section of the interference area in larger magnification. c) SPP interference at 90 degrees angle, the second SPP beam has a beam waist of $w_{SPP2} = 5 \mu\text{m}$, equal to w_{SPP1} . d) The central section of the interference area in larger magnification. e) SPP interference at 90 degrees angle, the second SPP beam has a beam waist of $w_{SPP2} = 10 \mu\text{m}$. f) The central section of the interference area in larger magnification. g) SPP interference at 45 degrees angle, the second SPP beam has a beam waist of $w_{SPP2} = 5 \mu\text{m}$, equal to w_{SPP1} . h) The central section of the interference area in larger magnification.

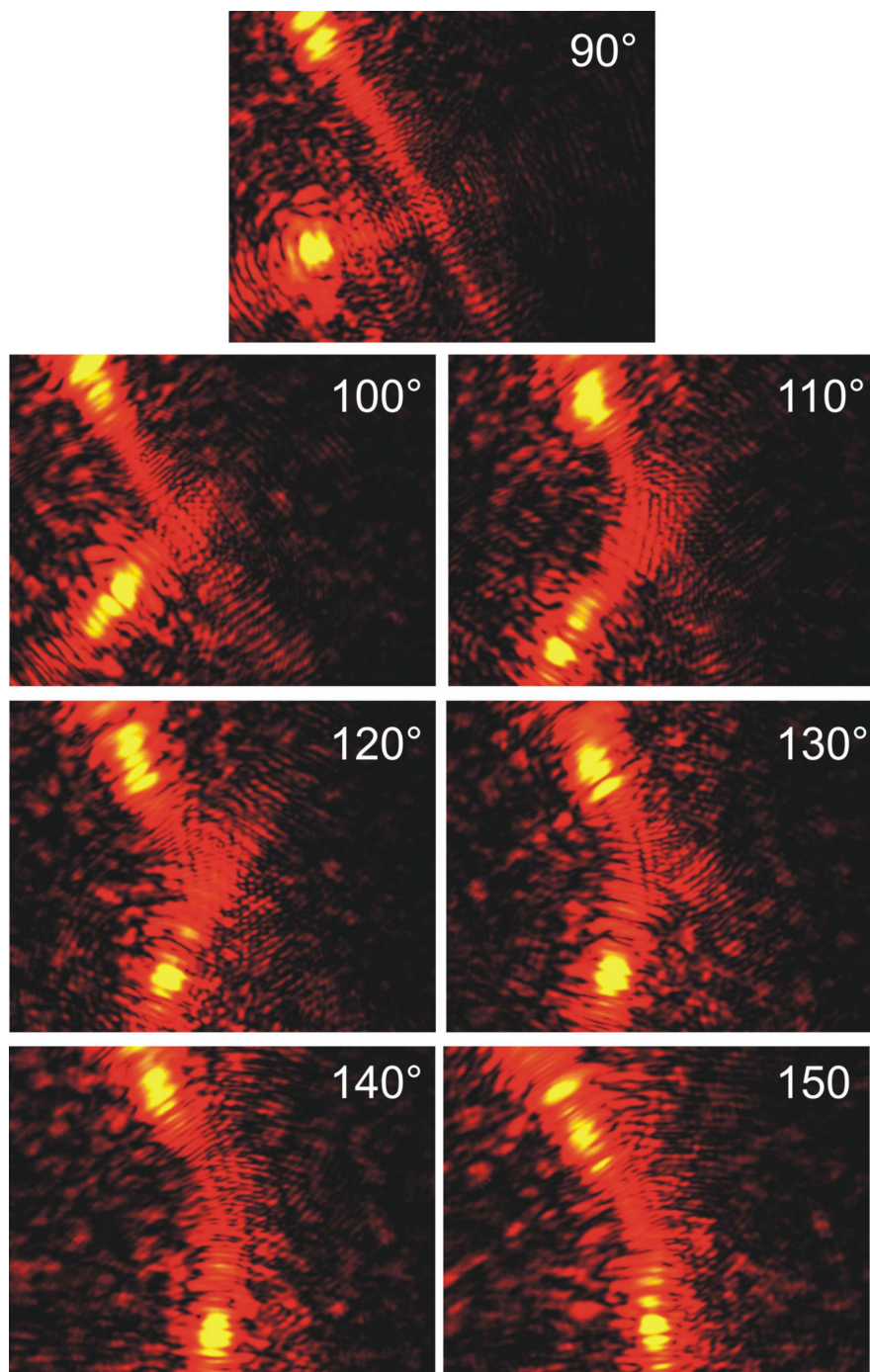


Figure 7.67: LRM images of two SPPs interfering at angles from 90 degrees to 150 degrees. The excitation laser wavelength is 632.8 nm. The SPP beam width remains constant.

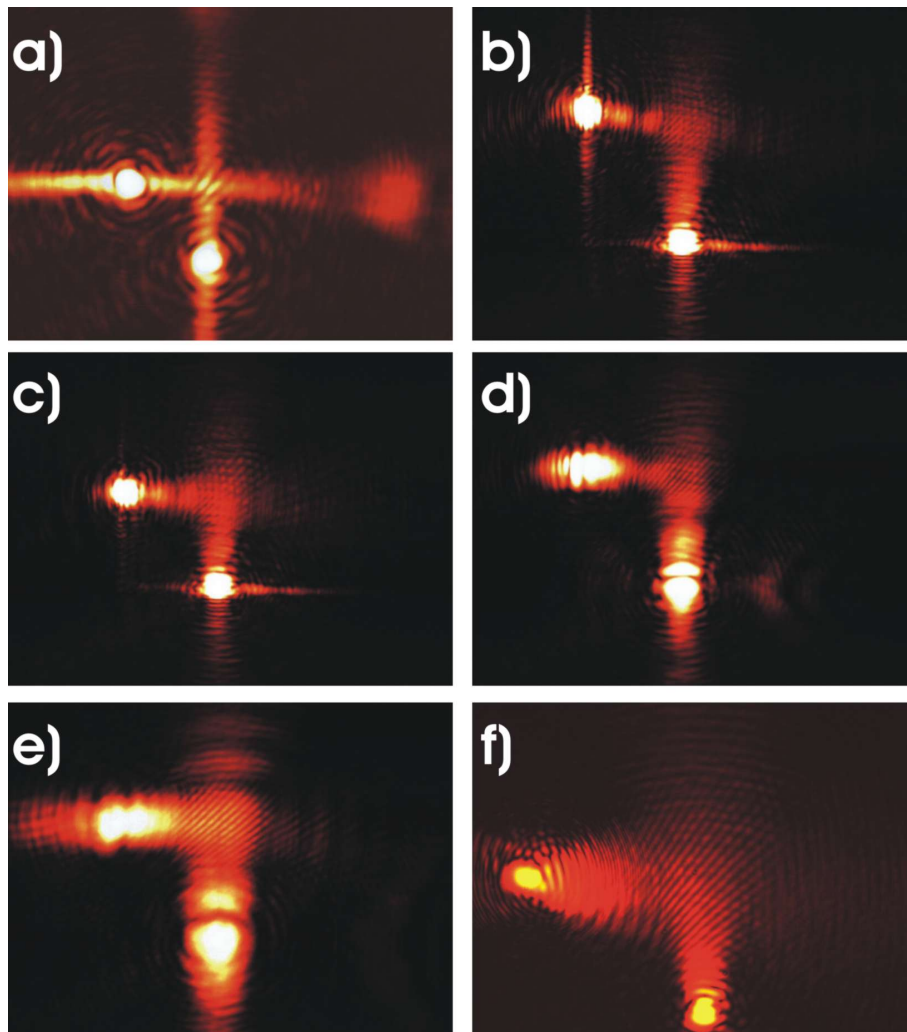


Figure 7.68: LRM images of two plasmons crossing each other at 90 degrees, with varying SPP widths, increasing from a) to f). The excitation laser wavelength is 632.8 nm.

an active field today [144, 289, 290]. It was then found that nanoparticle chains have other uses than mere guiding, and metal nanoparticles have been used to form a variety of plasmonic and nano-optical components such as nanolenses [291, 292], reflectors, refractors, and splitters [293, 294, 295, 296, 297]. Going even further, some suggestions have been made to use nanoparticles as the crucial element of a so-called "spaser", surface plasmon amplification by stimulated emission of radiation [298, 299]. The characterization of metal nanoparticles and their interaction with SPPs must therefore be considered a very important and very recent field of research.

The method chosen to fabricate and position the gold nanoparticles as investigated in this thesis is laser-induced forward transfer (LIT or LIFT) [216, 300, 301]. In this method, a femtosecond laser is focused onto a thin film of gold. The energy of the laser pulse is enough to locally melt the gold and give a droplet of molten gold enough momentum to leave the surface. A receiving substrate can be very accurately positioned so that the droplet lands exactly in its intended location. The LIFT method is very accurate and produces almost spherical gold droplets, which can be positioned to within a few micrometers accuracy, and has advantages over mask-based methods to fabricate gold nanoparticle arrays [302]. All the particles presented in this thesis were fabricated by Arseniy Kuznetsov using LIFT.

In order to obtain good interaction between gold nanoparticles and SPPs, it is necessary to choose a structure geometry that facilitates SPP excitation exactly in the direction of an already existent nanoparticle. Polymer lines and metallic nanoparticles must be brought into close proximity. Since the lines and the particles require different fabrication methods, and fabrication of the whole sample is at least a two-step process, two possibilities for fabrication present themselves, depending on which step is done first.

In principle, both fabrication sequences are feasible, but due to the low adhesion between the substrate and the nanoparticles and the necessity of developing the sample after 2PP structuring, the procedure 2PP first, LIFT second became the preferred practice. Polymer structures were fabricated by 2PP on a gold layer and then LIFT fabrication of gold nanoparticles was performed on these samples.

In many of the experiments, a plasmonic focus structure was used. It has already been shown that an appropriately shaped structure can be used to focus SPPs [253, 303, 304]. Auxiliary polymer lines were added to the focus structure in the shape of 'crosshairs' to aid in the deposition of the gold nanoparticle during the LIFT process. Examples of fabricated structures are shown in figure 7.69. The images include an indication of the expected location of the SPP used in experiments as well as the direction of propagation and the intended location of the focal point.

The structures are investigated using leakage radiation microscopy. Both the He-Ne wavelength of 632.8 nm and the telecommunications wavelength of 1550 nm were used. The scattering effect of a gold nanoparticle can be observed in the images shown in figure 7.70. Both the straight line and focus structures are shown with and without nanoparticle, and the effect of SPP scattering is evident. The SPP

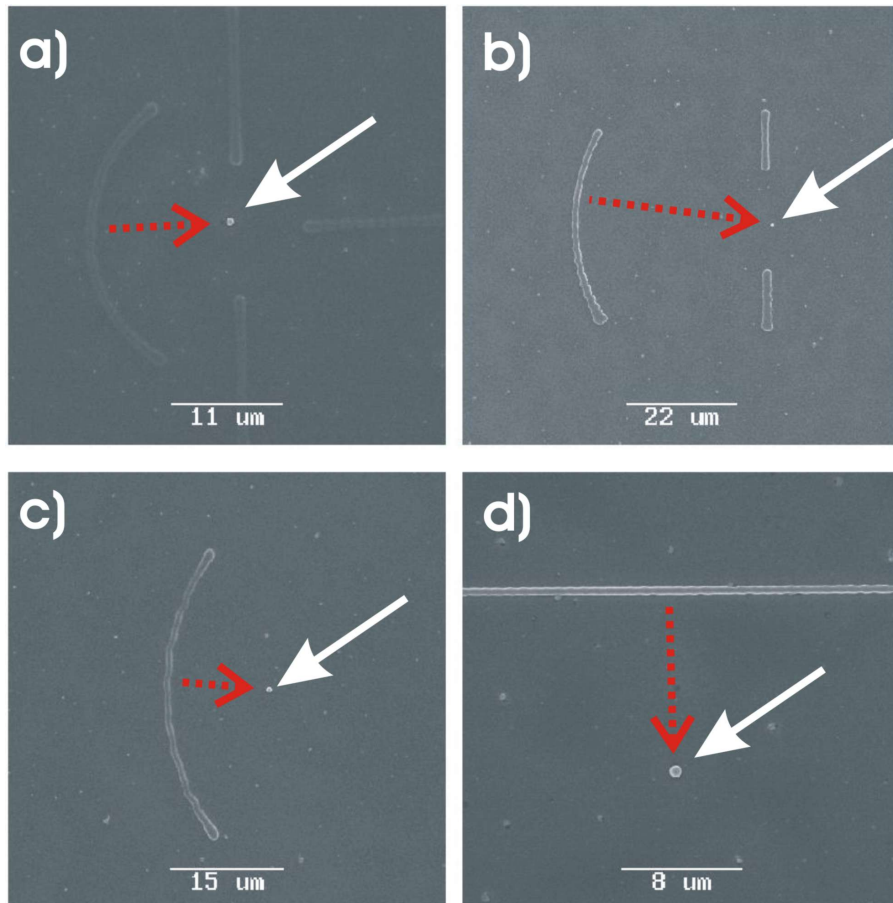


Figure 7.69: SEM images of the combined structures with polymer lines and gold nanoparticles. The white solid arrow indicates the position of the nanoparticle and the red dotted line indicates the propagation path of the SPP to investigate the particle, which is used in the experiment. a) A curved plasmonic focus structure with three 'crosshairs' to aid accurate particle deposition. b) A curved plasmonic focus structure with only two navigation lines in place. c) A curved plasmonic focus structure without navigation aids. d) A straight line structure with the particle placed adjacent to it.

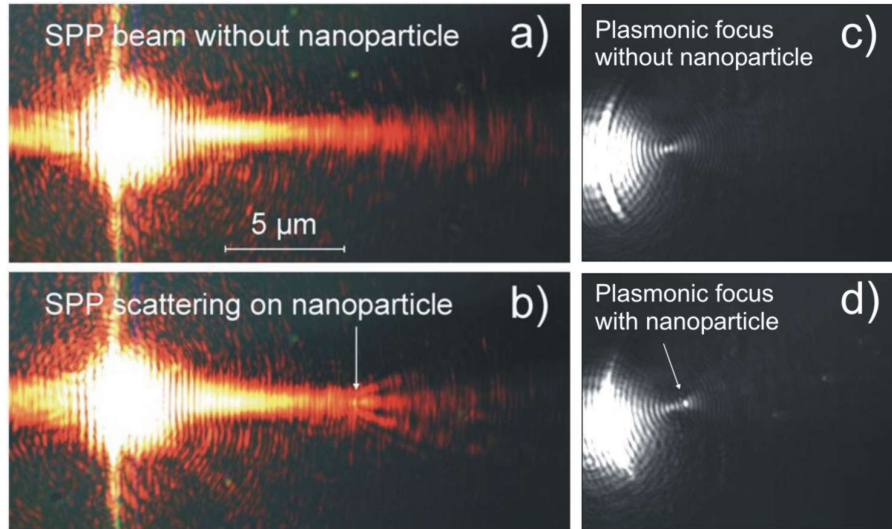


Figure 7.70: a) An SPP at the He-Ne-wavelength of 632.8 nm is excited on a straight polymer line. The focus of the excitation beam lies 10 μm below the sample surface, which means that the SPP beam has a focus 10 μm distant from the excitation spot. b) The SPP beam at the He-Ne-wavelength of 632.8 nm is scattered on a gold nanoparticle with 800 nm diameter. c) A focus structure is used to excite a focused SPP at 1550 nm wavelength. d) The focused SPP at 1550 nm wavelength now lies exactly on a spherical gold nanoparticle inside the focus structure and scatters.

was always focused onto the nanoparticle, either by adjusting the focus point of the excitation beam or employing the focus structures.

The experimental results can be used to test the viability of the Green's function numerical modeling method introduced previously in this thesis. In figure 7.71, images (d) to (f) show the normalized SPP intensity just above the gold-air interface for an incident Gaussian SPP beam that scatters on a 200 nm diameter spherical gold nanoparticle. At 200 nm radius, the deviations from the electric dipole approximation are estimated to be low. The images (a) to (c) in the same figure show the experimental results, where 800 nm diameter gold particles are used. The experimental and theoretical results show a strong agreement, although there is a stronger contrast between the minima and the maxima of the intensity distribution in the experimental case. This difference between theory and experiment is due to the difference between the gold nanoparticle sizes used, which leads to an increase of the higher-order multipole contributions in the experimental case.

Another experiment brought together the spherical gold nanoparticles and DL-SPPW structures directly. The potential use of scattering on gold nanoparticles as a mechanism to couple light into a DLSPW structure was investigated. The motivation behind this is that, if the gold particle size is tuned to give a resonance with the excitation wavelength, a far greater coupling efficiency than with the standard method will be obtained, which is important for any application.

After fabrication of DLSPW structures on glass, spherical gold nanoparticles

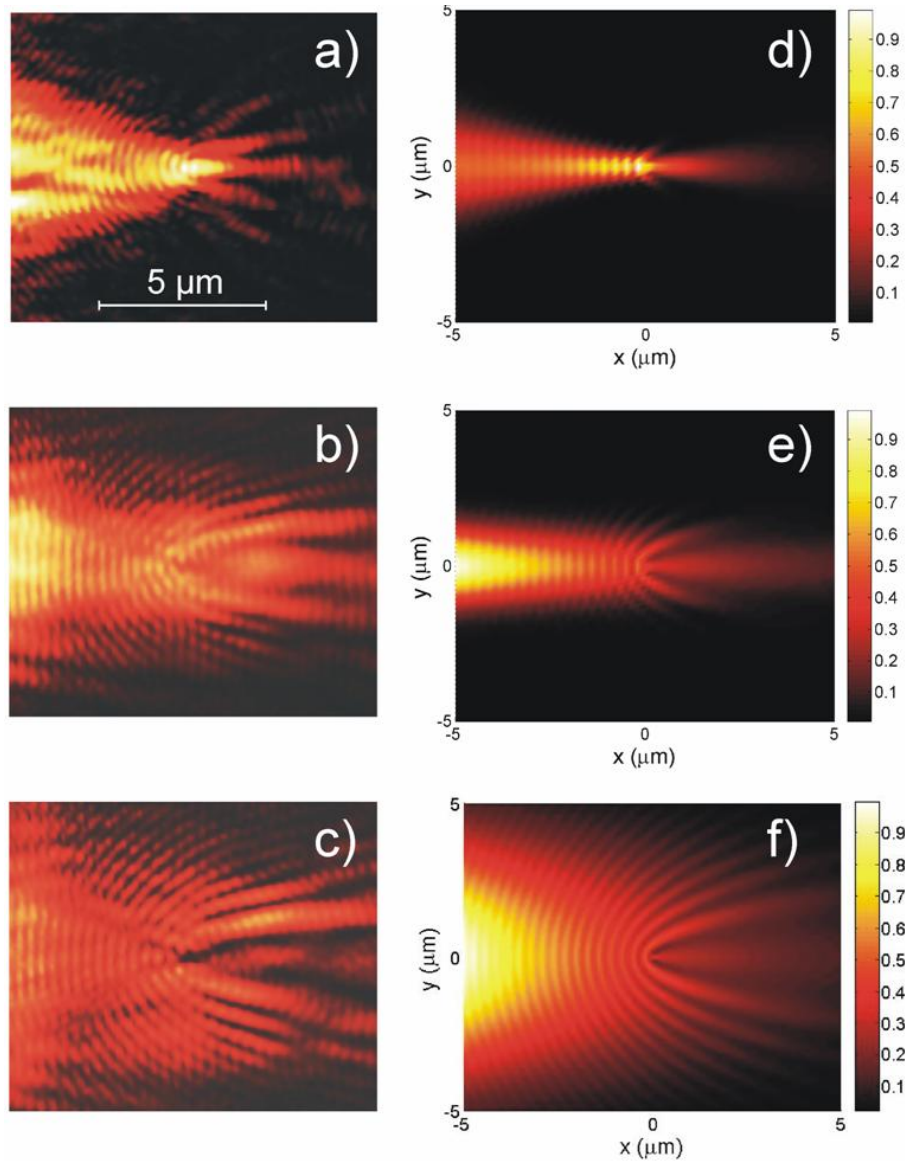


Figure 7.71: (a)-(c) Leakage radiation microscope images showing the interaction of focused SPP beams with a gold nanoparticle of 800 nm diameter. The SPPs are excited by a He–Ne laser with the 632.8 nm wavelength. The waist of the SPP beam is (a) 500 nm, (b) 1500 nm, and (c) 5000 nm. (d–f) Numerical simulations of the same scattering process using the same SPP beam waists respectively, but with a particle diameter of 200 nm. In all images, the gold nanoparticle is located in the image centre.

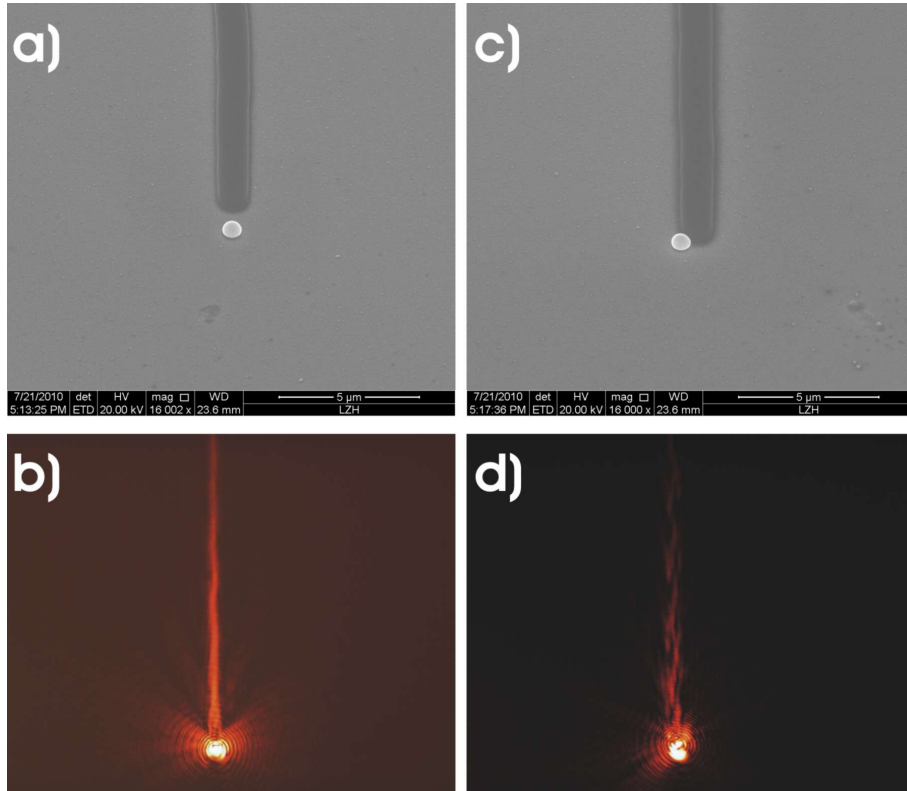


Figure 7.72: SEM and LRM images of spherical gold nanoparticles used to couple light into DLSPW structures. a) SEM image of centrally-located gold nanoparticle. b) LRM image of the excited DLSPW mode. It is a 00 mode, as is apparent by an absence of beating. c) SEM image of a nanoparticle located at one side of the waveguide. d) LRM image of the excited DLSPW mode, in which the 01 mode is also present. The excitation wavelength of the laser is $\lambda = 632.8$ nm.

are deposited at the waveguide entrance using the LIFT method. The results of the fabrication are shown in figure 7.72 a) and c). The structures are then investigated using leakage radiation microscopy (LRM) with a He-Ne-laser at 632.8 nm wavelength. The results are shown in figure 7.72 b) and d). As in the case where conventional excitation is used ([250] and above), both the 00 and 01 mode can be excited.

Another interesting aspect is to see whether gold nanoparticles close to the DLSPPW structure can couple to the DLSPPW mode. Such investigations are useful as a test of the environmental robustness of the DLSPPW technology and also to measure the mode-field diameter of the DLSPPW mode. For these experiments, DLSPPW structures were fabricated on gold by 2PP and gold nanoparticles deposited adjacent to the waveguides by LIFT technology. The results of the fabrication are shown in two SEM images in figure 7.73.

The structures were then investigated using LRM at 632.8 nm. The coupling to the gold nanoparticle is very weak, even when the gold nanoparticle lies exactly adjacent to the waveguide without an air gap in between and can hardly be seen in the

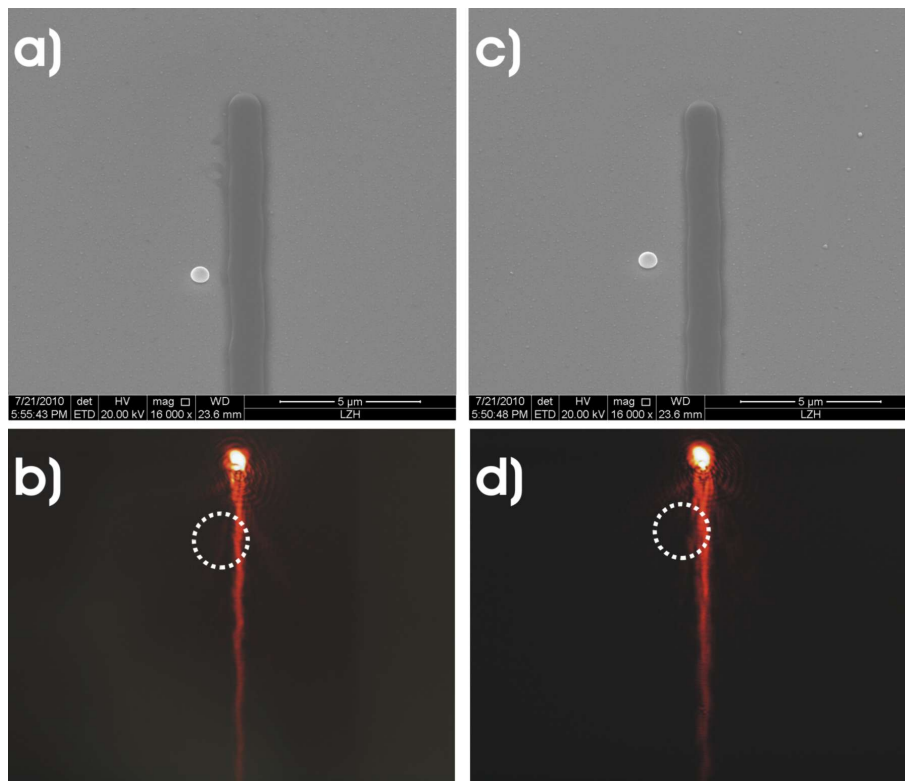


Figure 7.73: SEM and LRM images of spherical gold nanoparticles used in coupling experiments with DLSPW structures. a) and c) show SEM images of gold nanoparticles spaced at different distances from the DLSPW structure. b) and d) show the corresponding LRM images. The coupling effect is very weak, barely visible. The excitation wavelength of the laser is $\lambda = 632.8$ nm.

LRM images. This is evidence that the DLSPPW technology is indeed very robust concerning environmental deterioration (such as dust particles) and also shows that the DLSPPW mode is strongly confined within the waveguide structure.

7.3 Plasmonic Black Holes

A somewhat unusual development - one where nano-optics comes into close contact with astronomy and cosmology - is the development of structures known as optical, electromagnetic or plasmonic "black holes". What this label stands for is an omnidirectional optical absorber based on metamaterials [305, 306], whose electromagnetic physics bear some resemblance to the gravitational physics of an astronomical black hole.

It is hoped that these structures, or further developments of them, can be used to provide compact lab-based experiments to test astronomical theories [307], such as the simulation of a spinning cosmic string [308] or a rotating black hole [309]. Others believe these structures will also serve in more conventional optics experiments and be suitable to act as a thermal emitting source and to harvest electromagnetic waves [306] or to store light in a controllable fashion [310].

The design of a plasmonic black hole structure must allow for similar physics as an astronomical black hole, with an "event horizon" and "curved space". The design of the structure should be engineered to give a dependence of the dispersion for the surface plasmon on the local thickness of the structure [311]. By choosing a design where the thickness of the structure decreases with radius, the condition is met where at the centre of the structure the dispersion will be approximately equal to the case of a metal-dielectric interface, whereas at the edge it will correspond to the metal-air interface. The images in figure 7.74 show some examples of fabricated plasmonic black hole structures. The centre of the structure is formed by a cylinder, from which the thickness decreases nearly exponentially to the outer edge according to the equation

$$d(r) = d_0 e^{-ar} \quad (7.37)$$

where $d(r)$ is the polymer thickness, d_0 is the thickness in the centre and a is a variable factor governing the rate of decline, which can be adapted to the best parameters for any given characterization wavelength.

The experimental behaviour of such structures has not yet been thoroughly studied, and is something best left for future investigations. Simulations performed for similar structures, such as in reference [305], provide a good idea of the results to be expected, however. In figure 7.75, the results from said reference are reproduced. The structure is simulated for both off- and on-centre incidence at the wavelength of $1.5 \mu\text{m}$. In the on-centre incidence case, the intensity rapidly diminishes towards the centre of the structure as the electromagnetic radiation is simply swallowed up by the photonic black hole. In the off-centre case, we see something more interesting,

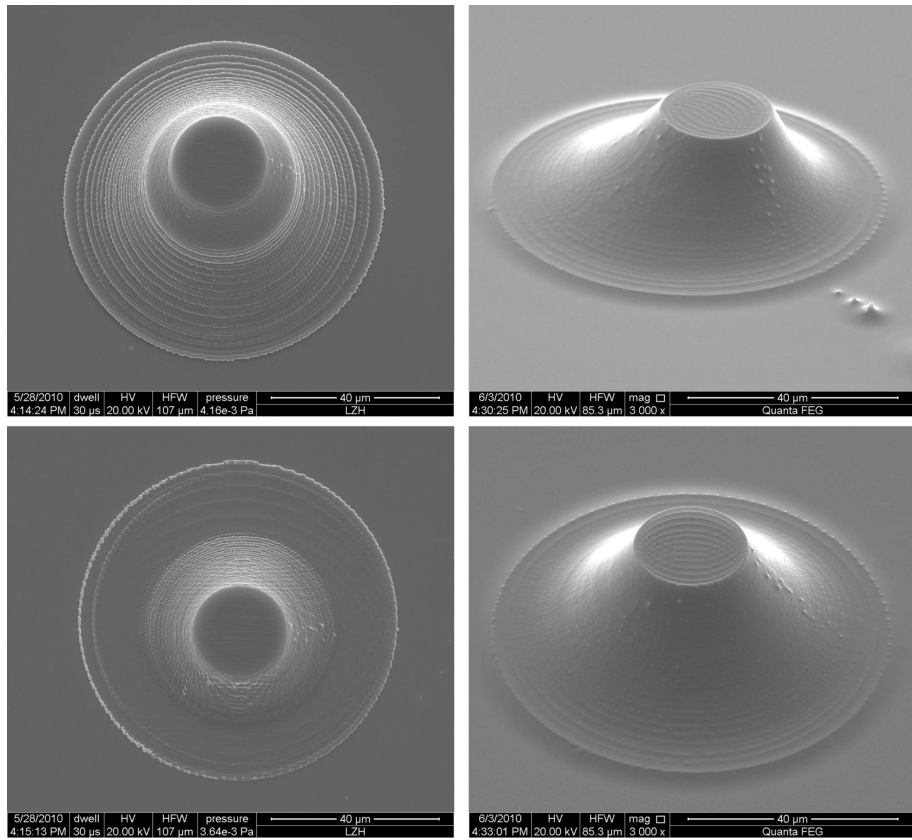


Figure 7.74: SEM images of symmetrical and asymmetrical plasmonic black hole structures.

namely that the radiation is attracted towards the centre of the photonic black hole, analogous to the behaviour of light inside an astronomical black hole.

These preliminary results show that 2PP-fabricated structures have some potential to become an important simulation tool of celestial physics in the near- to mid-term future, and it is strongly suggested that experiments in this field be encouraged, since the vast majority of astrophysical problems do not yet have a laboratory equivalent. This will likely be a major focus of plasmonic research in the coming decade.

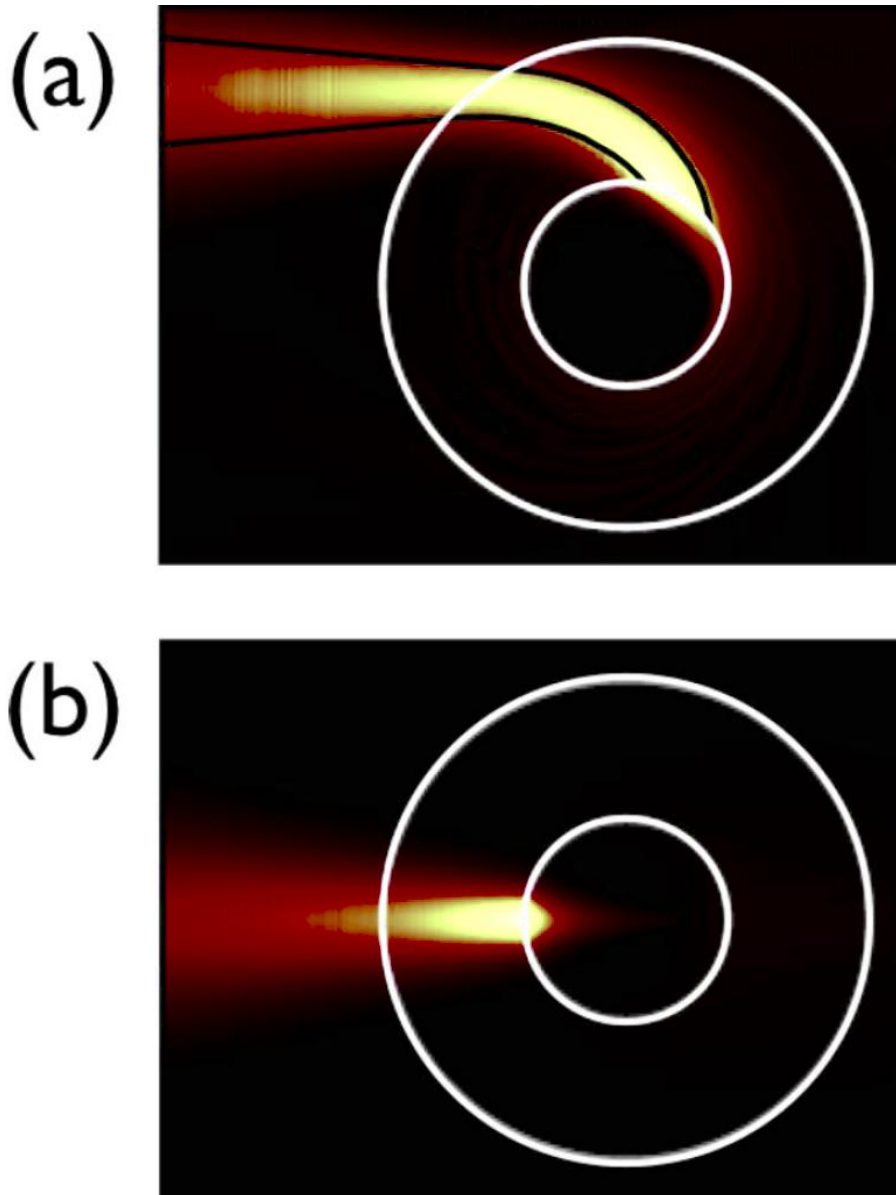


Figure 7.75: Simulated incidence of a Gaussian beam on an optical black hole at different incidence points. a) off-centre incidence and b) on-centre incidence. Source: [305]

8 Conclusion & Outlook

This thesis is focused on the study of surface plasmon-polaritons SPPs and their interactions with matter. A large part of the thesis is concentrated on the topic of dielectric-loaded surface plasmon-polariton waveguides (DLSPW), while another focuses on their interactions with each other and other materials, such as nanoparticles.

Conventional 2PP fabrication of DLSPW structures was enhanced by improvements to the fabrication setup. An entirely new fabrication method for DLSPW structures was introduced in this thesis through nanoimprint lithography coupled with 2PP fabrication, which allows DLSPW to go where no DLSPW has gone before. A comparison of fabrication methods for DLSPW structures shows that the methods introduced and developed in this thesis have the highest degrees of flexibility and accuracy combined with high fabrication speed. The laser-induced forward transfer technology used to deposit gold nanoparticles has been used in a novel fashion to position spherical gold nanoparticles for experiments with SPPs for the first time.

A wide range of DLSPW devices has been fabricated and studied. The devices include lines, bends, splitters, which were already studied previously in one form or another, as well as Mach-Zehnder interferometers and racetrack resonators, which have never been characterized before. The components were characterized by leakage radiation microscopy (LRM) using an entirely new LRM setup that harnessed the telecommunications wavelength of 1550 nm, the near infra-red wavelength of 974 nm and the optical wavelength of the He-Ne laser at 632.8 nm. This thesis also represents the first comprehensive approach of characterizing DLSPW components by LRM at the telecommunications wavelength.

This thesis also directly led to the first characterization of DLSPW structures using optical fibres to couple the light in and out, and represents the first successful experiments with laser-fabricated DLSPW structures in a fibre-coupled environment.

The interference of two separately excited SPP beams was shown for the first time in this thesis, a result which may eventually lead to an ultrafast and compact high-speed all-optical switch. The interaction of SPPs with gold nanoparticles was studied, and gold nanoparticles were for the first time used to couple light into a DLSPW waveguide. The influence of gold nanoparticles adjacent to a DLSPW waveguide was examined experimentally for the first time, which provides an insight into the robustness of DLSPW technology and shows that it is suitable for use outside a laboratory environment.

The experimental results are supported by two different numerical simulation tools, FDTD simulations using the Rsoft programme FullWAVE and a Green's Function Method simulation tool developed in-house. The experimental results match the theoretical predictions in every case.

This thesis paves the way for future research into a variety of fields. Significant advances have been made in DLSPW technology, which is still a major contender

in the technology race in the increasing involvement of from photonics in what was formerly electronics-dominated computing and communication. A wide range of individual components have been shown to be both functional and easy to produce, enabling the future creation of complex and versatile plasmonic and photonic devices from these building blocks. The fact that they are compatible with the use of optical fibres, as shown in this thesis, only continues to improve the outlook for DLSPW technology as a whole.

The increased study of the interaction of SPPs and nanoparticles as well as the SPP-SPP interaction may lead to a deeper understanding of the properties of SPPs and the way plasmonic resonances in nanoparticles may be harnessed to shape electromagnetic fields and signals on the nanoscale. Efforts are already under way, directly based on the work presented in this thesis, to create a plasmonic resonator for plasmon amplification and spaser applications. Micro- and nanoscale plasmonic detectors and sources are the next step in this field of research.

A highly interesting field, not least due to its exotic breath, is the potentially extremely promising combination of plasmonics, photonics, and astrophysical modelling, which may lead to a vast increase in our understanding of celestial and cosmic phenomena such as black holes, which are nearly impossible to study under laboratory conditions or directly.

In the near future, the most anticipated advances in this field are most likely to take place in the area of non-linear plasmonics. Fast non-linear switches have the potential to further integrate plasmonic circuits and to increase their usefulness. At the same time, research into active plasmonics, that is components with gain instead of loss, appear to be on the verge of producing practical spasers. The development of spasers, surface plasmon amplification by stimulated emission of radiation, would provide miniaturized sources of SPPs, which would take photonic integration a great leap forward. The need for external light sources would be removed, and it would be possible to produce true on-chip integrated photonic circuits. Bright new world, indeed.

9 Bibliography

References

- [1] N. I. Zheludev, *The next photonic revolution*, J. Opt. A **11**, 110202 (2009).
- [2] F. Hapgood, *Metamaterial Revolution: The New Science of Making Anything Disappear*, Discover **2009**, 1 (2009).
- [3] H. Wong, V. Filip, C. K. Wong, and P. S. Chung, *Silicon integrated photonics begins to revolutionize*, Microelectronics Reliability **47**, 1 (2007).
- [4] D. B. Keck, *Fiber optics - a communications revolution*, International Competitiveness and Business Techniques in Advanced Optics and Imaging, Proc. SPIE **1617**, 2 (1992).
- [5] A. Einstein, *Lens-Like Action of a Star by the Deviation of Light in the Gravitational Field*, Science **84**, 506 (1936).
- [6] H. Weaver, D. R. Williams, N. H. Dieter, and W. T. Lum, *Observations of a strong unidentified microwave line and of emission from OH molecule*, Nature **208**, 29 (1965).
- [7] M. Gray, *Astrophysical masers*, Philos. Trans. R. Soc. London, Ser. A **357**, 3277 (1999).
- [8] S. Johansson and V. S. Letokhov, *Astrophysical lasers and nonlinear optical effects in space*, New Astronomy Reviews **51**, 443 (2007).
- [9] B. Schoenemann, *Trilobite eyes and a new type of neural superposition eye in an ancient system*, Palaeontographica, Abteilung A: Palaeozoologie - Stratigraphie **281**, 63 (2007).
- [10] A. R. Parker, *A geological history of reflecting optics*, Journal of the Royal Society Interface **2**, 1 (2005).
- [11] J. M. Malville, F. Wendorf, A. A. Mazar, and R. Schild, *Megaliths and Neolithic astronomy in southern Egypt*, Nature **392**, 488 (1998).
- [12] C. Ruggles and M. Hoskin, *Astronomy before History, in the Cambridge concise history of astronomy* (Cambridge University Press, Cambridge, 1999).
- [13] J. M. Enoch and V. Lakshminarayanan, *Duplication of unique optical effects of ancient Egyptian lenses from the IV/V Dynasties: lenses fabricated ca 2620-2400 BC or roughly 4600 years ago*, Ophthal. Physiol. Opt. **20**, 126 (2000).
- [14] D. Brewster, *On an account of a rock-crystal lens and decomposed glass found at Niniveh*, Communication published in: Die Fortschritte der Physik im Jahre 1852 **8**, 355 (1855).

- [15] D. Plantzos, *Crystals and Lenses in the Graeco-Roman World*, American Journal of Archaeology **101**, 451 (1997).
- [16] R. Rashed, *A pioneer in anaclastics: Ibn Sahl on burning mirrors and lenses*, Isis **81**, 464 (1990).
- [17] W. Snellius, *Cyclometricus: de circuli dimensione secundum logistarum abacos, & ad mechanicam accuratissima; atque omnium parabilissima: eiusdemque usus in quarumlibet, adscriptarum inventione longe elegantissimus, & quidem ex ratione diametri ad suam peripheriam data* (ex officina Elzeviriana, Lugdunum Batavorum (Leiden), 1621).
- [18] A. Kwan, J. Dudley, and E. Lantz, *Who really discovered Snell's law?*, Physics World **64** (2002).
- [19] S. Drake, *Galileo at Work* (University of Chicago Press, Chicago, 1978).
- [20] J. C. Maxwell, *On physical lines of force*, Philos. Mag. Series 4 **21**, 161 (1861).
- [21] J. C. Maxwell, *A dynamical theory of the electromagnetic field*, Philos. Trans. R. Soc. London **155**, 459 (1865).
- [22] T. H. Maiman, *Stimulated optical radiation in ruby*, Nature **187**, 493 (1960).
- [23] J. Kahn, *Nanotechnology*, National Geographic **June**, 98 (2006).
- [24] I. Freestone, N. Meeks, M. Sax, and C. Higgitt, *The Lycurgus Cup – A Roman Nanotechnology*, Gold Bulletin **40**, 270 (2007).
- [25] P. Colomban, *The Use of Metal Nanoparticles to Produce Yellow, Red and Iridescent Colour, from Bronze Age to Present Times in Lustre Pottery and Glass: Solid State Chemistry, Spectroscopy and Nanostructure*, J. Nano Res. **8**, 109 (2009).
- [26] L. Hunt, *The True Story of Purple of Cassius*, Gold Bulletin **9**, 134 (1974).
- [27] P. Colomban, A. Tournie, and P. Ricciardi, *Raman spectroscopy of copper nanoparticle-containing glass matrices: ancient red stained-glass windows*, J. Raman Spectrosc. **40**, 1949 (2009).
- [28] R. Kerr and N. Wood, *Science and Civilisation in China Volume 5: Chemistry and Chemical Technology, Part 12, Ceramic Technology* (Cambridge University Press, 2004).
- [29] A. Libavius, *Alchemia* (Peter Kopff, Frankfurt, 1597).
- [30] J. R. Glauber, *Dess Teutschlandts Wohlfahrt / Prosperitatis Germaniae* (Amsterdam, 1665-1660).
- [31] A. Cassius, *De auro* (Georg Wolff, Hamburg, 1685).

- [32] J. C. Orschall, *Sol sine veste* (Jakob Koppmayr, Augsburg, 1684).
- [33] J. Kunckel, *Ars vitraria experimentalis* (Christoph Riegel, Nürnberg, 1743).
- [34] R. A. Zsigmondy, *Ueber wässrige Lösungen metallischen Goldes*, Justus Liebig's Annalen der Chemie **301**, 29 (1898).
- [35] P. Drude, *Zur Elektronentheorie der Metalle; I. Teil*, Annalen der Physik **306**, 566 (1900).
- [36] P. Drude, *Zur Elektronentheorie der Metalle; II. Teil; Galvanomagnetische und thermomagnetische Effecte*, Annalen der Physik **308**, 369 (1900).
- [37] A. Sommerfeld, *Zur Elektronentheorie der Metalle*, Naturwissenschaften **15**, 825 (1927).
- [38] A. Sommerfeld, *Zur Elektronentheorie der Metalle*, Naturwissenschaften **16**, 374 (1928).
- [39] L. Tonks and I. Langmuir, *Oscillations in Ionized Gases*, Phys. Rev. **33**, 195 (1929).
- [40] J. Zenneck, *Über die Fortpflanzung ebener elektromagnetischer Wellen längs einer ebenen Leiterfläche und ihre Beziehung zur drahtlosen Telegraphie*, Annalen der Physik **328**, 846 (1906).
- [41] A. Sommerfeld, *Über die Ausbreitung der Wellen in der drahtlosen Telegraphie*, Annalen der Physik **333**, 665 (1909).
- [42] J. Zenneck, *Aus der Kindheit der drahtlosen Telegraphie*, Die Naturwissenschaften **39**, 409 (1952).
- [43] D. Bohm and D. Pines, *A collective description of electron interactions .2. Collective vs individual particle aspects of the interactions*, Phys. Rev. **85**, 338 (1952).
- [44] D. Bohm and D. Pines, *A collective description of electron interactions .3. Coulomb interactions in a degenerate electron gas*, Phys. Rev. **92**, 609 (1953).
- [45] H. Watanabe, *Experimental Evidence for the Collective Nature of the Characteristic Energy Loss of Electrons in Solids - Studies on the Dispersion Relation of Plasma Frequency*, J. Phys. Soc. Jpn. **11**, 112 (1955).
- [46] R. H. Ritchie, *Plasma Losses by Fast Electrons in Thin Films*, Phys. Rev. **106**, 874 (1957).
- [47] F. Fujimoto and K. Komaki, *Plasma Oscillations Excited by a Fast Electron in a Metallic Particle*, J. Phys. Soc. Jpn. **25**, 1679 (1968).

- [48] A. Otto, *Excitation of Nonradiative Surface Plasma Waves in Silver by the Method of Frustrated Total Reflection*, Zeitschrift für Physik **216**, 398 (1968).
- [49] E. Kretschmann, *Die Bestimmung optischer Konstanten von Metallen durch Anregung von Oberflächenplasmonschwingungen*, Zeitschrift für Physik **241**, 333 (1971).
- [50] B. Schechter, *Bright New World*, New Scientist **178**, 30 (2003).
- [51] T. W. Ebbesen, H. J. Lezec, H. F. Ghaemi, T. Thio, and P. A. Wolff, *Extraordinary optical transmission through sub-wavelength hole arrays*, Nature **391**, 667 (1998).
- [52] R. Zia, J. A. Schuller, A. Chandran, and M. L. Brongersma, *Plasmonics: the next chip-scale technology*, Mater. Today **9**, 20 (2006).
- [53] S. A. Maier, *Plasmonics - Fundamentals and Applications* (Springer, New York, 2007).
- [54] H. Raether, *Surface Plasmons on Smooth and Rough Surfaces and on Gratings* (Springer, New York, 1988).
- [55] S. Massenet, J. C. Weeber, A. Bouhelier, G. C. D. Francs, J. Grandidier, L. Markey, and A. Dereux, *Differential method for modelling dielectric-loaded surface plasmon polariton waveguides*, Opt. Express **22**, 17599 (2008).
- [56] E. Hecht, *Optik* (Oldenbourg, München, 2009).
- [57] W. Demtröder, *Experimentalphysik 2: Elektrizität und Optik* (Springer, Berlin, 2008).
- [58] U. Fano, *Effects of Configuration Interaction on Intensities and Phase Shifts*, Physical Review **124**, 1866 (1961).
- [59] M. L. Dakss, L. Kuhn, P. F. Heidrich, and B. A. Scott, *Grating Coupler for Efficient Excitation of Optical Guided Waves in Thin Films*, Appl. Phys. Lett. **16**, 523 (1970).
- [60] S. G. Tikhodeev, A. L. Yablonski, E. A. Muljarov, N. A. Gippius, and T. Ishihara, *Quasiguide modes and optical properties of photonic crystal slabs*, Phys. Rev. Lett. B **66**, 045102 (2002).
- [61] N. A. Gippius, S. G. Tikhodeev, A. Christ, J. Kuhl, and H. Giessen, *Waveguide Plasmon Polaritons in Metal-Dielectric Photonic Crystal Slabs*, Physics of the Solid State **47**, 145 (2005).
- [62] S. G. Tikhodeev, N. A. Gippius, A. Christ, J. Kuhl, and H. Giessen, *Waveguide-plasmon polaritons in photonic crystal slabs with metal nanowires*, Physica Status Solidi **2**, 795 (2005).

- [63] A. Seidel, *A Photonic-Crystal-Based Hydrogen Sensor: Fundamentals and Prototype Development* (Diplomarbeit, Universität Bonn, Bonn, 2007).
- [64] F. Pincemin, A. Sentenac, and J. J. Greffet, *Near-field scattered by a dielectric rod below a metallic surface*, J. Opt. Soc. Am. A **11**, 1117 (1994).
- [65] P. J. Valle, F. Moreno, J. M. Saiz, and F. Gonzalez, *Near-field scattering from subwavelength metallic protuberances on conducting flat substrates*, Phys. Rev. B **51**, 13681 (1995).
- [66] J. A. Sanchez-Gil, *Surface defect scattering of surface plasmon polaritons: Mirrors and light emitters*, Appl. Phys. Lett. **73**, 3509 (1998).
- [67] J. A. Sanchez-Gil and A. A. Maradudin, *Near-field and far-field scattering of surface plasmon polaritons by one-dimensional surface defects*, Phys. Rev. B **60**, 8359 (1999).
- [68] R. H. Ritchie, E. T. Arkawa, J. J. Cowan, and R. N. Hamm, *Surface-plasmon resonance effect in grating diffraction*, Phys. Rev. Lett. **21**, 1530 (1968).
- [69] E. Popov, L. Tsonev, and D. Maystre, *Losses of plasmon surface-waves on metallic grating*, Journal of Modern Optics **37**, 379 (1990).
- [70] G. P. Bryanbrown, S. J. Elston, and J. R. Sambles, *Comparison of metal parameters obtained from prism and grating coupling to surface-plasmon polaritons*, Journal of Modern Optics **38**, 1181 (1991).
- [71] A. P. Hibbins, J. R. Sambles, and C. R. Lawrence, *Grating-coupled surface plasmons at microwave frequencies*, J. Appl. Phys. **86**, 1791 (1999).
- [72] J. F. O'Hara, T. Okada, T. Kobayashi, K. A. Nelson, and S. DeSilvestri, *Terahertz surface plasmon polariton coupling on metallic grating structures*, Ultrafast Phenomena XIV **79**, 696 (2005).
- [73] K. A. Tetz, R. Rokitski, M. Nezhad, and Y. Fainman, *Excitation and direct imaging of surface plasmon polariton modes in a two-dimensional grating*, Appl. Phys. Lett. **86**, 111110 (2005).
- [74] A. Kocabas, A. Dana, and A. Aydinli, *Excitation of a surface plasmon with an elastomeric grating*, Appl. Phys. Lett. **89**, 041123 (2006).
- [75] A. Christ, T. Zentgraf, S. G. Tikhodeev, N. A. Gippius, O. J. F. Martin, J. Kuhl, and H. Giessen, *Interaction between localized and delocalized surface plasmon polariton modes in a metallic photonic crystal*, Phys. Stat. Sol. B **243**, 2344 (2006).
- [76] Y. Shevchenko, C. Chen, M. A. Dakka, and J. Albert, *Polarization-selective grating excitation of plasmons in cylindrical optical fibers*, Opt. Lett. **35**, 637 (2010).

- [77] C. K. Chen and P. Berini, *Grating couplers for broadside input and output of long-range plasmons*, *Opt. Express* **18**, 8006 (2010).
- [78] D. W. Pohl, *Near-Field Optics and Surface Plasmon Polaritons; Topics in Applied Physics* (Springer, Berlin / Heidelberg, 2001).
- [79] B. Hecht, H. Bielefeldt, L. Novotny, Y. Inouye, and D.W. Pohl, *Local Excitation, Scattering, and Interference of Surface Plasmons*, *Phys. Rev. Lett.* **77**, 1889 (1996).
- [80] L. Novotny, B. Hecht, and D. W. Pohl, *Interference of locally excited surface plasmons*, *J. Appl. Phys.* **81**, 1798 (1997).
- [81] J. C. Ashley, T. L. Ferrell, and R. H. Ritchie, *X-ray excitation of surface plasmons in metallic spheres*, *Phys. Rev. B* **10**, 554 (1974).
- [82] G. E. Moore, *Cramming more components onto integrated circuits*, *Electronics* **38**, 114 (1965).
- [83] G. E. Moore, *Progress in digital integrated electronics*, *Electron Devices Meeting, 1975 International* **1**, 11 (1975).
- [84] G. E. Moore, *Cramming more components onto integrated circuits*, *Proceedings of the IEEE* **86**, 82 (1998).
- [85] The International Technology Roadmap for Semiconductors, *Lithography, The International Technology Roadmap for Semiconductors* **1**, 1 (2009).
- [86] G. W. Stroke, *Optical Computing*, *IEEE Spectrum* **9**, 24 (1972).
- [87] R. A. Athale and S. H. Lee, *Development of an optical parallel logic device and half-adder circuit for digital optical-processing*, *Opt. Eng.* **18**, 513 (1979).
- [88] R. P. Bocker, *Photonic Computing*, *Appl. Opt.* **25**, 3019 (1986).
- [89] B. L. Drake, R. P. Bocker, M. E. Lasher, R. H. Patterson, and W. J. Miceli, *Photonic computing using the modified signed-digit number representation*, *Opt. Eng.* **28**, 38 (1986).
- [90] E. Swartzlander, *Digital Optical Arithmetic*, *Appl. Opt.* **25**, 3021 (1986).
- [91] M. J. Potasek, *Novel femtosecond solitons in optical fibers, photonic switching, and computing*, *J. Appl. Phys.* **65**, 941 (1989).
- [92] P. K. Tien, *Integrated optics and new wave phenomena in optical waveguides*, *Rev. Mod. Phys.* **49**, 361 (1977).
- [93] M. A. Fischetti, *Integrated photonics comes out of the laboratory*, *Photonics Spectra* **26**, 98 (1992).

- [94] N. Paniccia, M. Morse, and M. Salib, *Integrated photonics*, Silicon Photonics **94**, 51 (2004).
- [95] R. Soref, *The impact of silicon photonics*, IEICE Transactions on Electronics **E91C**, 129 (2008).
- [96] G. Overton, *Can optical integration solve the computational bottleneck?*, Laser Focus World **45**, 64 (2009).
- [97] T. Yatagai, S. Kawai, and H. Hijang, *Optical Computing and Interconnects*, Proc. IEEE **84**, 828 (1994).
- [98] D. Casasent, *Coherent Optical Computing*, Computer (IEEE) **12**, 27 (1979).
- [99] J. P. Colinge, *Trends in silicon-on-insulator technology*, Microelectronic Engineering **19**, 795 (1992).
- [100] B. N. Kurdi and D. G. Hall, *Optical waveguides in oxygen-implanted buried-oxide silicon-on-insulator structures*, Opt. Lett. **13**, 175 (1988).
- [101] J. Schmidtchen, A. Splett, B. Schuppert, K. Petermann, and G. Burbach, *Low-loss singlemode optical wave-guides with large cross-section in silicon-on-insulator*, Electronics Lett. **27**, 1486 (1991).
- [102] W. Bogaerts, R. Baets, P. Dumon, V. Wiaux, S. Beckx, D. Taillaert, B. Luyssaert, J. Van Campenhout, P. Bienstman, and D. Van Thourhout, *Nanophotonic waveguides in silicon-on-insulator fabricated with CMOS technology*, J. Lightwave Technol. **23**, 401 (2005).
- [103] W. M. J. Green, M. J. Rooks, L. Sekaric, and Y. A. Vlasov, *Ultra-compact, low RF power, 10 Gb/s silicon Mach-Zehnder modulator*, Opt. Express **15**, 17106 (2008).
- [104] Q. Xu, D. Fattal, and R. G. Beausoleil, *Silicon microring resonators with 1.5- μm radius*, Opt. Express **16**, 4309 (2008).
- [105] Y. A. Vlasov and S. J. McNab, *Losses in single-mode silicon-on-insulator strip waveguides and bends*, Opt. Express **12**, 1622 (2004).
- [106] J. W. Wu and A. K. Sarma, *Ultrafast all-optical XOR logic gate based on a symmetrical Mach-Zehnder interferometer employing SOI waveguides*, Opt. Comm. **283**, 2914 (2010).
- [107] Z. Han, A. Y. Elezzabi, and V. Van, *Wideband Y-splitter and aperture-assisted coupler based on sub-diffraction confined plasmonic slot waveguides*, Appl. Phys. Lett. **96**, 131106 (2010).
- [108] W. Bogaerts, P. Bienstman, and R. Baets, *Scattering at sidewall roughness in photonic crystal slabs*, Opt. Lett. **28**, 689 (2003).

- [109] S. Ossicini, L. Pavesi, and F. Priolo, *Light emitting silicon for microphotronics* (Springer, Berlin / Heidelberg, 2003).
- [110] T. Trupke, J. Zhao, A. Wang, R. Corkish, and M. Green, *Very efficient light emission from bulk crystalline silicon*, Appl. Phys. Lett. **82**, 2996–2998 (2003).
- [111] L. Pavesi, L. D. Negro, C. Mazzoleni, G. Franzo, and F. Priolo, *Optical gain in silicon nanocrystals*, Nature **408**, 440–444 (2000).
- [112] Z. H. Liu, J. D. Huang, P. C. Joshi, A. T. Voutsas, J. Hartzell, F. Capasso, and J. M. Bao, *Polarity-controlled visible/infrared electroluminescence in Si-nanocrystal/Si light-emitting devices*, Appl. Phys. Lett. **97**, 071112 (2010).
- [113] P. G. Kik, M. L. Brongersma, and A. Polman, *Strong exciton-erbium coupling in Si nanocrystal-doped SiO₂*, Appl. Phys. Lett. **76**, 2325 (2000).
- [114] S. Yerci, R. Li, and L. Dal Negro, *Electroluminescence from Er-doped Si-rich silicon nitride light emitting diodes*, Appl. Phys. Lett. **97**, 081109 (2010).
- [115] D. J. Lockwood, Z. H. Lu, and J. M. Baribeau, *Quantum confined luminescence in Si/SiO₂ superlattices*, Phys. Phys. Lett. **76**, 539 (1996).
- [116] G. Dehlinger, L. Diehl, U. Gennser, H. Sigg, J. Faist, K. Ensslin, D. Grützmacher, and E. Müller, *Intersubband electroluminescence from silicon-based quantum cascade structures*, Science **290**, 2277 (2000).
- [117] H. S. Rong, A. S. Liu, O. Cohen, D. Hak, R. Nicolaescu, A. Fang, and M. Paniccia, *An all-silicon Raman laser*, Nature **433**, 292 (2005).
- [118] J. Leuthold, C. Koos, and W. Freude, *Nonlinear silicon photonics*, Nature Phot. **4**, 535 (2010).
- [119] T. F. Krauss, R. M. DeLaRue, and S. Brand, *Two-dimensional photonic-bandgap structures operating at near infrared wavelengths*, Nature **383**, 699 (1996).
- [120] J. D. Joannopoulos, J. N. Winn, and R. D. Meade, *Photonic Crystals* (Princeton University Press, Princeton, 1995).
- [121] V. R. Almeida, C. A. Barrois, R. R. Panepucci, and M. Lipson, *All-optical control of light on a silicon chip*, Nature **431**, 1081 (2004).
- [122] Y. A. Vlasov, M. O’Boyle, H. F. Hamann, and S. J. McNab, *Active control of slow light on a chip with photonic crystal waveguides*, Nature **438**, 65 (2005).
- [123] J. W. S. Rayleigh, *On the remarkable phenomenon of crystalline reflexion described by Prof. Stokes*, Phil. Mag. **26**, 256 (1888).
- [124] V. P. Bykov, *Spontaneous emission in a periodic structure*, Soviet Journal of Experimental and Theoretical Physics **35**, 269 (1972).

- [125] E. Yablonovitch, *Inhibited spontaneous emission in solid-state physics and electronics*, Phys. Rev. Lett. **58**, 2059 (1987).
- [126] S. John, *Strong localization of photons in certain disordered dielectric superlattices*, Phys. Rev. Lett. **58**, 2486 (1987).
- [127] E. Yablonovitch, T. J. Gmitter, and K. M. Leung, *Photonic band-structure - the face-centered-cubic case employing nonspherical atoms*, Phys. Rev. Lett. **67**, 2295 (1991).
- [128] J. C. Knight, J. Broeng, T. A. Birks, and P. Russell, *Photonic band gap guidance in optical fibers*, Science **282**, 1476 (1998).
- [129] B. Jia, D. Buso, J. van Embden, J. Li, and M. Gu, *Highly Non-Linear Quantum Dot Doped Nanocomposites for Functional Three-Dimensional Structures Generated by Two-Photon Polymerization*, Adv. Mater. **22**, 2463–2467 (2010).
- [130] J. M. Dudley, G. Genty, and S. Coen, *Supercontinuum generation in photonic crystal fiber*, Reviews of Modern Physics **78**, 1135 (2006).
- [131] M. Chen, Q. Yang, T. S. Li, M. S. Chen, and N. He, *New high negative dispersion photonic crystal fiber*, Optik **121**, 867 (2010).
- [132] M. Francardi, A. Gerardino, L. Balet, N. Chauvin, D. Bitauld, L. H. Li, B. Alloing, and A. Fiore, *Cavity-enhanced photonic crystal light-emitting diode at 1300 nm*, Microelectronic Engineering **86**, 1093 (2009).
- [133] T. Czyszanowski, *Thermal properties and wavelength analysis of telecom oriented photonic crystal VCSELs*, Opto-Electronics Review **18**, 56 (2010).
- [134] T. Takano and J. Hamasaki, *Propagating Modes of a Metal-Clad-Dielectric Slab Waveguide for Integrated Optics*, IEEE J. Quantum Electron. **QE 8**, 206 (1972).
- [135] T. E. Batchman and S. C. Rashleigh, *Mode-Selective Properties of a Metal-Clad-Dielectric-Slab Waveguide for Integrated Optics*, IEEE J. Quantum Electron. **QE 8**, 848 (1972).
- [136] A. Reisinger, *Attenuation properties of optical waveguides with a liquid boundary*, Appl. Phys. Lett. **23**, 237 (1973).
- [137] P. Kaminow, *Metal-Clad Optical Waveguides: Analytical and Experimental Study*, Appl. Optics **13**, 396 (1974).
- [138] Y. Yamamoto, T. Kamiya, and H. Yanai, *Propagation Characteristics of a Partially Metal-Clad Optical Guide: Metal-Clad Optical Strip Line*, Appl. Optics **14**, 322 (1975).

- [139] V. Volkov, S. Bozhevolnyi, K. Leosson, and A. Boltasseva, *Experimental studies of surface plasmon polariton band gap effect*, Journal of Microscopy - Oxford **223**, 25 (2003).
- [140] J. Krenn and J. C. Weeber, *Surface plasmon polaritons in metal stripes and wires*, Philos. Trans. R. Soc. London **362**, 739 (2004).
- [141] J. Takahira, S. Yamagishi, H. Taki, A. Morioto, and T. Kabayashi, *Guiding of a one-dimensional optical beam with nanometer diameter*, Opt. Lett. **22**, 475 (1997).
- [142] S. Bozhevolnyi, V. Volkov, E. Devaux, J.-Y. Laluet, and T. Ebbesen, *Channel plasmon subwavelength waveguide components including interferometers and ring resonators*, Nature **440**, 508 (2006).
- [143] L. Chen, B. Wang, and G. P. Wang, *High efficiency 90 degrees bending metal heterowaveguides for nanophotonic integration*, Appl. Phys. Lett. **89**, 243120 (2006).
- [144] S. A. Maier, P. G. Kik, H. A. Atwater, S. Meltzer, E. Harel, B. E. Koel, and A. Requicha, *Local detection of electromagnetic energy transport below the diffraction limit in metal nanoparticle plasmon waveguides*, Nat. Mater. **2**, 229 (2003).
- [145] S. A. Maier and H. A. Atwater, *Plasmonics: Localization and guiding of electromagnetic energy in metal/dielectric structures*, J. Appl. Phys. **98**, 011101 (2005).
- [146] B. Wang and G. P. Wang, *Planar metal heterostructures for nanoplasmonic waveguides*, Appl. Phys. Lett. **90**, 013114 (2007).
- [147] C. Reinhardt, S. Passinger, B.N. Chichkov, C. Marquardt, I.P. Radko, and S.I. Bozhevolnyi, *Laser-fabricated dielectric optical components for surface plasmon polaritons*, Opt. Lett. **31**, 1307 (2006).
- [148] B. Steinberger, A. Hohenau, H. Ditlbacher, A. L. Stepanov, A. Drezet, F. R. Aussenegg, A. Leitner, and J. R. Krenn, *Dielectric stripes on gold as surface plasmon waveguides*, Appl. Phys. Lett. **88**, 094104 (2006).
- [149] A. V. Krasavin and A. V. Zayats, *Passive photonic elements based on dielectric-loaded surface plasmon polariton waveguides*, Appl. Phys. Lett. **90**, 211101 (2007).
- [150] T. Holmgaard and S.I. Bozhevolnyi, *Theoretical analysis of dielectric-loaded surface plasmon-polariton waveguides*, Phys. Rev. B **75**, 245405 (2007).
- [151] M. Göppert Mayer, *Über Elementarakte mit zwei Quantensprüngen*, Annalen der Physik **9**, 273 (1931).

- [152] W. Kaiser and C. G. B. Garrett, *Two-photon excitation in $\text{CaF}_2:\text{Eu}^{2+}$* , Phys. Rev. Lett. **7**, 229 (1961).
- [153] W. Denk, J. H. Strickler, and W. W. Webb, *Two-photon laser scanning fluorescence microscopy*, Science **248**, 73 (1990).
- [154] C. Xu, J. Shear, R. Williams, and W. Webb, *Multiphoton fluorescence excitation: new spectral windows for biological nonlinear microscopy*, Proceedings of the National academy of Sciences of the United States of America **93**, 10763–10768 (1996).
- [155] H. de Riedmatten, *Light storage at record bandwidths*, Nature Photonics **94**, 206 (2010).
- [156] M. Pawlicki, H. A. Collins, R. G. Denning, and H. L. Anderson, *Two-Photon Absorption and the Design of Two-Photon Dyes*, Angewandte Chemie - International Edition **48**, 3244–3266 (2009).
- [157] M. Rumi, S. Barlow, J. Wang, and S. R. Marder, *Two-Photon Absorbing Materials and Two-Photon-induced Chemistry*, Advances in Polymer Science (Photoresponsive Polymers I) **213**, 1–95 (2008).
- [158] T. C. Lin, S. J. Chung, K. S. Kim, X. Wang, G. S. He, J. Swiatkiewicz, H. E. Pudavar, and P. N. Prasad, *Organics and polymers with high two-photon activities and their applications*, Advances in Polymer Science (Photoresponsive Polymers II) **161**, 157–193 (2003).
- [159] V. G. Plotnikov, V. A. Smirnov, and M. V. Alfimov, *Two-photon photoprocesses in molecular systems*, High Energy Chemistry **4**, 241 (2009).
- [160] N. Aratani, D. Kim, and A. Osuka, *π -Conjugation Enlargement Toward the Creation of Multi-Porphyrinic Systems with Large Two-Photon Absorption Properties*, Chemistry - An Asian Journal **4**, 1172 (2009).
- [161] J. H. Strickler and W. W. Webb, *2-photon excitation in laser scanning fluorescence microscopy*, Proc. SPIE **1398**, 107 (1991).
- [162] E. S. Wu, J. H. Strickler, W. R. Harrell, and W. W. Webb, *2-photon lithography for microelectronic application*, Proc. SPIE **1674**, 776 (1992).
- [163] S. R. Desai, C. S. Feigerle, and J. C. Miller, *Laser-induced polymerization within carbon-disulfide clusters*, J. Phys. Chem. **99**, 1786 (1995).
- [164] O. K. Song, J. N. Woodford, and C. H. Wang, *Effects of two-photon fluorescence and polymerization on the first hyperpolarizability of an azobenzene dye*, J. Phys. Chem. A **101**, 3222 (1997).
- [165] S. Maruo, O. Nakamura, and S. Kawata, *Three-dimensional microfabrication with two-photon-absorbed photopolymerization*, Opt. Lett. **22**, 132 (1997).

- [166] A. Yariv A. S. Kewitsch, *Self-focusing and self-trapping of optical beams upon photopolymerization*, Opt. Lett. **21**, 24 (1996).
- [167] R. A. Borisov, G. N. Dorojkina, N. I. Koroteev, V. M. Kozenkov, S. A. Magnitskii, D. V. Malakhov, A. V. Tarasishin, and A. M. Zheltikov, *Femtosecond two-photon photopolymerization: A method to fabricate optical photonic crystals with controllable parameters*, Laser Phys. **8**, 1105 (1998).
- [168] B. H. Cumpston, J. E. Ehrlich, L. L. Erskine, A. A. Heikal, Z. Y. Hu, L. Y. S. Lee, M. D. Levin, S. R. Marder, D. J. McCord, J. W. Perry, H. Rockel, M. Rumi, and X. L. Wu, *New photopolymers based on two-photon absorbing chromophores and application to three-dimensional microfabrication and optical storage*, Mater. Res. Soc. Symp. Proc. **488**, 217 (1998).
- [169] S. M. Kirkpatrick, J. W. Baur, C. M. Clark, L. R. Denny, D. W. Tomlin, B. R. Reinhardt, R. Kannan, and M. O. Stone, *Holographic recording using two-photon-induced photopolymerization*, Appl. Phys. A **69**, 461 (1999).
- [170] C. Schizas, V. Melissinaki, A. Gaidukeviciute, C. Reinhardt, C. Ohrt, V. Dedoussis, B. N. Chichkov, C. Fotakis, M. Farsari, and D. Karalekas, *On the design and fabrication by two-photon polymerization of a readily assembled micro-valve*, Int. J. Adv. Manuf. Technol. **48**, 435 (2010).
- [171] F. Heinroth, I. Bremer, S. Munzer, P. Behrens, C. Reinhardt, S. Passinger, C. Ohrt, and B. Chichkov, *Microstructured templates produced using femtosecond laser pulses as templates for the deposition of mesoporous silicas*, Microporous and Mesoporous Materials **119**, 104 (2009).
- [172] S. D. Gittard, A. Ovsianikov, H. Akar, B. Chichkov, N. A. Monteiro-Riviere, S. Stafslin, B. Chisholm, C. C. Shin, C. M. Shih, S. J. Lin, Y. Y. Su, and R. J. Narayan, *Two photon polymerization-micromolding of polyethylene glycol-gentamicin sulfate microneedles*, Adv. Eng. Mat. **12**, B77 (2010).
- [173] A. Ovsianikov, S. Schlie, A. Ngezahayo, and B. Chichkov, *Direct laser writing of Cad-designed 3D scaffolds for tissue engineering*, Tissue Engineering Part A **14**, 839 (2008).
- [174] Intel Corporation, *Light Peak Technology*, <http://techresearch.intel.com/articles/None/1813.htm> **1**, 1 (2010).
- [175] R. Houbertz, L. Frohlich, M. Popall, U. Streppel, P. Dannberg, A. Brauer, J. Serbin, and B. N. Chichkov, *Inorganic-organic hybrid polymers for information technology: from planar technology to 3D nanostructures*, Adv. Eng. Mater. **5**, 551 (2003).
- [176] C. Reinhardt, A. Ovsianikov, S. Passinger, and B. N. Chichkov, *Fabrication of micromechanical and microoptical systems by two-photon polymerization*, Proc. SPIE **6466**, 64660M (2007).

- [177] K. S. Lee, R. H. Kim, D. Y. Yang, and S. H. Park, *Advances in 3D nano/microfabrication using two-photon initiated polymerization*, Prog. Polym. Sci. **33**, 631 (2008).
- [178] M. Kühn, P. Drisse, and M. Joost, *Progress in the use of BOF slag*, Stahl und Eisen **126**, 159 (2006).
- [179] K. Yamada, J. Sone, and J. Chen, *Three-dimensional photochemical microfabrication of conductive polymers in transparent polymer sheet*, Opt. Rev. **16**, 208 (2009).
- [180] J. F. Remacle, C. Geuzaine, G. Compere, and E. Marchandise, *High-quality surface remeshing using harmonic maps*, Int. J. Numer. Methods Eng. **83**, 403 (2010).
- [181] J. E. Petrzela and M. C. Frank, *Advanced process planning for subtractive rapid prototyping*, Rapid Prototyping Journal **16**, 216 (2010).
- [182] C. S. Wang, *An analysis and evaluation of fitness for shoe lasts and human feet*, Comput. Ind. **61**, 532 (2010).
- [183] A. Boltasseva, *Plasmonic components fabrication via nanoimprint*, J. Opt. A: Pure Appl. Opt. **11**, 114001 (2009).
- [184] A. Seidel, C. Ohrt, S. Passinger, C. Reinhardt, R. Kiyon, and B.N. Chichkov, *Nanoimprinting of dielectric loaded surface-plasmon-polariton waveguides using masters fabricated by 2-photon polymerization technique*, J. Opt. Soc. Am. B **62**, 810 (2009).
- [185] C. Reinhardt, S. Passinger, V. Zorba, B. N. Chichkov, and C. Fotakis, *Replica molding of picosecond laser fabricated Si microstructures*, Appl. Phys. A **87**, 673 (2007).
- [186] B. Fay, *Advanced optical lithography development, from UV to EUV*, Microelectron. Eng. **61-2**, 11 (2002).
- [187] T. Holmgaard, S.I. Bozhevolnyi, L. Markey, and A. Dereux, *Dielectric-loaded surface plasmon-polariton waveguides at telecommunication wavelengths: Excitation and characterization*, Appl. Phys. Lett. **92**, 011124 (2008).
- [188] J. Grandidier, G.C. des Francs, S. Massenot, A. Bouhelier, L. Markey, J. C. Weeber, C. Finot, and A. Dereux, *Gain-Assisted Propagation in a Plasmonic Waveguide at Telecom Wavelength*, Nano Lett. **9**, 2935 (2009).
- [189] S. Massenot, J. Grandidier, A. Bouhelier, G. C. des Francs, L. Markey, J. C. Weeber, A. Dereux, J. Renger, M. U. Gonzalez, and R. Quidant, *Polymer-metal waveguides characterization by Fourier plane leakage radiation microscopy*, Appl. Phys. Lett. **91**, 243102 (2007).

- [190] M. Rothschild, T. M. Bloomstein, N. Efremow, T. H. Fedynyshyn, M. Fritze, I. Pottebaum, and M. Switkes, *Nanopatterning with UV optical lithography*, MRS Bull. **30**, 942 (2006).
- [191] G. Möllenstedt and R. Speidel, *Elektronenoptischer Mikroschieber unter elektronenmikroskopischer Arbeitskontrolle*, Physikalische Blätter **14**, 192 (1960).
- [192] A. N. Broers, E. G. Lean, , and M. Hatzakis, *1.75-GHz Acoustic-Surface-Wave Transducer Fabricated by an Electron Beam*, Appl. Phys. Lett. **15**, 98 (1969).
- [193] A. N. Broers, A. C. F. Hoole, and J. M. Ryan, *Electron Beam Lithography - Resolution Limits*, Microelectron. Eng. **32**, 131 (1996).
- [194] U. Huebner, R. Boucher, W. Morgenroth, M. Schmidt, and M. Eich, *Fabrication of photonic crystal structures in polymer waveguide material*, Microelectron. Eng. **83**, 1138 (2006).
- [195] Y. Matsubara, J. Taniguchi, and I. Mimamoto, *Fabrication of three-dimensional hydrogen silsesquioxane resist structure using electron beam lithography*, Jpn. J. Appl. Phys. **45**, 5538 (2006).
- [196] T. Zentgraf, T. P. Meyrath, A. Seidel, S. Kaiser, and H. Giessen, *Babinet's principle for optical frequency metamaterials and nanoantennas*, Phys. Rev. B **76**, 033407 (2007).
- [197] G. Dolling, C. Enkrich, M. Wegener, C. M. Soukoulis, and S. Linden, *Simultaneous negative phase and group velocity of light in a metamaterial*, Science **312**, 892 (2006).
- [198] J. Stodolka, D. Nau, M. Frommberger, C. Zanke, H. Giessen, and E. Quandt, *Fabrication of two-dimensional hybrid photonic crystals utilizing electron beam lithography*, Microelectron. Eng. **78-79**, 442 (2005).
- [199] D. Watanabe, H. Kubota, Y. Ando, and T. Miyazaki, *A simple fabrication process using focused ion beam for deep submicron magnetic tunnel junctions*, Japan. J. Appl. Phys. **43**, 7489 (2004).
- [200] D. Ozkaya, R. M. Langford, W. L. Chan, and A. K. Petford-Long, *Effect of Ga implantation on the magnetic properties of permalloy thin films*, J. Appl. Phys. **91**, 9937 (2002).
- [201] A. Persson, G. Thornell, and H. Nguyen, *Rapid prototyping of magnetic tunnel junctions with focused ion beam processes*, J. Micromech. Microeng. **20**, 055039 (2010).
- [202] F. Cheng, *Photonic guiding structures in lithium niobate crystals produced by energetic ion beams*, J. Appl. Phys. **106**, 081101 (2009).

- [203] A. Dhawan, M. Gerhold, A. Madison, J. Fowlkes, P. E. Russell, T. Vo-Dinh, and D. N. Leonard, *Fabrication of Nanodot Plasmonic Waveguide Structures Using FIB Milling and Electron Beam-Induced Deposition*, *Scanning* **31**, 139 (2009).
- [204] A. Bertsch, S. Jiquet, P. Bernhard, and P. Renaud, *Microstereolithography: a review*, *Rapid Prototyping Technologies; Materials Research Society Symposium Proceedings* **758**, 3 (2003).
- [205] F. P. W. Melchels, J. Feijen, and D. W. Grijpma, *A review on stereolithography and its applications in biomedical engineering*, *Biomaterials* **31**, 6121 (2010).
- [206] A. Ovsianikov, A. Gaidukeviciute, B. N. Chichkov, M. Oubaha, B. D. MacCraith, I. Sakellari, A. Gaikoumaki, D. Gray, M. Vamvakaki, M. Farsari, and C. Fotakis, *Two-photon polymerization of hybrid sol-gel materials for photonics applications*, *Laser Chemistry* **2008**, 493059 (2008).
- [207] A. Ovsianikov, S. Z. Xiao, M. Farsari, M. Vamvakaki, C. Fotakis, and B. N. Chichkov, *Shrinkage of microstructures produced by two-photon polymerization of Zr-based hybrid photosensitive materials*, *Opt. Express* **17**, 2143 (2009).
- [208] A. Ovsianikov, J. Viertl, B. N. Chichkov, M. Oubaha, B. D. MacCraith, I. Sakellari, A. Gaikoumaki, D. Gray, M. Vamvakaki, M. Farsari, and C. Fotakis, *Ultra-low shrinkage hybrid photosensitive material for two-photon polymerization microfabrication*, *ACS Nano* **2**, 2257 (2008).
- [209] A. B. Evlyukhin, *Cross sections for surface plasmon polariton scattering from a nanoparticle in the dipole approximation*, *Tech. Phys. Lett.* **31**, 817 (2005).
- [210] A. B. Evlyukhin, E. V. Evlyukhina, A. L. Stepanov, R. Kiyani, and B. N. Chichkov, *Scattering of a surface plasmon polariton beam by chains of dipole nanoparticles*, *Appl. Phys. Lett. B* **93**, 203 (2008).
- [211] A. Taflove, *Application of the finite-difference time-domain method to sinusoidal steady state electromagnetic penetration problems*, *IEEE Trans. Electromagn. Compat.* **22**, 191–202 (1980).
- [212] Inc. RSoft Design Group, *FullWAVE 6.0 User Guide* (RSoft Design Group, Inc., Ossining, NY, 2007).
- [213] K. S. Yee, *Numerical solution of initial boundary value problems involving Maxwell's equations in isotropic media*, *IEEE Trans. Antennas Propagat.* **AP-14**, 302 (1966).
- [214] J. P. Berenger, *A perfectly matched layer for the absorption of electromagnetic waves*, *J. Comput. Phys.* **114**, 185 (1994).

- [215] R. Courant, K. Friedrichs, and H. Lewy, *Über die partiellen Differenzengleichungen der mathematischen Physik*, Math. Ann. **100**, 32 (1928).
- [216] A. I. Kuznetsov, A. B. Evlyukhin, C. Reinhardt, A. Seidel, R. Kiyam, W. Cheng, A. Ovsianikov, and B. N. Chichkov, *Laser-induced transfer of metallic nanodroplets for plasmonics and metamaterial applications*, J. Opt. Soc. Am. B **26**, B130 (2009).
- [217] L. D. Landau and E. M. Lifshitz, *Course of Theoretical Physics, Electrodynamics of Continuous Media* (Butterworth-Heinemann, Heidelberg, 1984).
- [218] C. F. Bohren and D. R. Huffman, *Absorption and scattering light by small particles* (Wiley-VCH, Weinheim, 1998).
- [219] C. Girard and A. Dereux, *Near-field optics theories*, Rep. Prog. Phys. **59**, 657 (1996).
- [220] T. Sondergaard and S. I. Bozhevolnyi, *Theoretical analysis of finite-size surface plasmon polariton band-gap structures*, Phys. Rev. B **71**, 125429 (2005).
- [221] T. Sondergaard and S. I. Bozhevolnyi, *Surface plasmon polariton scattering by a small particle placed near a metal surface: An analytical study*, Phys. Rev. B **69**, 045422 (2004).
- [222] A. B. Evlyukhin, G. Brucoli, L. Martín-Moreno, S. I. Bozhevolnyi, and F. J. García-Vidal, *Surface plasmon polariton scattering by finite-size nanoparticles*, Phys. Rev. B **76**, 075426 (2007).
- [223] K. L. Kelly, E. Coronado, L. L. Zhao, and G. C. Schatz, *The optical properties of metal nanoparticles: the influence of size, shape, and dielectric environment*, J. Phys. Chem. B **107**, 668 (2003).
- [224] B. T. Draine, *The discrete-dipole approximation and its application to interstellar graphite grains*, Astrophys. J. **333**, 848 (1988).
- [225] J. P. Kottmann and O. J. F. Martin, *Accurate solution of the volume integral equation for high-permittivity scatterers*, IEEE Trans. Antennas Propagat. **48**, 1719 (2000).
- [226] M. Paulus and O. J. F. Martin, *Light propagation and scattering in stratified media: a Green's tensor approach*, J. Opt. Soc. Am. A **18**, 854 (2001).
- [227] A. B. Evlyukhin and S. I. Bozhevolnyi, *Point-dipole approximation for surface plasmon polariton scattering: Implications and limitations*, Phys. Rev. B **71**, 134304 (2005).
- [228] A. V. Zayats, I. I. Smolyaninov, and A. A. Maradudin, *Nano-optics of surface plasmon polaritons*, Phys. Rep. **408**, 131–314 (2005).

- [229] M. Perner, T. Klar, S. Gross, U. Lemmer, G. von Plessen, W. Spirkl, and J. Feldmann, *Homogeneous line widths of surface plasmons in gold nanoparticles measured by femtosecond pump-and-probe and near-field optical spectroscopy*, Scanning **76-7**, 181 (J. Lumin.).
- [230] T. Holmgaard, Z. Chen, S.I. Bozhevolnyi, L. Markey, A. Dereux, and A. V. Krasavin, *Bend- and splitting loss of dielectric-loaded surface plasmon-polariton waveguides*, Opt. Express **16**, 13585 (2008).
- [231] T. Holmgaard, S.I. Bozhevolnyi, L. Markey, A. Dereux, A. V. Krasavin, P. Bolger, and A. V. Zayats, *Efficient excitation of dielectric-loaded surface plasmon-polariton waveguide modes at telecommunication wavelengths*, Phys. Rev. B **78**, 165431 (2008).
- [232] A. Drezet, A. L. Stepanov, H. Ditlbacher, A. Hohenau, B. Steinberger, F. R. Aussenegg, A. Leitner, and J. R. Krenn, *Surface plasmon propagation in an elliptical corral*, Appl. Phys. Lett. **86**, 074104 (2005).
- [233] A. Drezet, A. L. Stepanov, A. Hohenau, B. Steinberger, N. Galler, H. Ditlbacher, A. Leitner, F. R. Aussenegg, J. R. Krenn, M. U. Gonzalez, and J. C. Weeber, *Surface plasmon interference fringes in back-reflection*, Europhys. Lett. **74**, 693 (2006).
- [234] A. Drezet, A. Hohenau, D. Koller, A. L. Stepanov, H. Ditlbacher, B. Steinberger, F. R. Aussenegg, A. Leitner, and J. R. Krenn, *Leakage radiation microscopy of surface plasmon polaritons*, Mater. Sci. Eng., B **149**, 220 (2008).
- [235] J. Grandidier, S. Massenot, G. C. des Francs, A. Bouhelier, J. C. Weeber, L. Markey, A. Dereux, J. Renger, M. U. Gonzalez, and R. Quidant, *Dielectric-loaded surface plasmon polariton waveguides: Figures of merit and mode characterization by image and Fourier plane leakage microscopy*, Phys. Rev. B **78**, 245419 (2008).
- [236] D. G. Zhang, X. C. Yuan, and A. Bouhelier, *Direct image of surface-plasmon-coupled emission by leakage radiation microscopy*, Appl. Opt. **49**, 875 (2010).
- [237] A. Drezet, A. Hohenau, A. L. Stepanov, H. Ditlbacher, B. Steinberger, N. Galler, F. R. Aussenegg, A. Leitner, and J. R. Krenn, *How to erase surface plasmon fringes*, Europhys. Lett. **89**, 091117 (2006).
- [238] R. Charbonneau, P. Berini, E. Berolo, and F. Lisicka-Skrzek, *Long-range plasmon-polariton wave propagation in thin metal films of finite-width excited using an end-fire technique*, Applications of Photonic Technology 4 - Closing the Gap Between Theory, Development, and Application; Proc. SPIE **4087**, 534 (2000).

- [239] A. Lewis, M. Isaacson, A. Harootunian, and A. Muray, *Development of a 500-Å spatial resolution light microscope: I. light is efficiently transmitted through $\lambda/16$ diameter apertures*, Ultramicroscopy **13**, 227 (1984).
- [240] D. W. Pohl, W. Denk, and M. Lanz, *Optical stethoscopy: Image recording with resolution $\lambda/20$* , Appl. Phys. Lett. **44**, 651 (1984).
- [241] Y. Ohikane, T. Kataoka, M. Okuda, S. Hara, H. Inoue, and M. Nakano, *Observation of nanostructure by scanning near-field optical microscope with small sphere probe*, Sci. Technol. Adv. Mater. **8**, 181 (2007).
- [242] H. Ditlbacher, J. R. Krenn, N. Felidj, B. Lamprecht, G. Schider, M. Salerno, A. Leitner, and F. R. Aussenegg, *Fluorescence imaging of surface plasmon fields*, Appl. Phys. Lett. **80**, 404 (2001).
- [243] D. Heitmann, *Radiative decay of surface plasmons excited by fast electrons on periodically modulated silver surfaces*, J. Phys. C **10**, 397 (1977).
- [244] M. V. Bashevoy, F. Jonsson, A. V. Krasavin, N. I. Zheludev, Y. Chen, and M. I. Stockman, *Generation of Traveling Surface Plasmon Waves by Free-Electron Impact*, Nano Lett. **6**, 1113 (2006).
- [245] T. Suzuki and N. Yamamoto, *Cathodoluminescent spectroscopic imaging of surface plasmon polaritons in a 1-dimensional plasmonic crystal*, Opt. Express **17**, 23664 (2009).
- [246] A. Seidel, C. Reinhardt, T. Holmgaard, W. Cheng, T. Rosenzweig, K. Leosson, S. I. Bozhevolnyi, and B. N. Chichkov, *Demonstration of Laser-Fabricated DLSPPW at Telecom Wavelength*, IEEE Photonics Journal **2**, 421 (2010).
- [247] A. Seidel, J. Gosciniak, M. U. Gonzalez, J. Renger, C. Reinhardt, R. Kiyon, R. Quidant, S. I. Bozhevolnyi, and B. N. Chichkov, *Fiber-Coupled Surface Plasmon Polariton Excitation in Imprinted Dielectric-Loaded Waveguides*, International Journal of Optics **2**, 891497 (2010).
- [248] J. Nelayah, J. Gu, W. Sigle, C. T. Koch, I. Pastoriza-Santos, L. M. Liz-Marzan, and P. A. Aken, *Direct imaging of surface plasmon resonances on single triangular silver nanoprisms at optical wavelength using low-loss EFTEM imaging*, Opt. Lett. **34**, 1003 (2009).
- [249] H. J. Levinson, *Principles of Lithography* (SPIE Press, Bellingham, 2001).
- [250] C. Reinhardt, A. Seidel, A.B. Evlyukhin, W. Cheng, and B.N. Chichkov, *Mode-selective excitation of laser-written dielectric-loaded surface plasmon polariton waveguides*, J. Opt. Soc. Am. B: Opt. Phys. **26**, B55 (2009).
- [251] X. Guo, M. Qiu, J.M. Bao, B.J. Wiley, Q. Yang, X.N. Zhang, Y.G. Ma, H.K. Yu, and L.M. Tong, *Direct Coupling of Plasmonic and Photonic Nanowires for Hybrid Nanophotonic Components and Circuits*, Nano Lett. **9**, 4515 (2009).

- [252] J. Serbin, A. Ovsianikov, and B.N. Chichkov, *Fabrication of woodpile structures by two-photon polymerization and investigation of their optical properties*, Opt. Express **12**, 5221 (2004).
- [253] R. Kiyam, C. Reinhardt, S. Passinger, A. L. Stepanov, A. Hohenau, H. R. Krenn, and B. N. Chichkov, *Rapid prototyping of optical components for surface plasmon polaritons*, Opt. Express **15**, 4205 (2007).
- [254] S. Passinger, A. Seidel, C. Ohrt, C. Reinhardt, A. Stepanov, R. Kiyam, and B. N. Chichkov, *Novel efficient design of Y-splitter for surface plasmon polariton applications*, Opt. Express **16**, 14369 (2008).
- [255] L. Mach, *Ein neuer Interferenzrefraktor*, Zeitschrift für Instrumentenkunde **12**, 89–93 (1892).
- [256] L. Zehnder, *Über einen Interferenzrefraktor*, Zeitschrift für Instrumentenkunde **11**, 275–285 (1891).
- [257] Y. Ogiso, Y. Tsuchiya, S. Shinada, S. Nakajima, T. Kawanishi, and H. Nakajima, *High Extinction-Ratio Integrated Mach-Zehnder Modulator With Active Y-Branch for Optical SSB Signal Generation*, IEEE Photonics Technol. Lett. **22**, 941 (2010).
- [258] G. Testa, Y. J. Huang, P. M. Sarro, L. Zeni, and R. Bernini, *High-visibility optofluidic Mach-Zehnder interferometer*, Opt. Lett. **35**, 1584 (2010).
- [259] E. Mach, *Die Analyse der Empfindungen und das Verhältnis der Physischen zum Psychischen* (Fischer, Jena, 1900).
- [260] E. Mach, *Über Erscheinungen an fliegenden Projectilen* (Separatum ex Ver. nw. Kenntn., Wien, 1898).
- [261] J. Gosciniaak, S. I. Bozhevolnyi, T. B. Andersen, V. S. Volkov, J. Kjelstrup-Hansen, L. Markey, and A. Dereux, *Thermo-optic control of dielectric-loaded plasmonic waveguide components*, Opt. Express **18**, 1207 (2010).
- [262] A. V. Krasavin, P. M. Bolger, A. V. Zayats, T. Holmgaard, Z. Chen, S. I. Bozhevolnyi, L. Markey, and A. Dereux, *Active components for integrated plasmonic circuits*, IEEE/LEOS Winter Topicals Meeting **2009**, 40 (2009).
- [263] G. Nemova, A. V. Kabashin, and R. Kashyap, *Surface plasmon-polariton Mach-Zehnder refractive index sensor*, J. Opt. Soc. Am. B **25**, 1673 (2008).
- [264] T. Holmgaard, Z. Chen, S. I. Bozhevolnyi, L. Markey, and A. Dereux, *Dielectric-loaded plasmonic waveguide-ring resonators*, Opt. Express **17**, 2968 (2009).
- [265] B. Wang and G. P. Wang, *Plasmonic waveguide ring resonator at terahertz frequencies*, Appl. Phys. Lett. **89**, 133106 (2006).

- [266] N. Talebi, A. Mahjoubfar, and M. Shahabadi, *Plasmonic ring resonator*, J. Opt. Soc. Am. B **25**, 2116 (2008).
- [267] T. Holmgaard, Z. Chen, S. I. Bozhevolnyi, L. Markey, and A. Dereux, *Design and characterization of dielectric-loaded plasmonic directional couplers*, J. Lightw. Technol. **24**, 5521 (2009).
- [268] X. L. Wang, P. Wang, C. C. Chen, J. X. Chen, Y. H. Lu, H. Ming, and Q. W. Zhan, *Plasmonic racetrack resonator with high extinction ratio under critical coupling condition*, J. Appl. Phys. **107**, 124517 (2010).
- [269] U. Trutschel, F. Ouellette, V. Delisle, M. A. Dugay, G. Fogarty, and F. Lederer, *Polarization splitter based on antiresonant reflecting optical waveguides*, J. Lightwave Technol. **13**, 239 (1995).
- [270] J. Zhang, M. B. Yu, G. Q. Lo, and D. L. Kwong, *Silicon-Waveguide-Based Mode Evolution Polarization Rotator*, IEEE JOURNAL OF SELECTED TOPICS IN QUANTUM ELECTRONICS **16**, 53 (2010).
- [271] H. Fukuda, K. Yamada, T. Tsuchizawa, T. Watanabe, H. Shinojima, and S. I. Itabashi, *Polarization rotator based on silicon wire waveguides*, Opt. Express **16**, 2628 (2008).
- [272] R. M. de Ritter, A. F. M. Sander, A. Driessen, and J. H. J. Fluitman, *An integrated optic adiabatic TE/TM polarization splitter on silicon*, J. Lightwave Technol. **11**, 1806 (1993).
- [273] J. J. G. M. van der Tol, J. W. Peterson, E. G. R. Metall, Y. S. Oei, H. van Brug, and I. Moerman, *Mode evolution type polarization splitter on InGaAsP/InP*, IEEE Photon. Technol. Lett. **5**, 1412 (1993).
- [274] S. Maruo and J.T. Fourkas, *Recent progress in multiphoton microfabrication*, Laser & Photonics Reviews **2**, 100 (2008).
- [275] C. Reinhardt, R. Kiyon, S. Passinger, A. L. Stepanov, A. Ostendorf, and B. N. Chichkov, *Rapid laser prototyping of plasmonic components*, Appl. Phys. A **89**, 321 (2007).
- [276] A. Hohenau, J. R. Krenn, A. L. Stepanov, A. Drezet, H. Ditlbacher, B. Steinberger, A. Leitner, and F. R. Aussenegg, *Dielectric optical elements for surface plasmons*, Opt. Lett. **30**, 893 (2005).
- [277] S. Markatos, M. N. Zervas, and I. P. Giles, *Optical fiber surface-plasmon wave devices*, Electron. Lett. **24**, 287 (1988).
- [278] C. H. Dong, X. F. Ren, R. Yang, J. Y. Duan, J. G. Guan, G. C. Guo, and G. P. Guo, *Coupling of light from an optical fiber taper into silver nanowires*, Appl. Phys. Lett. **95**, 221109 (2009).

- [279] S. Park, J. J. Ju, J. T. Kim, M. S. Kim, S. K. Park, J. M. Lee, W. J. Lee, and M. H. Lee, *Sub-dB/cm propagation loss in silver stripe waveguides*, Opt. Express **17**, 697 (2009).
- [280] J. E. Goell, *A circular-harmonic computer analysis of rectangular dielectric waveguides*, Bell Syst. Tech. J. **48**, 2133 (1969).
- [281] E. A. J. Mercatili, *Dielectric Rectangular Waveguide and Directional Coupler for Integrated Optics*, Bell Syst. Tech. J. **48**, 2071 (1969).
- [282] K. Bierwirth, N. Schulz, and F. Arndt, *Finite-Difference Analysis of Rectangular Dielectric Waveguide Structures*, IEEE Trans. Microwave Theory Tech. **MTT34**, 1104 (1986).
- [283] B. Bhuian, R.J. Winfield, S. O'Brien, and G.M. Crean, *Investigation of the two-photon polymerisation of a Zr-based inorganic-organic hybrid material system*, Appl. Surf. Sci. **252**, 4845 (2006).
- [284] A. Drezet, D. Koller, A. Hohenau, A. Leitner, F. R. Aussenegg, and J. R. Krenn, *Plasmonic Crystal Demultiplexer and Multiports*, Nano Lett. **7**, 1697 (2007).
- [285] L. A. Sweatlock, S. A. Maier, and H. A. Atwater, *Microwave analogue to a sub-wavelength plasmon switch*, IEEE 53rd Electronic Components & Technology Conference **2003 Proceedings**, 1648 (2003).
- [286] C. Noguez, *Surface plasmons on metal nanoparticles: the influence of shape and physical environment*, J. Phys. Chem. C **111**, 3806 (2007).
- [287] M. Quinten, A. Leitner, J. R. Krenn, and F. R. Aussenegg, *Electromagnetic energy transport via linear chains of silver nanoparticles*, Opt. Lett. **23**, 1331 (1998).
- [288] M. L. Brongersma, J. W. Hartman, and H. A. Atwater, *Electromagnetic energy transfer and switching in nanoparticle chain arrays below the diffraction limit*, Phys. Rev. B **62**, R16356 (2000).
- [289] V. Lomakin, M. Lu, and E. Michielssen, *Optical wave properties of nanoparticle chains coupled with a metal surface*, Opt. Express **15**, 11827 (2007).
- [290] D. van Orden, Y. Fainman, and V. Lomakin, *Optical waves on nanoparticle chains coupled with surfaces*, Opt. Lett. **34**, 422 (2009).
- [291] K. Li, M. I. Stockman, and D. J. Bergman, *Self-similar chain of metal nanospheres as an efficient nanolens*, Phys. Rev. Lett. **91**, 227402 (2003).
- [292] J. Dai, F. Cajko, I. Tsukerman, and M. I. Stockman, *Electrodynamic effects in plasmonic nanolenses*, Phys. Rev. B **77**, 115419 (2008).

- [293] J. R. Krenn, H. Ditlbacher, G. Schider, A. Hohenau, A. Leitner, and F. R. Aussenegg, *Surface plasmon micro- and nano-optics*, J. Microsc. **209**, 167 (2003).
- [294] A. L. Stepanov, J. R. Krenn, H. Ditlbacher, A. Hohenau, A. Drezet, B. Steinberger, A. Leitner, and F. R. Aussenegg, *Quantitative analysis of surface plasmon interaction with silver nanoparticles*, Opt. Lett. **30**, 1524 (2005).
- [295] A. B. Evlyukhin, S. I. Bozhevolniy, A. L. Stepanov, and J. R. Krenn, *Splitting of a surface plasmon polariton beam by chains of nanoparticles*, Appl. Phys. B **84**, 29 (2006).
- [296] A. B. Evlyukhin, S. I. Bozhevolniy, A. L. Stepanov, R. Kiyani, C. Reinhardt, S. Passinger, and B. N. Chichkov, *Focusing and directing of surface plasmon polaritons by curved chains of nanoparticles*, Opt. Express **15**, 16667 (2007).
- [297] I. P. Radko, A. B. Evlyukhin, A. Boltasseva, and S. I. Bozhevolnyi, *Refracting surface plasmon polaritons with nanoparticle arrays*, Opt. Express **16**, 3924 (2008).
- [298] K. Li, X. Li, M. I. Stockman, and D. J. Bergman, *Surface plasmon amplification by stimulated emission in nanolenses*, Phys. Rev. B **71**, 115409 (2005).
- [299] M. I. Stockman, *Spasers explained*, Nature Photonics **2**, 327 (2008).
- [300] A. I. Kuznetsov, J. Koch, and B. N. Chichkov, *Laser-induced backward transfer of gold nanodroplets*, Opt. Express **17**, 18820 (2009).
- [301] D. A. Willis and V. Grosu, *Microdroplet deposition by laser-induced forward transfer*, Appl. Phys. Lett. **86**, 244103 (2005).
- [302] A. Boltasseva, T. Sondergaard, T. Nikolajsen, K. Leosson, S. I. Bozhevolnyi, and J. M. Hvam, *Propagation of long-range surface plasmon polaritons in photonic crystals*, J. Opt. Soc. Am. B **22**, 2027 (2005).
- [303] I. P. Radko, S. I. Bozhevolnyi, A. B. Evlyukhin, and A. Boltasseva, *Surface plasmon polariton beam focusing with parabolic nanoparticle chains*, Opt. Express **15**, 6576 (2007).
- [304] C. Reinhardt, R. Kiyani, A. Seidel, S. Passinger, A. L. Stepanov, A. B. Evlyukhin, and B. N. Chichkov, *Focusing and manipulation of surface plasmon polaritons by laser fabricated dielectric structures*, Plasmonics: Nanoimaging, Nanofabrication, and their Applications III; Proc. SPIE **6642**, 64205 (2007).
- [305] E. E. Narimanov and A. V. Kildishev, *Optical black hole: Broadband omnidirectional light absorber*, Appl. Phys. Lett. **95**, 041106 (2009).
- [306] Q. Cheng, T. J. Cui, W. X. Jiang, and B. G. Cai, *An omnidirectional electromagnetic absorber made of metamaterials*, New J. Phys. **12**, 063006 (2010).

- [307] D. A. Genov, S. Zhang, and X. Zhang, *Mimicking celestial mechanics in metamaterials*, Nat. Physics **5**, 687 (2009).
- [308] T. G. Mackay and A. Lakhtakia, *Towards a metamaterial simulation of a spinning cosmic string*, Phys. Lett. A **374**, 2305 (2010).
- [309] I. I. Smolyaninov, *Surface plasmon toy model of a rotating black hole*, New J. Phys. **5**, 147 (2003).
- [310] Q. Bai, J. Chen, N. H. Shen, C. Cheng, and H. T. Wang, *Controllable optical black hole in left-handed materials*, Opt. Express **18**, 2106 (2010).
- [311] I. I. Smolyaninov and C. C. Davis, *Linear and nonlinear optics of surface-plasmon whispering-gallery modes*, Phys. Rev. B **69**, 205417 (2004).

A List of Scientific Publications by the Author

A.1 List of Journal Articles

- B. N. Chichkov, R. Kiyam, C. Reinhardt, S. Passinger, A. Seidel, and A. L. Stepanov
Laser-based 2D and 3D nanomanufacturing for plasmonic applications
Int. J. Nanomanuf. **6**, Iss. 1/2/3/4, 3-11 (2010).
- D. Nau, A. Seidel, R. B. Orzekowsky, S.-H. Lee, S. Deb, and H. Giessen
Hydrogen sensor based on metallic photonic crystal slabs
Opt. Lett. **35**, Iss. 18, 3150–3152 (2010).
- C. Reinhardt, A. Seidel, A. B. Evlyukhin, W. Cheng, R. Kiyam, and B. N. Chichkov
Direct laser-writing of dielectric-loaded surface plasmon–polariton waveguides for the visible and near infrared
Appl. Phys. A **100**, Iss. 2, 347-352 (2010).
- A. Seidel, J. Gosciniak, M. U. Gonzalez, J. Renger, C. Reinhardt, R. Kiyam, R. Quidant, S. I. Bozhevolnyi, and B. N. Chichkov
Fiber-Coupled Surface Plasmon Polariton Excitation in Imprinted Dielectric-Loaded Waveguides
International Journal of Optics **2010**, 897829 (2010).
- A. Seidel, C. Reinhardt, T. Holmgaard, W. Cheng, T. Rosenzweig, K. Leosson, S. I. Bozhevolnyi, and B. N. Chichkov
Demonstration of Laser-Fabricated DLSPW at Telecom Wavelength
IEEE Photonics Journal **2**, Iss. 4, 652-658 (2010).
- A. B. Evlyukhin, C. Reinhardt, A. Seidel, B. S. Luk'yanchuk, and B. N. Chichkov
Optical response features of Si-nanoparticle arrays
Phys. Rev. B **82**, 045404 (2010).
- A. Kuznetsov, A. B. Evlyukhin, C. Reinhardt, A. Seidel, R. Kiyam, and B. N. Chichkov
Laser-induced transfer of metallic nanodroplets for plasmonics and metamaterial applications
J. Opt. Soc. Am. B **26**, Iss. 12, B130-B138 (2009).
- C. Reinhardt, A. Seidel, A. B. Evlyukhin, W. Cheng, and B. N. Chichkov
Mode-selective excitation of laser-written dielectric-loaded surface plasmon polariton waveguides
J. Opt. Soc. Am. B **26**, Iss. 12, B55-B60 (2009).

- A. Seidel, C. Ohrt, S. Passinger, C. Reinhardt, R. Kiyani, and B. Chichkov
Nanoimprinting of dielectric loaded surface plasmon-polariton waveguides from masters fabricated by 2-photon polymerization technique
J. Opt. Soc. Am. B **26**, Iss. 4, 810–812 (2009).
- S. Passinger, A. Seidel, C. Ohrt, C. Reinhardt, A. Stepanov, R. Kiyani, and B. Chichkov
Novel efficient design of Y-splitter for surface plasmon polariton applications
Opt. Express **16**, Iss. 19, 14369-14379 (2008).
- T. Zentgraf, T. P. Meyrath, A. Seidel, S. Kaiser, and H. Giessen, C. Rockstuhl and F. Lederer
Babinet's principle for optical frequency metamaterials and nanoantennas
Phys. Rev. B **76**, 033407 (2007).

A.2 List of Invited and Post Deadline Talks

- A. Seidel, A. Kuznetsov, A. Evlyukhin, C. Reinhardt, R. Kiyani, W. Cheng, A. Ovsianikov, and B. N. Chichkov
Creation of ordered arrays of metallic nanoparticles for plasmonics and meta-material applications by laser-induced transfer
Post deadline talk at the Annual General Meeting of the Surface Science Division , DPG Spring Meeting, March 2010, Regensburg (Germany), Verhandlungen DPG **VI** 45, 3/O 80 (2010).
- A. Seidel, C. Reinhardt, C. Ohrt, A. Ovsianikov, S. Passinger, and B. N. Chichkov
Fabrication of micromechanical and microoptical systems by two-photon polymerization
Invited seminar talk at the Institute of Radiobiology of the Bundeswehr (2008).
- A. Seidel
Teleportation
Invited seminar talk at the Institute of Radiobiology of the Bundeswehr (2008).

A.3 List of Conference Contributions and Proceedings

- A. Seidel, A. Kuznetsov, R. Kiyani, C. Reinhardt, and B. N. Chichkov
Investigations of Laser-Fabricated Plasmonic Structures at Telecom Wavelength
Ninth International Conference on Photonic and Electromagnetic Crystal Structures PECS-IX, September 2010, Granada (Spain), P89 A288 (2010).

- C. Reinhardt, A. Kuznetsov, A. B. Evlyukhin, W. Cheng, A. Seidel, and B. N. Chichkov
Theoretical modelling and leakage radiation microscopy of surface plasmon polariton excitation and scattering on laser fabricated surface structures
SPIE Photonics Europe, April 2010, Brussels (Belgium), 7712-08 (2010).
- A. Kuznetsov, C. Reinhardt, A. B. Evlyukhin, W. Cheng, A. Seidel, A. Ovsianikov, and B. N. Chichkov
Laser-induced transfer approach to fabrication of nanoparticle structures for nanophotonics
SPIE Photonics Europe, April 2010, Brussels (Belgium), 7712-15 (2010).
- C. Reinhardt, W. Cheng, A. Seidel, A. B. Evlyukhin, and B. N. Chichkov
Characterization of laser-written dielectric-loaded surface plasmon polariton waveguides by leakage radiation microscopy
SPIE Photonics Europe, April 2010, Brussels (Belgium), 7712-109 (2010).
- A. Seidel, W. Cheng, A. Evlyukhin, C. Reinhardt, and B. N. Chichkov
Efficient surface plasmon-polariton excitation on nanoparticle structures by inclined incident light
DPG Spring Meeting, March 2010, Regensburg (Germany), Verhandlungen DPG VI 45, 3/O 44.11 (2010).
- B.N. Chichkov, M. Farsari, R. Kiyani, C. Reinhardt, and A. Seidel
Guiding of surface plasmon polaritons in laser fabricated structures
18th International Laser Physics Workshop - LPHYS'09, July 2009, Barcelona (Spain), 8.2.6 (2009).
- A. Seidel, R. Wilhelm, C. Ohrt, R. Kiyani, Y. Acar, C. Reinhardt, and B. N. Chichkov
Fibre-Coupled Plasmonics
Fourth International Conference on Surface Plasmon Photonics - SPP4, June 2009, Amsterdam (the Netherlands), P-TUE-014-D (2009).
- C. Reinhardt, A. Seidel, R. Wilhelm, C. Ohrt, R. Kiyani, Y. Acar, A. Gaidukeviciute, M. Farsari, C. Fotakis, and B. N. Chichkov
Nanoimprinting waveguiding plasmonic components
Fourth International Conference on Surface Plasmon Photonics - SPP4, June 2009, Amsterdam (the Netherlands), P-TUE-011-A (2009).
- C. Reinhardt, A. Gaidukeviciute, V. Melissinaki, R. Wilhelm, A. Seidel, K. Terzaki, A. Giakoumaki, M. Vamvakaki, M. Farsari, C. Fotakis, and B. N. Chichkov
2D and 3D isotropic metamaterials
Fourth International Conference on Surface Plasmon Photonics - SPP4, June 2009, Amsterdam (the Netherlands), P-MON-034-B (2009).

- A. L. Stepanov, R. Kiyan, C. Reinhardt, A. Seidel, S. Passinger, and B. N. Chichkov
Rapid laser prototyping of polymer-based nanoplasmonic components
NATO ASI - Nanostructured Materials for Advanced Technological Applications; Springer (2009).
- A. Seidel, C. Ohrt, R. Kiyan, S. Passinger, C. Reinhardt, and B. N. Chichkov
Dielectric loaded surface plasmon-polariton waveguides from 2-photon polymerization-made master structures by nanoimprint lithography
Nanometa, January 2009, Seefeld in Tirol (Austria), Wed4f.78 (2009).
- D. Nau, R. B. Orzekowsky, A. Seidel, T. P. Meyrath, and H. Giessen
A Hydrogen Sensor Based on Metallic Photonic Crystal Slabs
2008 Conference on Lasers and Electro-Optics & Quantum Electronics and Laser Science Conference **1-9**, 3012-3013 (2008).
- A. L. Stepanov, A. B. Evlyukhin, R. Kiyan, S. Passinger, A. Seidel, and B. N. Chichkov
Excitation and focusing of surface plasmon polaritons by nanostructuring
Proceedings of the Society of Photo-Optical Instrumentation Engineers (SPIE) **6988**, 98804-98804 (2008).
- A. Seidel, C. Ohrt, C. Reinhardt, S. Passinger, R. Kiyan, and B. N. Chichkov
2-photon polymerization as highly flexible lithography technique
International Congress on Applications of Lasers & Electro-Optics - ICALEO, October 2008, Temecula, CA (USA), N402 (2008).
- A. Seidel, C. Ohrt, W. Cheng, C. Reinhardt, S. Passinger, R. Kiyan, and B. N. Chichkov
High speed two-photon polymerization structuring of 3D microstructures
International Congress on Applications of Lasers & Electro-Optics - ICALEO, October 2008, Temecula, CA (USA), M1203 (2008).
- C. Reinhardt, R. Kiyan, A. Seidel, S. Passinger, A. Stepanov, A. Evlyukhin, and B. Chichkov
Focusing and manipulation of surface plasmons by laser fabricated dielectric structures
Plasmonics: Nanoimaging, Nanofabrication, and Their Applications III, Proc. SPIE **6642**, 64205-64205 (2007).

B Curriculum Vitae

Name	Andreas Peter Christian Seidel
Date of Birth	27 th of January, 1981
Place of Birth	Heidelberg, Germany
Nationality	German
Marital Status	married, no children
Address	Nanotechnology Department Laser Zentrum Hannover e.V. Hollerithallee 8 30419, Hannover Germany
Telephone	+49 (0)511 2788 437
Telefax	+49 (0)511 2788 100
Email	a.seidel@lzh.de
Education	
1986 - 1991	St. Richard's with St. Andrew's Primary School (London, United Kingdom)
1991 - 1995	Aloisiuskolleg (Bonn-Bad Godesberg, Germany)
1995 - 1998	Deutsche Schule Singapur (Singapore, Singapore)
1998 - 2000	Aloisiuskolleg (Bonn-Bad Godesberg, Germany), Abitur
2000 - 2001	Military Service (Bundeswehr, Germany)
2001 - 2007	Student of physics at the University of Bonn (Bonn, Germany), graduated as Diplom-Physiker Topic: A Photonic-Crystal-Based Hydrogen Sensor: Fundamentals and Prototype Development
2007 - 2010	PhD student of physics at the University of Hannover and Laser Zentrum Hannover (Hannover, Germany) Topic: Plasmonic Components Fabricated by Two-Photon Polymerization and Nanoimprint Lithography
Academic Appointments	
2006 - 2007	Assistant researcher at the University of Stuttgart (Stuttgart, Germany)
2007 - 2008	Scientific assistant at the Hannoversches Zentrum für Optische Technologien (Hannover, Germany)
2007 -	Scientific assistant at the Laser Zentrum Hannover (Hannover, Germany)

C Acknowledgements

A major scientific work is rarely the work of only one single person, or even only a small number of people. Very many people collaborated to make this work possible, and I would like to take this opportunity to address words of gratitude to all of them.

First of all, I would like to acknowledge the splendid support of Prof. Dr. Boris Chichkov, head of the Nanotechnology Department at the Laser Zentrum Hannover e.V., whose scientific guidance and institutional support is the primary reason this work could be performed at all.

Special thanks go to Dr. Carsten Reinhardt, head of the Nanophotonics Group at the Laser Zentrum Hannover e.V., for the frequent giving of substantial aid, advice, and encouragement. Many of the results in this work find their origins in one or another of his imaginative and refreshing scientific ideas, and he should be given a large amount of credit for his enduring and exceptional support.

I would also like to acknowledge the constant and highly professional counsel and assistance given by Dr. Roman Kiyon and Dr. Ulf Hinze, who provided critical and useful stimuli, and who, in more than one case, made crucial suggestions when the fate of this entire work seemed to hang in the balance.

Much of this work stems from a collaborative project with international partners, of whom many must receive some credit for the part they had as collaborators and partners in this work. Thanks go to Prof. Dr. Sergey I. Bozhevolnyi and Jacek Gosciniak of the University of Southern Denmark and Tobias Holmgaard of Aalborg University. I am also indebted to Stephane Tisserand, Fabien Reservat and Thierry Berthou of the company SILIOS in Rousset, France.

Credit also goes to Prof. Dr. Andrey Evlyukhin concerning the work on the Green's Function Method numerical simulations, and to Ralf Wilhelm for his cooperation concerning the FDTD simulations.

Further thanks go to my colleagues Kestutis Kurselis, Dr. Arseniy Kuznetsov, Christoph Ohrt and Wei Cheng, with whom I had frequent fruitful discussions, which greatly aided the progress of this work. Particular thanks goes to Prof. Dr. Andrey Stepanov and Melanie Welge, who made the completion of this work anything but boring.

I would like to express my gratitude to the large number of assistant researchers, who spent time working on projects which eventually influenced this thesis, particularly Albertas Zukauskas, who was a great help both during 2PP fabrication and sample characterization, but also to Rebecca Cotton, Michael Reisgies, Jan Gosman and Mathias Nguyen Ba.

Finally, and perhaps most importantly, I would like to thank my family for their loyal support throughout the course of my academic studies of physics in Bonn, Stuttgart, and Hannover, both my parents and my sister Antje. I am especially grateful to the aid provided by my mother regarding the early and ancient glasses discussed in the introduction of this work. Above all, for her continuous loving care, and much else besides, I would like to thank my dear wife Victoria.

